LONGITUDINAL DOUBLE-SPIN ASYMMETRIES FOR DI-JET PRODUCTION AT INTERMEDIATE PSEUDORAPIDITY IN POLARIZED P+P COLLISIONS AT $\sqrt{s}$ = 200 GEV

Ting Lin

Submitted to the faculty of the University Graduate School
in partial fulfillment of the requirements
for the degree
Doctor of Philosophy
in the Department of Physics,
Indiana University
December, 2017

Accepted by the Graduate Faculty, Indiana University, in partial fulfillment of the requirements for the degree of Doctor of Philosophy.

Doctoral Committee

Scott W. Wissink, Ph.D (Chair)

Charles J. Horowitz, Ph.D

William W. Jacobs, Ph.D

Rex Tayloe, Ph.D

December 5, 2017

Copyright ©2017
Ting Lin

Acknowledgements

I would like to thank my adviser, Scott Wissink, thank you for your guidance and patience during my graduate study. To Will Jacobs, thanks for teaching me everything about the Endcap Electromagnetic Calorimeter and all the useful discussions about my research. It was really great to work with you both. I would also like to acknowledge and thank Rex Tayloe and Charles Horowitz for the support as my committee members.

I also would like to thank former group member Brian Page who initialized this study and has done a lot work, thanks for your comments and further suggestions on this work. I want to thank Mike Skoby, who is also a former member of our local group, he guided me to the things needed as an EEMC software coordinator. I would also like to thank the remaining members of the IU STAR/Belle group: Anselm Vossen, Hairong Li, William Solyst, Dmitry Kalinkin, Huanzhao Liu and Joe Kwasizur, thanks for the friendship and helpful discussion in the past four years.

In addition, I want to thank the members of the STAR jet-finder group: Elke Aschenauer, Carl Gagliardi, Renee Fatemi, Zilong Chang, Grant Webb, James Drachenberg, Oleg Eyser, Danny Olvitt, Kevin Adkins and all the other members of the group. Thanks for the very useful discussions and suggestions on my research. I also want to thank the members from Valparaiso University: Shirvel Stanislaus, Adam Gibson and Donald Koetke for the useful discussion in the Endcap Electromagnetic Calorimeter calibration. I am also grateful to the STAR software and computing group: Jerome Lauret, Gene Van Buren and Jason Webb for their guidance when I served as an EEMC software coordinator.

Finally, to my parents, Guorong Lin and Bihua Lin, my elder sister Jia Lin, thanks for encouraging me to pursue a dream, thanks for your love and support over the passed decades.

Ting Lin

LONGITUDINAL DOUBLE-SPIN ASYMMETRIES FOR DI-JET PRODUCTION AT INTERMEDIATE PSEUDORAPIDITY IN POLARIZED P+P COLLISIONS AT $\sqrt{s} = 200$ GEV

The spin of the proton can be decomposed into the contributions from the intrinsic quark spin, the partonic orbital angular momentum and the gluon spin. The contributions from the spins of quarks within the proton are well constrained by Deep Inelastic Scattering (DIS) experiments, but determining the orbital angular momentum and the gluon helicity distribution inside the proton remain important challenges in nuclear physics. The Relativistic Heavy Ion Collider (RHIC) provides a unique facility to unravel the internal structure and the QCD dynamics of nucleons by colliding beams of high-energy polarized protons, which enable direct studies of the gluon via the gluon-gluon and quark-gluon scattering processes.

We present the first measurement of longitudinal double-spin asymmetries A_{LL} for dijets within the intermediate pseudorapidity range $0.8 < \eta < 1.8$. The dijets are produced in polarized pp collisions at a center-of-mass energy $\sqrt{s} = 200$ GeV. Values for A_{LL} are determined for several distinct event topologies, defined by the jet pseudorapidities, and span a range of Bjorken-x down to $x \approx 0.01$, a regime where the gluon helicity distribution $\Delta g(x)$ is poorly constrained. The measured asymmetries are found to be consistent with the predictions of global analyses that incorporate the results of previous STAR measurements.

Scott W. Wissink, Ph.D (Chair)

Charles J. Horowitz, Ph.D

William W. Jacobs, Ph.D

Rex Tayloe, Ph.D

Contents

1 Introduction **1**

1.1 Quantum Chromodynamics and the Parton Model 1
  1.1.1 Inelastic $e - p$ Scattering 1
  1.1.2 The Parton Model 3
  1.1.3 Scaling Violations 5
  1.1.4 Parton Distribution Function Measurements 5
1.2 Proton Helicity Structure and the Spin Crisis 9
  1.2.1 Polarized Deep Inelastic Scattering 9
  1.2.2 The Proton Spin Puzzle 13
  1.2.3 Polarized Parton Distribution Functions 17
1.3 Gluon Polarization at RHIC 21
  1.3.1 Inclusive Jet Analysis 22
  1.3.2 Di-jet Analysis 24
1.4 Jets at Higher Pseudorapidity 29
1.5 Dissertation Structure 30

2 Experimental Facilities and Detectors **31**

2.1 The Relativistic Heavy Ion Collider 31
  2.1.1 Spin Dynamics and Siberian Snakes 33
  2.1.2 Measuring Beam Polarization in RHIC 34
  2.1.3 Zero-Degree Calorimeters (ZDC) 36

2.1.4 Beam Beam Counter (BBC) 37

2.2 Solenoidal Tracker at RHIC (STAR) 38

2.2.1 Time Projection Chamber (TPC) 39

2.2.2 Barrel Electromagnetic Calorimeter (BEMC) 39

2.2.3 Endcap Electromagnetic Calorimeter (EEMC) 40

2.2.4 EEMC Calibration 42

2.3 Data Sample 50

2.3.1 Data Quality Assurance 50

2.3.2 Trigger System 51

3 Jet Reconstruction and Di-jet Selection 54

3.1 Jet Reconstruction 54

3.1.1 Jet Algorithms 55

3.1.2 Jet Selection 57

3.2 Di-Jet Selection 60

3.3 Di-Jet Kinematics 62

3.4 Trigger Selection 63

4 Simulation Studies 65

4.1 Simulation / Embedding Details 65

4.2 Levels of Jet Information 66

4.3 Data - Simulation Comparison 67

4.3.1 Jet Association 68

4.4 'Fudge Factor' Reweighting of the p_T Bins 71

4.4.1 Weight and Fudge Factor Issues 71

4.4.2 Fudge Factor Reweighting 72

5 Underlying Events 75

5.1 Off-Axis Cone Method 76

5.2 Underlying Event Correction 77

6 Experimental Methods in the EEMC 80

6.1 Challenges in the Forward (EEMC) Region 80

6.2 Machine Learning Approaches 80

6.2.1 Artificial Neural Networks 81

6.2.2 Other Machine Learning Methods 84

6.3 Jet p_T Corrections 86

6.3.1 Variable Selection 86

6.3.2 Corrections to the Jet Transverse Momentum 87

6.4 Regression Performance Evaluation 91

6.4.1 Variable Correlation 91

6.4.2 Overtraining 91

6.4.3 Di-Jet p_T Imbalance 93

6.5 Jet Mass Correction 95

6.6 Other Jet Corrections 99

7 Double-spin Asymmetries 103

7.1 Beam Polarization 104

7.2 Spin Patterns 105

7.3 Relative Luminosities 106

7.4 False Asymmetries 107

7.5 Data Corrections 111

7.5.1 Dijet Invariant Mass Shift 111

7.5.2 Trigger and Reconstruction Bias 111

7.6 Systematic Errors 117

7.6.1 Residual Transverse Component 117

7.6.2 Underlying Events Asymmetry 119

7.6.3 Jet Energy Scale 120
7.6.4 Tracking Efficiency Uncertainty 122
7.6.5 Dijet Mass Shift Systematic 124
7.6.6 Underlying Events Systematic Errors on Dijet Mass 124
7.6.7 PYTHIA Tune Uncertainties 125
7.6.8 Jet p_T and Mass Correction Systematic Uncertainties 127
7.7 Final Results 130
7.8 Comparison to Theory 136

8 Conclusions and Outlook 138

A List of Runs and Fills Used in this Analysis 141

B Some Derivations 146
B.1 Di-jet Kinematics Derivation 146
B.1.1 Di-jet Invariant Mass 146
B.1.2 Scattering Kinematic Approximations 147
B.2 A_{LL} Derivation 150
B.2.1 Double Spin Asymmetry, A_{LL} 150
B.2.2 A_{LL} Uncertainty 151
B.3 χ^2 Derivation 152

C Code Structure and Parameters 155
C.1 EEMC Gains Into the Simulation 155
C.2 TMVA Parameters 155

References 157

Curriculum Vitae

List of Figures

1.1 Schematic diagram of the Deep Inelastic Scattering process. 2

1.2 The proton structure function F_2^p as function of Q^2 at a wide range of fixed x values (from Particle Data Group [12]) 6

1.3 The bands are Bjorken-x times the unpolarized a), b) parton distributions f(x) obtained in NNLO NNPDF3.0 global analysis at scales $\mu^2 = 10\ GeV^2$ (left) and $\mu^2 = 10\ GeV^4$ (right), with $\alpha_s^{M_Z^2} = 0.118$. The corresponding polarized parton distributions are shown c), d), obtained in NLO with NNPDFpol1.1 (from Particle Data Group [12]) 8

1.4 World data for $g_1(x, Q^2)$ for the proton with $Q^2 > 1 GeV^2$ and $W > 2.5 GeV$. For clarity a constant $c_i - 0.28(11.6 - i)$ has been added to the g_1 values within a particular x bin starting with i=0 for x=0.006. Error bars are statistical errors only (from [19]). 13

1.5 Gluon density from the LSS group [34]. 17

1.6 Gluon helicity distributions at $Q^2 = 10\ GeV^2$ for the new fit, the original DSSV analysis, and for an updated analysis without using the new 2009 RHIC data sets ($DSSV*$). The dotted lines present the gluon densities for alternative fits that are within the 90% C.L. limits [35]. 18

1.7 90% C.L. areas in the plane spanned by the truncated moments of Δg computed for $0.05 \leq x \leq 1$ and $0.001 \leq x \leq 0.05$ at $Q^2 = 10\ GeV^2$. Results for DSSV, DSSV* and new analysis, with the symbols corresponding to the respective central values of each fit, are shown. 19

1.8 Gluon helicity distribution from the NNPDF group [17]. 20

1.9 Feynman diagram for the gg, qg and qq sub processes (from left to right). 22

1.10 Inclusive jet cross section fraction for the subprocesses gg, gq, qq from NLO calculations [38]. 23

1.11 Mid-rapidity ($|\eta| < 0.5$ upper panel) and forward rapidity ($0.5 < |\eta| < 1$, lower panel) inclusive jet A_{LL} vs. parton jet p_T, compared to predictions from several NLO global analyses. The error bars are statistical. The gray boxes show the size of the systematic uncertainties [39]. 24

1.12 A_{LL} vs. x_T for inclusive jet production at mid-rapidity in 200 GeV (blue) [39] and 510 GeV (red) [41] p+p collisions, compared to NLO predictions from three recent NLO global analyses. 25

1.13 Values of gluon x_1 and x_2 obtained from the PYTHIA detector level simulation for the same-sign (upper) and opposite-sign (lower) dijet topologies, compared to the gluon x distributions for inclusive jets scaled by an additional factor of 20 in each panel [46]. 26

1.14 The particle-level dijet differential cross section measured by the STAR experiment (points plotted at bin center). The lower panel provides a relative comparison to theory [46]. 27

1.15 Di-jet A_{LL} vs. parton-level invariant mass for the same-sign (top) and opposite-sign (bottom) topological configurations measured by the STAR experiment [46]. 28

1.16 Gluon helicity integral with different starting x value from DSSV analysis [48]. . . 29

1.17 STAR tracking efficiency vs. pseudorapidity. 30

2.1 Layout of the RHIC facility for polarized proton operation [49]. 31

2.2 A cross section of the RHIC pC polarimeter setup. 35

2.3 Schematic layout of the H-jet polarimeter. 36

2.4 Setup of inner and outer hexagonal tile annuli for BBC East and BBC West. 37

2.5 Cross sectional view of the STAR detectors. 38

2.6 Schematic EEMC tower structure. 41
2.7 SMD ADC - pedestal spectrum. 44
2.8 Pre-shower 1, ADC - pedestal spectrum before the MIP cuts (upper plot) and after the MIP cuts (lower plot). 45
2.9 Tower, ADC - pedestal spectrum before the MIP cuts (upper plot) and after the MIP cuts (lower plot). 46
2.10 2009 pp200 final tower gains vs. η bins. 47
2.11 Jet η distribution using 2006 EEMC gains. 47
2.12 Jet η distribution using 2009 EEMC gains. 47
2.13 2009 pp 200 GeV di-photon invariant mass distribution. 48
2.14 2009 pp 200 GeV EEMC Relative Gain Comparison. 49
2.15 2012, 2013, 2017 EEMC Relative Gain Comparison. 49

3.1 Track: number of fit points vs. η from data. 58
3.2 Track: number of fit points vs. η from simulation. 58
3.3 Average jet particle over detector level p_T ratio vs. detector η with different number of fit points required. 59

4.1 Z vertex distribution for L2All. 67
4.2 Z vertex distribution for JPAll. 67
4.3 Di-jet invariant mass L2All. 67
4.4 Di-jet invariant mass JPAll. 67
4.5 Hi p_T jet p_T L2All. 68
4.6 Hi p_T jet p_T JPAll. 68
4.7 Hi p_T jet ϕ L2All. 69
4.8 Hi p_T jet ϕ JPAll. 69
4.9 Hi p_T jet η L2All. 69
4.10 Hi p_T jet η JPAll. 69

4.11 Barrel jet R_T L2All. 70

4.12 Endcap jet R_T L2All. 70

4.13 Fraction of the total jet transverse energy found within a cone of radius ΔR centered on the reconstructed thrust axis, illustrating the jet profile. 70

4.14 Pythia partonic p_T distribution: without fudge factors. 71

4.15 Pythia partonic p_T distribution: without fudge factors. 72

4.16 Pythia partonic p_T distribution: with fudge factors. 72

4.17 Pythia partonic p_T distributions: the black line is generated using the bin range from 0 to ∞; the other colors are from separate bins. 73

4.18 Pythia partonic p_T cross section ratio: integrated bins over the separate bins. 74

4.19 Simulation: dijet invariant mass distribution with and without reweighting. 74

4.20 Simulation: jet p_T distribution with and without reweighting. 74

5.1 Geometry of the off-axis cone method. 77

5.2 Jet P_T comparision after underlying event subtraction. 78

5.3 Jet p_T before and after underlying event subtraction. 79

5.4 Jet mass before and after underlying event subtraction. 79

5.5 Di-jet mass before and after underlying event subtraction. 79

6.1 Multilayer perceptron with one hidden layer, from Ref. [77]. 82

6.2 Schematic view of a decision tree from Ref. [77]. Starting from the root node, a sequence of binary splits using the discriminating variables x_i is applied and each split uses the variable that gives the best separation between signal and background at this node. The same variable may thus be used at several nodes, while others might not be used at all. The leaf nodes at the bottom end of the tree are labeled ‘S’ for signal and ‘B’ for background, depending on the majority of events that end up in the respective nodes. For regression trees, the node splitting is performed on the variable that gives the maximum decrease in the average squared error when attributing a constant value of the target variable as output of the node, given by the average of the training events in the corresponding (leaf) node. 85
6.3 p_T shift: JP2 Endcap jet particle/detector p_T ratio vs. detector η; upper left: before shift; upper right - variable: p_T, $\eta_{detector}$; lower left: add R_t; lower right: add R_t and p_T^{Barrel}. 87
6.4 p_T shift: Barrel jet particle/detector p_T ratio vs. detector η for different triggers. . . 88
6.5 p_T shift: Barrel jet particle/output from the machine learning p_T ratio vs. detector η for different triggers. 89
6.6 p_T shift: Endcap jet particle/detector p_T ratio vs. detector η for different triggers. . 90
6.7 p_T shift: Endcap jet particle/output from the machine learning p_T ratio vs. detector η for different triggers. 90
6.8 Correlation between different variables for Endcap jet p_T corrections. 92
6.9 Convergence test for the MLP method. 93
6.10 Average quadratic deviations for different machine learning methods. 94
6.11 Uncorrected relative difference in p_T for back-to-back Barrel-Endcap di-jets. 94
6.12 Corrected relative difference in p_T for back-to-back Barrel-Endcap di-jets. 94
6.13 Correlation between different variables for Endcap jet mass corrections. 95
6.14 Mass shift: Barrel jet particle/detector mass ratio vs. detector η for different triggers. 97

6.15 Mass shift: Barrel jet particle/output from the machine learning mass ratio vs. detector η for different triggers. 97
6.16 Mass shift: Endcap jet particle/detector mass ratio vs. detector η for different triggers. 98
6.17 Mass shift: Endcap jet particle/output from the machine learning mass ratio vs. detector η for different triggers. 98
6.18 Barrel jet particle - detector η difference vs. detector η for different triggers. 100
6.19 Endcap jet particle - detector η difference vs. detector η for different triggers. . . . 100
6.20 Barrel jet particle - detector ϕ difference vs. detector η for different triggers. 101
6.21 Endcap jet particle - detector ϕ difference vs. detector η for different triggers. . . . 101
6.22 Di-jet mass comparision between the particle level and detector level: particle level over detector level ratio before the corrections are made (upper left); particle level over detector level after the corrections (upper right); difference ratio before corrections (lower left); difference ratio after corrections (lower right). 102

7.1 Dijet false asymmetries: Barrel-Endcap full topology. 109
7.2 Dijet false asymmetries: EastBarrel-Endcap. 109
7.3 Dijet false asymmetries: WestBarrel-Endcap. 110
7.4 Dijet false asymmetries: Endcap-Endcap. 110
7.5 Dijet invariant mass shifts for Barrel-Endcap dijet full topology (upper left), East Barrel-Endcap (upper right), West Barrel-Endcap (lower left) and Endcap-Endcap topology. 113
7.6 Dijet NNPDF 100 replica A_{LL} of the Barrel-Endcap full topology: parton level (upper left), detector level (upper right), parton level fit extractions (lower left) and final corrections (lower right). 115
7.7 Dijet NNPDF 100 replica A_{LL} of the East Barrel-Endcap: parton level (upper left), detector level (upper right), parton level fit extractions (lower left) and final corrections (lower right). 115

7.8 Dijet NNPDF 100 replica A_{LL} of the West Barrel-Endcap: parton level (upper left), detector level (upper right), parton level fit extractions (lower left) and final corrections (lower right). 116

7.9 Dijet NNPDF 100 replica A_{LL} of the Endcap-Endcap: parton level (upper left), detector level (upper right), parton level fit extractions (lower left) and final corrections (lower right). 116

7.10 2006 inclusive jet δA_{Σ} as function of the jet transverse momentum p_T. 119

7.11 Dijet underlying events systematic: δA_{LL}, Barrel-Endcap full topology (upper left), East Barrel-Endcap (upper right), West Barrel-Endcap (lower left) and Endcap-Endcap(lower right). 120

7.12 Dijet mass shift due to tracking inefficiency: 7% track loss (blue) and no track loss (red); Barrel Endcap Full topology (upper left); EastBarrel Endcap (upper right); WestBarrel Endcap (lower left); Lower right-Endcap Endcap (lower right). 124

7.13 Dijet underlying event delta mass comparison for different topologies. 125

7.14 Dijet PYTHIA tune systematic: Barrel-Endcap full topology (upper left), East Barrel-Endcap (upper right), West Barrel-Endcap (lower left) and Endcap-Endcap (lower right). 127

7.15 *pp* 200 GeV Dijet kinematics for Barrel-Endcap full topology (upper left), East Barrel-Endcap (upper right), West Barrel-Endcap (lower right) and Endcap-Endcap (lower left) for the lowest dijet invariant mass bin 16.0 – 19.0 GeV/c^2. x_1 is always associated with the parton moving initially toward the Endcap. 132

7.16 Dijet A_{LL} vs. parton-level invariant mass for Barrel-Endcap full topology. 134

7.17 Dijet A_{LL} vs. parton-level invariant mass for Endcap-Endcap topology. 134

7.18 Dijet A_{LL} vs. parton-level invariant mass for East Barrel-Endcap (upper plot) and West Barrel-Endcap (lower plot). 135

8.1 *pp* 500 GeV dijet kinematics for Barrel-Barrel same sign (upper left), Barrel-Barrel opposite sign (upper right) and inclusive jet (black line); Barrel-Endcap full topology (middle left), East Barrel-Endcap(middle right), West Barrel-Endcap (lower right) and Endcap-Endcap (lower left). 140

List of Tables

2.1 2009 jet patch geometry. 52

2.2 2009 jet patch thresholds. Set 1 ends with run 10125061. 52

4.1 Pythia jet embedding weight factors. 72

7.1 The four spin patterns used in 2009. The ‘+’ indicates positive helicity and the ‘-’ indicates negative helicity. 105

7.2 Spin pattern and polarization states. 105

7.3 Dijet parton level corrections for Barrel-Endcap and Endcap-Endcap topologies. . . . 112

7.4 Dijet parton level corrections for the two Barrel-Endcap topologies. 112

7.5 Transverse polarization factors before rotator adjustment. 118

7.6 Transverse polarization factors after rotator adjustment. 118

7.7 Average R_t for each jet in dijet mass bins. 123

7.8 Average R_t for each jet in dijet mass bins. 123

7.9 PYTHIA tune and its variants. 126

7.10 Dijet invariant mass systematics. 128

7.11 Dijet invariant mass systematic. 129

7.12 Dijet A_{LL} systematics. 129

7.13 Dijet A_{LL} systematics. 130

7.14 Dijet A_{LL}: full topology. 131

7.15 Dijet A_{LL}: Barrel-Endcap different topologies. 131

7.16 χ^2 and r_1, r_2 for data/theory comparison for the DSSV model. 137

7.17 χ^2 and r_1, r_2 for data/theory comparison for the NNPDF model. 137

CHAPTER 1

Introduction

1.1 Quantum Chromodynamics and the Parton Model

The proton is an essential part of the nucleus. It was first discovered by Ernest Rutherford in 1917, by passing an alpha particle through nitrogen gas, using the $^{14}N + \alpha \rightarrow {}^{17}O + p$ nuclear reaction. In 1933, the large anomaloous magnetic moment of the proton was measured by Otto Stern, which suggested that the proton possesses internal structure. In the 1960s, the quark model [1], [2], [3] was confirmed by experiments at the Stanford Linear Accelerator Center (SLAC) [4] [5]. The development of Quantum Chromodynamics (QCD) in the 1970s demonstrated that quarks are confined inside the proton and are asymptotically free, the strong interactions are mediated by massless gluons [6] [7].

The existence and properties of the proton can be explained by a local quantum field theory based on the gauge group SU(3). From experimental measurements, the proton is found to be a complex dynamical system comprised of quarks, gluons, and antiquarks. As will be discussed below, Deep Inelastic Scattering has contributed significantly to our understanding of the internal structure of proton. The QCD and parton model have been discussed in detail in many books and articles [8]. An overview of DIS can be found in [9] [10] [11].

1.1.1 Inelastic $e - p$ Scattering

The cross section of electron-proton elastic scattering process decreases rapidly with energy due to the finite size of the proton. Consequently, high energy $e - p$ interactions are dominated

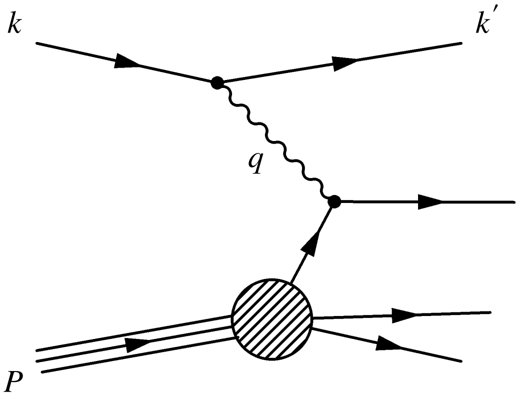

Figure 1.1: Schematic diagram of the Deep Inelastic Scattering process.

by inelastic scattering processes in which the proton breaks up. A schematic diagram of the deep inelastic scattering process is shown in Fig. 1.1. In the lab frame, we define E and $E^{'}$ as the incoming and outgoing electron energies, and θ as the angle between $\vec{k}$ and $\vec{k}'$. The cross section can be written as:

$$(\frac{d\sigma}{d\Omega dE'})_{lab} = \frac{\alpha_e^2}{4\pi m_p q^4}\frac{E^{'}}{E}L^{\mu\nu}W_{\mu\nu}. \tag{1.1}$$

where $L^{\mu\nu}$ is the leptonic tensor, which encodes polarization information for the electron, or equivalently, the off-shell photon. The hadronic tensor $W^{\mu\nu}$ gives the rate for $\gamma^* p \rightarrow anything$ which includes an integral over all the phase space for all final state particles. The variables used are $Q = \sqrt{-q^2} > 0$, the energy scale of the collision, and

$$x = \frac{Q^2}{2P \cdot q} \tag{1.2}$$

which is known as Bjorken-x. Detailed discussion can be found in [8]. The laboratory cross section can be expressed in terms of the scattering angle θ as:

$$(\frac{d\sigma}{d\Omega dE'})_{lab} = \frac{\alpha_e^2}{8\pi E^2 sin^4\frac{\theta}{2}}[\frac{m_p}{2}W_2(x,Q)cos^2\frac{\theta}{2} + \frac{1}{m_p}W_1(x,Q)sin^2\frac{\theta}{2}]. \tag{1.3}$$

This equation has been set up so W_1 and W_2 can be completely determined by measuring only the energy and angular dependence of the outgoing electron. Sometimes for convenience, the dimensionless structure functions are used here:

$$F_1(x) = \frac{1}{4\pi} W_1(x), \; F_2(x) = \frac{Q^2}{8\pi x} W_2(x). \tag{1.4}$$

The first systematic studies of proton structure functions were obtained in a series of experiments at the Stanford Linear Accelerator Center (SLAC) [5]. The first observation, known as **Bjorken scaling**, was that both $F_1(x, Q^2)$ and $F_2(x, Q^2)$ are (almost) independent of Q^2. The Q^2 independence of the structure function is strongly suggestive of scattering from point-like constituents within the proton. The second observation was that in the deep inelastic scattering regime, where Q^2 is greater than a few GeV^2, the two structure functions are not independent, but satisfy the **Callan-Gross relation**:

$$F_2(x, Q^2) = 2x F_1(x, Q^2). \tag{1.5}$$

This observation can be explained by the **parton model** which assumes that the underlying process in electron-proton inelastic scattering is the elastic scattering of electrons from point-like spin-half constituent particles within the proton, namely the quarks. In this case, the electric and magnetic contributions to the scattering process are related by the fixed magnetic moment of the particles.

1.1.2 The Parton Model

The defining assumption of the parton model, originally due to Feynman, is that some objects called partons within the proton are essentially free. If we assume that there exist partons within the proton, some of which are charged, then in DIS the electron was scattered elastically off partons of mass m_q, allowing the structure functions to be determined.

For elastic parton scattering, assume that the parton has some fraction ξ of the proton's momentum, so the scattered parton's initial momentum is $p_i^\mu = \xi P^\mu$. If p_f^μ is its final momentum, using the conservation law $p_i^\mu + q^\mu = p_f^\mu$, then squaring both sides gives $m_q^2 + 2p_i \cdot q + q^2 = m_q^2$, which means $\frac{Q^2}{2p_i \cdot q} = 1$. Thus, in the parton model, we find that $x = \xi$. By measuring x, we can determine the fraction of the proton's momentum involved in the parton-level scattering.

Suppose the partons are weakly interacting. Then the form factors are expected to have only a weak, logarithmic dependence on Q^2 when the initial partonic momentum is fixed, that is, at fixed x. The cross section's approximate independence of Q^2 at fixed x is known as **Bjorken scaling**, as shown in Fig. 1.2.

Another important ingredient embedded in the parton model is the **parton distribution function (PDF)**, which assumes a classical probability $f_i(\xi)d\xi$ of a photon hitting a parton species i with momentum fraction ξ. The physical justification of PDFs is that the separation of scales $Q \gg \Lambda_{QCD}$ allows us to treat the wave functions as being decoherent; more details can be found in QFT books (factorization) [8].

With PDFs, the ep cross section can be written as follows:

$$\sigma(e^- p^+ \to e^- X) = \sum_i \int_0^1 d\xi f_i(\xi) \hat{\sigma}(e^- p_i \to e^- X), \tag{1.6}$$

where p_i is a parton with momentum $p_i^\mu = \xi P^\mu$. Assuming the partons are free except for the QED interactions, the electron can only scatter off the charged particles, known as quarks. Then the $e^- q \to e^- q$ cross section is just the pointlike scattering cross section in QED, given by the Rosenbluth formula. Integrating over the incoming quark momentum, we can re-write the cross section as:

$$(\frac{d\sigma}{d\Omega dE'})_{lab} = \sum_i f_i(x) \frac{\alpha_e^2 e_i^2}{4E^2 sin^4\frac{\theta}{2}} [\frac{2m_p}{Q^2} x^2 cos^2\frac{\theta}{2} + \frac{1}{m_p} sin^2\frac{\theta}{2}], \tag{1.7}$$

where e_i is the charge of the quark.

Comparing the cross section with the one given in equation 1.3, we find that:

$$W_1(x, Q) = 2\pi \sum_i e_i^2 f_i(x), \tag{1.8}$$

$$W_2(x,Q) = 8\pi \frac{x^2}{Q^2} \sum_i e_i^2 f_i(x). \tag{1.9}$$

So $W_1(x,Q) = \frac{Q^2}{4x^2} W_2(x,Q)$ for $Q \gg m_p$. This is known as the **Callan-Gross relation** or $F_1(x) = \frac{1}{2x} F_2(x) = \frac{1}{2} \sum_i e_i^2 f_i(x)$. Bjorken scaling is confirmed by the experimental data, as shown in Fig. 1.2.

1.1.3 Scaling Violations

While Bjorken scaling holds over a wide range of x values, relatively small deviations are observed at very low and very high values of x. As shown in Fig. 1.2, there is some weak (logarithmic) Q^2 dependence visible. This behaviour is known as **scaling violation**. These scaling violations are not only expected, but the observed Q^2 dependence is calculable in QCD. By combining perturbative QCD and the parton model, the Q^2 dependence of the PDFs is calculable using the parton evolution function known as the DGLAP (after Dokshitzer, Gribov, Lipatov, Altarelli and Parisi) evolution equation [13], [14], [15], which allows us to re-sum large logarithms in the structure function. These equations are based on universal parton splitting functions for the QCD processes $q \to qg$ and $g \to q\bar{q}$. The observed scaling violations in deep inelastic scattering therefore provide a powerful validation of the fundamental QCD theory of the strong interaction.

1.1.4 Parton Distribution Function Measurements

Parton distribution functions must satisfy some constraints. Inside the proton, the quark flavor is conserved, so $\int d\xi |f_d(\xi) - f_{\bar{d}}(\xi)| = 1$ and $\int d\xi |f_u(\xi) - f_{\bar{u}}(\xi)| = 2$, while these integrals must be zero for strange, bottom, top and charm quarks. There is no conserved gluon number, so f_g has no associated sum rule. The classical probability following momentum conservation can be written as:

$$\sum_j \int d\xi |\xi f_j(\xi)| = 1. \tag{1.10}$$

In practice, information about the parton distribution functions of the proton can be extracted from many high-energy measurements involving protons, such as: fixed-target electron-proton and

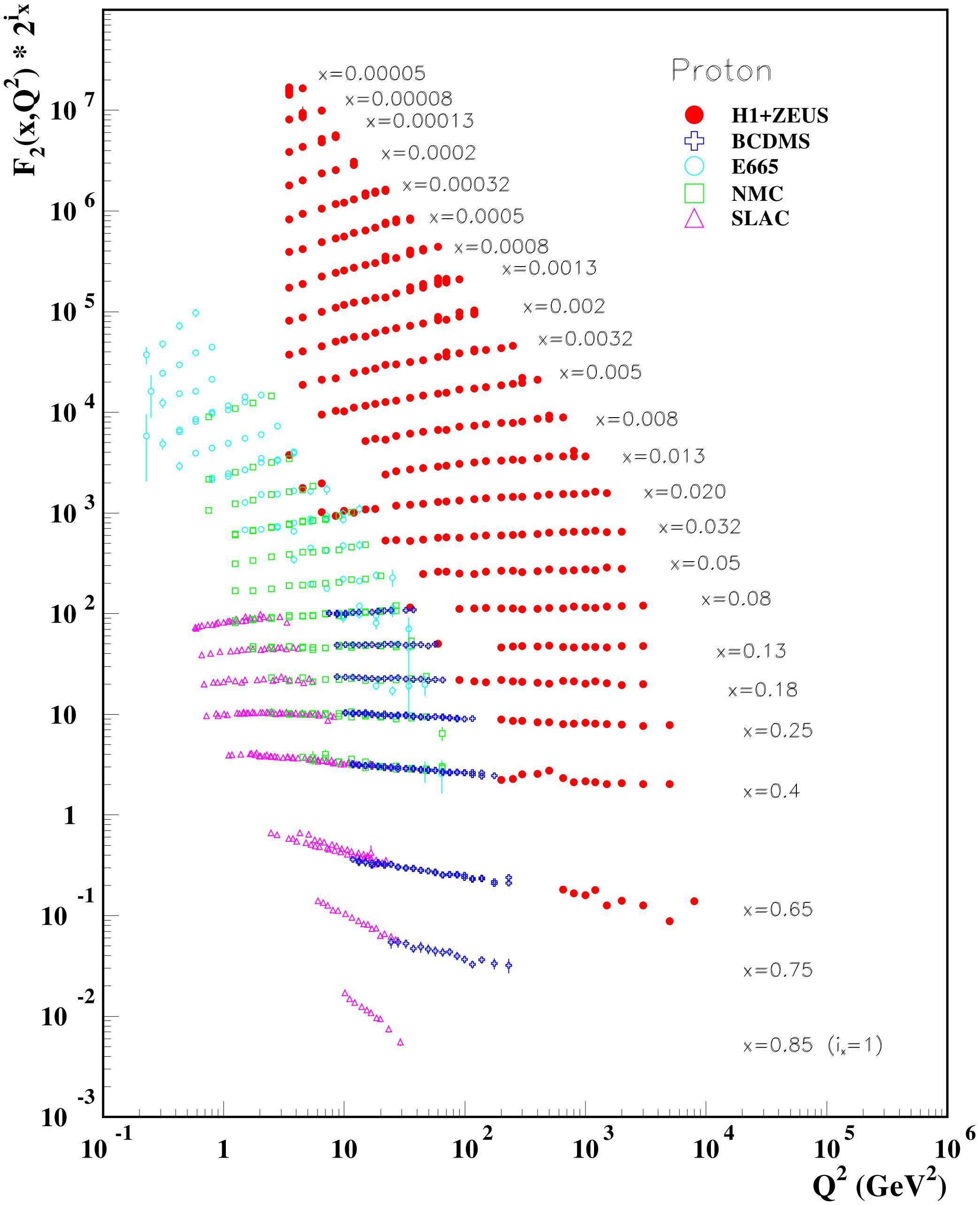

Figure 1.2: The proton structure function F_2^p as function of Q^2 at a wide range of fixed x values (from Particle Data Group [12])

electron-neutron scattering; high-energy electron-proton collider data; neutrino-nucleon scattering data; high-energy $p\bar{p}$ collider data from the Tevatron; very-high-energy pp collider data from the LHC; and Drell-Yan data from Fermilab. The different experimental measurements provide complementary information about the PDFs.

The proton PDFs are then extracted from a global fit to a wide range of experimental data. Owing to the complementary nature of the different measurements, tight constraints on the PDFs are obtained. In practice, the PDFs are varied, subject to the constraints imposed by the theoretical framework of QCD such as the DGLAP evolution equations, to obtain the best agreement with experimental data. The output of this procedure is a set of PDFs at a particular Q^2 scale. Fig. 1.3 shows the unpolarized parton distribution functions from NNLO NNPDF3.0 [16] (upper two plots) and polarized parton distribution functions from NLO NNPDFpol1.1 [17] (lower two plots). The contribution from gluons is large and, as expected, is peaked towards low values of x. The antiquark PDFs are relatively small and, because the antiquarks originate from $g \to q\bar{q}$, also are peaked towards low values of x. Finally, it is worth noting that although the PDFs for $\bar{u}$ and $\bar{d}$ are similar, there is a small difference, with $\bar{d}(x) > \bar{u}(x)$. This may be explained by a relative suppression of the $g \to u\bar{u}$ process due to the exclusion principle and the larger number of up-quark states which are already occupied.

Numerically, it turns out that $\int d\xi \ \xi(f_u(\xi) + f_d(\xi)) \approx 0.38$. Thus, only 38% of the proton momentum is contained in the valence quarks (u and d). The gluon content of the proton should be 35% to 50% depending on the scale. The remainder of the proton momentum is in sea quarks (meaning s, c, or b quarks and $\bar{d}$, $\bar{u}$, $\bar{c}$, $\bar{s}$ or $\bar{b}$ antiquarks).

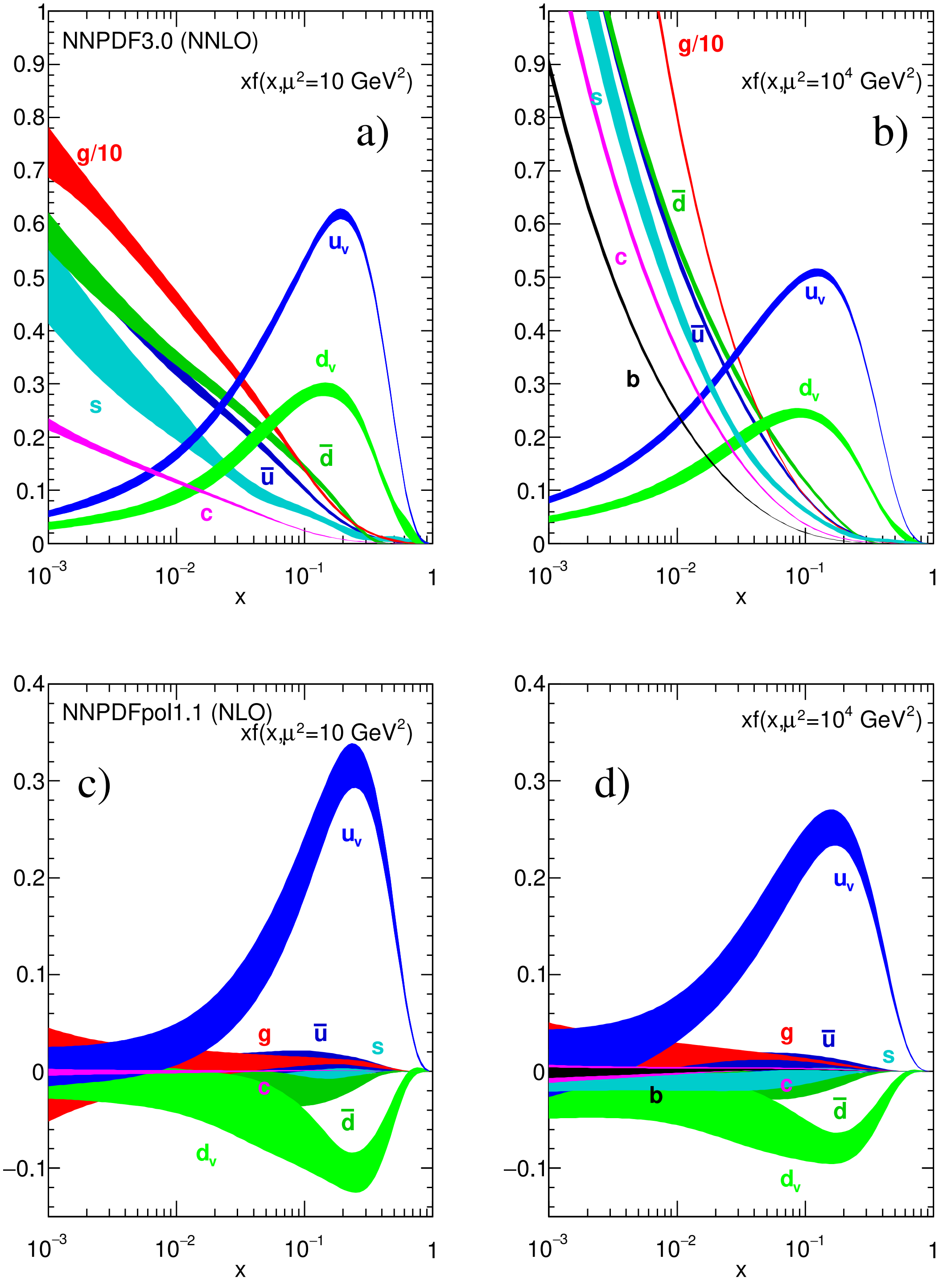

Figure 1.3: The bands are Bjorken-x times the unpolarized a), b) parton distributions f(x) obtained in NNLO NNPDF3.0 global analysis at scales $\mu^2 = 10\ GeV^2$ (left) and $\mu^2 = 10\ GeV^4$ (right), with $\alpha_s^{M_Z^2} = 0.118$. The corresponding polarized parton distributions are shown c), d), obtained in NLO with NNPDFpol1.1 (from Particle Data Group [12])

1.2 Proton Helicity Structure and the Spin Crisis

Understanding the spin structure of the proton is a fundamental question in strong interaction physics. The proton is a spin $\frac{1}{2}$ fermion, a complex system of quarks and transient quark-antiquark pairs, bound together by gluons. Unlike the charge, a simple vector sum of the valence quarks' spin can not fully describe the spin content of the proton. The formalism of the previous section was derived under the assumption that the spins of the incoming and outgoing lepton, as well as that of the target, were all averaged out. Tremendous progress has been made recently in unraveling the proton's spin structure. The details can be found in the reviews: [18], [19], [20] and [21].

1.2.1 Polarized Deep Inelastic Scattering

As has been discussed before, deep inelastic lepton-hadron scattering (DIS) played a seminal role in the development of our present understanding of the sub-structure of elementary particles. Polarized deep inelastic scattering (pDIS), involving the collision of a longitudinally polarized lepton beam with a longitudinally or transversely polarized target, can provide complementary and equally important insight into the structure of the nucleon.

Different polarization configurations in the experiments emphasize different aspects of the spin structure. Measurements with longitudinally polarized targets and beams tell us about the helicity distributions of quarks and gluons in the nucleon, which at leading order can be thought of as the difference in probability of finding a parton with longitudinal polarization parallel or anti-parallel to that of the nucleon. Measurements with transversely polarized targets are particularly sensitive to quark transverse spin and partonic orbital angular momenta. The longitudinal polarization has been studied in several experiments with good precision. Studies of transverse degrees of freedom in the nucleon and in fragmentation processes are a current subject of experimental investigation with sensitivity to spin-orbit couplings in QCD.

Similar to what has been calculated before, but using the variables $\nu = \frac{p \cdot q}{M} = E - E^{'}$, $y = \frac{p \cdot q}{p \cdot k} = \frac{\nu}{E}$

and $\gamma = \frac{2Mx}{Q}$, the unpolarized differential cross section can be rewritten as [22]:

$$\frac{d^2\sigma \uparrow\Downarrow}{dxdy} + \frac{d^2\sigma \uparrow\Uparrow}{dxdy} = \frac{2\pi\alpha^2}{MEx^2y^2}[(1 - y - \frac{Mxy}{2E})F_2(x, Q^2) + xy^2F_1(x, Q^2)], \tag{1.11}$$

where the $\uparrow\downarrow$ denote the longitudinal polarization of the lepton beam and the longitudinal polarization of the proton target is denoted as $\Uparrow\Downarrow$. The longitudinally polarized differential cross section is:

$$\frac{d^2\sigma \uparrow\Downarrow}{dxdy} - \frac{d^2\sigma \uparrow\Uparrow}{dxdy} = \frac{4\alpha^2}{MExy}[(2 - y - \frac{Mxy}{E})g_1(x, Q^2) - \frac{2Mx}{E}g_2(x, Q^2)], \tag{1.12}$$

while the cross section for the transversely polarized nucleons is:

$$\frac{d^2\sigma \uparrow\Rightarrow}{dxdy} - \frac{d^2\sigma \uparrow\Leftarrow}{dxdy} = \frac{-8\alpha^2}{MExy}\gamma\sqrt{1 - y - \frac{xy}{2E}}[yg_1(x, Q^2) + 2g_2(x, Q^2)], \tag{1.13}$$

The spin-dependent structure functions are g_1 and g_2, and the mass of the lepton is neglected. Details of the derivation can be found in [19]. With these equations, **the cross section asymmetry** for longitudinal polarization is defined by:

$$A_{||} = \frac{\Delta\sigma}{2\bar{\sigma}} \cong D\frac{g_1(x, Q^2)}{F_1(x, Q^2)}, \tag{1.14}$$

The coefficient D can be directly calculabled from the kinematic factors [23]. This asymmetry is the main result of most experiments in polarized DIS, and can provide access to the spin structure function g_1 using the unpolarized structure function.

For a longitudinally polarized target, the g_2 contribution to the differential cross-section and the longitudinal spin asymmetry is suppressed relative to the g_1 contribution by the kinematic factor $M/E \ll 1$. For a transversely polarized target, however, this kinematic suppression factor for g_2 is missing, implying that for transverse polarization it is vital to measure g_2.

At the constituent level, by angular momentum conservation, spin effects in DIS can be intuitively understood by the fact that a spin $\frac{1}{2}$ parton having its spin projection along the reference axis can absorb a virtual photon which has its spin projection along the opposite direction and then flip its spin, while no absorption can occur when the two spins in the initial state are oriented in the same direction. Hence it is customary to introduce the **virtual photon asymmetries** $A_{1,2}$ [23]:

$$A_1 = \frac{\sigma_{\frac{1}{2}} - \sigma_{\frac{3}{2}}}{\sigma_{\frac{1}{2}} + \sigma_{\frac{3}{2}}} = \frac{g_1 - \frac{Q^2}{\nu^2} g_2}{F_1}, \tag{1.15}$$

$$A_2 = \frac{2\sigma_{TL}}{\sigma_{\frac{1}{2}} + \sigma_{\frac{3}{2}}} = \frac{Q}{\nu} \frac{g_1 + g_2}{F_1}, \tag{1.16}$$

where $\sigma_{\frac{1}{2}}$ and $\sigma_{\frac{3}{2}}$ are the cross sections for the absorption of a transversely polarized photon with its spin polarized anti-parallel and parallel, respectively, to the spin of the longitudinally polarized nucleon, while σ_{TL} is a term arising from the interference between transverse and longitudinal amplitudes.

The asymmetry $A_{||}$ can be related to the virtual photon asymmetries by $A_{||} = D(A_1 + \eta A_2)$, where D and η are associated kinematic factors [24]. It is also possible to express g_1 (to first order) in terms of $\gamma = \sqrt{2Mx/Ey}$:

$$g_1 = F_1(A_1 + \gamma A_2) \tag{1.17a}$$
$$= F_1(\frac{A_{||}}{D} + (\gamma - \eta)A_2) \tag{1.17b}$$
$$\simeq \frac{F_1 A_{||}}{D}. \tag{1.17c}$$

In some experiments, A_2 can be neglected in certain kinematic ranges, hence the structure function g_1 can be evaluated directly using the polarized cross section asymmetries. Most detailed discussioins can be found in [24].

At high Q^2 (the Bjorken limit, or Deep Inelastic Scattering (DIS) regime), the structure functions F_1, F_2 and g_1 exhibit approximate scaling. They are to a very good approximation independent of Q^2 and depend only on Bjorken-x (Fig. 1.4 shows the world data on g_1). As noted before, F_1 and

F_2 satisfy the Callan-Gross relation:

$$F_1(x) = \frac{1}{2x}F_2(x) = \frac{1}{2}\sum_i e_i^2 f_i(x). \tag{1.18}$$

and similarly the polarized structure function is:

$$g_1(x) = \frac{1}{2}\sum_i e_i^2 \Delta f_i(x). \tag{1.19}$$

Here e_i denotes the electric charge of the parton i and

$$f_i(x) = f_i^{\uparrow}(x) + f_i^{\downarrow}(x) \tag{1.20}$$

$$\Delta f_i(x) = f_i^{\uparrow}(x) - f_i^{\downarrow}(x) \tag{1.21}$$

denote the spin-independent (unpolarized) and spin-dependent quark parton distributions, respectively, which characterize the distribution of quark momentum and spin in the proton [19]. For example, $f_i^{\uparrow}(x)$ is interpreted as the probability to find a parton i with the momentum fraction x and spin polarized in the same direction as the spin of the target proton.

Concerning the second spin structure function, there are many different, inconsistent results for $g_2(x)$ in the literature [18]. In fact there is no unambiguous way to extract g_2 in the simple parton model. An explanation of this problem can be found in [18], section 3.3 and 3.4.

We can define $q(x) = f_q(x) + f_{\bar{q}}(x)$ as the sum of quarks and anti-quarks of flavor q. When we integrate out the momentum fraction x, the quantity $\Delta q = \int_0^1 dx \Delta f(x)$ is interpreted as the fraction of the proton's spin which is carried by quarks (and anti-quarks) of flavor q. Hence summing over the up, down, and strange quark Δq contributions, gives the total fraction of the proton's spin carried by the spins of these quarks.

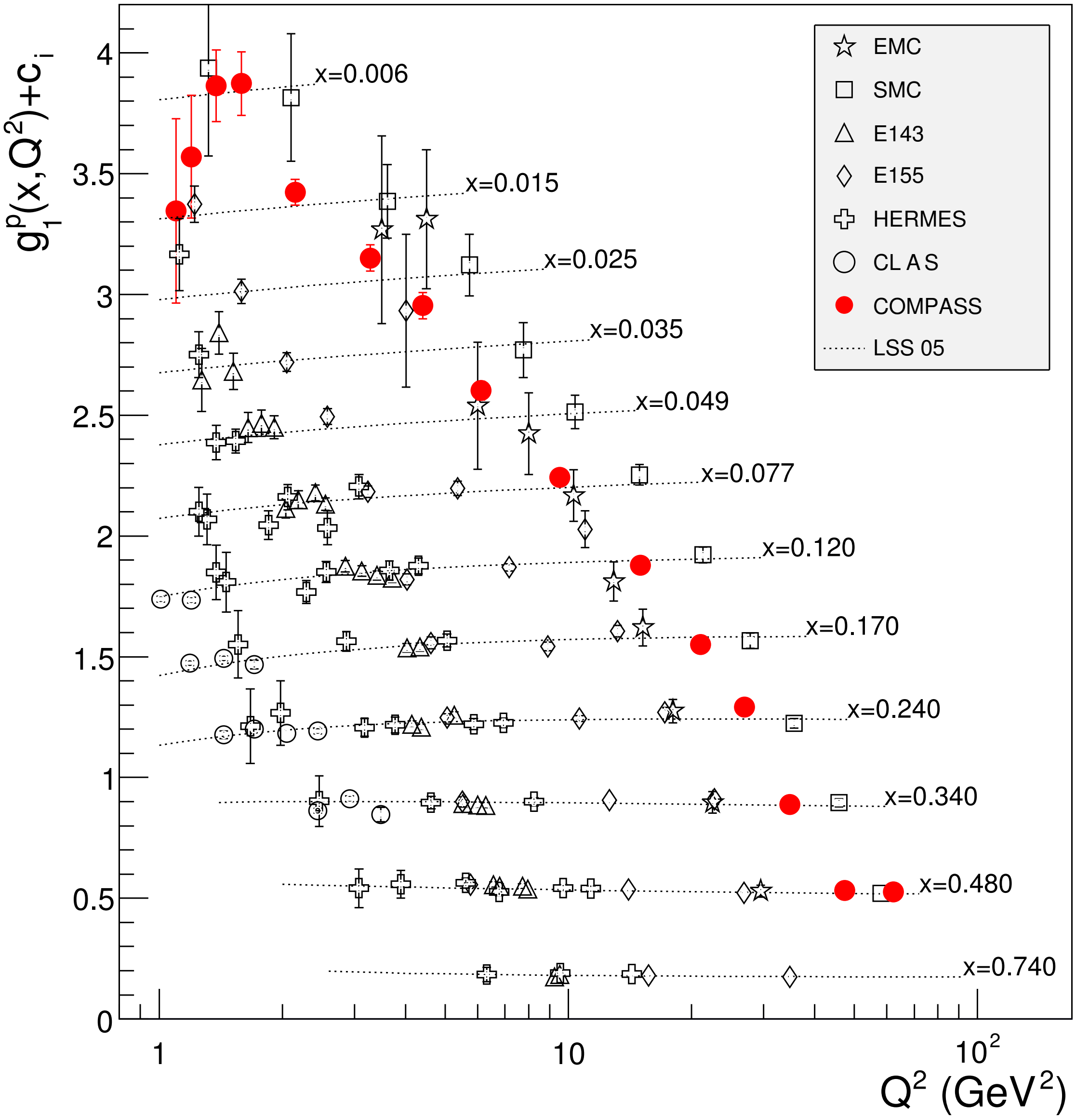

Figure 1.4: World data for $g_1(x, Q^2)$ for the proton with $Q^2 > 1GeV^2$ and $W > 2.5GeV$. For clarity a constant $c_i - 0.28(11.6 - i)$ has been added to the g_1 values within a particular x bin starting with i=0 for x=0.006. Error bars are statistical errors only (from [19]).

1.2.2 The Proton Spin Puzzle

The expression for $g_1(x)$ can be rewritten in terms of the linear combinations of quark densities which have specific transformation properties under the group of flavor transformations SU(3):

$$\Delta q_3 = (\Delta u + \Delta\bar{u}) - (\Delta d + \Delta\bar{d}), \tag{1.22}$$

$$\Delta q_8 = (\Delta u + \Delta \bar{u}) + (\Delta d + \Delta \bar{d}) - 2(\Delta s + \Delta \bar{s}), \tag{1.23}$$

$$\Delta \Sigma = (\Delta u + \Delta \bar{u}) + (\Delta d + \Delta \bar{d}) + (\Delta s + \Delta \bar{s}). \tag{1.24}$$

These transform, respectively, as the third component of an isotopic spin triplet, the eighth component of an SU(3) octet, and a flavor singlet. We can express $g_1(x)$ in the form:

$$g_1(x) = \frac{1}{9}\Big[\frac{3}{4}\Delta q_3 + \frac{1}{4}\Delta q_8 + \Delta\Sigma\Big]. \tag{1.25}$$

The integral of $g_1(x)$ can be expressed in terms of the naive parton model:

$$\int_0^1 dx g_1(x) = \frac{1}{9}\Big[\frac{3}{4}a_3 + \frac{1}{4}a_8 + a_0\Big], \tag{1.26}$$

where a_3, a_8 and a_0 are the corresponding integrals [22]. The quantity a_0 is therefore interpreted as the fraction of the proton's spin which is carried by the intrinsic spin of its quark and anti-quark constituents.

The European Muon Collaboration reported their measurements in 1989 [24]. They found that for the proton, $\int_0^1 dx g_1^p(x) = 0.126 \pm 0.010 \pm 0.015$. Using the QCD corrected g_1^p expression based on the sum rule developed by Bjorken [25]:

$$\int_0^1 dx g_1^p(x) = \frac{1}{9}\{[1 - \frac{\alpha_s}{\pi}][\frac{3}{4}a_3 + \frac{1}{4}a_8] + [1 - \frac{33-8f}{33-2f}\frac{\alpha_s}{\pi}]a_0\}, \tag{1.27}$$

where f is the number of quark flavors, $(1 - \frac{\alpha_s}{\pi})$ arises from QCD radiative corrections, and knowing $a_s = 0.27 \pm 0.02$, $a_3 = 1.254 \pm 0.006$ and $a_8 = 0.688 \pm 0.035$, then $a_0^{EMC} = 0.120 \pm 0.062 \pm 0.138$.

In the naive parton model, $a_0 = \Delta\Sigma = a_8 + 3(\Delta s + \Delta \bar{s})$. The Ellis-Jaffe sum rule [26] assumes that $\Delta s = \Delta \bar{s} = 0$, so $a_0 \simeq a_8 \simeq 0.688$. Thus there is a gross contradiction here. To appreciate the physical significance of $\Delta\Sigma(x)$, count the spin of the quark $= \pm\frac{1}{2}$ and express them in the integral.

Then the total contribution to the spin of the proton from the spin of a given flavor quark is:

$$\langle S_z \rangle = \int_0^1 \{\frac{1}{2} q_\uparrow(x) + \frac{-1}{2} q_\downarrow(x)\} = \frac{1}{2} \int_0^1 dx \Delta q(x), \tag{1.28}$$

so $a_0 = 2\langle S_z^{quark} \rangle$. Thus, the results from the EMC measurements suggested that the quarks' intrinsic spin contributes little of the proton's spin. It was this discrepancy between the contribution of the quark spins to the total angular momentum of the proton, as measured in DIS and as computed in both non-relativistic and relativistic constituent models of the proton, that was termed a **'spin crisis in the parton model'** [22].

The non-perturbative structure of the proton needs to be considered in order to resolve this discrepancy. In QCD, the g_1 spin sum-rules are derived starting from the dispersion relation for polarized photon-nucleon scattering and, for deep inelastic scattering, the light-cone operator product expansion. In this framework, the structure function is related to the scale-invariant axial charges of the target nucleon by [19]:

$$\begin{aligned}\int_0^1 dx g_1^p(x, Q^2) = \frac{1}{9}\{[1 + \sum_{l \geq 1} c_{NSl} \alpha_s^l(Q)][\frac{3}{4} a_3 + \frac{1}{4} a_8] + [1 + \sum_{l \geq 1} c_{Sl} \alpha_s^l(Q)] E(\alpha_s) a_0\} \\ + O(\frac{1}{Q^2}) + \beta_\infty.\end{aligned} \tag{1.29}$$

This expression is very close to the QCD-corrected g_1^p expression. The flavor non-singlet c_{NSl} and singlet c_{Sl} Wilson coefficients are calculable in perturbative QCD. $E(\alpha_s)$ is a renormalization group factor. The β_∞ represents a possible leading-twist subtraction constant that affects just the first moment, and corresponds to a contribution at Bjorken-x equal to zero. In alternate notation, some authors use $g_A^{(3)} = a_3$, $g_A^{(8)} = a_8$ and $g_A^{(0)}|_{inv}/E(\alpha_s) \equiv g_A^{(0)} = a_0$.

It was further noticed that the triangle anomalous gluonic contribution is not negligible, and if we consider the gluon's contribution to g_1^p, we find that:

$$a_0 = (\sum_q \Delta q - 3\frac{\alpha_s}{2\pi} \Delta g)_{partons}, \tag{1.30}$$

Here Δg is the amount of the proton's spin carried by polarized gluons. Thus, the interpretation of the flavor-singlet axial-charge a_0 in physics is not simply the one from the naive parton model. The small value of a_0 can be explained in several ways: positive gluon polarization, possible SU(3) breaking in the extraction of a_8, negative strangeness polarization in the nucleon, and/or a possible topological contribution at $x = 0$ [19].

Deep inelastic scattering measurements of g_1 have been performed in experiments at CERN, DESY, JLab and SLAC, as shown in Fig. 1.4, and there is a general consistency among all data sets. The NLO QCD-motivated fits, which take into account the scaling violations associated with perturbative QCD, are used to evolve all data points to the same value of Q^2, which is necessary for the test of deep inelastic sum-rules and to extract $g_A^{(0)}|_{pDIS}$. If we use the most recent data from COMPASS [27], the corresponding experimental value is $g_A^{(0)}|_{pDIS} = 0.33 \pm 0.03 \pm 0.05$. So the spins of the quarks contribute $\sim 30\%$ to the total spin of the proton. This value is not far from the current theoretical predictions; thus the spin crisis is not as significant as before, but it still indicates the complex vacuum structure of QCD and the interplay of valence quarks with chiral dynamics.

The proton polarization can be decomposed into frame-independent quark and gluon contributions, and the related angular momenta. The spin sum rule is usually expressed as:

$$\frac{1}{2} = \frac{1}{2}\sum_q \Delta q + \Delta g + L_q + L_g, \tag{1.31}$$

where L_q and L_g denote the quark and gluon orbital angular momentum contributions, while Δq and Δg are related to the quark and gluon spin contributions. Operator definitions of the different terms or combinations of terms in this equation are discussed in Refs. [28], [29], [30], [31], [32] and [33]. In general, this expression can be derived from the angular momentum operator in QCD, which is defined according to the generators of Lorentz transformations of the angular momentum density.

There is presently a vigorous global program to disentangle the different contributions. Key experiments include semi-inclusive polarized deep inelastic scattering (COMPASS experiment at

CERN and HERMES experiment at DESY) and polarized proton-proton collisions (PHENIX and STAR experiments at BNL).

1.2.3 Polarized Parton Distribution Functions

There are several different theory groups working on global fits for the NLO global polarized PDF analysis. Here I will only summarize some recent results from the LSS, DSSV and NNPDF groups.

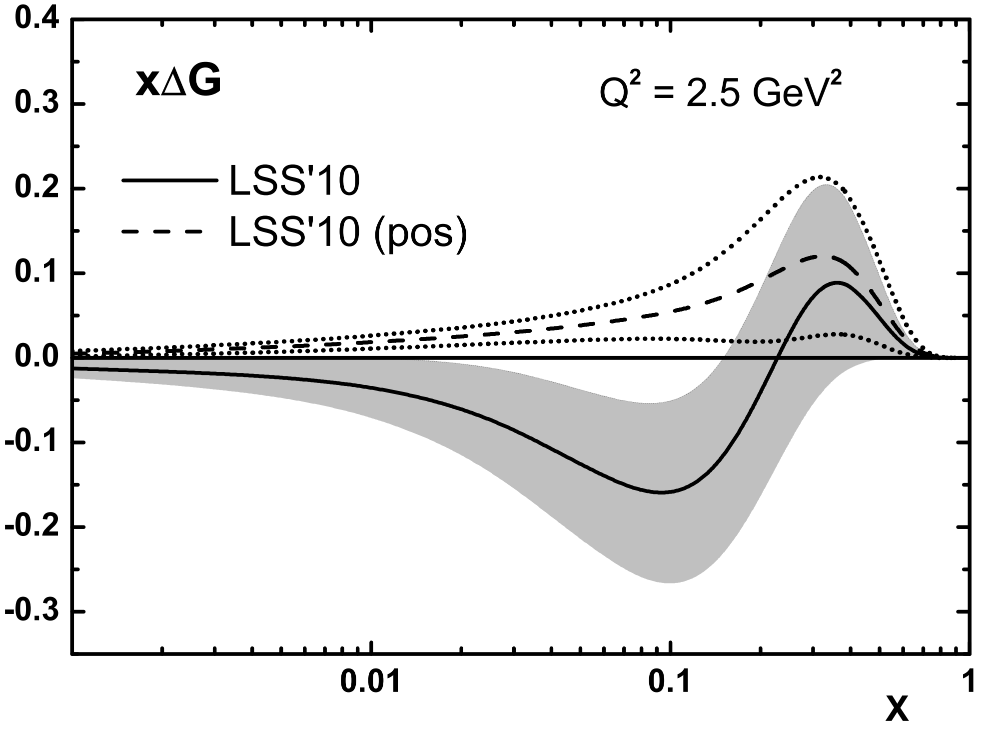

Figure 1.5: Gluon density from the LSS group [34].

In 2010, the LSS group (Elliot Leader, Aleksander V. Sidorov and Dimiter B. Stamenov) reported a new combined next-to-leading-order QCD analysis of the polarized inclusive and semi-inclusive DIS data [34]. The polarized gluon density is shown in Fig. 1.5. They found that the combined NLO QCD analysis of the present polarized inclusive DIS and SIDIS data cannot distinguish between the positive and sign-changing gluon densities $\Delta G(x)$, resulting in the two fits shown in the plot. This ambiguity is the main reason that the quark-gluon contributions to the total spin of the proton are still not well determined in this analysis. Their final conclusion is that at $Q^2 = 4\ GeV^2$, if one assumes a positive $x\Delta G$, then $\Delta\Sigma = 0.207 \pm 0.034$ and $\Delta G = 0.316 \pm 0.190$; for a sign-changing $x\Delta G$, $\Delta\Sigma = 0.254 \pm 0.042$ and $\Delta G = -0.339 \pm 0.458$. Thus, even the sign of ΔG is not constrained by DIS data alone.

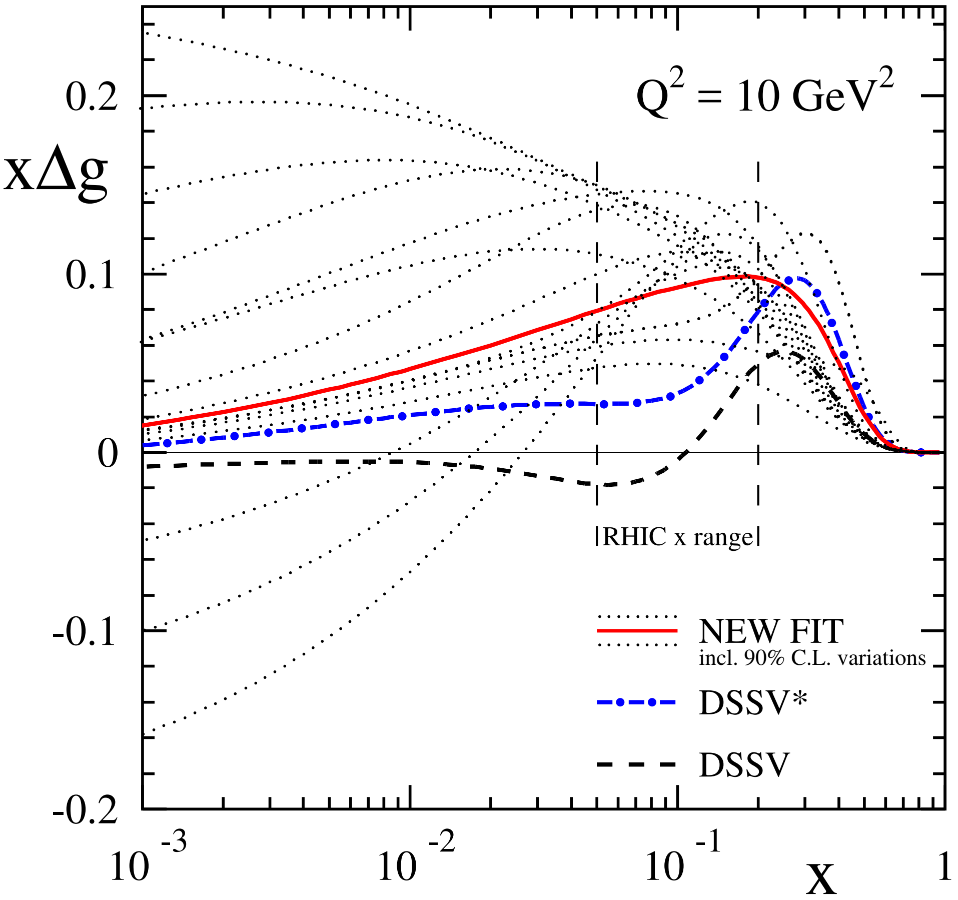

Figure 1.6: Gluon helicity distributions at $Q^2 = 10\ GeV^2$ for the new fit, the original DSSV analysis, and for an updated analysis without using the new 2009 RHIC data sets ($DSSV*$). The dotted lines present the gluon densities for alternative fits that are within the 90% C.L. limits [35].

The DSSV model was developed by Daniel de Florian, Rodolfo Sassot, Marco Stratmann and

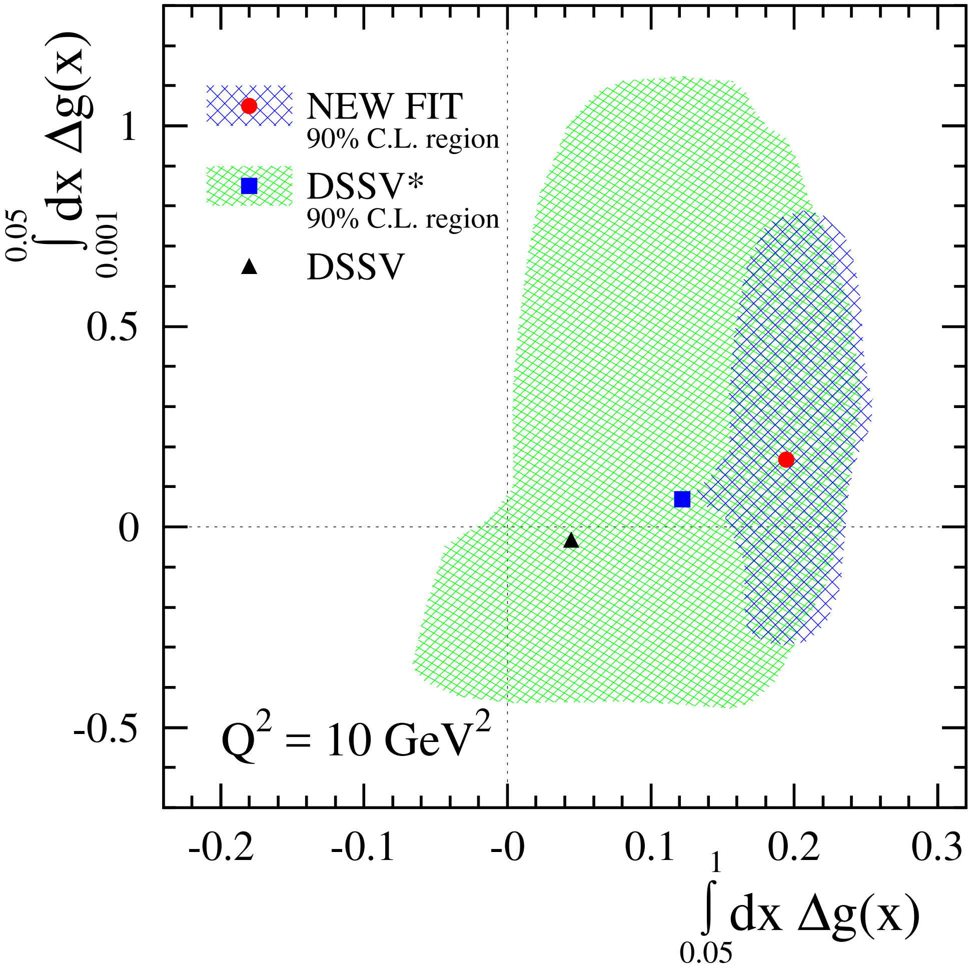

Figure 1.7: 90% C.L. areas in the plane spanned by the truncated moments of Δg computed for $0.05 \leq x \leq 1$ and $0.001 \leq x \leq 0.05$ at $Q^2 = 10\ GeV^2$. Results for DSSV, DSSV* and new analysis, with the symbols corresponding to the respective central values of each fit, are shown.

Werner Vogelsang, using the data not only from the inclusive and semi-inclusive DIS experiments, but also from the RHIC inclusive jet and π^0 analyses [35] (of the data taken through 2009). Their new result is shown in Fig. 1.6, which includes a comparison of their earlier result to the new one, with and without the RHIC 2009 data. The original fit from 2008 (labelled DSSV) shows small gluon polarization in the range of momentum fraction accessible at RHIC; but including the RHIC 2009 data (NEW FIT) for the first time implies a non-zero polarization of gluons in the proton at intermediate momentum scales. However, comparing the integrals in two different Bjorken-x ranges (Fig. 1.7) shows that the lower x values are still poorly constrained. In that figure, the y-axis is the integral of the gluon helicity in the x range 0.001-0.05 while the x-axis is the integral over the range 0.05-1. The y-axis uncertainty region is much larger than that of the x-axis for the new fit values; note the change in scale of the two axies. New results from STAR at $\sqrt{s}$ = 500 GeV and at forward rapidity are essential to provide the constraints in this region, as described below.

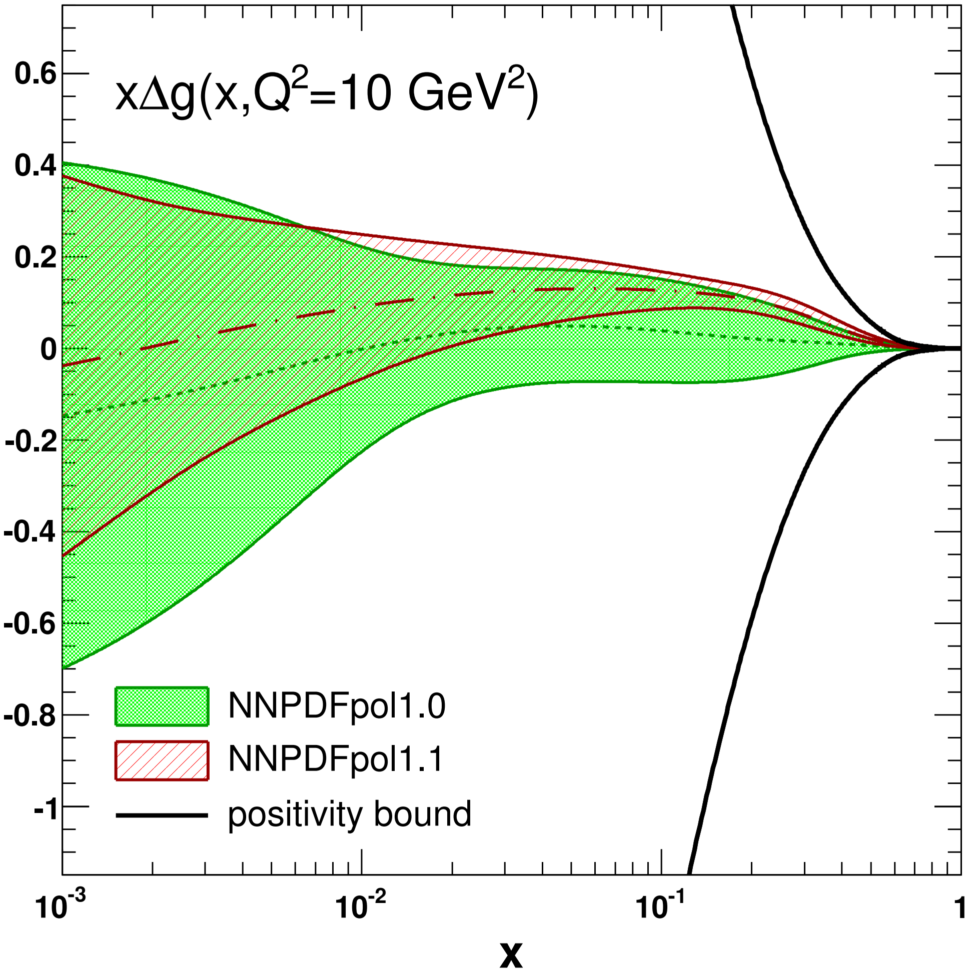

Figure 1.8: Gluon helicity distribution from the NNPDF group [17].

The NNPDF group [17] also uses the data from RHIC to perform global fits. The NNPDF technique uses a robust set of statistical tools, which include Monte Carlo methods for error propagation, neural networks for PDF parametrization, and genetic algorithms for their training. Their new result on the gluon helicity distribution is shown in Fig. 1.8 [17]. Their polarized parton distribution functions are shown in Fig. 1.3. By including the RHIC 2009 data (NNPDFPol1.1), a significant improvement in accuracy in the determination of the gluon distribution is found in the medium and small-x region.

1.3 Gluon Polarization at RHIC

RHIC includes several different and independent spin programs. Measuring the longitudinal double spin asymmetries A_{LL} for inclusive jet, dijet and inclusive π_0 production is used to probe the gluon polarization. The production of $W^{\pm}$ bosons in longitudinally-polarized proton-proton collisions serves as a powerful and elegant tool to access valence and sea quark helicity distributions. The transverse single spin asymmetries (SSA) for inclusive hadron production that are seen in p+p collisions provides insight into the transverse spin structure. And $p^{\uparrow} + A$ collisions are used to study the dynamics of partons in nuclear matter and investigate the existence of nonlinear evolution effects [36].

Understanding the gluon polarization is important in two ways. First, gluons can directly contribute to the spin of the proton, as shown in equation 1.31. It is also one of the key observables needed to understand the small value of the singlet axial-charge $g_A^{(0)}|_{pDIS}$ (another one is polarized strangeness), since polarized glue makes a scaling contribution to the first moment of g_1, $\alpha_s \Delta g \approx constant$. This suggestion sparked a vigorous and ambitious program to measure Δg.

The observable measured at RHIC is the longitudinal double spin asymmetry:

$$A_{LL} \equiv \frac{\sigma_{++} - \sigma_{+-}}{\sigma_{++} + \sigma_{+-}}. \tag{1.32}$$

Assuming factorization, it can be further expressed for the process $a + b \to c + X$ in the form [37]:

$$A_{LL} = \frac{\sum_{abc} \Delta f_a \otimes \Delta f_b \otimes d\hat{\sigma}^{f_a f_b \to f_c x} \hat{a}_{LL}^{f_a f_b \to f_c x} \otimes D_{f_c}^{h}}{\sum_{abc} f_a \otimes f_b \otimes d\hat{\sigma}^{f_a f_b \to f_c x} \otimes D_{f_c}^{h}}, \tag{1.33}$$

where $\hat{\sigma}$ and $\hat{a}_{LL}$ represent the hard partonic cross section and the partonic double helicity asymmetry, respectively, and both are calculable within perturbative QCD (pQCD). $D^h_{f_c}$ is the probability for a parton c to fragment into a hadron h. $f_{a,b}$ is the unpolarized parton distribution, while $\Delta f_{a,b}$ is the polarized parton distribution function. When the partonic scattering involves gluons, Δf would become Δg. Thus, we see that A_{LL} is directly sensitive to the gluon polarization.

1.3.1 Inclusive Jet Analysis

Inclusive jet production from longitudinally polarized *pp* collisions is the major emphasis and strength of the RHIC spin physics program to probe gluon polarization. Jets are mainly produced in the 2 → 2 hard scatterings from quark and gluon interactions (Fig. 1.9) in proton-proton collisions, and are very good observables for gluon polarization studies since they arise predominantly from quark-gluon and gluon-gluon scattering at RHIC energies, as shown in Fig. 1.10.

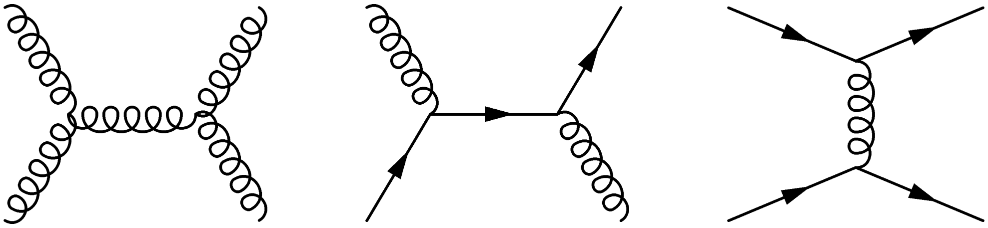

Figure 1.9: Feynman diagram for the gg, qg and qq sub processes (from left to right).

In 2009, the p+p inclusive jet double-spin asymmetries at $\sqrt{s} = 200$ GeV from STAR [39], combined with the π^0 results [40] from PHENIX, for the first time showed that gluons are polarized inside the proton. The published STAR A_{LL} data in Fig. 1.11 is plotted as a function of parton jet p_T, and is divided into two pseudorapidy ranges, $|\eta| < 0.5$ and $0.5 < |\eta| < 1.0$, that emphasize different kinematic ranges in x. The theoretical curves illustrate the A_{LL} expected for the polarized PDFs associated with the corresponding global analyses (see section 1.2.3).

LSS10p [34] provides a good description of the STAR jet data. The STAR results lie above the predictions of DSSV [42], [43] and NNPDF [44] but below the predictions of BB10 [45]. As noted before, the DSSV and NNPDF groups have performed new global analyses including the new STAR data, and their results are now consistent. In both analyses, the inclusion of the STAR

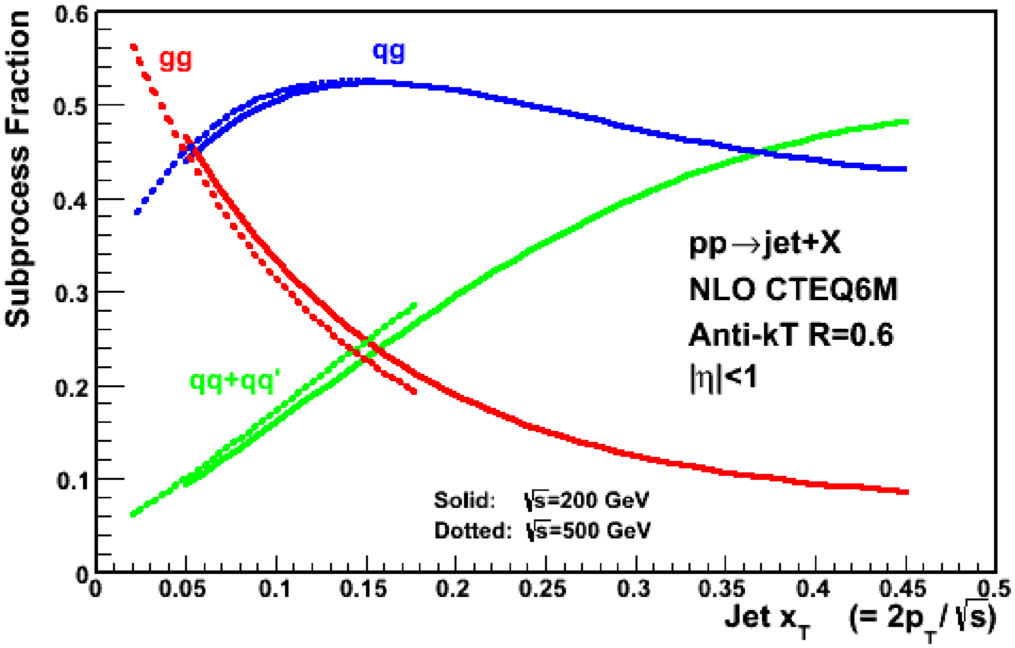

Figure 1.10: Inclusive jet cross section fraction for the subprocesses gg, gq, qq from NLO calculations [38].

jet data results in a substantial reduction in the uncertainty for the gluon polarization, and indicates a preference for the gluon helicity contribution to be positive in the RHIC kinematic range. DSSV found that the integral of $\Delta g(x, Q^2 = 10\ \text{GeV}^2)$ over the range $x > 0.05$ is $0.20^{+0.06}_{-0.07}$ at 90% C.L. The NNPDF group finds that the integral of $\Delta g(x, Q^2 = 10\text{GeV}^2)$ over the range $0.05 < x < 0.20$ is 0.17 ± 0.06, while the value over the range $x > 0.05$ is 0.23 ± 0.06. Thus, both groups obtain consistent results for $x > 0.05$, indicating Δg is positive at the 3σ level.

In 2012, the first inclusive jet double-spin asymmetries at 510 GeV were measured at STAR. The higher energy allows access to the polarized gluon distribution at lower sampled x values, as shown in Fig. 1.12. The preliminary STAR 2012 510 GeV inclusive jet A_{LL} resutls are plotted with the 2009 200 GeV data as functions of $x_T = 2p_T/\sqrt{s}$, and are seen to be consistent with each other in the overlapping x_T region. The higher $\sqrt{s}$ data extend the gluon helicity measurements to lower x regions where they are also in good agreement with several different theoretical predictions.

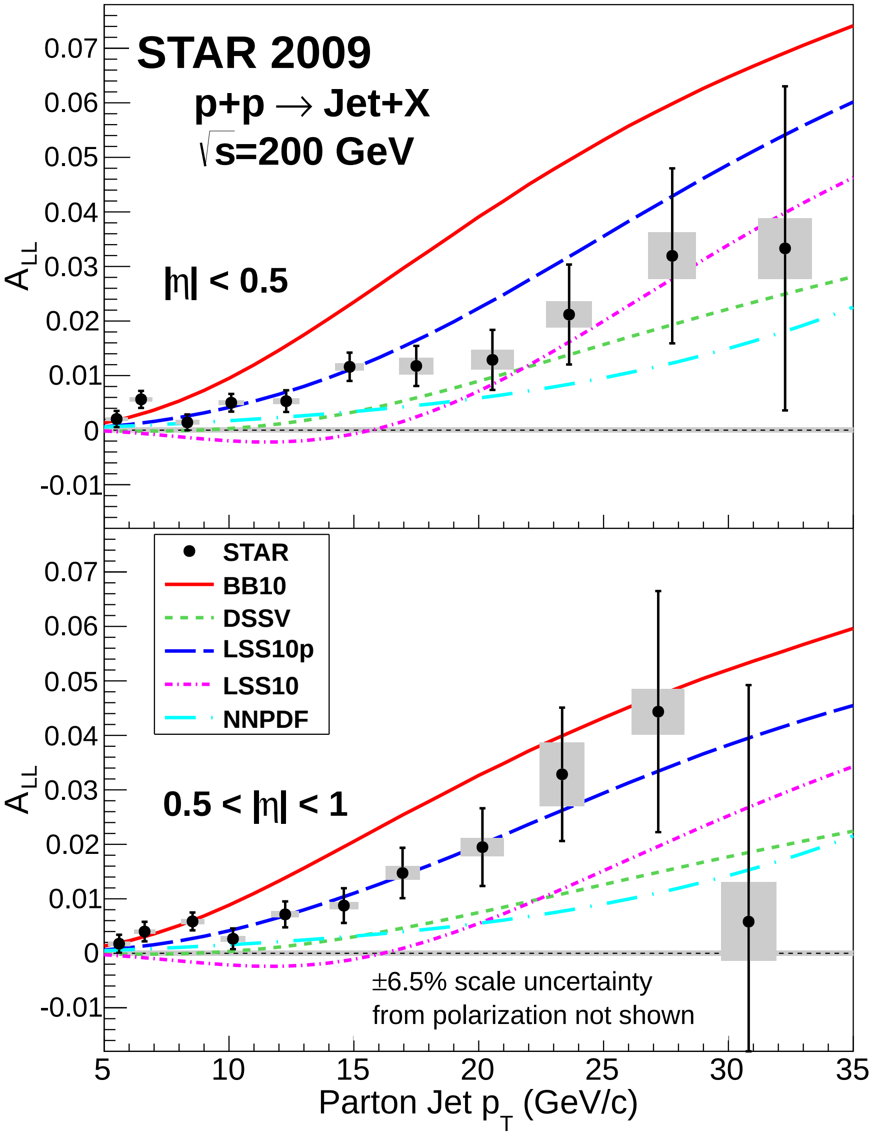

Figure 1.11: Mid-rapidity ($|\eta| < 0.5$ upper panel) and forward rapidity ($0.5 < |\eta| < 1$, lower panel) inclusive jet A_{LL} vs. parton jet p_T, compared to predictions from several NLO global analyses. The error bars are statistical. The gray boxes show the size of the systematic uncertainties [39].

1.3.2 Di-jet Analysis

Inclusive jet measurements necessarily integrate over a large range in the x of the initial state partons for a given transverse momentum of the final state. To gain more direct sensitivity to the x dependence of Δg, correlation measurements, such as dijet production, are required, as these more tightly constrain the kinematics of the colliding partons. For example, to leading order in a $2 \to 2$ collision, the dijet invariant mass is proportional to the square-root of the product of the initial state

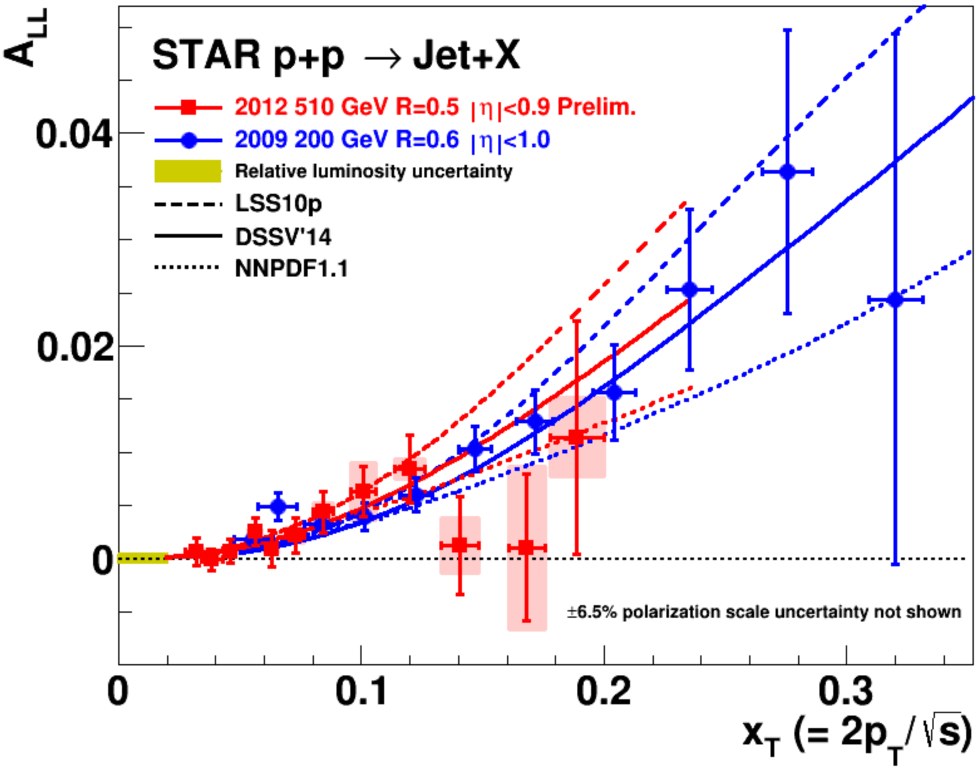

Figure 1.12: A_{LL} vs. x_T for inclusive jet production at mid-rapidity in 200 GeV (blue) [39] and 510 GeV (red) [41] p+p collisions, compared to NLO predictions from three recent NLO global analyses.

momentum fractions, $M = \sqrt{s}\sqrt{x_1 x_2}$, while the sum of the jet pseudorapidities determines their ratio, $\eta_1 + \eta_2 = \ln(x_1/x_2)$.

The first measurement of the longitudinal double-spin asymmetry A_{LL} for mid-rapidity dijet production from STAR was published using the 2009 pp200 GeV data [46]. The initial state kinematics achievable with dijets can be seen in Fig. 1.13, which presents the partonic momentum fraction distributions (weighted by partonic $\hat{a}_{LL}$) of the gluons as obtained from PYTHIA [47] for a sample of detector level dijets with $19.0 < M < 23.0$ GeV/c^2, as well as for inclusive jets with $8.4 < p_T < 11.7$ GeV/c. Di-jet measurements place tighter constraints on the kinematics of the colliding partons, compared to inclusive jet measurements, as the increase in x resolution achievable with dijets compared to inclusive jets is evident from the much narrower dijet x distributions. The

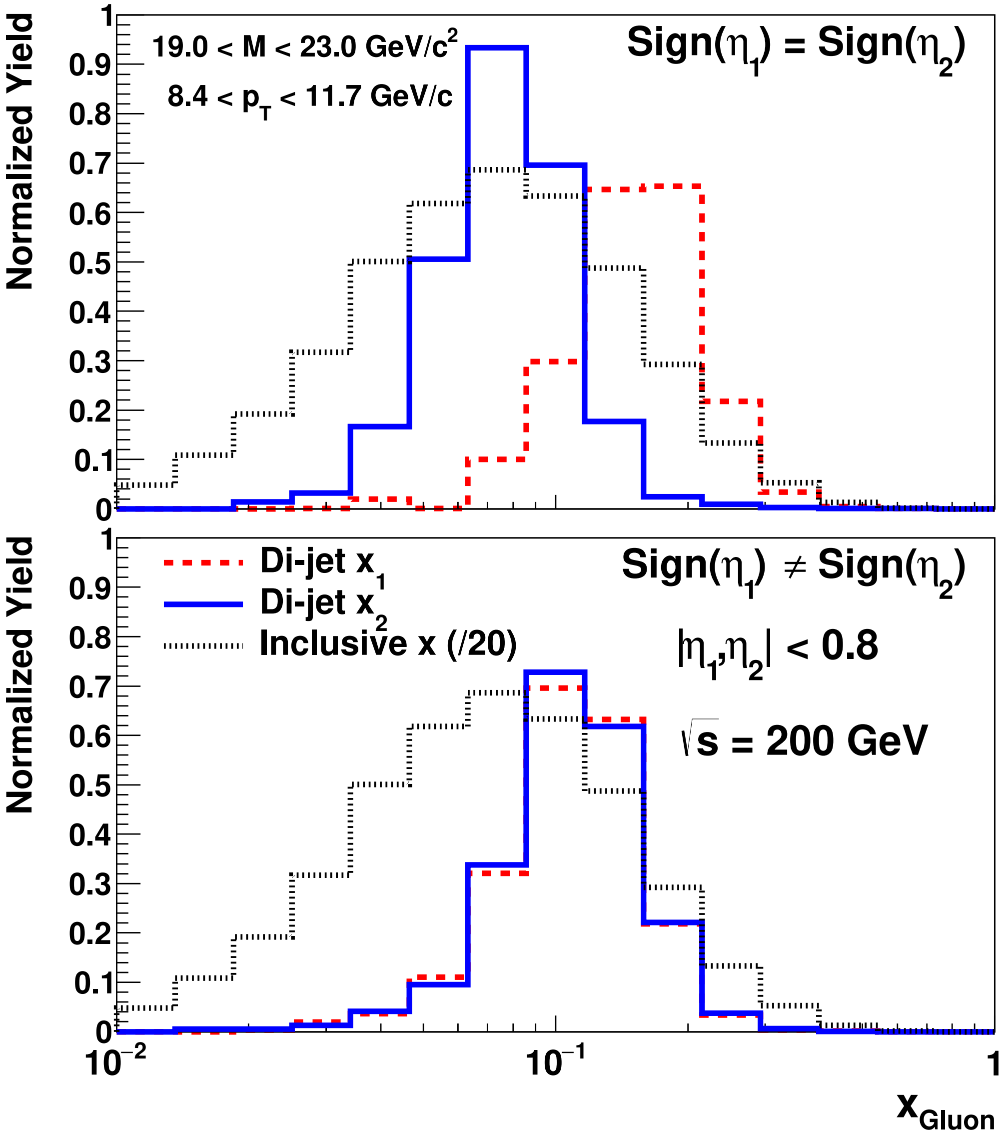

Figure 1.13: Values of gluon x_1 and x_2 obtained from the PYTHIA detector level simulation for the same-sign (upper) and opposite-sign (lower) dijet topologies, compared to the gluon x distributions for inclusive jets scaled by an additional factor of 20 in each panel [46].

asymmetric nature of the collisions in the same-sign η events (upper plot) can be seen in the separation of the high- and low-x distributions, whereas the opposite-sign η events (lower plot) sample an intermediate x range.

The dijet cross section was also measured, and is presented as a function of dijet invariant mass and is shown in Fig. 1.14, including the associated systematic uncertainty (solid green band) and a theoretical prediction (single-hatched blue bar) obtained from the NLO predictions. The

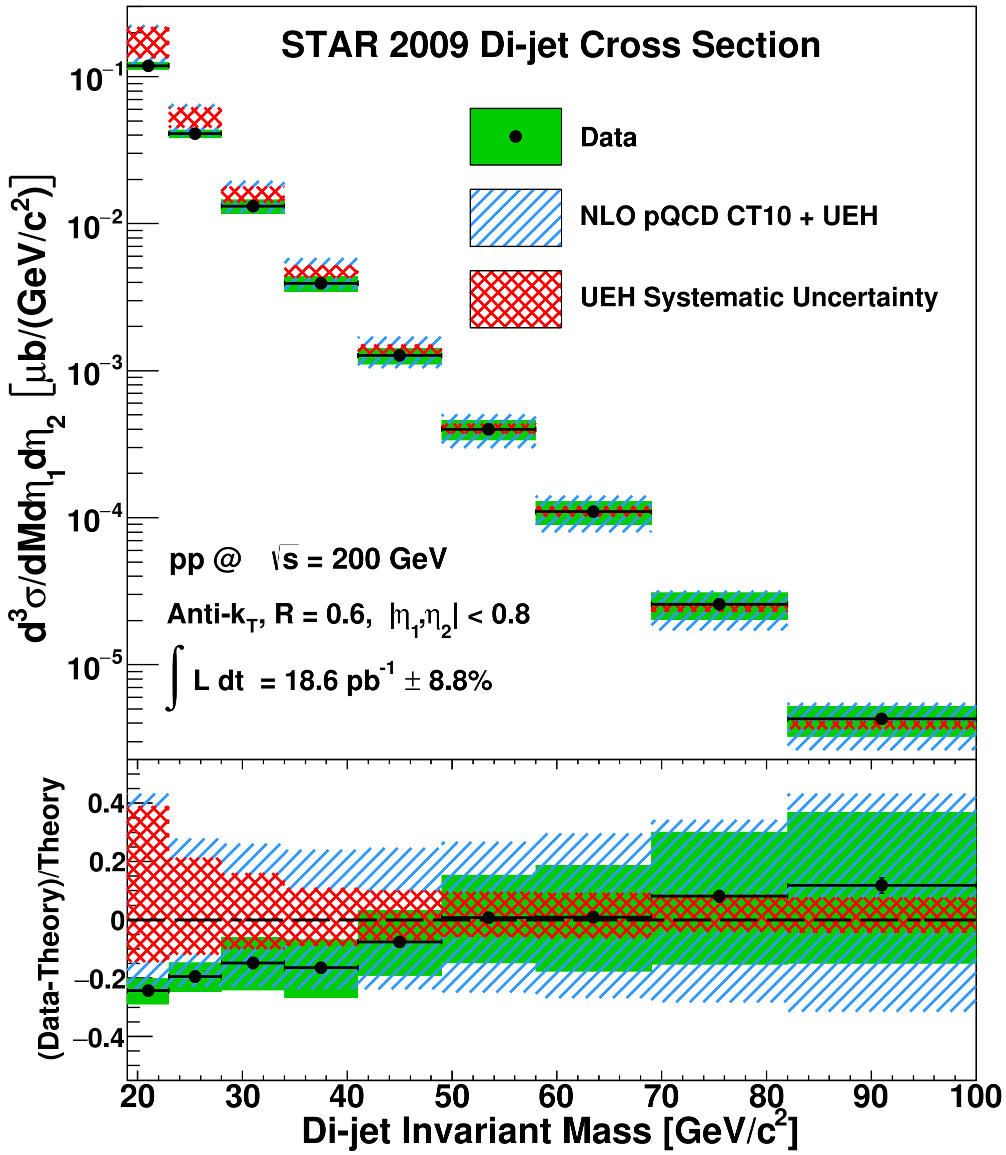

Figure 1.14: The particle-level dijet differential cross section measured by the STAR experiment (points plotted at bin center). The lower panel provides a relative comparison to theory [46].

theoretical cross section was corrected for underlying event and hadronization (UEH) effects. The good agreement of the dijet cross section with the NLO pQCD expectations indicates that dijet production at STAR is well understood in these measurements.

The dijet longitudinal double spin asymmetries A_{LL} displayed in Fig. 1.15, are also plotted as a function of dijet invariant mass, and are divided into two different pseudorapidity ranges. The results tend to lie above the theoretical predictions at low invariant masses, which suggests the dijet data may prefer a somewhat higher gluon polarization at low x than the current global analyses.

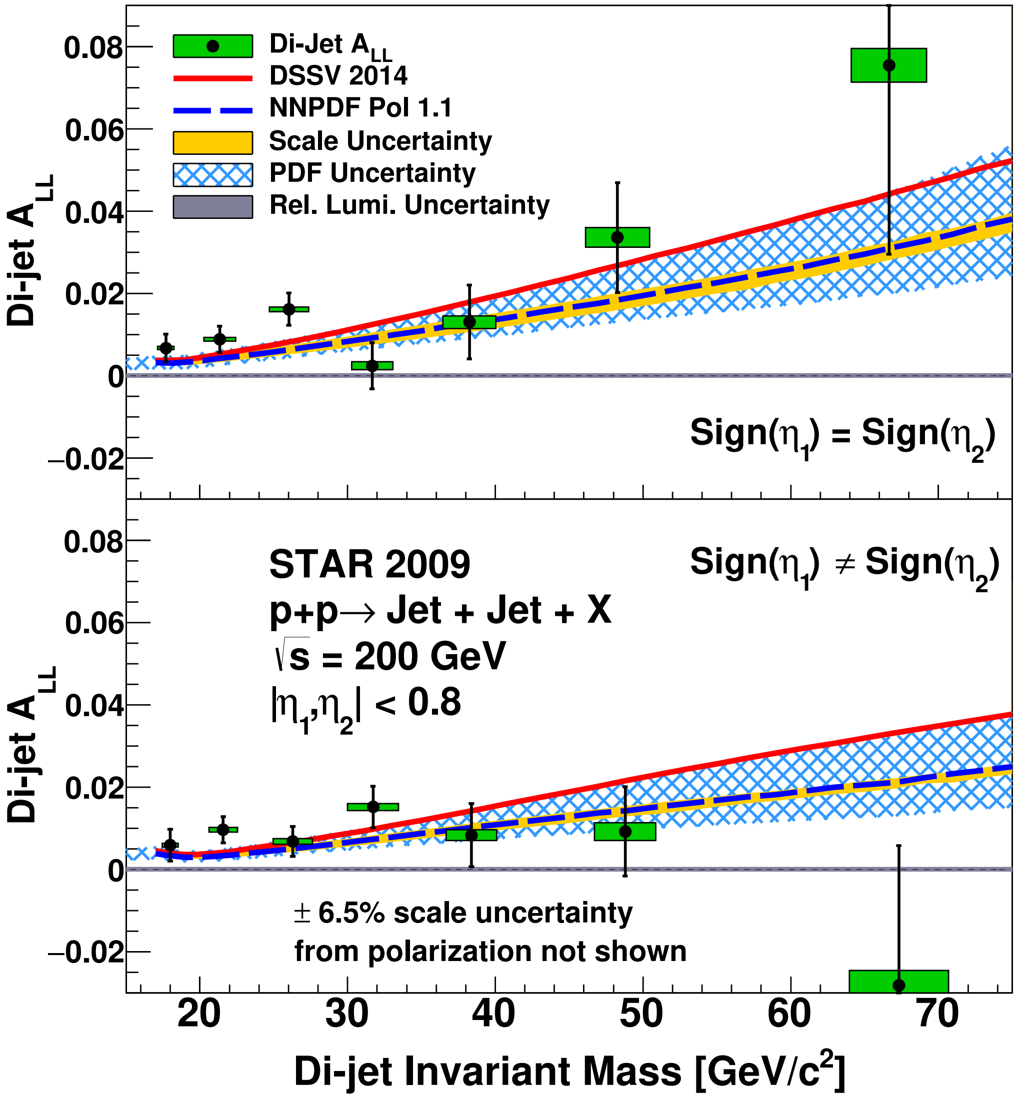

Figure 1.15: Di-jet A_{LL} vs. parton-level invariant mass for the same-sign (top) and opposite-sign (bottom) topological configurations measured by the STAR experiment [46].

Correlation measurements capture a more complete picture of the hard scattering kinematics, and therefore offer a better determination of the gluon momentum fraction than is possible with inclusive jet measurements. This improvement in x resolution will allow global analyses to better constrain the behavior of $\Delta g(x)$ as a function of x, thus reducing the uncertainty on extrapolations to poorly measured lower x regions and, ultimately, the integrated value of $\Delta g(x)$. The results from the 2009 *pp* 200 GeV represent an important advance in the experimental investigation of the gluon polarization at STAR, and are the basis of the analyses in this dissertation.

1.4 Jets at Higher Pseudorapidity

As shown in Fig. 1.16, in addition to the measurements using the higher collision energy, extending the measurement to more forward rapidity region also help to probe the lower x values. More forward jets are indicative of more asymmetric collisions which contain lower momentum gluons.

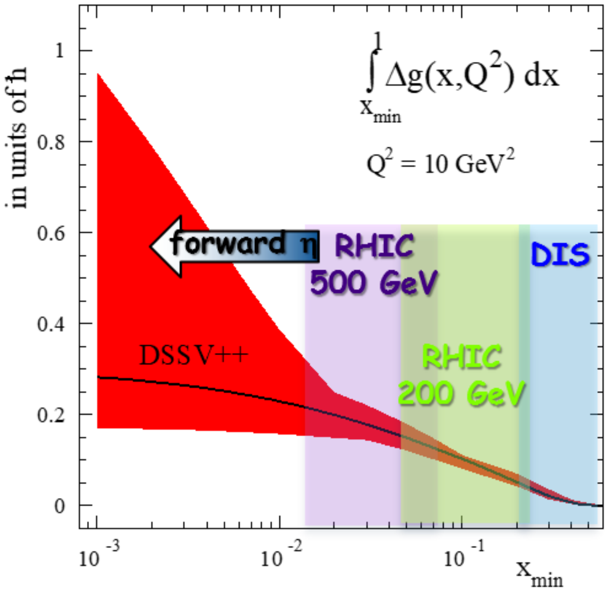

Figure 1.16: Gluon helicity integral with different starting x value from DSSV analysis [48].

The difficulty of the measurements at forward rapidity is that the tracking efficiency decreases rapidly in forward region of the STAR detector, as shown in Fig. 1.17. Lower tracking efficiency means the reconstructed jets will have lower p_T on average. This inaccurate p_T reconstruction skews the extraction of the initial state parton momenta. Jets with a high percentage of neutral energy are preferentially selected, both in triggering and reconstruction, leading to a biased sample.

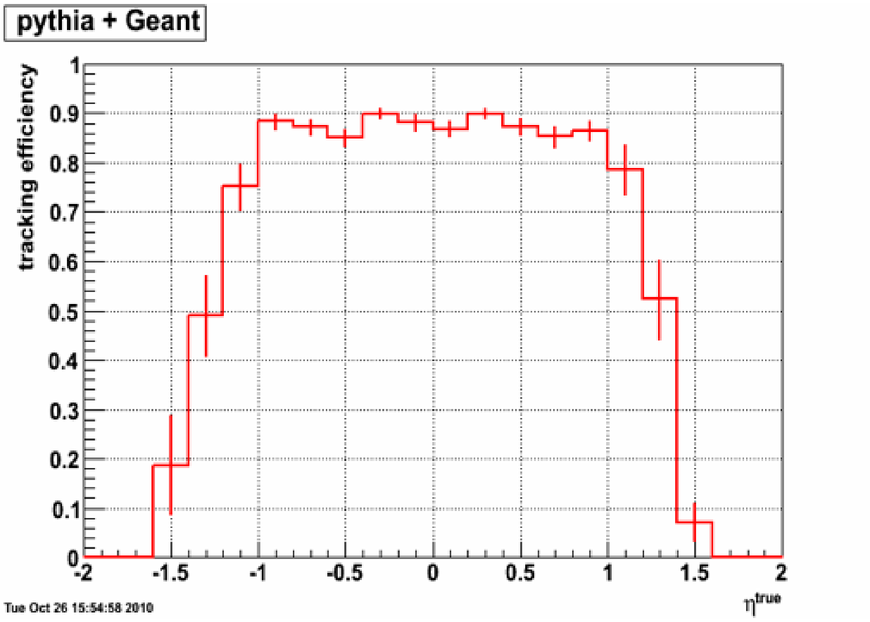

Figure 1.17: STAR tracking efficiency vs. pseudorapidity.

1.5 Dissertation Structure

This dissertation presents an analysis that extends the dijet measurements at $\sqrt{s}$ = 200 GeV to a higher rapidity range, which will probe a kinematic region that is much less constrained by data compared to the measurement at mid-rapidity.

In the following chapters, I will first describe the RHIC facility as well as the STAR detectors and the subsystems which are relevant to these analyses in chapter 2. I will give a summary of the data set (chapter 2) and simulation sample (chapter 4) used. The main focus will be on the jet and dijet events and these are described in chapter 3. The most important part in this analysis is the method used to solve the problems faced at higher rapidities, which will be described in chapter 6. Compared to the dijet analysis at mid-rapidity, several different updates are made, including the underlying event subtraction (In chapter 5) and several new methods on the corrections and systematic error estimations (in chapter 7). In chapter 8 we present our final results and conclusions.

CHAPTER 2

Experimental Facilities and Detectors

2.1 The Relativistic Heavy Ion Collider

The Relativistic Heavy Ion Collider (RHIC) located at Brookhaven National Lab (BNL) is the first machine in the world capable of colliding heavy ions at ultra-relativistic energies. The primary goal of the heavy ion program is to create and study the quark-gluon plasma. Furthermore, RHIC is the world's only machine capable of colliding high-energy beams of polarized protons, and is a unique tool for exploring the puzzle of the proton's 'missing' spin. More details about the RHIC project can be found in [49], [50] and [51]. A general layout of the RHIC facility can be seen in Fig. 2.1

A new optically pumped polarized H^- (hydrogen) ion source (OPPIS) was developed for the RHIC polarization program which was based on the KEK OPPIS that was successfully used for production of a vector polarized D (deuterium) beam at KEK [52], and upgraded at TRIUMF for high current H^- operation. This OPPIS routinely produces 0.5 mA current in a 300 μs pulse and can be expanded to 500 μs, about the maximum LINAC pulse duration. The polarized H^- ions are produced in OPPIS [53] at 35 keV beam energy with about 80% polarization, and then accelerate to 200 MeV with a RFQ and LINAC for strip injection to the booster. The 300 μs H^- ion pulse is captured in a single booster bunch which contains about 4×10^{11} polarized protons. The single bunch is accelerated to 1.5 GeV kinetic energy in the booster, and then transferred to the Alternating Gradient Synchrotron (AGS), where it is accelerated to 25 GeV for injection into RHIC.

The OPPIS initial longitudinal polarization is converted to the transverse direction while the

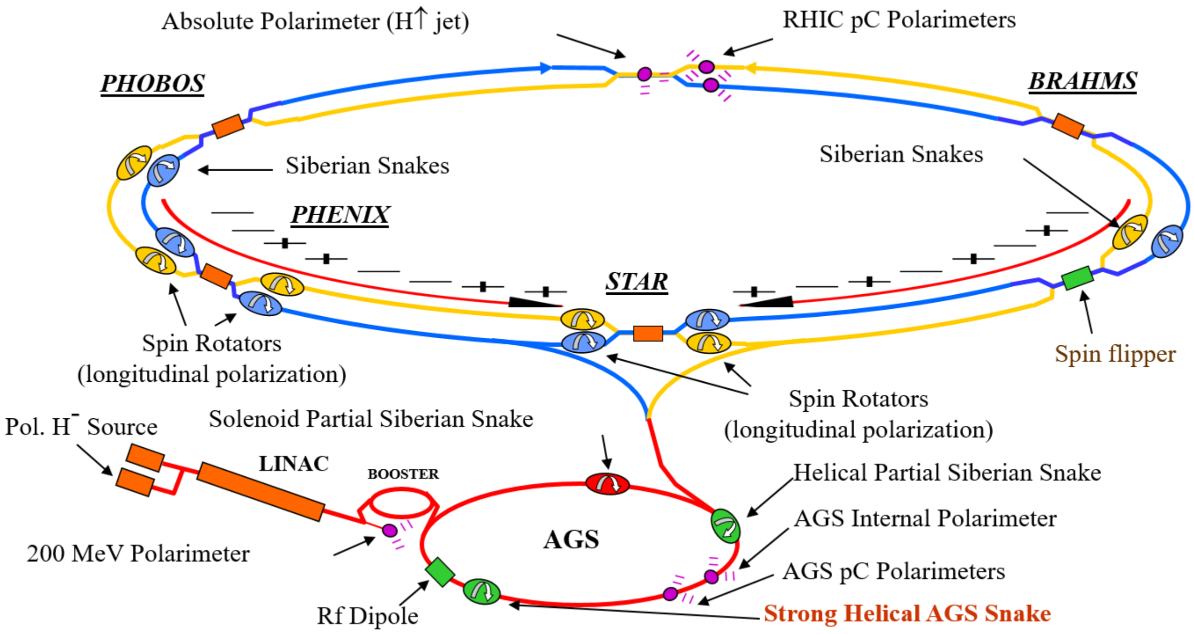

Figure 2.1: Layout of the RHIC facility for polarized proton operation [49].

beam passes through two bending magnets during injection. The final polarization alignment to the vertical direction can be adjusted by a spin rotator solenoid in the 750 keV beam transport line before injection to the linac. The AGS cycle for polarized beam operation is 3 s. The OPPIS operates at 1Hz repetition rate; the two additional source pulses can be directed to the 200 MeV p-carbon polarimeter for polarization monitoring. The polarization alignment to the vertical plane is done using a 200 MeV polarimeter.

The RHIC collider consists of two quasi-circular concentric accelerator/storage rings on a common horizontal plane, one ('Blue Ring') for clockwise and the other ('Yellow Ring') for counter-clockwise beams. The overall efficiency of the acceleration and beam transfer is better than 50%, giving 2×10^{11} protons per bunch. 120 bunches for each ring are filled repeatedly, and accelerating to full energy takes about 10 minutes, which is short compared to the expected lifetime of the stored polarized proton beams in RHIC of many hours [54].

2.1.1 Spin Dynamics and Siberian Snakes

The evolution of the spin direction of a beam in external magnetic fields is governed by the Thomas-BMT equation:

$$\frac{d\vec{P}}{dt} = -(\frac{e}{\gamma m})[G\gamma\vec{B}_{\perp} + (1+G)\vec{B}_{||}] \times \vec{P}, \tag{2.1}$$

where the polarization vector $\vec{P}$ is expressed in the frame that moves with the particle, $\vec{B}_{\perp}$ is the magnetic field perpendicular to the particle's velocity, and $\vec{B}_{||}$ is the magnetic field along the direction of the particle's velocity. G is the anomalous gyromagnetic ratio (anomoulous g-factor) and γ is the Lorentz factor.

Compared to the Lorentz force equation that governs the evolution of the orbital motion in an external field:

$$\frac{d\vec{v}}{dt} = -(\frac{e}{\gamma m})\vec{B}_{\perp} \times \vec{v}, \tag{2.2}$$

we see that the spin rotates at $G\gamma$, know as spin tune ν_{sp}, faster than the orbital motion. From the Thomas-BMT equation, we find that at low energies longitudinal fields ($\vec{B}_{||}$) can be quite effective in manipulating the spin motion, while at high energies the transverse fields ($\vec{B}_{\perp}$) are needed to have effect beyond the vertical holding field.

The presence of numerous depolarizing resonances makes the acceleration process complicated. There are two main types of depolarizing resonances during the acceleration: one are the imperfection resonances driven by magnet errors and misalignments; the other are the intrinsic resonances driven by the focusing fields. A 'Siberian Snake' [54] was introduced to overcome these resonances at high energy at RHIC.

The Siberian Snake generates a 180° spin rotation about a horizontal axis, and the stable spin direction remains unperturbed at all times as long as the spin rotation from the Siberian Snake is much larger than the spin rotation due to the resonance driving fields. In this way, the beam polarization is preserved. Two full Siberian Snakes are inserted on opposite sides of the RHIC lattice for each of the two counter-rotating rings to maintain the polarization during the acceleration process. In addition to these Snakes, spin rotators are located on each side of the two major interaction points, which allow the spin orientation to be altered from the vertical plane to the longitudinal plane. These devices are the primary magnetic components of the polarized beam project at RHIC. In addition, ‘spin flip’ devices are inserted to allow for the manipulation of the spin orientation during a store, as well as polarimetry instrumentation. A detailed review of the polarized proton collider at RHIC can be found in [54].

2.1.2 Measuring Beam Polarization in RHIC

The measurement of the beam polarization is based on the spin asymmetry in proton-Carbon elastic scattering in the Coulomb-Nuclear Interference (CNI) region. Two different polarimetries are used in the measurement: proton-Carbon (pC) polarimeters are used to measure the relative polarization, while a hydrogen gas jet (H-Jet) is used for the absolute polarization measurements.

The pC detector consisted of a carbon ribbon target and six silicon strip detectors which mounted in a vacuum chamber at azimuthal angles of 90 (detector 2 and 5) and ±45 degrees (detector 1, 3, 4 and 6) relative to the vertical direction (the stable proton spin direction at RHIC) as shown in Fig. 2.2.

The vertical beam polarization is measured by determining the asymmetry in the cross section for left and right scattering of the particle production, using a reaction with a known analyzing power A_N

$$P_{beam} = \frac{1}{A_N}\frac{N_L - N_R}{N_L + N_R} = \frac{\varepsilon_{beam}}{A_N}, \tag{2.3}$$

where P_{beam} is the beam polarization, N_L and N_R are the number of scatters left and right normalized by luminosity, and ε_{beam} is the raw asymmetry. Despite the fact that the pC polarimeter only measures the relative polarization, it provides fill-by-fill offline results and is an effective instrument for depolarization studies and polarization time-evolution monitoring during acceleration and storage in RHIC. The polarization profile is one of the key issues in the proton beam polarization measurements at RHIC. Scanning a carbon ribbon target across the beam allows one to measure the beam intensity and polarization profiles in both vertical and horizontal directions in the transverse

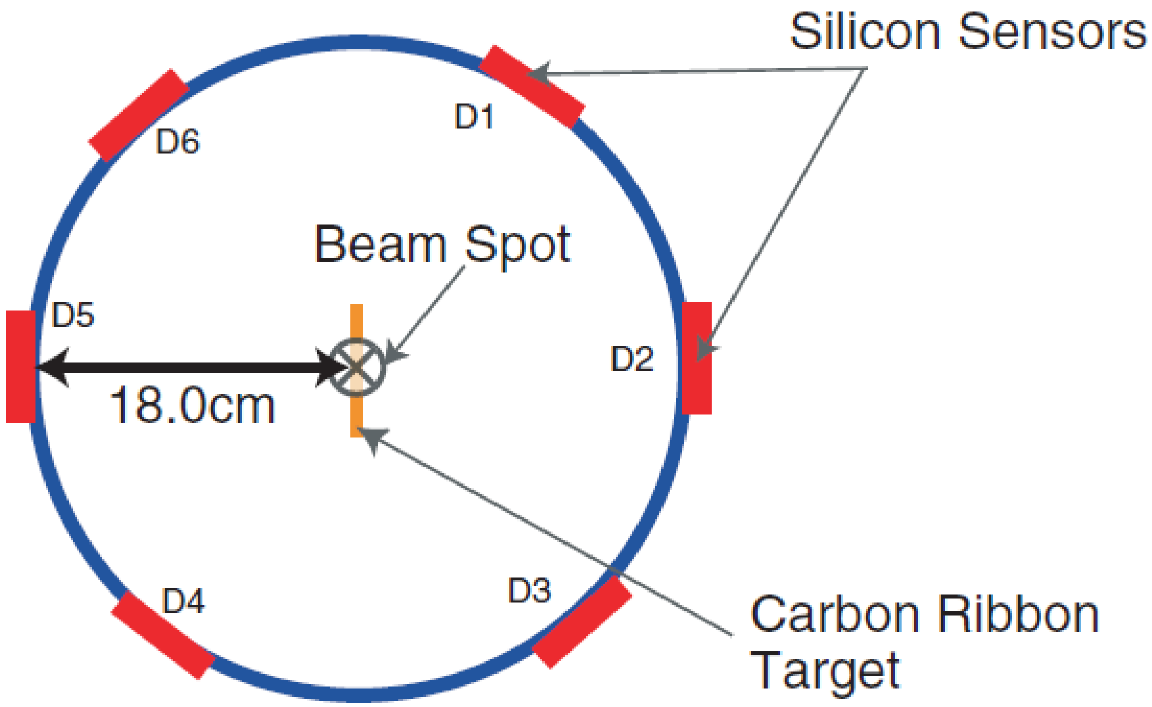

Figure 2.2: A cross section of the RHIC pC polarimeter setup.

plane.

A polarized Hydrogen Jet Target Polarimeter (H-Jet polarimeter) was used for the absolute polarization measurements, which are located at the 12 o'clock interaction point of RHIC. This polarimeter is based on elastic proton-proton scattering in the Coulomb-Nuclear Interference (CNI) region. Fig. 2.3 shows the schematic layout of the experiment. Due to particle identity in pp scattering, the polarization of the accelerated proton beam can be directly expressed in terms of proton target polarization, which can be precisely measured by a Breit-Rabi polarimeter (about 2% accuracy). The polarimeter target is a free atomic beam, which crosses the RHIC beam in the vertical direction. The *pp* elastic scattering is 2-body exclusive scattering with identical particles. A_N for the target polarization and the beam polarization is the same:

$$A_N = -\frac{\varepsilon_{target}}{P_{target}} = \frac{\varepsilon_{beam}}{P_{beam}}, \tag{2.4}$$

where ε_{target} is the raw asymmetry for the *pp* elastic scattering for the transversely polarized proton

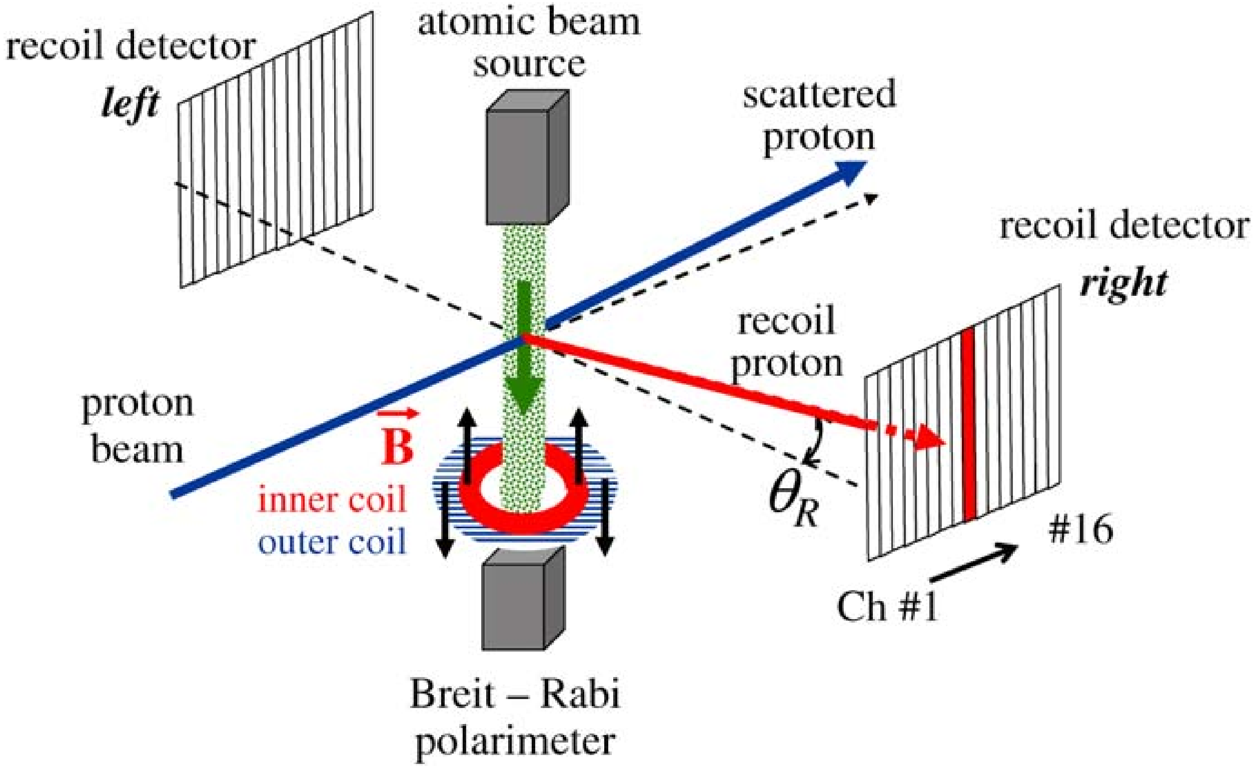

Figure 2.3: Schematic layout of the H-jet polarimeter.

target, and P_{target} is a well calibrated proton target polarization. Then the beam polarization is measured as:

$$P_{beam} = -P_{target}\frac{\varepsilon_{beam}}{\varepsilon_{target}}. \tag{2.5}$$

The beauty of the H-Jet polarimeter method is that the common factors of systematic uncertainty of ε_{beam} and ε_{target} can be cancelled. The final polarization values for each fill are obtained using the normalizations for the pC measurements, which is obtained from the comparison of H-Jet measurements with the beam polarization across the beam transverse profile obtained by pC. A more detailed description can be found in Refs. [55], [56] and [57].

2.1.3 Zero-Degree Calorimeters (ZDC)

The Zero-Degree Calorimeters (ZDC) at RHIC are hadron calorimeters that are installed on both the east and west sides of the STAR detector. The purpose of this detector is to detect neutrons emitted from the interaction region within a narrow cone along both beam directions, with a divergence angle less than 4 mrad. The ZDC measure their total energy (from which we calculate multiplicities in heavy ion reactions) [58]. The ZDC coincidence of the two beam directions is a minimal bias selection of the collisions, which makes it useful as an event trigger and a luminosity monitor.

2.1.4 Beam Beam Counter (BBC)

The Beam-Beam Counters (BBC) are scintillator annuli mounted around the beam pipe just beyond the east and west pole tips of the STAR magnet. Fig. 2.4 presents a schematic view of the counter configurations. Both BBC East and BBC West are 3.75 meters from the center of the STAR Interaction Region (IR) and consist of 18 large and 18 small tiles. The BBC inner tiles cover the pesudorapidity range $3.3 < |\eta| < 5.0$, and consists of two annuli. Each annuli is made up of closed packed hexagonal detectors in two rings, with six tiles in the inner ring and twelve tiles at outer ring [59].

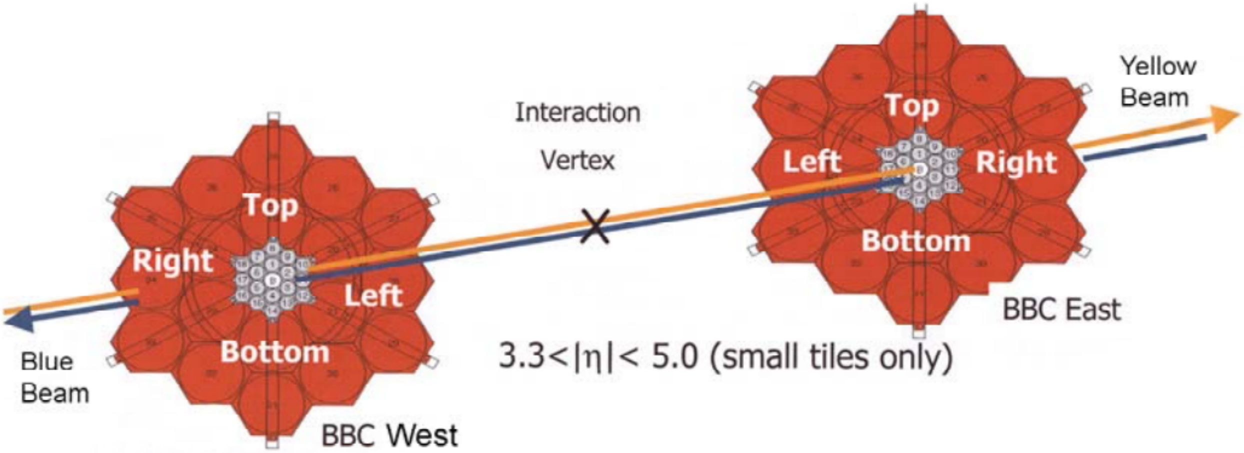

Figure 2.4: Setup of inner and outer hexagonal tile annuli for BBC East and BBC West.

The BBC is a very versatile tool for polarized proton beam diagnostics. The BBC setup provides an excellent minimum bias trigger; and for hits on the inner annuli of six hexagonal scintillator tiles, the BBC coincidence trigger with a suitable algorithm has a quite large single spin analyzing power, and so it can be used as a very effective local polarimeter. So the BBC tiles are used in STAR during proton runs to provide triggers, to monitor the overall luminosity, and to measure the relative luminosity for different proton spin orientations.

2.2 Solenoidal Tracker at RHIC (STAR)

The Solenoidal Tracker at RHIC, known as STAR, is a multipurpose detector for the measurements of hadronic and electromagnetic particles in heavy ion and polarized proton-proton collisions, as shown in Fig. 2.5. STAR consists of several types of detectors, each specializing in detecting certain types of particles or characterizing their motion. The Time Projection Chamber (TPC) is the heart of the system, which tracks and identifies particles emerging from the collisions. The Barrel Electromagnetic Calorimeter (BEMC) outside the TPC is used to measure the energy deposited by energetic photons and electrons with high precision. The Endcap Electromagnetic Calorimeter (EEMC), supplementing the BEMC, extends the measurements to higher rapidity. These three detectors are the primary sub-systems used in this analyses.

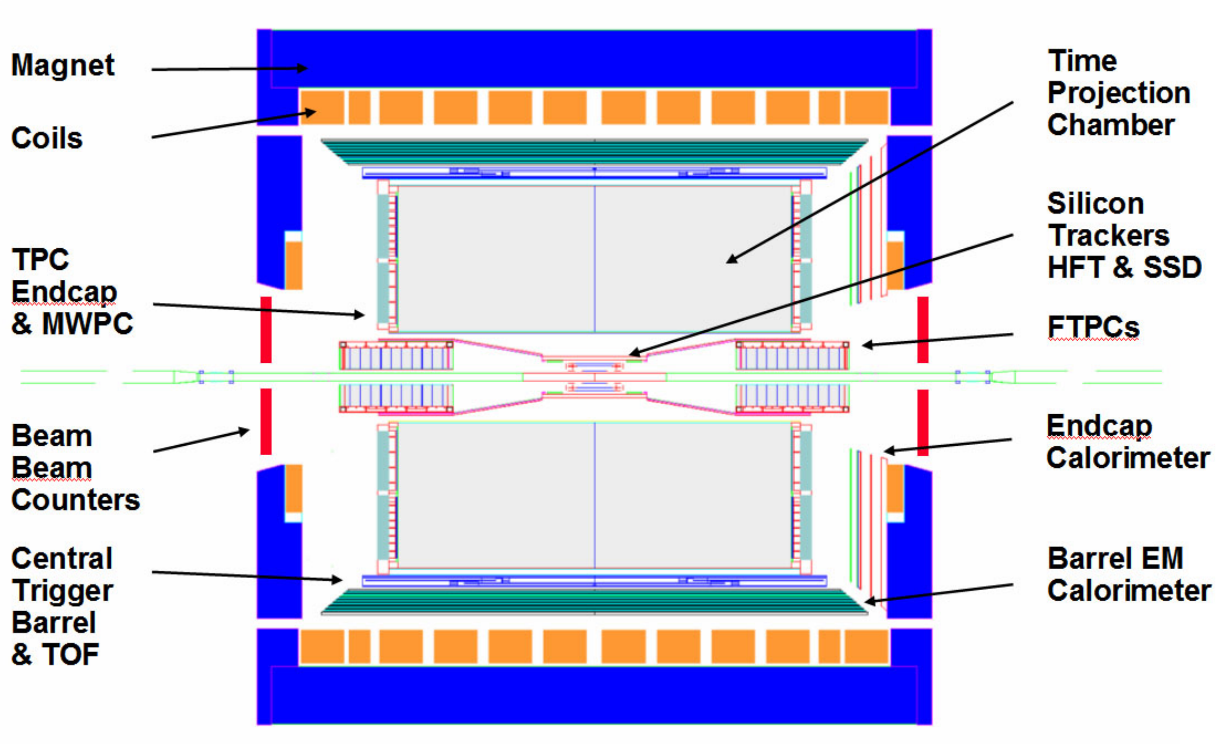

Figure 2.5: Cross sectional view of the STAR detectors.

2.2.1 Time Projection Chamber (TPC)

The central Time Projection Chamber (TPC) [60] provides charged particle tracking in a 0.5 T solenoidal magnetic field over the nominal range $|\eta| \leq 1.3$ in pseudorapidity and 2π in azimuthal angle. The TPC, which is 4.2 meters long and 4 meters in diameter, is an empty volume of P10 gas (10% methane, 90% argon) which has long been used in TPCs in a well defined, uniform, electric field of $\sim 135\ V/cm$. The paths of the ionizing particles through the gas volume are reconstructed with high precision from the released secondary electrons that drift to the readout end caps at the ends of the chamber.

The TPC readout system is based on a Multi-Wire Proportional Chambers (MWPC) with readout pads. The drifting electrons avalanche in the high fields at the $20\mu m$ anode wires, and the positive ions created in the avalanche induce a temporary image charge on the pads which disappears as the ions move away from the anode wire. The charge is measured by a preamplifier/shaper/waveform digitizer system. The original track position can be reconstructed to within a small fraction of a pad width, because the induced charge is shared over several adjacent pads.

The TPC records the tracks of charged particles, measures their momenta, and identifies the particles by measuring their ionization energy loss (dE/dx). The tracking efficiency is $\sim$ 85% for $|\eta| \leq 1.0$; but falls to $\sim$ 50% at $|\eta| \sim 1.3$.

2.2.2 Barrel Electromagnetic Calorimeter (BEMC)

The barrel electromagnetic calorimeter (BEMC) [61] is located inside the aluminum coil of the STAR solenoid. It consists of 4800 optically isolated projective towers with full azimuthal coverage for $|\eta| < 1$, thus matching the acceptance for full TPC tracking. The BEMC includes a total of 120 calorimeter modules that are mounted 60 in ϕ by 2 in η, with each subtending 6° in $\Delta\phi$ and 1.0 unit in $\Delta\eta$. The modules are each segmented into 40 towers, 2 in ϕ and 20 in η. Each of the towers subtends 0.05 rad in azimuth (ϕ) and 0.05 units in η, and is roughly 20 radiation lengths deep.

The calorimeter is a sampling calorimeter that consists of a lead-scintillator stack and has a shower maximum detector situated about 5 radiation lengths from the front. There are 20 layers of 5 mm thick lead and 19 layers of 5 mm thick scintillator, with 2 layers of 6 mm thick scintillator at the front.

The shower maximum detector (SMD) is used to provide fine spatial resolution for π^0 reconstruction and direct γ identification in a calorimeter which has segmentation (towers) significantly larger than an electromagnetic shower size. A unique feature of the STAR SMD is its double layer design. A two sided aluminum extrusion provides ground channels for two independent planes of proportional wires, which made it easy to satisfy the mechanical constraints for insertion within the BEMC stack. This double-sided SMD design feature also improves the reliability and functionality in a high occupancy environment, hadron rejection, and π^0/γ separation.

2.2.3 Endcap Electromagnetic Calorimeter (EEMC)

The Endcap Electromagnetic Calorimeter (EEMC) is located at one end of the TPC. It extends the measurement of electromagnetic energy to $1.09 < \eta < 2$ with 2π in azimuth, leaving a small gap between the endcap and barrel calorimeters which is needed for services to exit the solenoid. Within this acceptance, it adds the capabilities to detect photons and electromagnetically decaying mesons (π^0, η), to identify electrons and positrons, and to trigger on high-energy particles of these types.

The EEMC is a Pb/plastic scintillator sampling calorimeter that has a similar design to the BEMC. It is physically divided into two halves, with each half offset from $\phi = 0$ by 15°. A general schematic EEMC tower structure is shown in Fig. 2.6. The left side of the figure shows the tower divisions for half of the EEMC, and the right side shows a cross section in constant ϕ. The EEMC consists of 720 towers formed from 12 sections in pseudorapidity (η) and 60 sections in azimuth (ϕ). Each tower consists of 23 layers of lead radiator with 24 layers of scintillator. The (two) preshower, postshower, and shower maximum layers are indicated in Fig. 2.6. The scintillator layers are each 4 mm thick, with the preshower and postshower layers slightly thicker at 4.75 and 5 mm, respectively. The towers are all the same size in ϕ (6°), but vary in size in η, from ~ 0.06

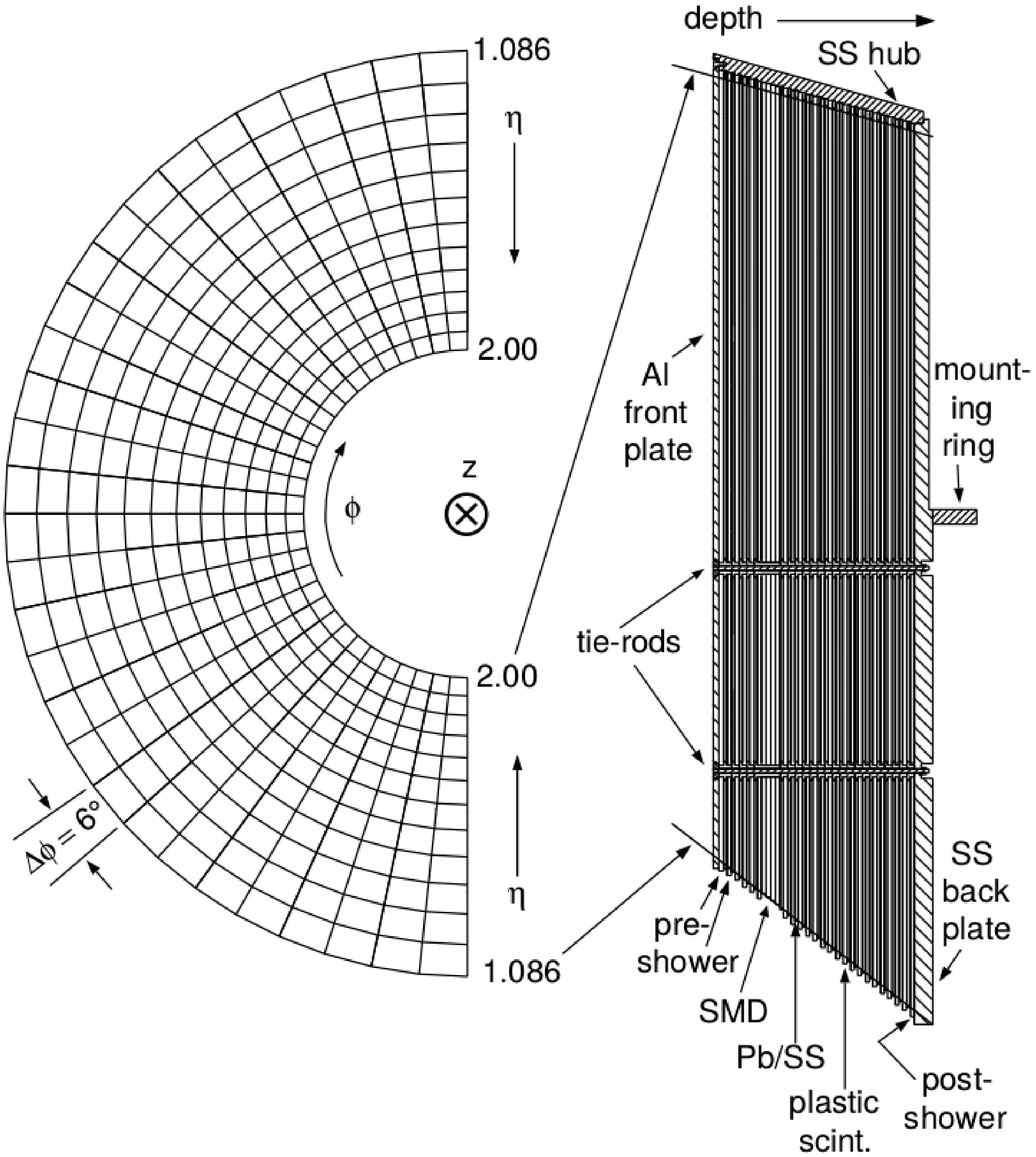

Figure 2.6: Schematic EEMC tower structure.

near η = 1 to ~ 0.10 at η = 2.

A pair of Shower Maximum Detector planes (SMD) is placed about 5 radiation lengths deep within the EEMC to provide the fine granularity crucial to distinguishing the transverse shower profile characteristic of single photons vs. the close-lying photon pairs from π^0 and η^0 decay. The

SMD is made of extruded polystyrene-based scintillator strips of triangular cross-section, organized into orthogonal u and v planes. This triangular strip shape forces energy sharing among nearby strips, improving position resolution and the stability of the measured shower profile shape.

2.2.4 EEMC Calibration

The Endcap Electromagnetic Calorimeter (EEMC) must be calibrated in order to relate an observed ADC signal to the actual transverse energy deposited in the calorimeter. One common method used for the gain calibration of electromagnetic calorimeters is to rely on the electron E/p, where the electron energy determined from the calorimeter is matched to the momentum measured by tracking chambers for identified electrons. The identification of well-known particles, such as the π^0 through its double photon decay, or the Z boson via its electron and positron decay, can also be used for calibration. However, due to the falling TPC tracking efficiency in the EEMC region, calibration methods which rely on the TPC, such as the electron E/p method used in the BEMC, are of limited use. In addition, an absolute calibration based on the reconstruction of the neutral pion invariant mass was not practical before 2009 due to problems with the simulation of the EEMC. Given these issues, the MIP method (identification of minimum ionizing particles) was chosen for the calibration of the EEMC.

Calibration Overview

The goal of this method is to identify the MIPs and determine tower gains using the mean expected energy loss of a MIP passing through the known thickness of scintillator. The Barrel Electromagnetic Calorimeter (BEMC) was initially calibrated using this method.

A MIP is an energetic charged hadron that passes through the detector and loses its energy slowly and uniformly by ionizing atoms, without depositing significant energy (that is, beyond ionization) or showering. In practice, these are mostly charged pions. MIPs are copiously produced with high purity, but there are several limitations:

1. the energy loss of a MIP in scintillator depends slightly on the type of particle, its energy,

and its angles of incidence, that is for the latter, the effective thickness of the scintillator;

2. the distribution of the deposited energy inside the scintillator is not Gaussian, especially for thin layers;
3. most importantly, a MIP does not generate electromagnetic showers, so the sampling fraction is needed to get the absolute gain factors.

The lack of particle identification from the TPC over a significant fraction of the EEMC means that charged hadron tracks could not be tagged as possible MIP candidates. A calorimeter-based MIP identification / calibration scheme was developed, using *pp* minimum bias events to set the gains for all the EEMC layers, including the towers, SMD strips and pre/post-shower layers. The MIP identification procedure relies on finding an isolated amount of energy, consistent with the expected MIP response, deposited in all layers of the calorimeter for a given tower. To ensure that there is only a single MIP present, transverse isolation is enforced by requiring a coincidence of “hits" in two neighbouring SMD strips in both planes, but requiring several empty strips on either side. The MIP trajectory is further required to be well within the tower boundaries by using a fiducial cut determined by the two sets of fired strips. With MIP candidates selected, the calibration of a given layer (preshower layers 1 and 2, SMD layers U and V, the postshower layer, and the entire tower) in a given EEMC tower proceeds by requiring an energy deposit consistent with a MIP in all other layers.

This “all but one" layer coincidence method is used to observe the MIP response in each layer. For example: we require that the energies deposited in the two SMD planes, the two preshowers and the postshower should be consistent with a MIP in order to calibrate the corresponding tower. This method works very well for a detector with lots of layers.

Calibration Procedure

First, in the SMD layers, we determine the strip-to-strip relative gains by fitting the slopes of ungated min-bias spectra; we then use isolation cuts in U and V and tower fiducial cuts to identify the MIP candidates. There are 6912 SMD stips in total, and a sample plot is shown in Fig. 2.7. In this step, we assume the spectra fall off exponentially with increasing ADC. This method works very well for determining the SMD relative gains among channels.

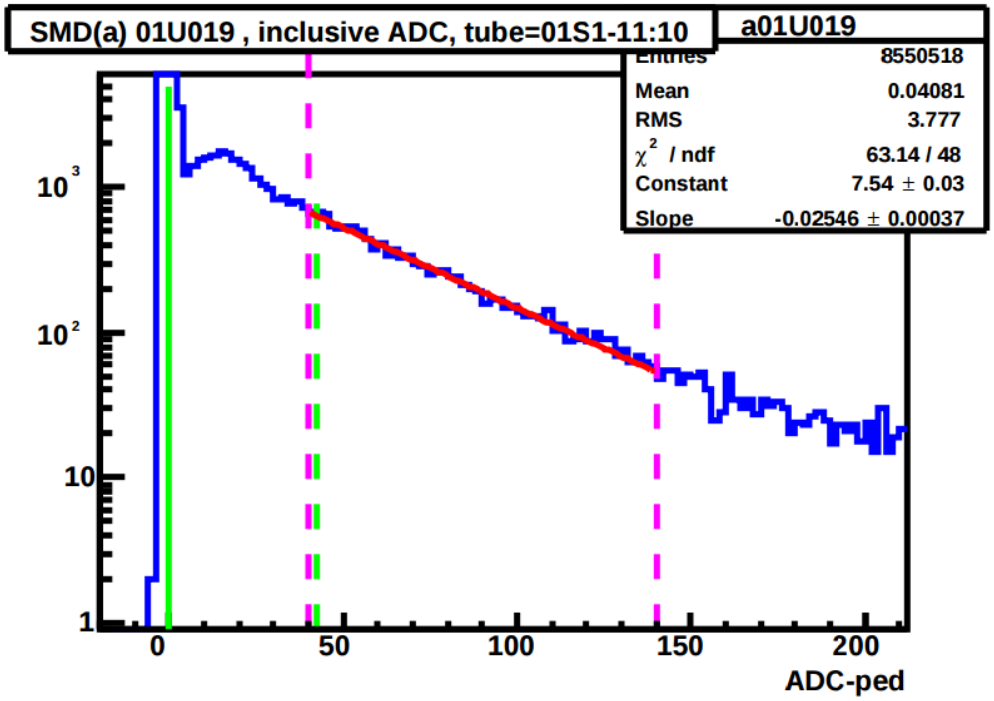

Figure 2.7: SMD ADC - pedestal spectrum.

After we get the MIP candidates from the SMD, gate all components in the stack (SMD, pre-shower 1, pre-shower 2 , tower and post-shower) by requiring valid hits in all other components of the stack, a pure MIP sample can be identified.

Imposing these cuts, we can calculate the absolute gains for pre/post-showers using the Landau fit parameters. The most probable value from the Landau distribution is then converted into the gain using the known factors through the formula:

$$gain_i(channel/\text{GeV}) = \frac{MPV_i \times \tanh(\eta_i)}{\Delta E_0}, \tag{2.6}$$

where η_i is the pseudorapidity of the sector i, $\Delta E_0 = thickness \times 1.8$ MeV/cm energy loss per layer. A sample plot for Pre-shower 1 is shown in Fig. 2.8.

Imposing the MIP cut, the absolute tower gains can be calculated, now using a Gaussian fit

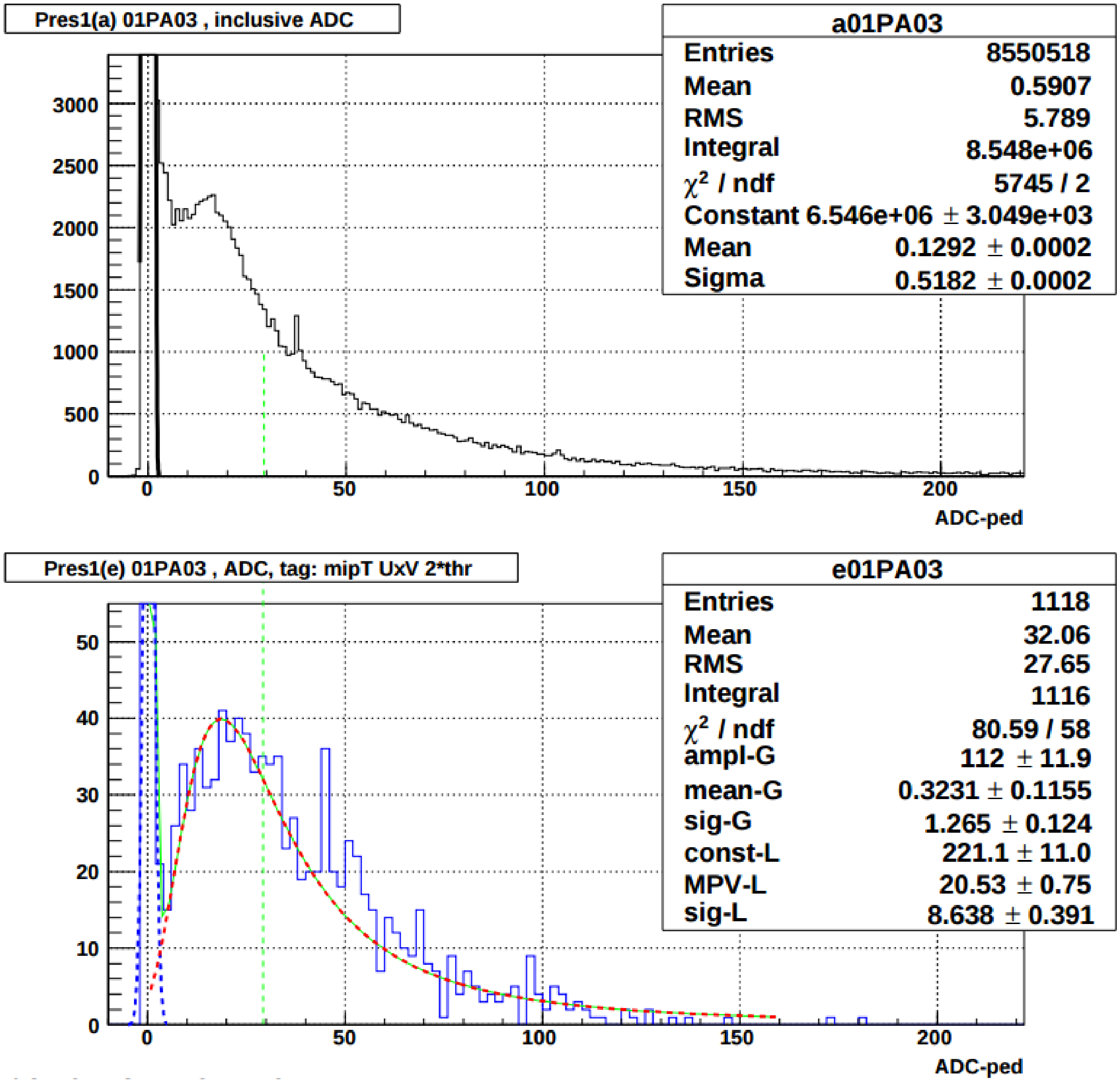

Figure 2.8: Pre-shower 1, ADC - pedestal spectrum before the MIP cuts (upper plot) and after the MIP cuts (lower plot).

distribution. The formula is the same as for the pre/post showers, $gain_i = \tanh(\eta_i) \times Mean/\Delta E_0$, but now encompassing all layers, and specifying a sampling fractions. For a tower, $\Delta E_0 = 24/5\% \times 0.4\, cm \times 1.8$ MeV/cm (each tower has 24 layers of 4 mm plastic with $dE/dx \sim 1.8$ GeV/cm and a sampling fraction of about 5%). A sample plot is shown in Fig. 2.9.

After following these procedures we get the first-pass gains, which are very close to the final values obtained with optimized cut settings. We sum sets of 12 consecutive SMD strips to get the

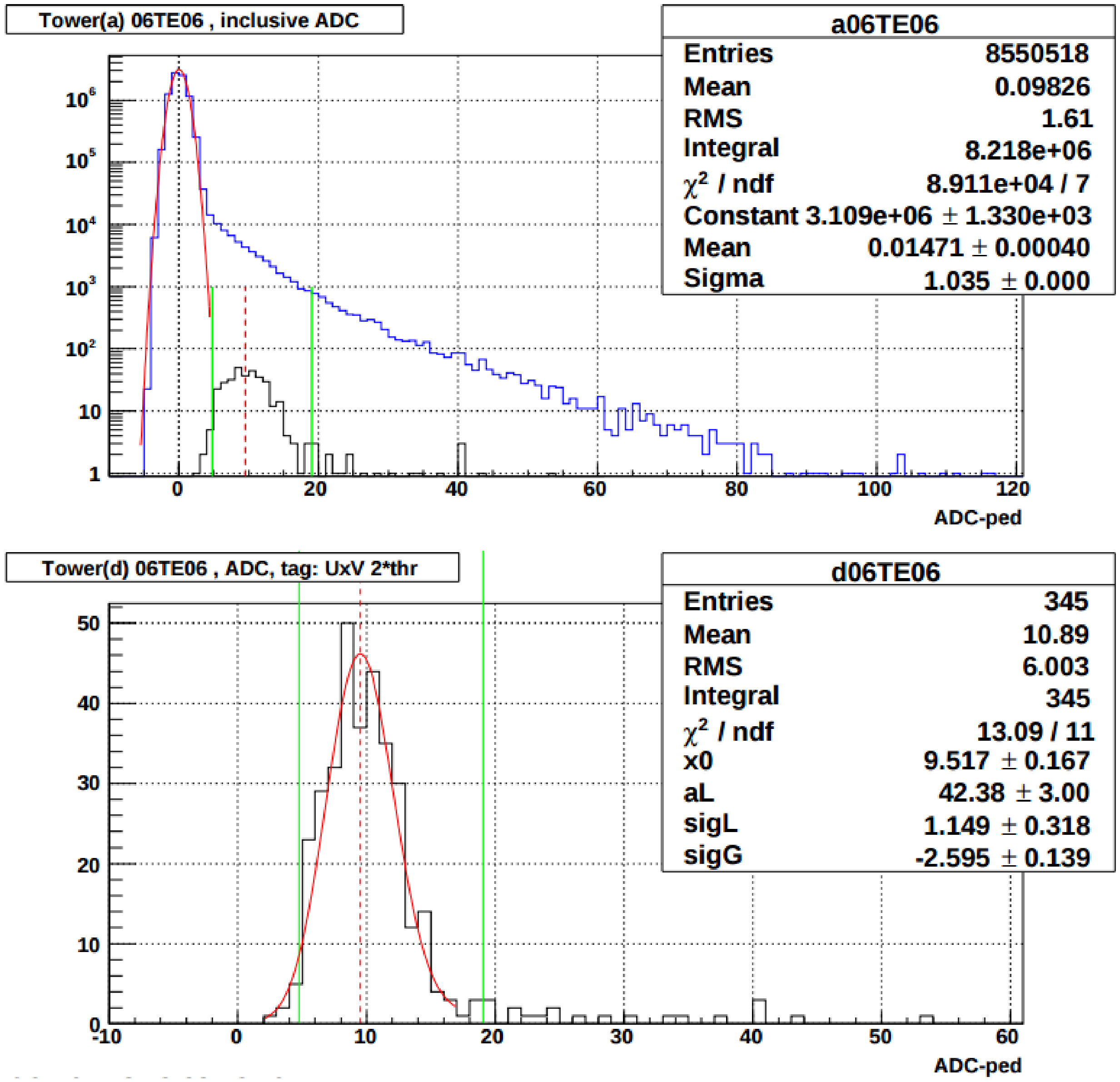

Figure 2.9: Tower, ADC - pedestal spectrum before the MIP cuts (upper plot) and after the MIP cuts (lower plot).

absolute SMD gains, and then do another iteration, to see if the deduced gains are stable.

The 2009 EEMC final tower gains as a function of the rapidity bins are shown in Fig. 2.10. The gains are about 10% lower than the ideal values.(Ideally, each tower HV should be adjusted so that E_T = 60 GeV would be in channel 4095).

The gains used in this analysis were based on the 2009 MIP calibrations [62]. Data and simulation agreement is better compared to previous samples using the final 2008 gains adopted

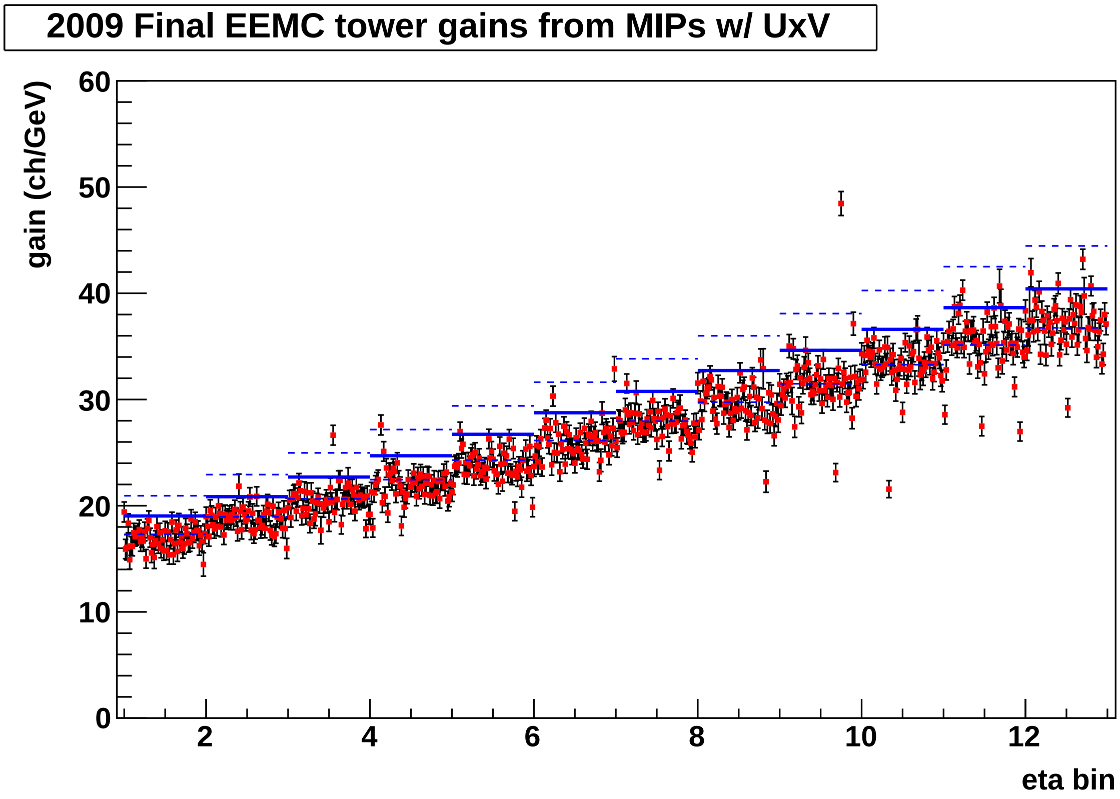

Figure 2.10: 2009 pp200 final tower gains vs. η bins.

from the 2006 MIP calibration, as shown in Fig. 2.11 and Fig. 2.12.

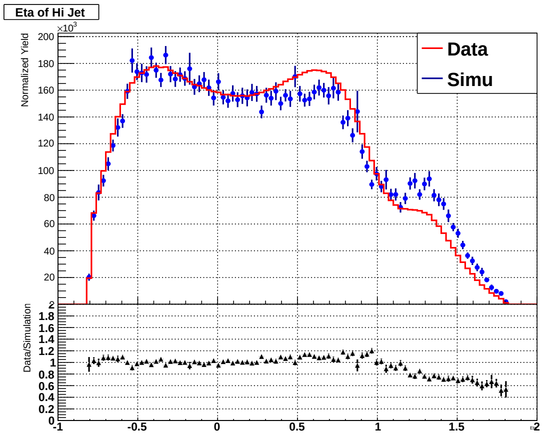

Figure 2.11: Jet η distribution using 2006 EEMC gains.

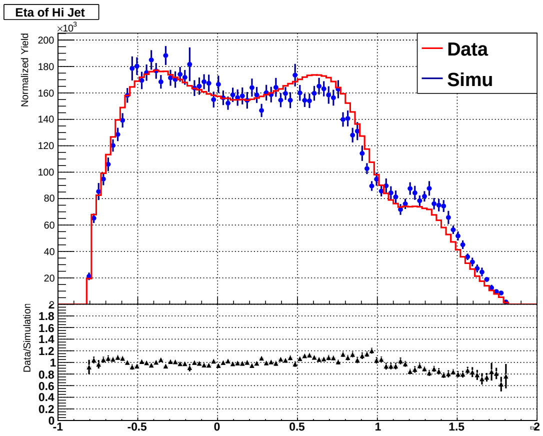

Figure 2.12: Jet η distribution using 2009 EEMC gains.

Absolute Uncertainty

The relative (tower to tower) uncertainties of the MIP calibration results are pretty good, and the big uncertainties lie in the conversion to absolute values. The absolute calibration should rely on the results from π^0 analyses at EEMC or using electrons at the outer rings where the EEMC has TPC coverage.

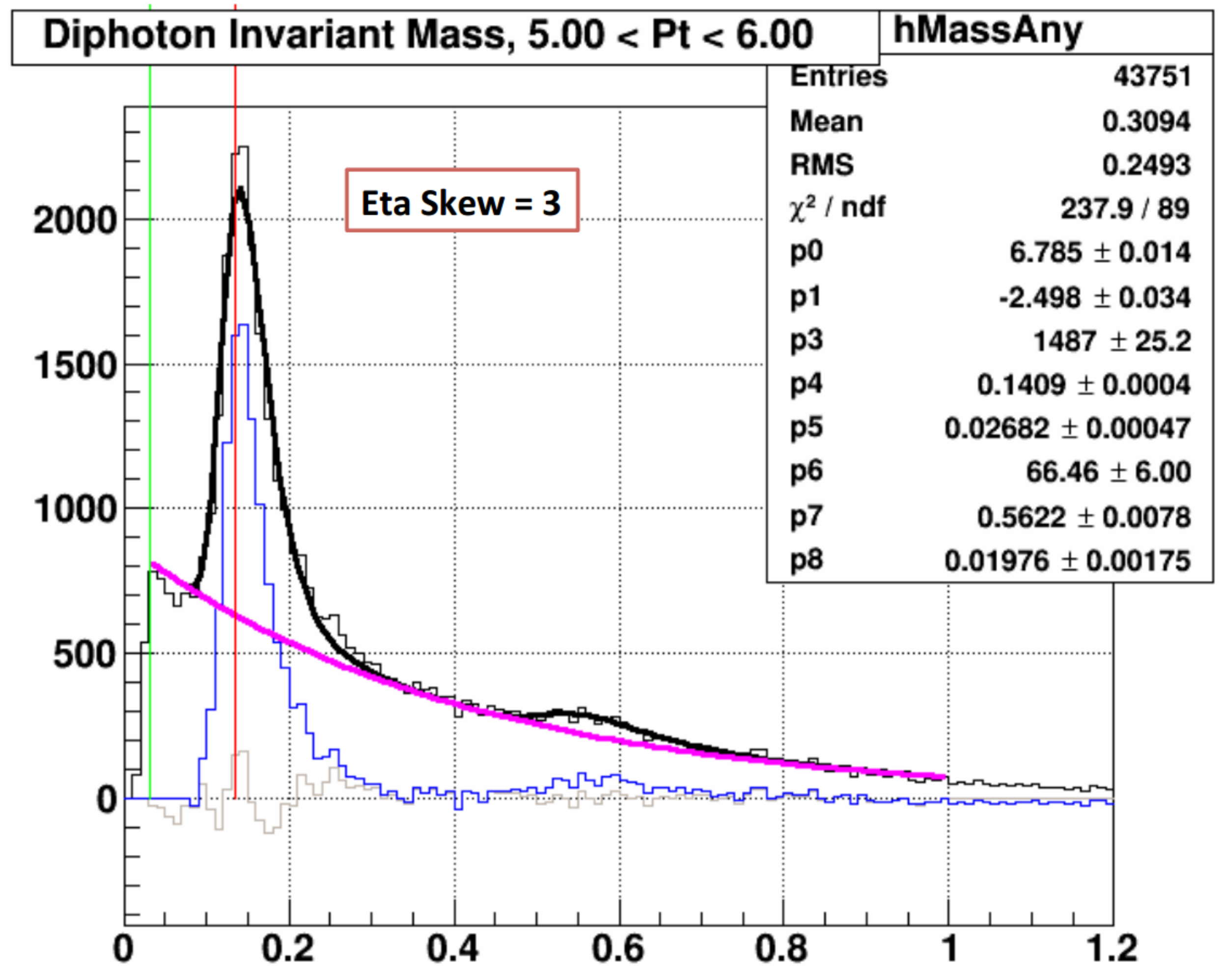

Figure 2.13: 2009 *pp* 200 GeV di-photon invariant mass distribution.

For the 2009 pp 200 GeV dataset, the scale uncertainty is found to be 4.5% from the π^0 results as shown in Fig. 2.13 (the p4 parameter is the fitted π^0 mass).

Relative Gain Change

Because MIP calibrations produces reliable and stable results, the relative gains can be used to check the performance and stability of the EEMC system over time. As shown in Fig. 2.14, we separate the whole 2009 data set into two different periods based on the time when those data were taken, and calibrate them individually. The y-axis is the average ratio of the MIP gains over the ideal tower gains, and the x-axis is the date, with January 1st, 2009 as 0. We found that the EEMC gains decreased about 1% during the 2009 run (Fig. 2.14), which is negligible. But if we use the same method for pp runs in 2012, 2013 and 2017, as shown in Fig. 2.15, in 2012 we see that both *pp* 200 GeV and *pp* 500 GeV decrease ~ 2%; but in 2013, the overall decrease is about 5%. A 1% increase of the EEMC high voltage would increase the gains by ~ 8%. Between the 2012 *pp* 200 GeV and *pp* 500 GeV runs, the high voltage was increased by 1%, and before 2017, there was a 2% high-voltage increase for the EEMC towers. These changes are clearly visible in the relative gain comparison plots.

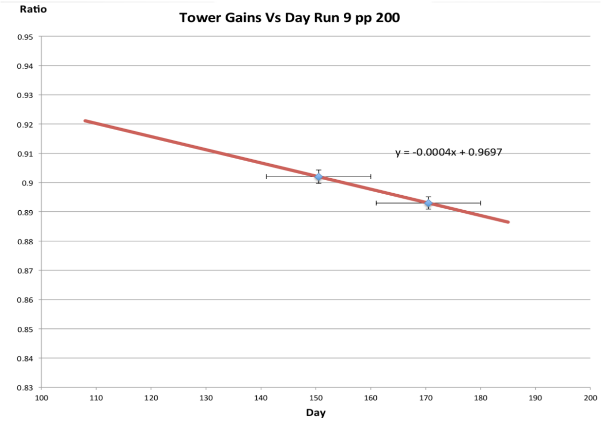

Figure 2.14: 2009 *pp* 200 GeV EEMC Relative Gain Comparison.

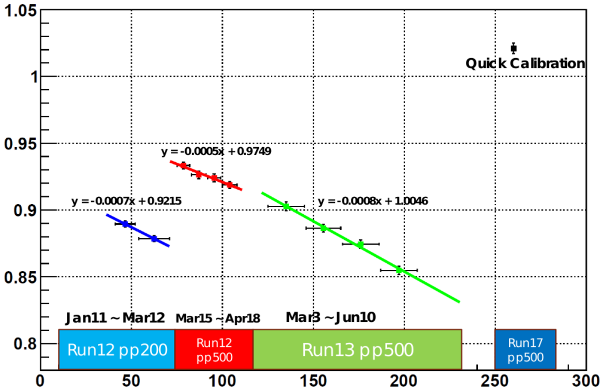

Figure 2.15: 2012, 2013, 2017 EEMC Relative Gain Comparison.

The reason for the gain decrease is still an unknown problem, though it may be related to the radiation damage of the scintillators. Typically the EEMC gains were calculated and used through the whole data set every year. Since 2013, knowing that the gains would change over time, and due to the limited statistics, a slightly different approach was proposed: for a given tower, calculate its average gain from the entire data set, and then split the running period into four equal quarters.

Extrapolate the tower gains at the middle of each quarter using the slope of a fit line and the average gains. The final values in the EEMC official database are the 4 gain sets with 4 different timestamps, which means the real data taken at different times would use different gain factors.

2.3 Data Sample

The data used in this analysis were recorded by the Solenoidal Tracker at RHIC (STAR) collaboration in 2009 at $\sqrt{s} = 200$ GeV with 21 pb^{-1} integrated luminosity. The luminosity-weighted polarizations of the two beams were $P_B = 56\%$ and $P_Y = 57\%$. The STAR detector subsystems used to reconstruct jets are the Time Projection Chamber (TPC) and the Barrel and Endcap Electromagnetic Calorimeters (BEMC, EEMC) [63]. In brief, the TPC provides charged particle tracking in a 0.5 T solenoidal magnetic field over the nominal range $|\eta| \leq 1.3$ in pseudorapidity and 2π in azimuthal angle. The BEMC and EEMC are segmented lead-scintillator sampling calorimeters, which provide full azimuthal coverage for $|\eta| < 1$ and $1.09 < \eta < 2$, respectively. The calorimeters measured electromagnetic energy deposition and provided the primary triggering information via fixed $\Delta\eta \times \Delta\phi = 1 \times 1$ calorimeter regions (jet patches). A jet patch trigger was satisfied if the transverse energy in a single jet patch exceeded either 5.4 GeV (JP1 trigger, prescaled) or 7.3 GeV (JP2 trigger), or if two jet patches adjacent in azimuth each exceeded 3.5 GeV (AJP trigger). In addition, the Beam-Beam Counters (BBCs) [59] were used in the determination of the integrated luminosity and, along with the zero-degree calorimeters (ZDCs) [63], in the determination of helicity-dependent relative luminosities.

The duration from when the beams are fully injected into the rings to when the beams are dumped is called a RHIC fill. Data samples are divided into different runs which are taken for a certain period for different fills. In this analysis, the same run list was used as for the 2009 dijet measurements at Mid-Rapidity [46], see appendix A.

2.3.1 Data Quality Assurance

The run selection and QA were done during the 2009 dijet measurement at mid-rapidity. It was completed in several steps. First, a list that contains all runs longer than 3 minutes and that included the TPC, BEMC and EEMC was created. This list includes a set of diagnostics by STAR collaborators recorded during the data taking. Next, only those runs with the trigger setups production2009_200Gev_Hi, production2009_200Gev_Lo, and production2009_200Gev_Single were retained. The trigger setup denotes the specific triggers included in the data: production2009_200Gev_Hi contains only the L2JetHigh triggered events, production2009_200Gev_Lo contains only the JP1 triggered events, and production2009_200Gev_Single contains both L2JetHigh and JP1 triggered events. More details are provided in the next section

Run-by-run QA was also done by looking at the various quantities of interest to the analyses, for example, the number of reconstructed tracks or the energy deposited in the calorimeter per event. Individual runs for which the per event mean of some quantity deviates more than 5σ from the global means were discarded. Furthermore, runs that do not have associated beam polarization values, relative luminosity, and valid spin bit values are also not used, as this information is essential for the double spin asymmetry calculations. Finally we obtain a list of 888 accepted runs from the 2009 pp 200 GeV data set.

2.3.2 Trigger System

The STAR Trigger system [64] was designed to facilitate the related heavy ion research and the quest to understand the interior of hadrons. It is a multi-level, modular, pipelined system in which digitized signals from the fast trigger detectors are examined at the RHIC crossing rate and then the information is used to determine whether to begin the full readout cycle for slower, more finely grained detectors, which provide information for most of the physics observables of interest. In this analysis, the relevant trigger systems are the Level-0 and Level-2.

Level-0

Level-0 is the 1st layer of trigger electronics, which consists of a tree of Data Storage and Manipulation (DSM) boards and a Trigger Control Unit (TCU). It processes the trigger data for every RHIC crossing and only accepts events that are potentially of interest to initiate the data taking. The detector front-end electronics that feeds Level-0 was spread out over several detectors and VME crates. The decision of the L0 trigger was based on energy deposition in fixed regions of the BEMC and EEMC which are called jet patches when triggering on jets. There were 30 jet patches in the 2009 configuration, as shown in Table 2.1. The trigger logic gets the ADC sums from the jet patch towers and compares them to the trigger thresholds; events passing the thresholds were recorded.

ϕ Location	BEMC East $-1 < \eta < 0$	BEMC Middle $-0.6 < \eta < 0.4$	BEMC West $0 < \eta < 1$	EMC Overlap $0.4 < \eta < 1.4$	EEMC $1 < \eta < 2$
10 o'clock (150°)	BEMC-JP6	BEMC-JP12	BEMC-JP0	Overlap-JP0	EEMC-JP0
12 o'clock (90°)	BEMC-JP7	BEMC-JP13	BEMC-JP1	Overlap-JP1	EEMC-JP1
2 o'clock (30°)	BEMC-JP8	BEMC-JP14	BEMC-JP2	Overlap-JP2	EEMC-JP2
4 o'clock (−30°)	BEMC-JP9	BEMC-JP15	BEMC-JP3	Overlap-JP3	EEMC-JP3
6 o'clock (−90°)	BEMC-JP10	BEMC-JP16	BEMC-JP4	Overlap-JP4	EEMC-JP4
8 o'clock (−150°)	BEMC-JP11	BEMC-JP17	BEMC-JP5	Overlap-JP5	EEMC-JP5

Table 2.1: 2009 jet patch geometry.

There are three different thresholds used for the trigger decision. JP2, JP1 or JP0 bits are set separately if the ADC sum of the jet patch is above the highest, middle or lowest thresholds, respectively. The jet patch thresholds were changed slightly over the course of Run 9 to normalize yields across the BEMC and EEMC. It was believed the latter had lower gains. The jet patch threshold changes are summarized in Table 2.2. Equivalent transverse energy is approximated by $E_T \approx 0.236 \times (ADC - 5)$ GeV. The Adjacent Jet Patch (AJP) triggers were implemented here for the jet patches overlapping in the ϕ direction, and is set if two of the 24 BEMC and EEMC jet patches (no EMC overlapping) that is adjacent in ϕ fire the lowest threshold. In this jet analyses, we were only interested in the JP2, JP1 and AJP triggers.

Label	set 1 (ADC)	set2 (ADC)	set 1 $E_T(GeV)$	set 2 $E_T(GeV)$
BEMC-JP-th0	20	20	3.5	3.5
BEMC-JP-th1	28	28	5.4	5.4
BEMC-JP-th2	36	36	7.3	7.3
EMC-overlap-JP-th0	20	19	3.5	3.3
EMC-overlap-JP-th1	28	26	5.4	5.0
EMC-overlap-JP-th2	36	34	7.3	6.8
EEMC-JP-th0	20	18	3.5	3.1
EEMC-JP-th1	28	25	5.4	4.7
EEMC-JP-th2	36	32	7.3	6.4

Table 2.2: 2009 jet patch thresholds. Set 1 ends with run 10125061.

Level-2

The events that are accepted by Level 0 ultimately reach Level 2, where they undergo more detailed analysis. This level is entirely software-based and more sophisticated triggering algorithms can be implemented here. The L2 Trigger used in this analyses is L2JetHigh, which includes events in which the JP2 or AJP bits are set. The algorithm also looks for energy deposits in 1×1 regions in the calorimeters, but with a much finer granularity than the 30 fixed jet patches at L0. It scans 330 unique 5×5 areas of the calorimeter, and finds the two 1×1 regions of the detector separated by at least 30 degrees in ϕ which contain the most energy.

There are three trigger categories here: monojet, dijet and random. A monojet trigger is satisfied if the high patch transverse energy is above the threshold, typically set around 6.5 GeV; the dijet trigger is fired if both patches are above a dijet threshold, which is somewhat lower than the monojet threshold. There are three sets of dijet thresholds; which set is used is based on the sum of the energy weighted η positions of the two patches. This functionality was included because patches at forward pseudorapidities tend to have lower transverse energies, so lower thresholds are needed in the forward region to keep the dijet acceptance rate somewhat constant across the detector. The random trigger accepts random events at a set rate regardless of whether or not the event would have passed either the monojet or dijet conditions. A given event can satisfy multiple L2Jet trigger categories simultaneously, but events which do not satisfy any of the above categories are dropped and not used in this analysis.

CHAPTER 3

Jet Reconstruction and Di-jet Selection

Almost every event of interest at high-energy colliders contains collimated collections of particles known as jets. Due to the color confinement, a parton radiates gluons and further splits into other gluons and quark-antiquark pairs as it moves out from the collision point. The quarks and gluons then hadronize into color-neutral objects, some of which decay into stable or metastable particles which can be measured in the experiments. The radiation is predominantly in the direction of the original hard parton; thus the 4-momentum sum of the final state particles should approximate the 4-momentum of the hard parton that was originally produced in the collison, which provide a window into short-distance physics. Jets are produced through the fragmentation and hadronization of the hard scattered partons, which reflects the configuration of quarks and gluons at short distances. These are important observables, both in Standard Model studies and in searches for physics beyond the Standard Model [65].

3.1 Jet Reconstruction

Jets are the collimated sprays of hadrons that result from the fragmentation of a high-energy quarks or gluons, and so one can probe the behavior of the original ‘parton’ that produced them by measuring the jet 4-momentum. The properties of the jets must be well defined and reproducible in order to be used. A jet definition includes its algorithms, parameters, and recombination scheme, which can be applied equally to experimental information such as calorimeter towers and charged particle tracks, final state particles, or the partonic events of perturbative QCD calculations [66].

3.1.1 Jet Algorithms

Most jet algorithms belong to one of two broad classes: sequential recombination algorithms and cone algorithms. Sequential recombination algorithms usually identify the pair of particles that are closest in some distance scale, estimate their total transverse momentum p_T, recombine them, and then repeat the procedure over and over again, until some stopping criterion is reached. Cone algorithms put together particles within specific conical angular regions, adjusting them such that the momentum sum of the particles contained in a given cone coincides with the cone axis [67].

Typically the algorithms are required to be infrared and collinear (IRC) safe, which means if one modifies an event by a collinear splitting or the addition of a soft emission, the set of hard jets that are found in the event should remain unchanged. This safety is important in several ways. Firstly, a hard parton undergoes many collinear splittings as part of the fragmentation process and the non-perturbative dynamics also lead to collinear splittings. There is always some emission of soft particles in QCD events, both through perturbative and non-perturbative effects. Secondly, the divergence cancellation between real and virtual corrections in fixed-order perturbative QCD calculations may be broken by an IRC unsafe jet algorithm. Furthermore, because of the finite resolution and non-zero momentum thresholds, the experimental detectors themselves also provide some regularization of collinear and infrared unsafety.

The STAR jet analyses have mainly used two different algorithms in their results. Before the 2009 run analysis, inclusive jet results [68] [69] used the midpoint cone algorithm; for all later runs the inclusive jet [39] and dijet [46] analyses used the anti-k_T algorithm.

Midpoint Cone

The midpoint cone algorithm is a cone algorithm originally used by the CDF and DØ groups for their Run II jet analysis [70]. Cone algorithms form jets by associating together particles that lie within a cone of a specific radius in $\eta \times \phi$ space around the energy-weighted centroid as shown in equation 3.1.

$$\eta^C = \frac{\sum_{i\subset C} E_T^i \eta^i}{E_T^C}, \qquad \phi^C = \frac{\sum_{i\subset C} E_T^i \phi^i}{E_T^C}, \qquad E_T^C = \sum_{i\subset C} E_T^i. \tag{3.1}$$

The algorithm begins by collecting a list of individual particles from tracks and fired towers which serve as seeds for the initial jet cones or proto-jets when passing through the cone algorithm. Then additional proto-jets are formed from the midpoints between seeds within a distance $\Delta R < 2R$ and added to the list; in this stage individual particles can be shared by several proto-jets. At the splitting and merging stage, the jet algorithm decides whether to split or merge two proto-jets with overlapping cones. The decision is based on the fraction of energy shared by the lower p_T proto-jet. Proto-jets that share a fraction greater than f (50%) would be merged, while the others would be split, with the shared particles individually assigned to the proto-jet that is closest in $\eta - \phi$ space. The algorithm always works with the highest E_T proto-jet, and the ordering of the list is checked after each instance of merging or splitting.

Anti-k_T Algorithm

This algorithm is a sequential recombination algorithm that repeatedly combines pairs of particles which are closest to each other. It was introduced and studied in Ref. [71]. This algorithm introduces the distance d_{ij} between entities (particles, pseudojets) i and j and d_{iB} between entity i and the beam (B):

$$\begin{aligned} d_{ij} &= min(1/p_{ti}^2, 1/p_{tj}^2)\frac{\Delta R_{ij}^2}{R^2} \\ d_{iB} &= 1/p_{ti}^2, \end{aligned} \tag{3.2}$$

where $\Delta R_{ij} = \sqrt{(\eta_i - \eta_j)^2 + (\phi_i - \phi_j)^2}$ and p_{ti}, η_i and ϕ_i are respectively the transverse momentum, rapidity and azimuth of particle i. R is the radius parameter of the jets in $\eta - \phi$ space. In this analysis R is set to 0.6. This algorithm finds the distances d_{ij} and d_{iB} for all the particles and pairs, and then identifies the minimum value. If the minimum value is d_{ij}, then it recombines the two particles i and j, and recalculates d_{ij} and d_{iB}. If the minimum value is d_{iB}, then particle i

is a final state jet and it is removed from the list of particles. The distances are recalculated and the procedure repeated until no entities are left. The anti-k_T algorithm essentially behaves like an idealised cone algorithm, and is less susceptible to diffuse soft backgrounds from underlying event and pile-up contributions. These latter concerns will be discussed in later chapters.

3.1.2 Jet Selection

The jet reconstruction procedures follow those used in the 2009 inclusive jet analysis [39]. Jets were found using the anti-kT algorithm [72] implemented in the FastJet [67] package, with resolution parameter $R = 0.6$. In addition to the jet algorithm's parameters, there are other requirements imposed on the TPC tracks and calorimeter towers which serve as input to the jet algorithm at the detector level.

Track Conditions

Tracks with $p_T \geq 0.2$ GeV/c and pseudorapidy η between -2.5 and 2.5 were analyzed. The tracks are also required to contain more than 5 fit points in the TPC, and $> 51\%$ of the maximum number of fit points allowed by the TPC geometry and active electronic channels. A p_T-dependent DCA cut (distance of closest approach) is applied, where the DCA is the distance between the event vertex and the charged particle track trajectory at the point when the trajectory is closest to the vertex. This helps reduce the pile-up effect. This cut retains tracks with a DCA $< 2\ cm$ for track p_T below 0.5 GeV/c, and DCA $< 1\ cm$ for p_T above 1.5 GeV/c. This cut is linearly interpolated in the intermediate p_T region.

The charged particle tracks are reconstructed when the ionization electrons they produce as they traverse the TPC volume drift to the endcaps and avalanche onto readout pads. These pads are situated in rows (padrows) oriented roughly perpendicular to a straight radial line emanating from the interaction point. A fit point is any padrow that contributes to a track in order for it to be reconstructed. The condition on the number of fit points differs from the 2009 inclusive jet analysis, which required that tracks have more than 12 hits in order to be reconstructed. Tracks which point

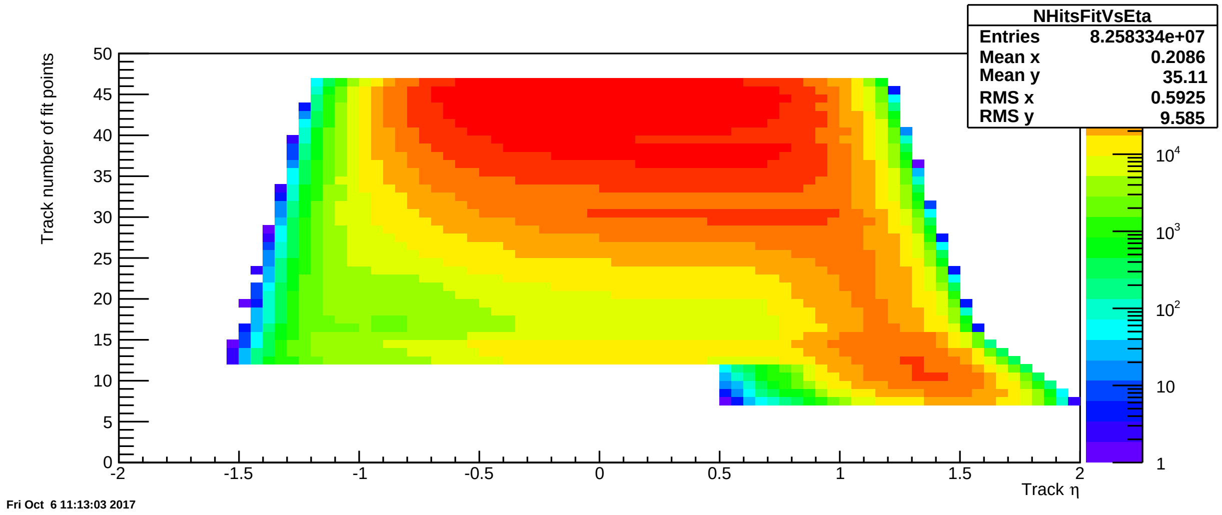

Figure 3.1: Track: number of fit points vs. η from data.

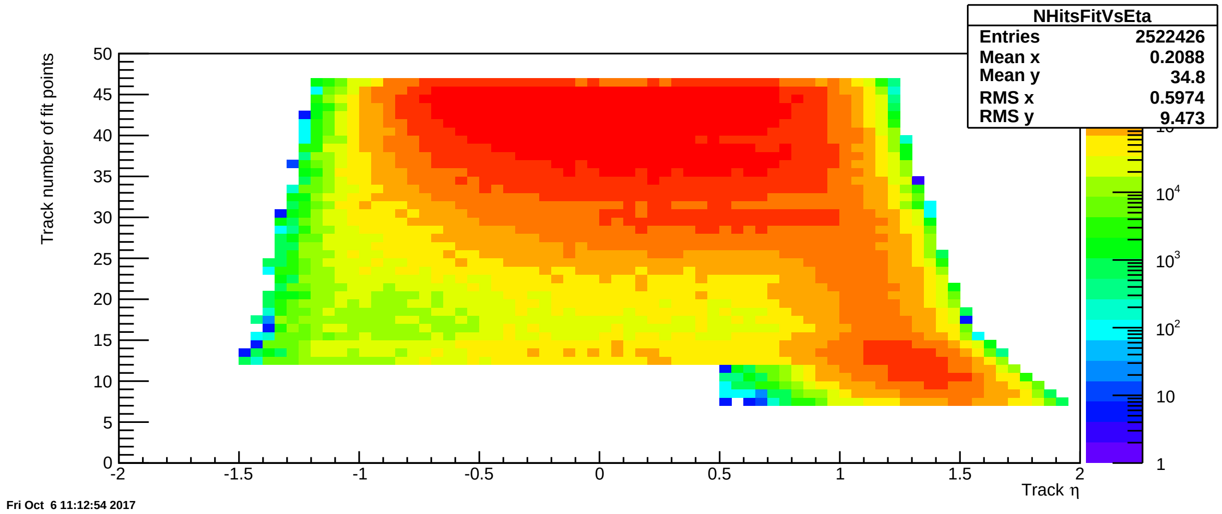

Figure 3.2: Track: number of fit points vs. η from simulation.

to the EEMC deposit charge over fewer points (padrows) due to the geometry of the TPC. Reducing the number of required hits allows more tracks to be included in the jet reconstruction, which improves our jet p_T determination. The 5 point tracking does not extend over the full TPC, and is only implemented for tracks with $\eta > 0.5$, as shown in Figs. 3.1 and 3.2.

Fig. 3.3 shows the average jet p_T ratio between the particle and detector level (see Chapter 4) as a function of the detector pseudorapitity. The red points are the results for 5 points fits, while blue is for 12 points. As expected, the average value below detector pseudorapidity 0.5 is the

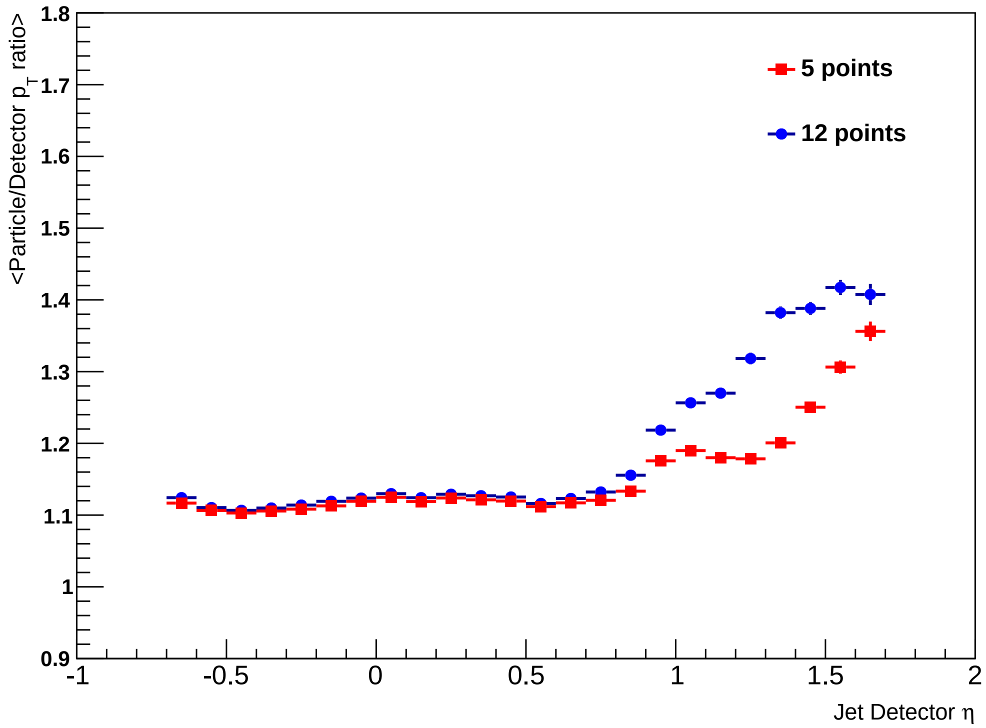

Figure 3.3: Average jet particle over detector level p_T ratio vs. detector η with different number of fit points required.

same after implementing the 5-points threshold. Detector pseudorapidity 1.0 to 1.3 is where the tracking efficiency decreases significantly, and great improvement is found there; the difference is also reduced at higher pseudorapidity range where even 5-point tracking fails.

Tower Conditions

All calorimeter towers with $E_T \geq 0.2$ GeV and tower ADC larger than the pedestal + 4 and pedestal + RMS were included in the jet analysis.

Particles measured as TPC trajectories are assumed to be charged pions (default mass 0.1396 GeV), whereas energy deposits in the electromagnetic calorimeters are assumed to be massless photons. To avoid double-counting the jet energy contributions from the TPC and calorimeters, towers with tracks pointing to them had the p_{TC} of the track subtracted from the E_T of the tower. If the track p_{TC} is greater than the energy of the tower, the tower E_T is set to zero. This method reduces the residual jet momentum corrections and sensitivity to fluctuations in the hadronic energy deposition, resulting in an improved jet momentum resolution [39]. Tracks and towers are both converted to Lorentz 4-momentum vectors and then merged as the input to the jet finder where the jet algorithm is applied. Reconstructed jets with $p_T > 5$ GeV/c were kept.

3.2 Di-Jet Selection

Di-jets are pairs of jets which arise from the same partonic hard scattering event. For each event, dijets were selected by choosing the two jets with the highest p_T that fell in the pseudorapidity range $-0.8 \leq \eta \leq 1.8$. Other conditions were the same as those used in the 2009 dijet measurements at mid-rapidity [46]. The steps used to determine which jets in an event are identified as a dijet candidate are below (in order):

1. Select the highest ranked vertex in event (vertex must have rank > 0),
2. Require vertex to have $|z| < 90$ cm,
3. Select all jets satisfying $-0.8 \leq \eta \leq 1.8$ and $-0.7 \leq \eta_{detector} \leq 1.7$,
4. Select the two highest p_T jets,
5. Require that at least one jet satisfies one of the trigger categories.

The steps above are exactly the same as those used for the 2009 Barrel-Barrel dijet measurement [46] except for the cuts on pseudorapidity, which are used for both the data and detector level simulation. When using the unbiased full Pythia sample, the $\eta_{detector}$ requirement in step 3 is omitted. The detector pseudorapidity $\eta_{detector}$ is defined by projecting the jet thrust axis from the collision vertex to the BEMC/EEMC detector, and taking the η component of the projected vector as expressed in the STAR detector coordinate.

The two jets selected using the steps above define a dijet candidate, and only one dijet candidate per event. The candidate dijets constructed using the procedure above must meet additional requirements in order to be used in the analyses. The procedures below are placed after the Underlying Event subtraction (chapter 5) and jet p_T shift (chapter 6):

- Opening angle cut: $\cos(\Delta\phi) \leq 0.5$,
- Neutral fraction cut: One jet must have a neutral fraction < 1.0,
- Asymmetric p_T cut: High p_T jet ≥ 8.0 GeV/c and low p_T jet ≥ 6.0 GeV/c,
- p_T balance cut.

The two jets arising from a partonic hard-scattering event should be roughly back-to-back in azimuth (ϕ). Jets which are closer to each other in azimuth likely do not represent the $2 \rightarrow 2$ hard scattering process. To remove these events from the analysis, an opening angle cut was placed on the two jets of the dijet event such that the azimuthal angle between them must be more than 120°.

A p_T balance cut is used to remove the highly unbalanced p_T events that are likely a result of finite resolution in the track curvature measurement (overestimating the track p_T) and not from the hard scattering. Jets which contain a track with $p_T \geq 30$ GeV are kept if the p_T ratio of this jet over the associated one is between $\frac{2}{3}$ and $\frac{3}{2}$, otherwise the event is discarded. To facilitate comparison with theoretical predictions, an asymmetric condition (one jet had $p_T \geq 8.0$ GeV/c and the other jet had $p_T \geq 6.0$ GeV/c) was placed on the transverse momentum of the jets.

In the inclusive jet analysis, a neutral energy cut is applied to remove jets comprised primarily of background energy. The cut was usually placed such that jets with greater than 95% of their transverse momentum coming from the calorimeter towers are rejected. This kind of cut is not useful when studying jets in the EEMC, because the falling TPC efficiency means that jets in this region will have few tracks and therefore large neutral fractions. It is unlikely that a background jet will be coincident with a physics jet, so the requirement can be loosened and we only reject the dijet candidates where both jets are purely neutral, instead of putting a neutral energy cut on the jets.

Detector-level dijets were reconstructed from the simulated TPC and calorimeter responses using the same algorithms as the data (see chapter 4). We also reconstruct the jets at particle and parton level using the anti-k_T algorithm. Particle-level dijets were formed from stable, final-state particles produced in the simulated event. All stable particles are used, including those which arise from the underlying event and beam remnants. The parton-level dijets were reconstructed from the hard-scattered partons emitted in the collision, including initial and final-state radiation, but not beam remnants or underlying event effects. Because there is no detector information, the neutral fraction cut and the p_T balance cut are not used when selecting dijets at the particle and parton levels from the full unbiased Pythia sample.

In order to compare with the theory calculation, in this analysis, jets with $-0.8 < \eta < 0.8$ are considered **Barrel Jets**, while those with $0.8 < \eta < 1.8$ are **Endcap Jets**. There is no detector pseudorapidity requirement here, so it is possible that Barrel jets would have a detector pseudorapidity larger than 0.8 (Endcap region), and Endcap jets might also have a detector pseudorapidity smaller than 0.8 (Barrel region).

3.3 Di-Jet Kinematics

The leading-order kinematics of the two scattered partons can be approximated by the relativistic two-body scatterings 1 + 2 → 3 + 4. This leads to the kinematic relations shown in equation 3.3, assuming massless partons:

$$x_1 = \frac{p_{T,3}}{\sqrt{s}}(e^{\eta_3} + e^{\eta_4}) \tag{3.3a}$$

$$x_2 = \frac{p_{T,4}}{\sqrt{s}}(e^{-\eta_3} + e^{-\eta_4}) \tag{3.3b}$$

$$M = \sqrt{x_1 x_2 s} \tag{3.3c}$$

$$y = \frac{1}{2}\ln\left(\frac{x_1}{x_2}\right) = \frac{\eta_3 + \eta_4}{2} \tag{3.3d}$$

$$|\cos\theta| = \tanh\left(\frac{\eta_3 - \eta_4}{2}\right), \tag{3.3e}$$

where x_1 and x_2 are the momentum fractions of the colliding partons, M is the invariant mass of this interaction, y is the rapidity, and θ is the center-of-mass scattering angle. $p_{T,3}$ and $p_{T,4}$ are the outgoing partonic transverse momenta, and η_3 and η_4 are their pseudorapidities, respectively. A detailed derivation is provided in appendix B.

The (squared) true dijet invariant mass is found by taking the square of the sum of the 4-momenta of the two jets which make up the dijet:

$$M^2 = (P_3 + P_4)^2 \tag{3.4}$$

$$M = \sqrt{m_3^2 + m_4^2 + 2\sqrt{m_3^2 + p_{T3}^2}\sqrt{m_4^2 + p_{T4}^2}cosh(\Delta y) - 2p_{T3}p_{T4}cos(\Delta\phi)}. \tag{3.5}$$

The dijet kinematics show the advantage of using correlation measurements in accessing the x dependence of Δg, compared to inclusive jet measurements, which integrate over a large range in x of the initial state partons for a given transverse momentum of the final state. For example, in leading order QCD, the dijet invariant mass is proportional to the square-root of the initial state momentum fractions, $M = \sqrt{s}\sqrt{x_1 x_2}$, while the sum of the jet pseudorapidities determines their ratio $\eta_1 + \eta_2 = \ln(x_1/x_2)$. The initial partons' information is therefore embedded in the dijet observables, which would allow us to characterize the initial state more completely.

3.4 Trigger Selection

A dijet event is categorized based on the triggers satisfied by the individual jets. An individual jet can fall into one of three categories: L2JetHigh, JP1Lo, and JP1Hi. If a jet does not fall into one of these categories, it is considered untriggered. The conditions a jet must satisfy to be placed in one of these categories are listed below:

- L2JetHigh: The jet must be geometrically matched to a jet patch which fired the L0 L2JetHigh trigger with $p_T \geq 8.4$ GeV.
- JP1Lo: The jet must be geometrically matched to a jet patch which fired the L0 JP1 trigger with $p_T \leq 8.4$ GeV.

- JP1Hi: The jet must be geometrically matched to a jet patch which fired the L0 JP1 trigger with $p_T \geq 8.4$ GeV, and the L0 L2JetHigh trigger did not fire.

The jet patch geometrical matching requires that the thrust axis of a jet must be within 0.6 in $\eta - \phi$-two dimensional space of the center of the jet patch (or the E_T-weighted centroid of two adjacent jet patches for the AJP component of L2JetHigh). The p_T conditions on the jets are used to make sure no jet can be placed into more than one category.

There are eight combinations of trigger categories for dijets: L2JetHigh-L2JetHigh, L2JetHigh-JP1Lo, L2JetHigh-Untriggered, JP1Lo-JP1Lo, JP1Lo-JP1Hi, JP1Lo-Untriggered, JP1Hi-JP1Hi, and JP1Hi-Untriggered. In the following chapters, **L2 dijet** events refer to the first three trigger samples, while **JP dijet** events are the remaining five combinations.

CHAPTER 4

Simulation Studies

4.1 Simulation / Embedding Details

To correct for detector effects on the measured jet quantities and study the systematic errors due to the hadronization and the detector response, simulated events generated from PYTHIA 6.425 [47] with the Perugia 0 tune [73] were chosen to run through a STAR detector response package (GSTAR) implemented in GEANT 3 [74]. The simulated events were embedded into 'zero-bias' data, which are real STAR events that were triggered on random bunch crossings over the span of the run, thus allowing the simulation sample to track accurately the same beam background, pile-up, and detector conditions as the real data set.

This simulation sample, originally produced for the 2009 pp200 inclusive jet analysis, has about 21 million events generated in ten separate partonic p_T bins. The simulation is also broken into individual runs, and then embedded into the corresponding 'zero-bias' data files. A trigger filter was used to reduce the time needed to run the simulation, by rejecting events that would not fire the JP1, AJP or BHT3 (Barrel high tower trigger) before the detector response is simulated. This filter rejected about 91% of the Pythia events. The full Pythia record for the rejected events is saved so that corrections to the unbiased sample can be made.

For the Endcap Electromagnetic Calorimeter (EEMC), we needed to incorporate the new gain calibration results into the simulation. An afterburner method was used, to save the substantial time needed for the simulation production. More details on this method can be found in appendix C.

4.2 Levels of Jet Information

The simulation includes three distinct levels of information, corresponding to the partonic hard scattering, the final state particles from fragmentation and hadronization of the partons, and the response of the detector to those particles. These divisions will be referred to as the parton level, particle level, and detector level, respectively.

Parton Level. The parton level contains information about the hard scattered partons involved in the $2 \rightarrow 2$ hard scattering event generated by Pythia. In this level, various kinematic properties of the hard scattering, such as the center of mass energy, scattering angle, and momentum fractions of the incoming partons, are stored. When we reconstruct the jets on the parton level from the simulation, only the partons involved in the hard scattering, and partons arising from initial or final state radiation, are used in the jet finder. Partons arising from the underlying event or beam remnants are not included in the parton-level jet reconstruction.

Particle Level. The partons generated by Pythia propagate and hadronize into the stable and color-neutral particles recorded at this level. The particle level of the simulation records the kinematic information, particle id, and index of the parent parton for all of these stable particles. When we reconstruct the jets at the particle level, all stable particles are used, including those which arise from the underlying event and beam remnants.

Detector Level. The last level of the the simulation records the detector response to the stable particles from the previous level. As the particles traverse the GEANT model of the detector, they interact with the various volumes in ways consistent with how that particular particle would behave in a specific material. This interaction includes ionizing the gas in the TPC, and depositing energy in the scintillator layers of the calorimeters. This, along with a simulation of the detector readout electronics, allows the simulation to respond to particles the same way as the real detector. When the jet finder is running on the detector level simulation, it constructs jets from the simulated response of the TPC and calorimeter towers, and their readout electronics.

4.3 Data - Simulation Comparison

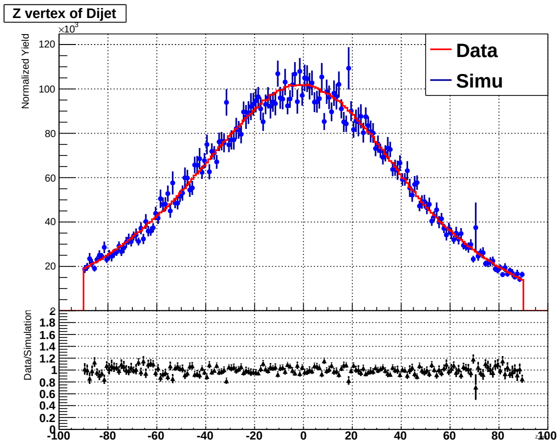

Figure 4.1: Z vertex distribution for L2All.

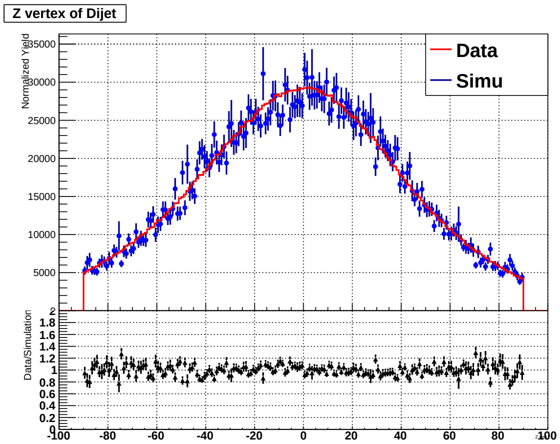

Figure 4.2: Z vertex distribution for JPAll.

The simulated events are generated with some distribution of z-vertex positions, which may not exactly match the z-vertex distribution of the data. In order to achieve the best matching between the data and simulation, the z-vertex distribution of the simulation should be altered to match that of the data. This is done by re-weighting the simulation events. The re-weighting is done by taking the ratio of the z-vertex distribution observed in the data to that of the simulation. This ratio is then fit with a 4th-order polynomial. Each simulation event is thus associated with a re-weighting factor from the 4th-order polynomial functions. Figs. 4.1 and 4.2 show the z-vertex distributions from data and simulation after the z-vertex re-weighting has been applied for two trigger combinations.

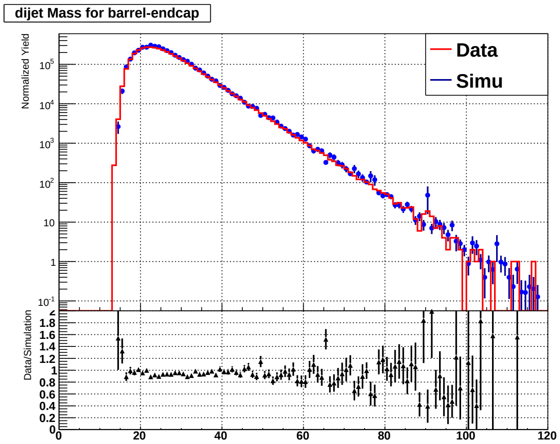

Figure 4.3: Di-jet invariant mass L2All.

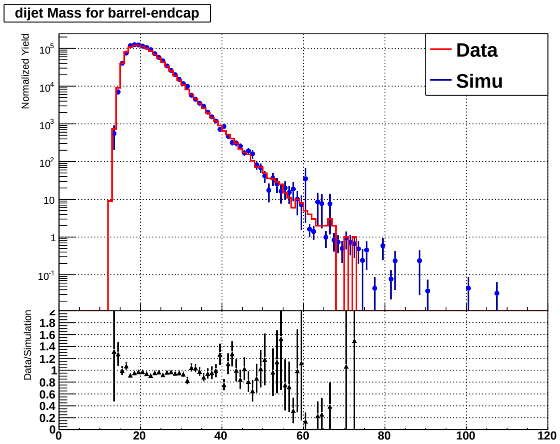

Figure 4.4: Di-jet invariant mass JPAll.

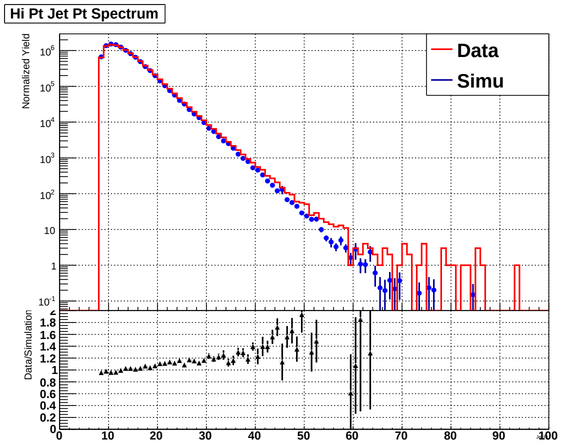

Figure 4.5: Hi p_T jet p_T L2All.

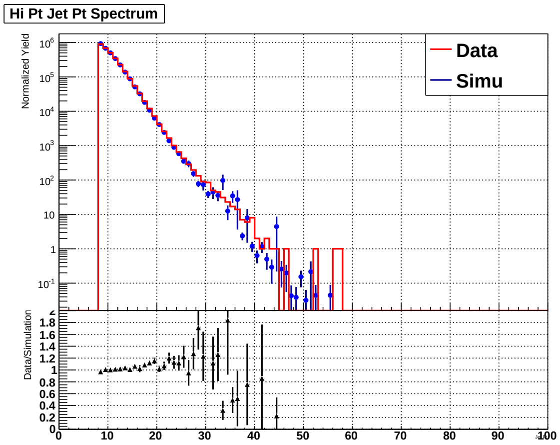

Figure 4.6: Hi p_T jet p_T JPAll.

Detector-level dijets were reconstructed from the simulated TPC and calorimeter responses using the same jet-finding algorithms as the data. Comparison of the dijets reconstructed from data and simulation confirms that the STAR detector response is well understood. The dijet invariant mass distribution is shown in Figs. 4.3 and 4.4 for L2 and JP triggers, respectively, and in Figs. 4.5 and 4.6 the (higher) jet p_T spectra are presented. Figs. 4.7, 4.8, 4.9 and 4.10 show good geometric matching, which means that the detector conditions are simulated very well, as the ϕ spectrum is particularly sensitive to the TPC hardware and its failures. Figs. 4.11 and 4.12 show the jet neutral energy fraction comparisons, also in good agreement, even into the endcap region where the tracking becomes inefficient. In Fig. 4.13 we show the integrated transverse energy profiles within the BEMC and EEMC jets. The shapes of the data distributions are reproduced sufficiently well. Taken together, this means that the detector response and event triggering are well simulated at STAR.

4.3.1 Jet Association

Dijets were also reconstructed in simulation at the particle and parton levels. After we find the detector level dijet, the particle and parton level dijet were associated via the geometric matching condition that $\Delta R = \sqrt{(\eta_{Det} - \eta_{Par})^2 + (\phi_{Det} - \phi_{Par})^2} < 0.5$ for each of the two jets.

A matching condition that requires the particle/parton level z-vertex and detector level z-vertex to be within two centimeters of each other is also imposed to improve the matching. The vertex associated with the particle/parton level is the one which is set when Pythia is run, whereas at the detector level, the vertex is found by emulating the vertex finder which is run on the actual data. The latter may be affected by the ‘zero-bias’ event, resulting in a different vertex position.

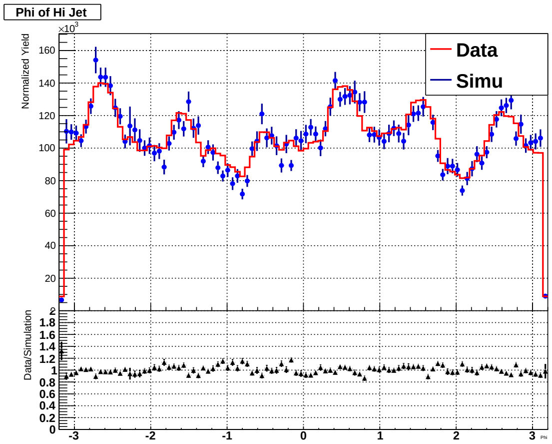

Figure 4.7: Hi p_T jet ϕ L2All.

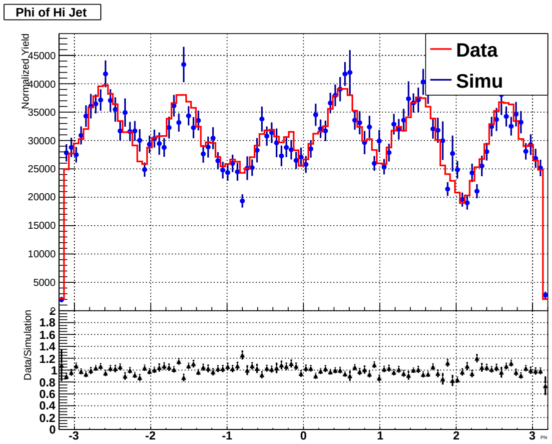

Figure 4.8: Hi p_T jet ϕ JPAll.

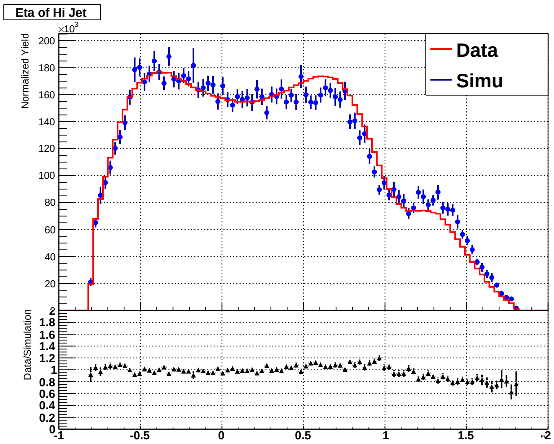

Figure 4.9: Hi p_T jet η L2All.

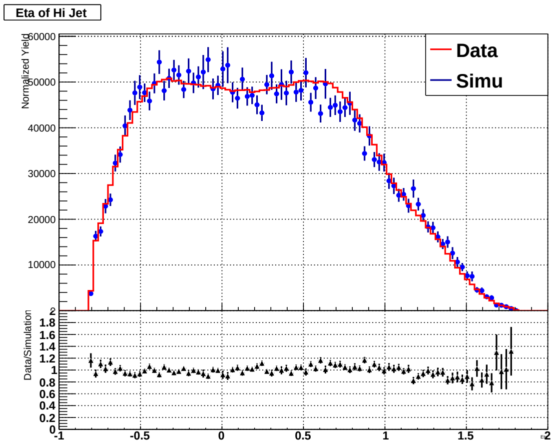

Figure 4.10: Hi p_T jet η JPAll.

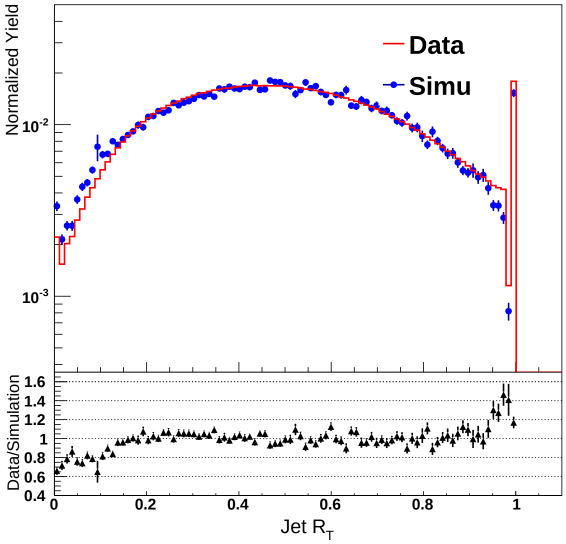

Figure 4.11: Barrel jet R_T L2All.

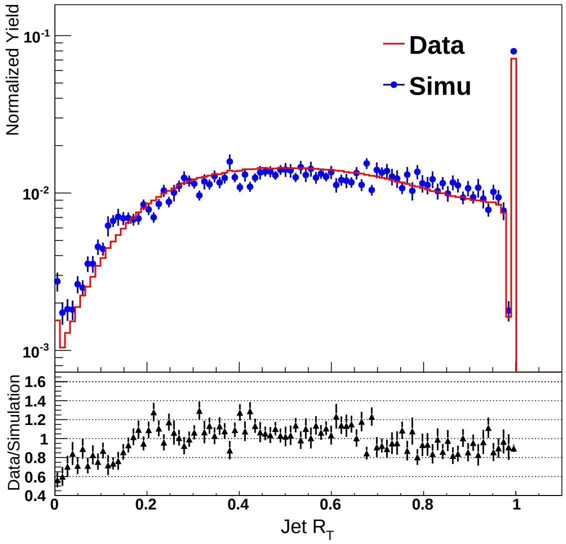

Figure 4.12: Endcap jet R_T L2All.

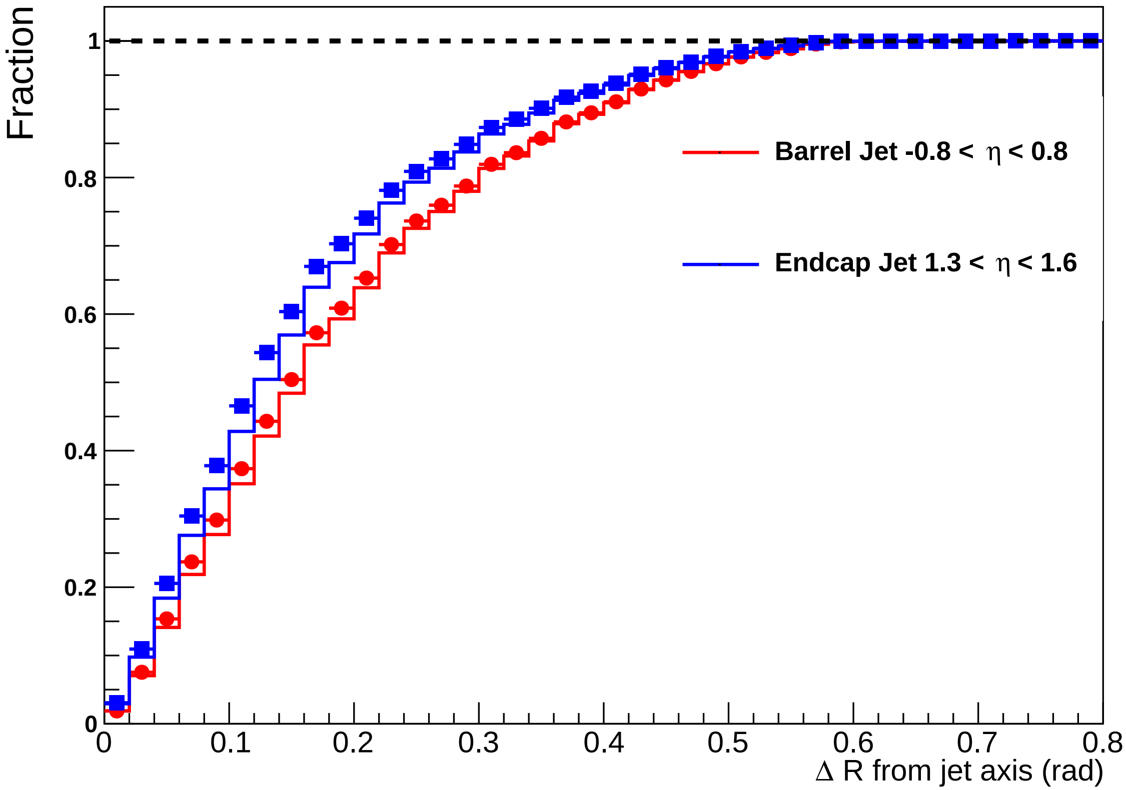

Tue Jun 20 11:36:06 2017

Figure 4.13: Fraction of the total jet transverse energy found within a cone of radius ΔR centered on the reconstructed thrust axis, illustrating the jet profile.

4.4 'Fudge Factor' Reweighting of the p_T Bins

4.4.1 Weight and Fudge Factor Issues

In order to obtain sufficient statistics at high jet p_T, where the jet cross section falls off exponentially, the simulation was subdivided into 10 bins of partonic $\hat{p}_T$: 2 to 3, 3 to 4, 4 to 5, 5 to 7, 7 to 9, 9 to 11, 11 to 15, 15 to 25, 25 to 35, and 35 to infinity, all in GeV/c. To make a smooth spectrum, the events from each partonic $\hat{p}_T$ bin needs to be weighted by a factor of (σ/N_{events}), where σ is the cross section for that partonic $\hat{p}_T$ bin, while N_{events} is the number of generated events from that bin. The weighted distribution is shown in Fig. 4.14.

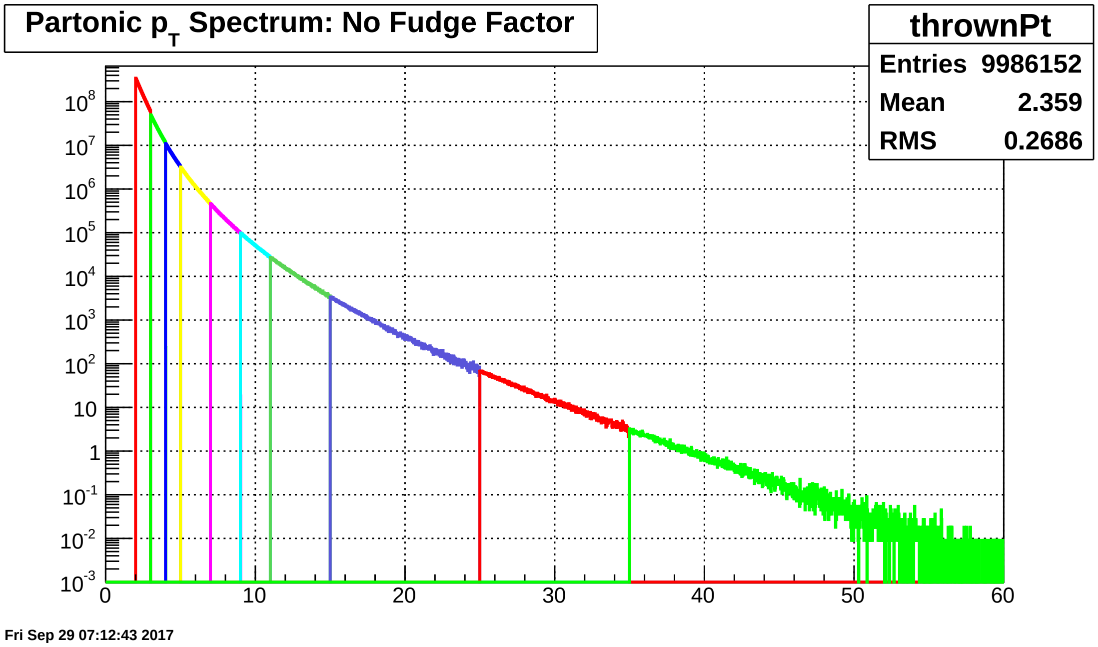

Figure 4.14: Pythia partonic p_T distribution: without fudge factors.

As can be seen in the figure, it was noticed that 'fudge factors' were needed to match the distributions between different bins, especially in the low p_T range where Pythia may get the relative cross section wrong. Fudge factors are necessary in order to compensate for the wrong normalization of Pythia yields, due to its incomplete ability to treat the multiple interactions (MI) contribution to QCD processes. A detailed description can be found in the Pythia manual [47], page 348.

The fudge factors were determined by fitting $e^{A+Bx+Cx^2}$ to each partonic $\hat{p}_T$ bin, and then taking the ratio of those functions at the bin edges. In Figs. 4.15 and 4.16 we show the four lowest p_T bins before and after the fudge factors are applied. It is obvious that this correction makes the distributions between different bins look better. The final values used are listed in Table 4.1

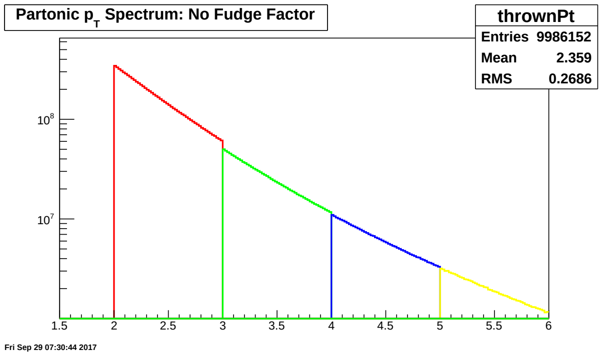

Figure 4.15: Pythia partonic p_T distribution: without fudge factors.

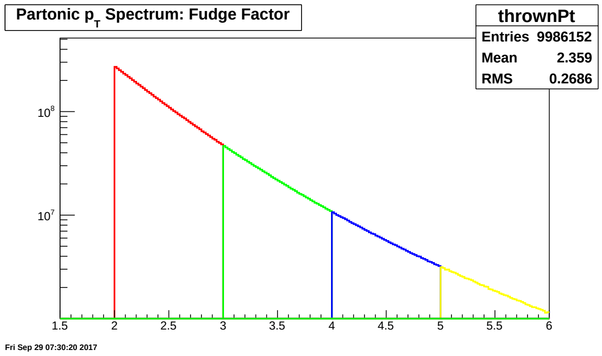

Figure 4.16: Pythia partonic p_T distribution: with fudge factors.

Partonic $\hat{p}_T$	Final Weight	Raw Weight	PYTHIA Events	$\sigma(mb)$	Fudge factor
2-3	70777.2	90056.2	9.98615e+06	8.10515	0.785922
3-4	24328.6	26098.3	5.50909e+06	1.29581	0.932191
4-5	9912.36	10207.8	3.41895e+06	0.314538	0.97106
5-7	9416.2	9529.65	1.58767e+06	0.136360	0.988095
7-9	2027.59	2027.59	1.25672e+06	0.0229651	1.0
9-11	739.407	739.407	827150	0.00551210	1.0
11-15	590.057	590.057	419029	0.00222837	1.0
15-25	145.624	145.624	297222	0.000390089	1.0
25-35	5.67755	5.67755	199332	0.0000101997	1.0
35-∞	1.0	1.00000	59541	0.000000536618	1.0

Table 4.1: Pythia jet embedding weight factors.

4.4.2 Fudge Factor Reweighting

In Pythia, the default for hadron-hadron collisions is to include QCD jet production by $2 \to 2$ processes. During this process a lower cut-off has to be introduced, as the differential cross section is divergent for $\hat{p}_\perp \to 0$. However, if we choose the Pythia simulation to run only for $\hat{p}_\perp > 1.25$ GeV, we disable the interpolation of low p_T cross section behavior. More details on this issue are available in the Pythia manual, section 8.9.3.

If we generate the Pythia simulation events in one bin ($\hat{p}_\perp = 0$ to ∞), instead of the 10 separated bins, the behavior looks quite different at low partonic values, as can be seen in Fig. 4.17.

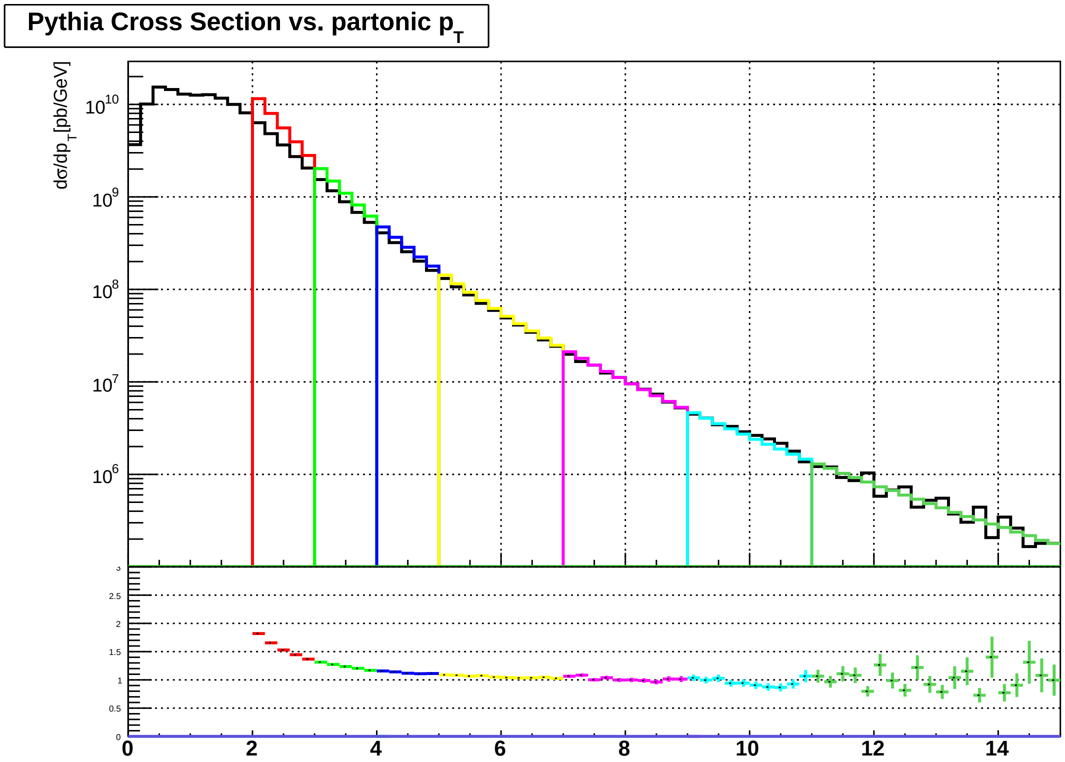

Figure 4.17: Pythia partonic p_T distributions: the black line is generated using the bin range from 0 to ∞; the other colors are from separate bins.

To compensate for this effect, a fudge factor reweighting was calculated by estimating the ratio of the cross section from the integrated bins (0 to ∞) to separated bins, as a function of the partonic $\hat{p}_T$ values. We then fit this curve with the function $w = \frac{1}{1+(p_0+p_1(x-2)+p_2(x-2)^2)e^{p_3(x-2)}}$, as shown in Fig. 4.18.

In Fig. 4.19 and 4.20 we show the jet p_T and dijet invariant mass spectra, respectively, after we applied the fudge factor reweighting (value extracted from the fitting function w). There is only about a 2% yield change to the simulation, so the overall effect is very small and was neglected.

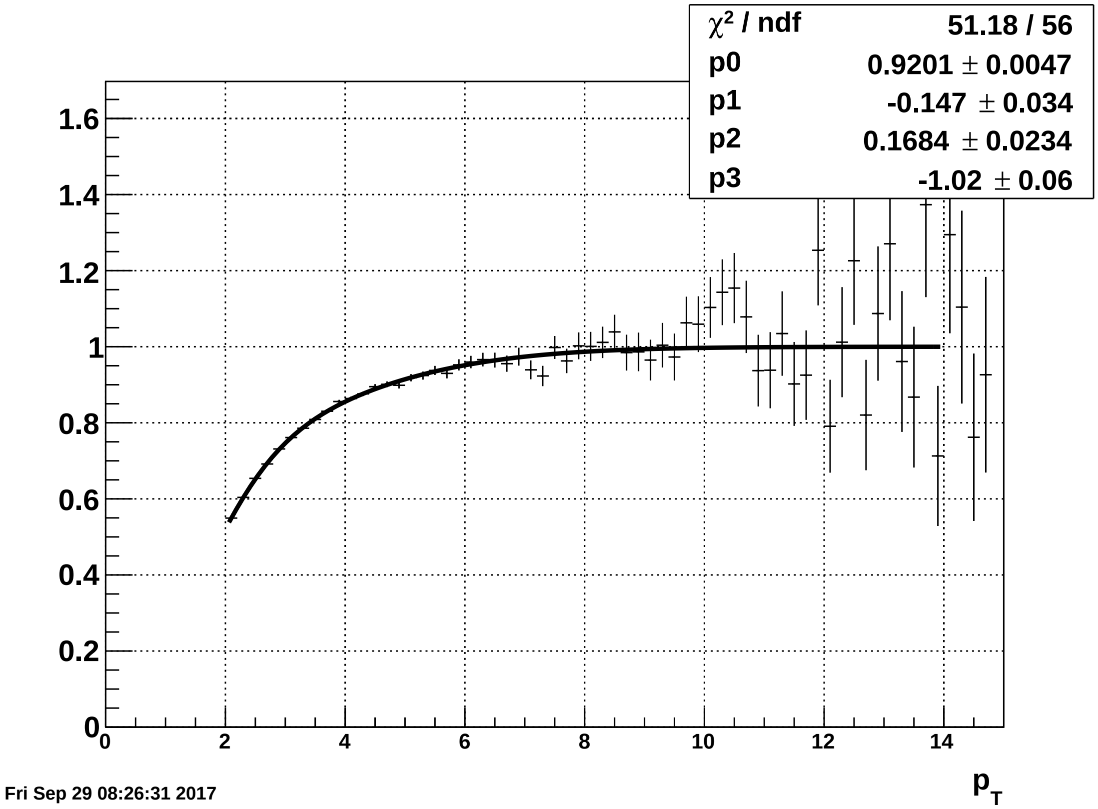

Figure 4.18: Pythia partonic p_T cross section ratio: integrated bins over the separate bins.

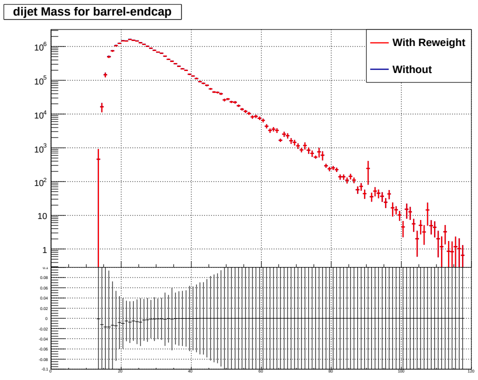

Figure 4.19: Simulation: dijet invariant mass distribution with and without reweighting.

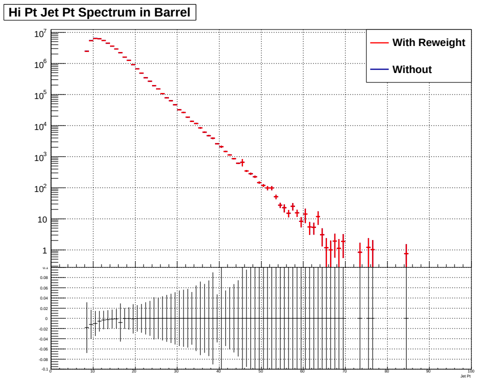

Figure 4.20: Simulation: jet p_T distribution with and without reweighting.

CHAPTER 5

Underlying Events

The hard parton-parton interactions in proton-proton collisions are often accompanied by other processes which collectively contribute additional particles to those from the hard scattering. In hadron-hadron scatterings, the underlying event (UE) is defined, in the presence of a hard parton-parton scattering with large transverse momentum transfer, as any hadronic activity beyond what can be attributed to the hadronization of partons involved in the hard scattering, and to related initial and final state QCD radiation. It is the sum of all the processes that build up the final hadronic state in a collision, excluding the hardest leading-order partonic interaction. The UE activity is thus attributed to the hadronization of partonic constituents that have undergone multiple parton interactions (MPI), as well as to beam-beam remnants, concentrated along the beam direction. We note that UE contributions are distinct from "pile-up" processes, including other p-p collisions that just happen to be close in time to the scattering of interest.

Events with hard jets are often accompanied by a more diffuse 'background' of relatively soft particles. In proton-proton collisions, the hardest parton scattering process is what we are interested in; but the other soft scatterings could be mixed into the hardest scattering and contribute to the signals that are finally measured. The background generated due to these multiple soft scatterings is classified as underlying events contributions. This background is different from detector pileup, because these collisions are coming from the same proton-proton collision as the hardest scattering.

5.1 Off-Axis Cone Method

For many physics applications, it is useful to estimate the characteristics of the background on an event-by-event basis, and then correct the hard jets for the soft contamination. The off-axis cone method is a method to study underlying events on the level of jet-by-jet, instead of on the level of an event. This method was developed by Zilong Chang for the STAR 2012 at 500 GeV inclusive jet analysis, which was adapted from the perpendicular cones method used in the ALICE experiment [75].

In this method, we draw two off-axis cones for each reconstructed jet, each of which is centered at the same η as the jet, but 90° away in ϕ from the jet ϕ, as shown in Fig. 5.1. We then collect particles falling inside the two cones. The particle candidate pool is the exact same input as is used for the jet finding algorithm. The off-axis cone radius was chosen to be the same as the jet parameter of the anti-k_T algorithm used in this analysis, R = 0.6. The p_T of the off-axis cone is defined as the scalar sum of all the particles inside the cone, denoted as $p_{T,ue}$ and the mass of the off-axis cone is the invariant mass of the vector sum of all the particles inside the cone. The energy density, $\rho_{ue,cone}$, is defined as the off-axis cone p_T divided by the cone area (πR^2) and the mass density, $\rho_{m,ue,cone}$, is the off-axis cone mass divided by the cone area. The multiplicity of the off-axis cone is the number of particles inside the cone. Finally the average density of the two cones is taken as the estimate to the underlying event density, $\rho_{ue} = \frac{1}{2}(\rho_{ue,1} + \rho_{ue,2})$.

Given that the physics of the underlying event is expected to be evenly distributed over $\eta - \phi$ space, the calculated underlying event energy density should be approximately uniform in $\eta - \phi$ space. However, detector acceptances and efficiencies are usually not uniform in $\eta - \phi$ space. For example, at STAR there is a gap between the BEMC and EEMC, and the TPC tracking efficiency degrades drastically over $1.0 < |\eta| < 1.5$. Fortunately the STAR detector has good symmetry in ϕ, and the two off-axis cones are centered at the same η as the jet, therefore it should be very applicable here.

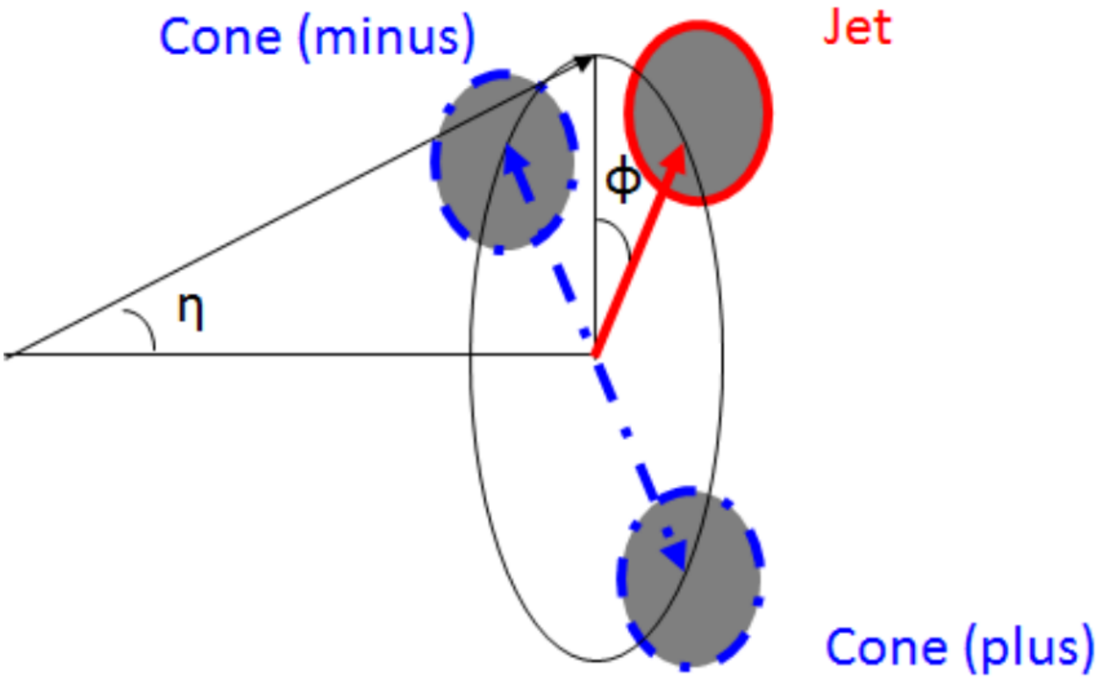

Figure 5.1: Geometry of the off-axis cone method.

5.2 Underlying Event Correction

Dijet measurements are sensitive to the jet's direction, and more generally to the jet's full 4-momentum (for example, for large jet radii, the contamination from the background can build up a significant invariant mass). For each jet in a dijet event, the underlying event 4-vector correction is calculated according to:

$$P_{\mu}^{corrected} = P_{\mu} - [\rho A_{jet}^{x}, \rho A_{jet}^{y}, (\rho + \rho_m) A_{jet}^{z}, (\rho + \rho_m) A_{jet}^{E}], \tag{5.1}$$

where P_{μ} is the jet's uncorrected 4-vector, ρ is the underlying event transverse momentum density and ρ_m is the underlying event mass density as determined using the Off-Axis cone method, and A_{μ} is the 4-vector area calculated in the fast-jet package [67] using the ghost particle technique [76].

The inclusive jet's main observable is the jet transverse momentum p_T. The correction method used is $p_T^{corrected} = p_T - \rho \times A_{jet}$, where A_{jet} is the jet scalar area. Fig. 5.2 shows the comparison of the jet p_T spectrum after the underlying event subtraction, using the two subtraction methods presented before. They are almost identical, as expected.

When performing this jet 4-vector momentum subtraction, two other requirements were imposed here to avoid over-corrections due to local fluctuations in the underlying event density:

1. If the jet area $\times \rho_{ue} >$ jet p_T, the corrected jet's 4-vector is set to be a vector with zero transverse momentum, zero mass, and the pseudorapidity and azimuth of the original unsubtracted jet.
2. If the squared jet mass is negative (imaginary jet mass), we replace the corrected jet 4-momentum with the same transverse components, zero mass, and the pseudorapidity of the original unsubtracted jet.

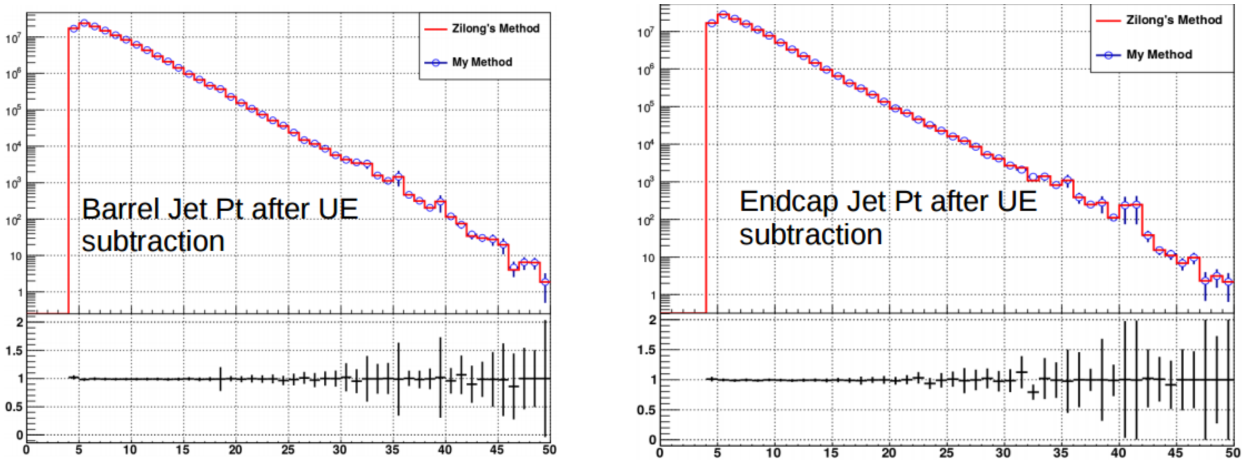

Figure 5.2: Jet P_T comparision after underlying event subtraction.

In Figs. 5.3, 5.4, and 5.5 we show the jet p_T, mass, and dijet invariant mass before and after making the underlying event subtraction. Overall, the spectra are shifted slightly toward lower values, as expected. We also note that the underlying event affects the jet invariant mass more significantly than either the transverse momentum or the dijet mass.

In the analysis that follows, the detector level and particle level jets used are those after the underlying event correction. More details about the 4-vector subtraction can be found in the fast-jet group's publications [67].

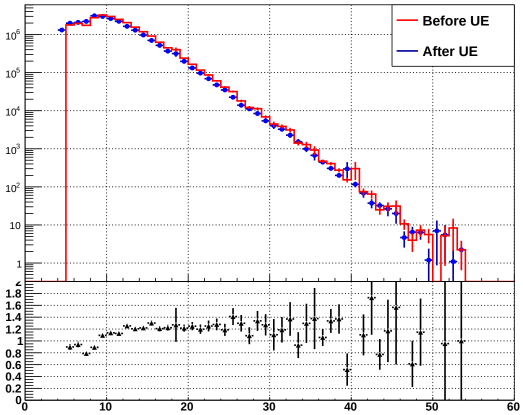

Figure 5.3: Jet p_T before and after underlying event subtraction.

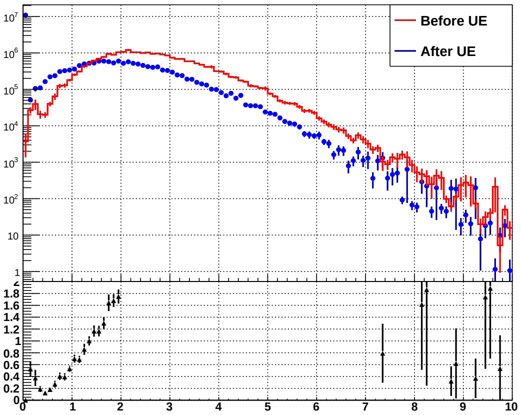

Figure 5.4: Jet mass before and after underlying event subtraction.

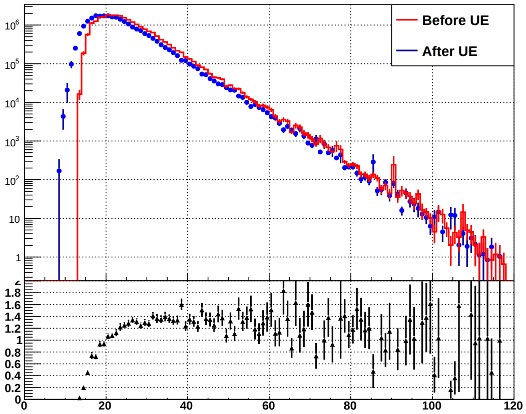

Figure 5.5: Di-jet mass before and after underlying event subtraction.

CHAPTER 6

Experimental Methods in the EEMC

6.1 Challenges in the Forward (EEMC) Region

As noted before, the STAR TPC only covers the nominal range $|\eta| \leq 1.3$; the tracking efficiency decreases rapidly in more forward regions, where the Endcap Electromagnetic Calorimeter (EEMC) is located. Lower tracking efficiency means the reconstructed jets will have lower p_T on average, as will be shown later. This inaccurate p_T reconstruction skews the extraction of the initial state parton momenta. Jets with a high percentage of neutral energy are preferentially selected, both in triggering and reconstruction, leading to a biased sample.

The jet invariant mass is also skewed during the jet reconstruction. In the jet-finder algorithm (chapter 3), tracks are assigned the mass of charged pions, while for the electromagnetic calorimeter towers the particles are assumed to be massless, which makes the detector-level jet invariant mass deviate from its true value. The limited tracking capabilities in forward region also makes the particle identification not possible for these di-jet measurements. The reconstructed jet parameters need to be corrected in order to have the right energy, direction, and neutral fraction. This is of crucial importance in these dijet measurements.

6.2 Machine Learning Approaches

A machine-learning regression method was used to make the corrections for the jet measurements. Machine learning methods have been a hot topic in recent years, and there are plenty of essential problems in High Energy Physics that can be solved using Machine Learning methods.

These vary from online data filtering and reconstruction to offline data analysis. Such supervised machine-learning regression algorithms make use of training events, for which the desired output is known, to determine an approximation of the underlying functional behavior defining the target value. This method is extremely helpful in making the corrections in this work.

Multilayer Perceptron (MLP from TMVA [77]) is the main algorithm applied in this analysis, with the parameters tuned properly. However, slightly changing the parameters, such as the number of layers and nodes, in the Multilayer Perceptron may impact the learning process. Different algorithms may emphasize slightly different behaviors, which would also have some influence. The systematic errors of this method are evaluated and added in quadrature from the outputs using different training sample sizes, changing the number of layers and nodes, and from using the Linear Discriminant algorithm (LD from TMVA) and K-Nearest Neighbors (KNN from TMVA) as alternate methods.

6.2.1 Artificial Neural Networks

An Artificial Neural Network (ANN) is a simulated collection of interconnected neurons, with each neuron producing a certain response to a given set of input signals. The network is put into a defined state that can be measured from the response of one or several (output) neurons after applying an external signal to the input neurons, or one can just simply view it as the mapping from the input space to multi-dimensional output space, which can be nonlinear if the response is nonlinear. The behavior of the neural network is determined by the layout of the neurons, the weights of the connections, and the response of the neurons to the input signals.

The multilayer perceptron method reduces the complexity of the mapping connections by organising the neurons in layers, and only allowing direct connections from a given layer to the following layer, as suggested in Fig. 6.1. The first layer of a multilayer perceptron is the input layer that holds the input values (x_i), while the last is the output layer that holds the output variable (y_{ANN}, the neural net estimator). All others are hidden layers with hidden neurons (y_i^n). A weight (w_{ij}^l) is associated with each directional connection between the neutrons, and the output values of all the connected neurons are multiplied with the weights when calculating the input value to the response of the given neuron.

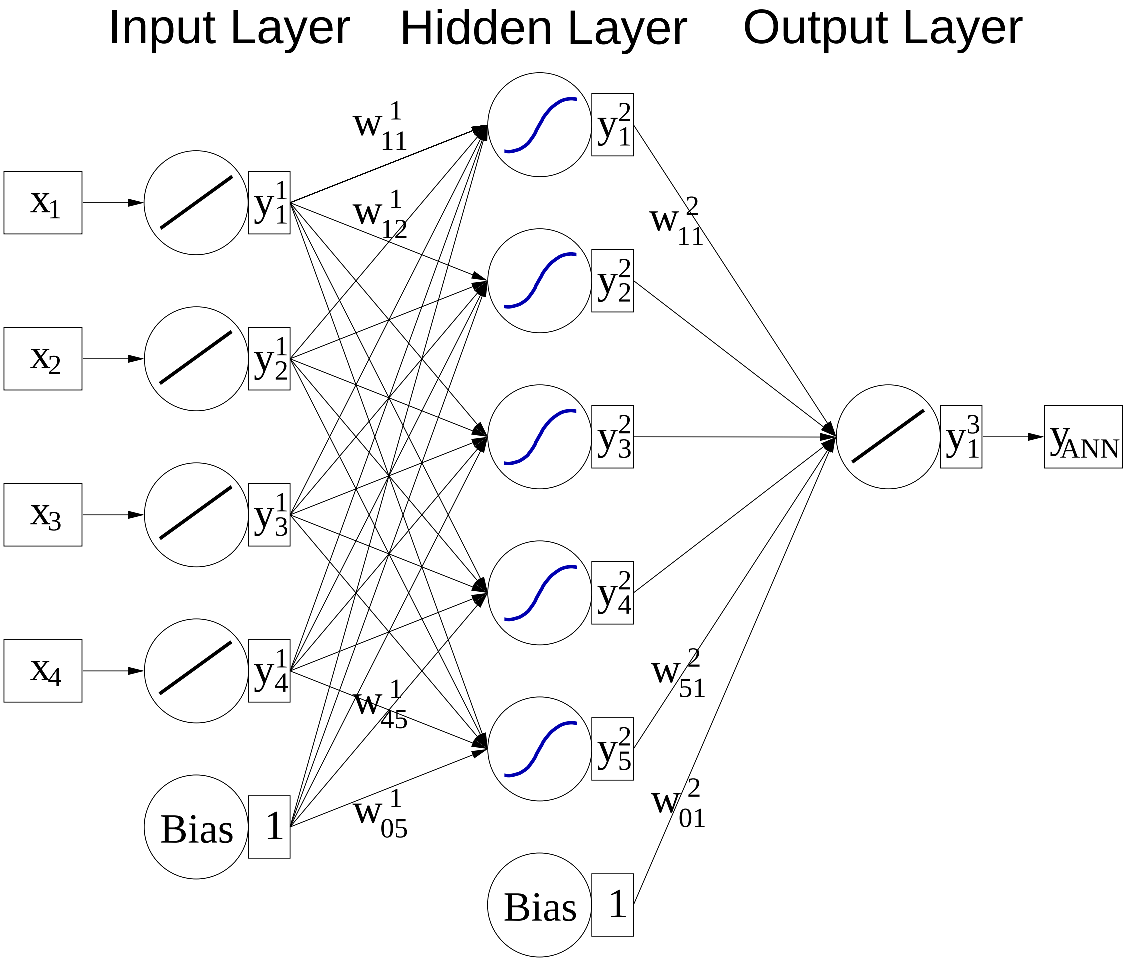

Figure 6.1: Multilayer perceptron with one hidden layer, from Ref. [77].

Response Function

The neuron response function ρ maps the input neuron onto the output neuron, and can be separated into a $R^n \mapsto R$ synapse function κ, and a $R \mapsto R$ synapse function α. The functions κ and α are allowed to have the following forms:

$$\kappa : (y_1^{(\ell)}, .., y_n^{(\ell)} | \omega_{0j}^{(\ell)}, .., \omega_{nj}^{(\ell)}) \rightarrow \begin{cases} \omega_{0j}^{(\ell)} + \sum_{i=1}^{n} y_i^{(\ell)} \omega_{ij}^{(\ell)}, & \text{Sum} \\ \omega_{0j}^{(\ell)} + \sum_{i=1}^{n} (y_i^{(\ell)} \omega_{ij}^{(\ell)})^2, & \text{Sum of squares} \\ \omega_{0j}^{(\ell)} + \sum_{i=1}^{n} |y_i^{(\ell)} \omega_{ij}^{(\ell)}|, & \text{Sum of absolutes} \end{cases} \tag{6.1}$$

$$\alpha : x \rightarrow \begin{cases} x & \text{Linear} \\ \frac{1}{1+e^{-kx}} & \text{Sigmoid} \\ \frac{e^x - e^{-x}}{e^x + e^{-x}} & \text{Tanh} \\ e^{-x^2/2} & \text{Radial} \end{cases} \tag{6.2}$$

Network Architecture

One can increase the number of neurons in the hidden layers if the computing power and the size of the training data sample suffice. However, for a multilayer perceptron, a single hidden layer is sufficient to approximate a given continuous correlation function to any precision when a sufficiently large number of neurons is used in the hidden layer. On average, in order to get a shorter training time and a more robust network, it is generally good to perform fits with a network of multiple hidden layers and fewer hidden neurons per layer.

Neural Network Training

There are several parameters that are important in order for the neural network to work well, such as the fraction of the events used for training, the total number of epochs for convergence, and the frequency of testing. For adjusting the weights that optimise the performance, the most common algorithm is back propagation (BP), which calculates the error contributions of each neuron after a batch of data is processed. The Broyden-Fletcher-Goldfarb-Shannon (BFGS) method differs from the BP method by the use of second derivatives of the error function to adapt the synapse weight. For more details on these topics, see [77] chapter 8.

6.2.2 Other Machine Learning Methods

Boosted Decision Tree (BDT)

Boosted decision trees are well known classifiers that allow a straightforward interpretation, as they can be visualized by a simple two-dimensional tree structure. As shown in Fig. 6.2, a decision tree is a binary tree structured classifier or regressor which repeatly makes left/right decisions based on one single variable at a time, until a stop criterion is fulfilled. The phase space is split this way into many regions that are eventually classified as signal or background, depending on the fraction of training events that end up in the final leaf node. In the case of regression trees, each output node represents a specific value of the target variable. The boosting of a decision tree extends the original concept to form a forest of several trees, which are derived from the same training ensemble by reweighting events. The final combined classifier or regressor is given by a weighted average of the individual decision trees.

The boosted decision tree method has the drawback that the theoretical best performance on a given problem is generally inferior to other techniques, due to the simplicity of the method where each training step (node splitting) involves only a one-dimensional cut optimisation. According to the TMVA user manual for BDT: ‘we have only very limited experience at the time with the regression, hence cannot really comment on the performance in this case’. In this di-jet analysis, we found that the performance of the BDT is not very good for this regression problem, compared to the neural network, so we decided not to use the latter method here.

Linear Discriminant (LD)

The linear discriminant (LD) analysis is a method used to find the linear combination of features that characterize the events. The ‘linear’ feature refers to the discriminant function $y(x)$ being linear in the parameters β:

$$y(x) = x^{\top}\beta + \beta_0 \tag{6.3}$$

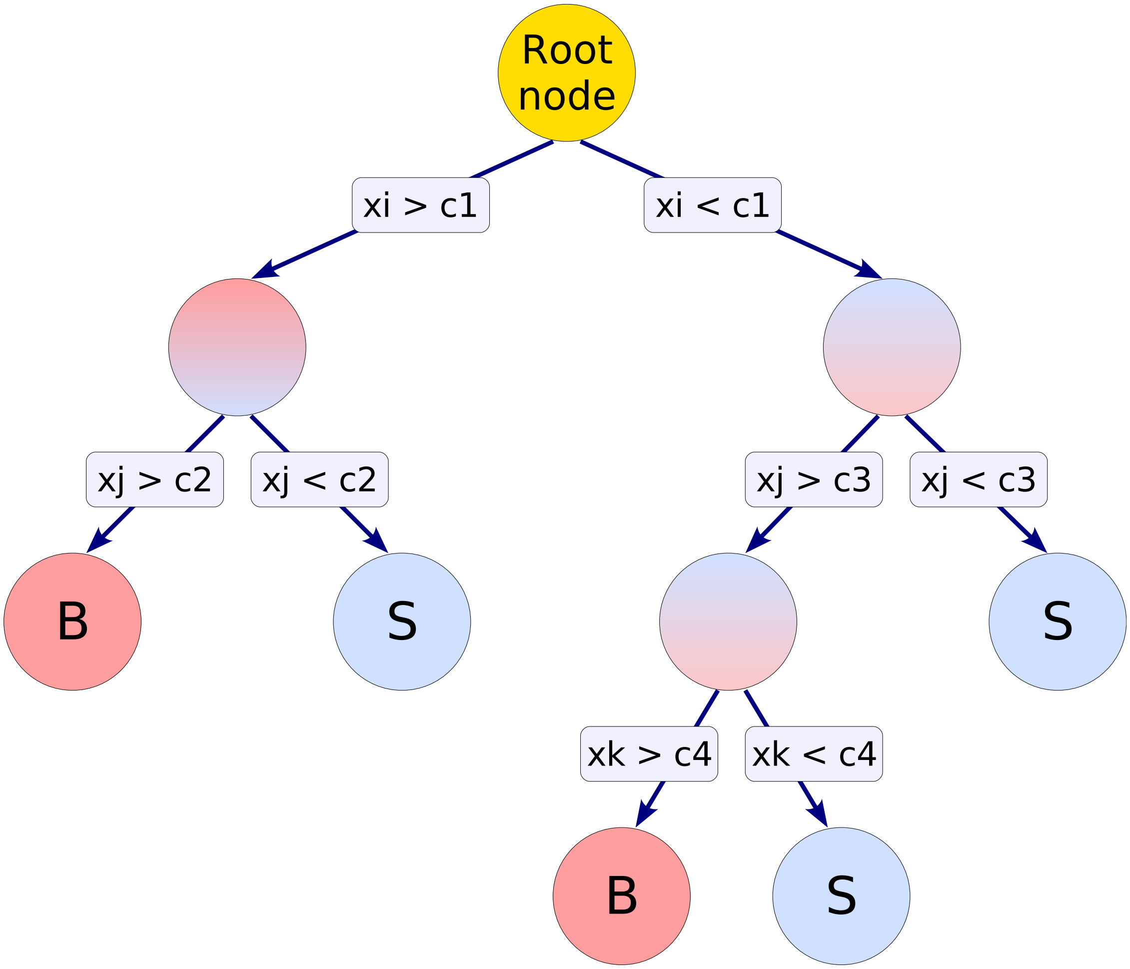

Figure 6.2: Schematic view of a decision tree from Ref. [77]. Starting from the root node, a sequence of binary splits using the discriminating variables x_i is applied and each split uses the variable that gives the best separation between signal and background at this node. The same variable may thus be used at several nodes, while others might not be used at all. The leaf nodes at the bottom end of the tree are labeled 'S' for signal and 'B' for background, depending on the majority of events that end up in the respective nodes. For regression trees, the node splitting is performed on the variable that gives the maximum decrease in the average squared error when attributing a constant value of the target variable as output of the node, given by the average of the training events in the corresponding (leaf) node.

In regression problems, the discriminant function $y(x)$ is the best estimate for the data obtained by a least-squares regression.

k-Nearest Neighbors (k-NN)

The k-nearest neighbors algorithm (k-NN) is a non-parametric method that compares an observed event to reference events from a training data set. The input consists of the k closest training examples in the feature space, which are then used by the algorithm to find the neighbours. Each training event contains a regression value and the output is the weighted average of its k nearest neighbors' regression values. We did not use this method in our analysis, except to estimate systematic uncertainties.

6.3 Jet p_T Corrections

6.3.1 Variable Selection

For the jet p_T correction, the target value used in training is the jet's true p_T (particle level). The choice of inputs is important in machine learning approaches. Jet transverse momentum p_T and detector pseudorapidity $\eta_{detector}$ are the key input variables, because they are directly related to the failing tracking efficiency in the EEMC region. In Fig. 6.3, upper left plot, is the jet particle level over the detector level p_T ratio before the correction; if we only use these two variables (detector p_T and $\eta_{detector}$) to train the network, the upper right plot is the jet particle level over the detector level after correction. We found that the output looks good after the regression method.

The jet neutral energy fraction R_t determines the relative energy of the charged and neutral particles inside the jet, and might help the regression learning process. As shown in Fig. 6.3 lower left plot, adding R_t as an additional variable improves the resolution by about $\sim 3\%$.

A di-jet is a correlation observable, and the energy of the jet in the Barrel Electromagnetic Calorimeter (BEMC) was measured much more precisely than the corresponding jet in the Endcap Electromagnetic Calorimeter (EEMC) due to the much higher efficiency of the TPC in the BEMC region. Adding the corresponding Barrel Jet p_T as another variable would also benefit the learning process for the Endcap jet for Barrel-Endcap di-jet topologies. Including this variable improves the resolution about 9%, as shown in the Fig. 6.3 lower right plot.

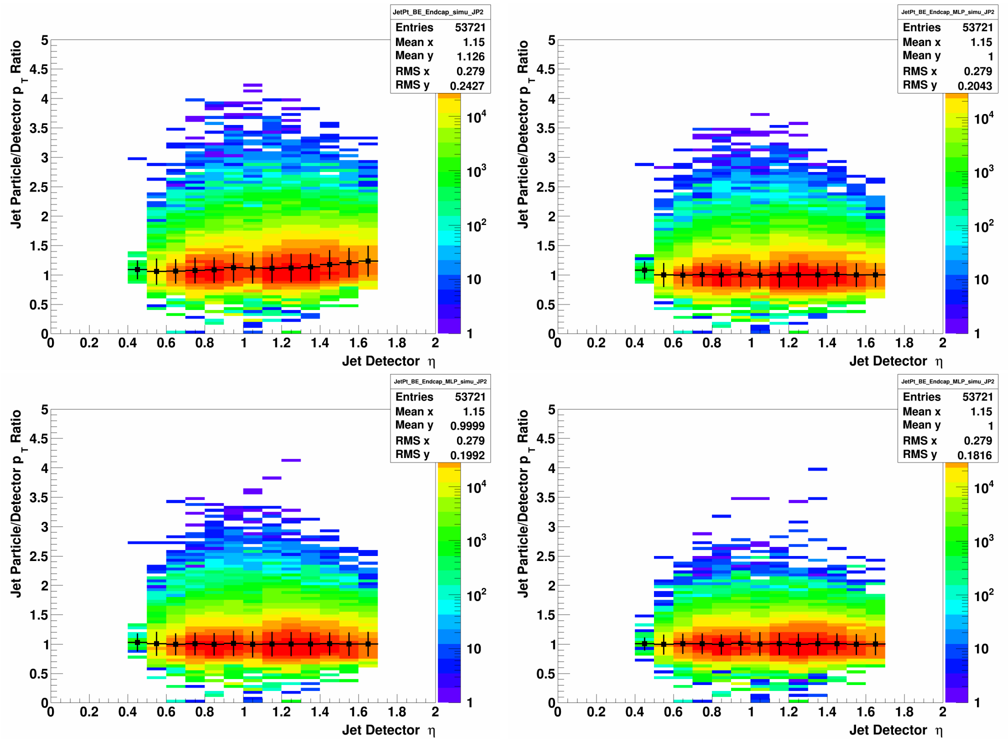

Figure 6.3: p_T shift: JP2 Endcap jet particle/detector p_T ratio vs. detector η; upper left: before shift; upper right - variable: p_T, $\eta_{detector}$; lower left: add R_t; lower right: add R_t and p_T^{Barrel}.

6.3.2 Corrections to the Jet Transverse Momentum

Jet p_T corrections are made for both the Barrel jet and Endcap jet. The Barrel jet's transverse momentum is more precisely measured than the Endcap jet, but it is still systematically lower than its true value due to the limits on detector resolution, such as the tracking efficiency limit (85% at $|\eta| \leq 1.0$) and the EMC tower size. For the Barrel Jet p_T correction, methods and variables were chosen as below:

- Methods: Multilayer Perceptron (MLP).
- Input Variables: jet detector level p_T, detector pseudorapidity $\eta_{detector}$, neutral fraction R_t.
- Target: particle level jet p_T.

As has been discussed in chapter 3, di-jet events have several different trigger combinations. As we only require at least one of the jets to be triggered, then the individual jets may fire a JP2, JP1 trigger or be untriggered (UnJP, not fire JP2 or JP1). Jets with different triggers may have slightly different characteristics, and to utilize this trigger separation, jets from the di-jet events are trained separately for each trigger. In Fig. 6.4 the ratio of Barrel jet particle level p_T over the uncorrected value for the different triggers is shown, while in Fig. 6.5 the ratio after the p_T correction is plotted. After we made the correction, the difference between the measured quantity and its true value is reduced, and the overall resolution is also improved.

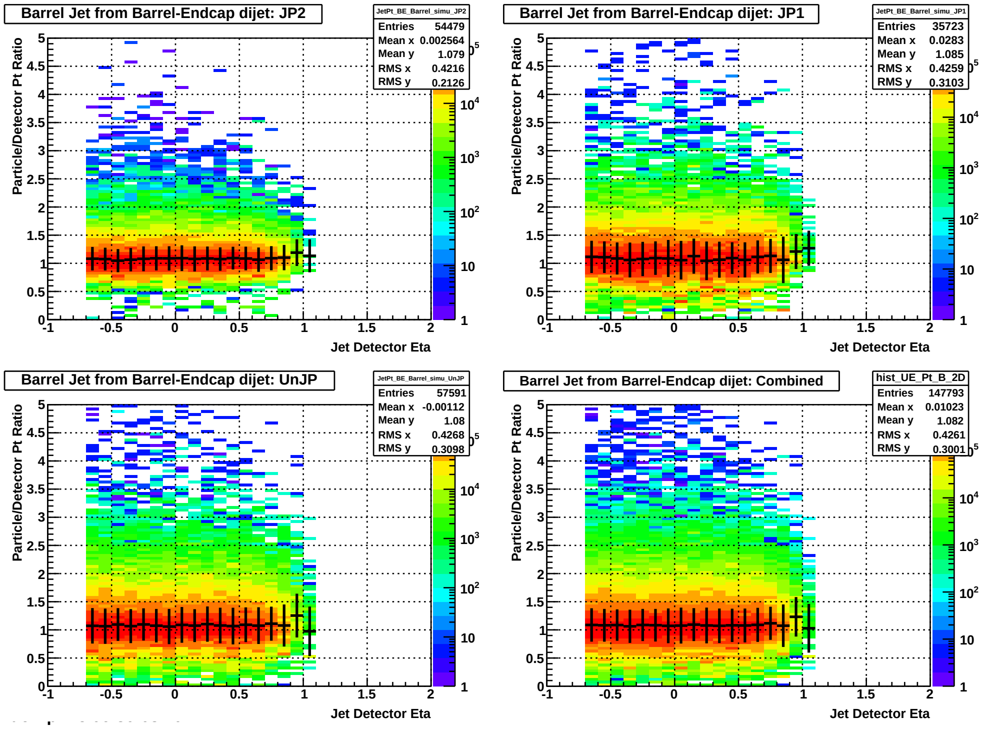
Barrel Jet from Barrel-Endcap dijet: JP2

Barrel Jet from Barrel-Endcap dijet: JP1

Barrel Jet from Barrel-Endcap dijet: UnJP

Barrel Jet from Barrel-Endcap dijet: Combined

Figure 6.4: p_T shift: Barrel jet particle/detector p_T ratio vs. detector η for different triggers.

For the Endcap Jet p_T, methods and variables were chosen as below (the Barrel jet transverse momentum p_T is used as input only for the Barrel-Endcap di-jet topology; it is not applicable for the Endcap-Endcap topology).

- Method: Multilayer Perceptron (MLP).
- Variables: Endcap jet detector level p_T, detector pseudorapidity $\eta_{detector}$, neutral fraction R_t; Barrel jet detector level p_T.
- Target: particle level jet p_T.

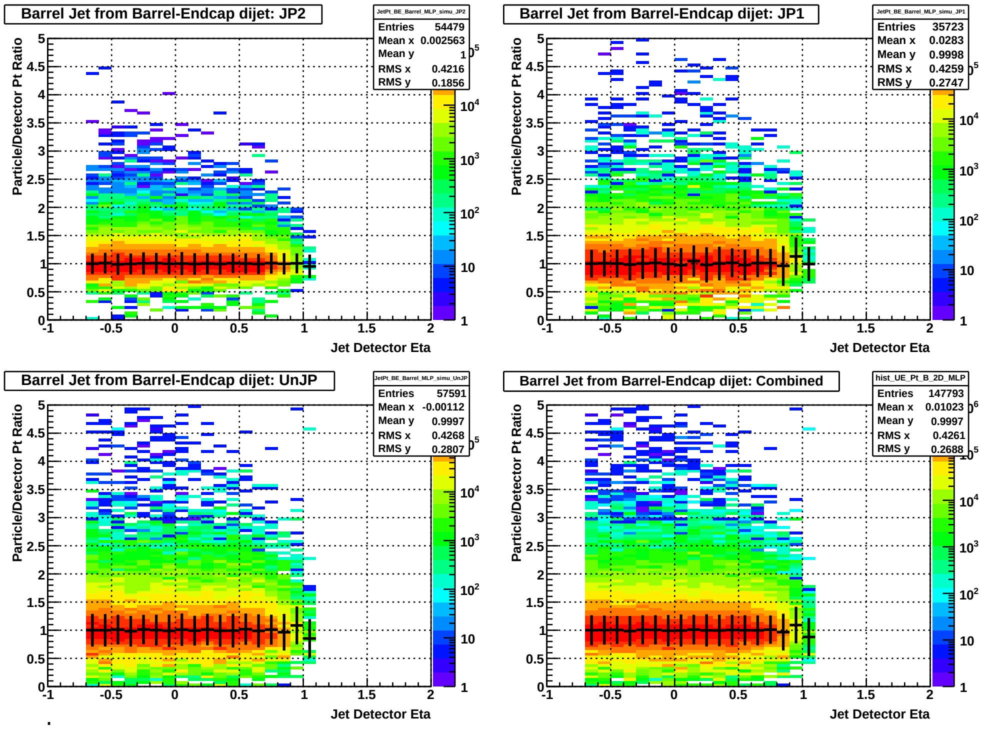

Figure 6.5: p_T shift: Barrel jet particle/output from the machine learning p_T ratio vs. detector η for different triggers.

The Endcap jet JP2, JP1 and UnJP samples are also trained and tested separately. Fig. 6.6 shows the ratio of the Endcap jet particle level p_T over the uncorrected value before the p_T correction. In these figures, the effect of the falling tracking efficiency is directly indicated by the increase of the average ratio at forward pseudorapidity. For the JP2 trigger, this effect is not as significant as for others, because the JP2 trigger has a higher energy threshold, indicates that the trigger separation in training is a good choice. Fig. 6.7 is the same ratio after the p_T correction. The detector pseudorapidity dependence of the jet p_T decrease is corrected, and the overall difference is reduced due to better p_T resolution.

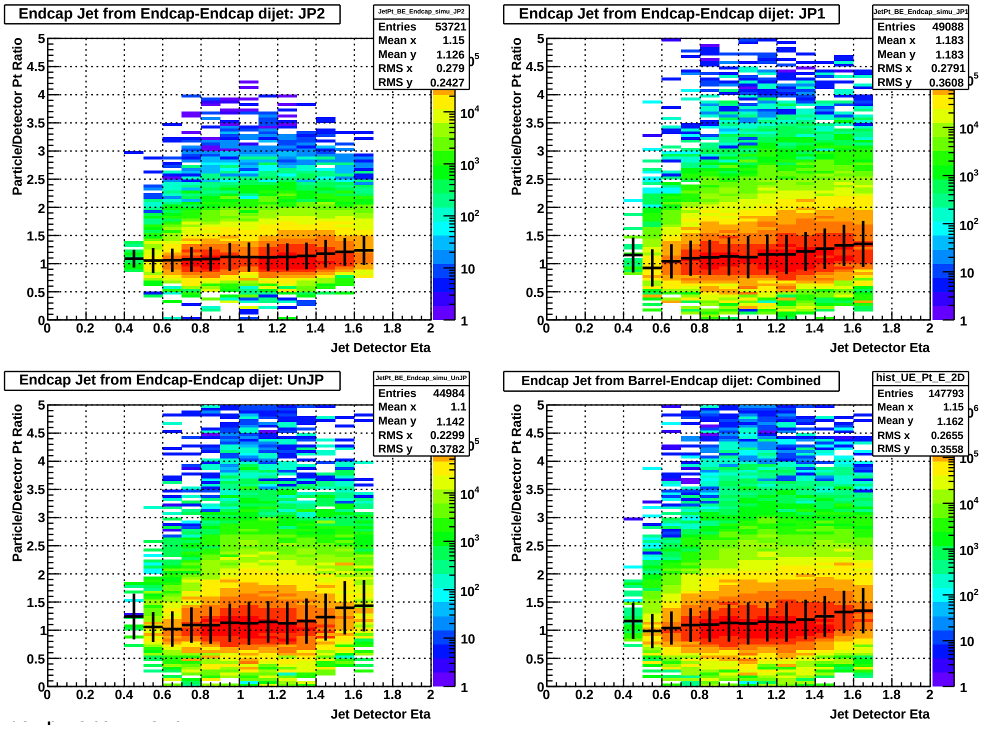

Figure 6.6: p_T shift: Endcap jet particle/detector p_T ratio vs. detector η for different triggers.

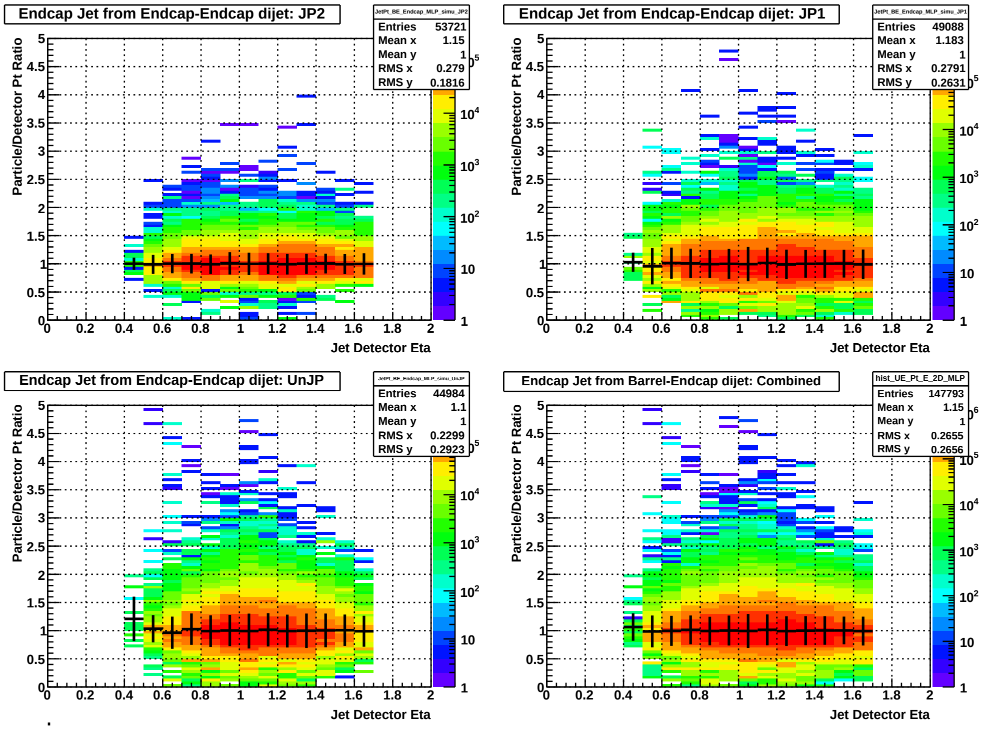

Figure 6.7: p_T shift: Endcap jet particle/output from the machine learning p_T ratio vs. detector η for different triggers.

6.4 Regression Performance Evaluation

Ranking for regression is based on the correlation strength between the input variables (or MVA method response) and the regression target. Several correlation measurements are implemented in TMVA to capture and quantify the nonlinear dependencies. Their results are printed to standard output.

6.4.1 Variable Correlation

The correlation between two random variables X and Y is usually measured with the correlation coefficient $\rho = \frac{\text{cov(X,Y)}}{\sigma_X \sigma_Y}$. This coefficient is symmetric and lies in $[-1, 1]$, which quantifies by definition a linear relationship. If $\rho = 0$, then X and Y are independent variables, but higher order functional or non-functional relationships may not, or only marginally, be reflected in the value of ρ. The correlations among the four variables used in the Endcap jet p_T correction are shown in Fig. 6.8. The Endcap jet p_T and Barrel jet p_T are positively correlated, as they are from the same di-jet events; the Endcap jet p_T is negatively correlated with its neutral fraction and detector pseudorapidity, in agreement with our expection. We would be more likely to underestimate the jet's p_T due to the falling tracking efficiency in the Endcap region, and the jets we measured there are likely to have higher neutral energies.

6.4.2 Overtraining

Overtraining occurs when a machine learning problem has too few degrees of freedom, because too many model parameters of an algorithm were adjusted to fit too few data points. The sensitivity to overtraining therefore depends on the MVA method. For example, a linear discriminant (LD) can hardly ever be overtrained, whereas without the appropriate counter measures, boosted decision trees usually suffer from at least partial overtraining, owing to their large number of nodes. Overtraining leads to a seeming increase in the classification or regression performance over the objectively achievable one if measured on the training sample, and to an effective performance decrease when measured with an independent test sample. A convenient way to detect overtraining

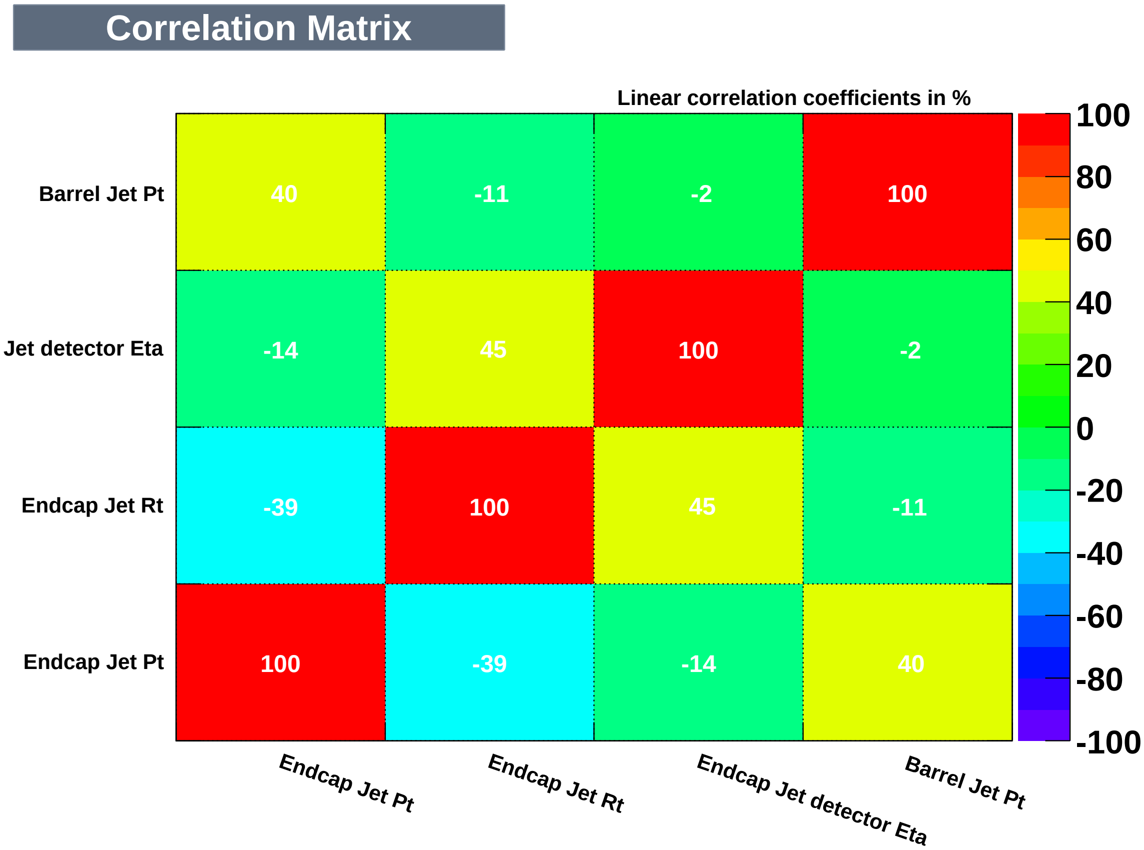

Figure 6.8: Correlation between different variables for Endcap jet p_T corrections.

and to measure its impact is therefore to compare the performance results between training and test samples. Such a test is performed by TMVA with the results printed to standard output.

There are various method-specific solutions to counteract overtraining. It is typically not known beforehand how many epochs (the number of iterations through the entire data set used to train the network) are necessary in order to achieve a sufficiently good training of the neural network. The neural networks steadily monitor the convergence of the error estimator between training and test samples, suspending the training when the test sample has passed its minimum. The convergence test for MLP is shown in Fig. 6.9. The agreement seen between the training and testing samples means that the MLP method is well suited for this problem.

Fig. 6.10 shows the average quadratic deviation of the learning output from its true values for three different machine learning methods. In each case, we find good agreement between the training and testing samples.

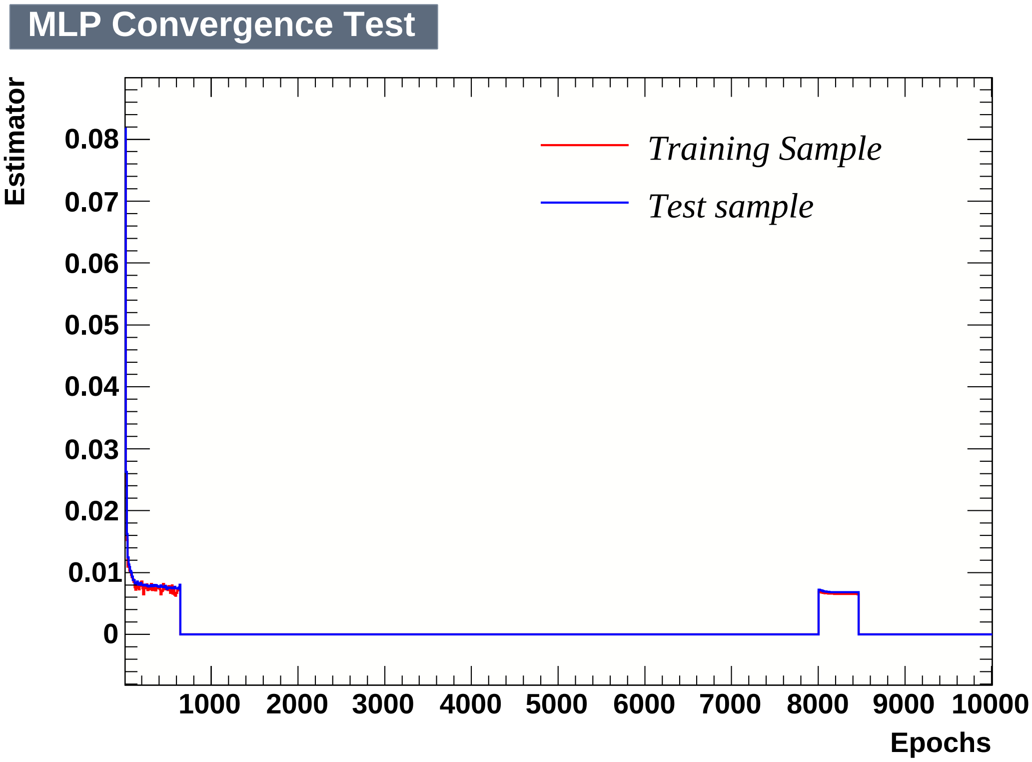

Figure 6.9: Convergence test for the MLP method.

6.4.3 Di-Jet p_T Imbalance

After we made the p_T correction for each jet, a di-jet transverse momentum imbalance distribution can be calculated. These distributions are shown in Fig. 6.11 before the correction, and in Fig. 6.12 after the correction. This distribution is more balanced (the mean is closer to zero) after the correction, and the average size of the imbalance (RMS) is significantly reduced. This means that the corrections we made really do work as expected.

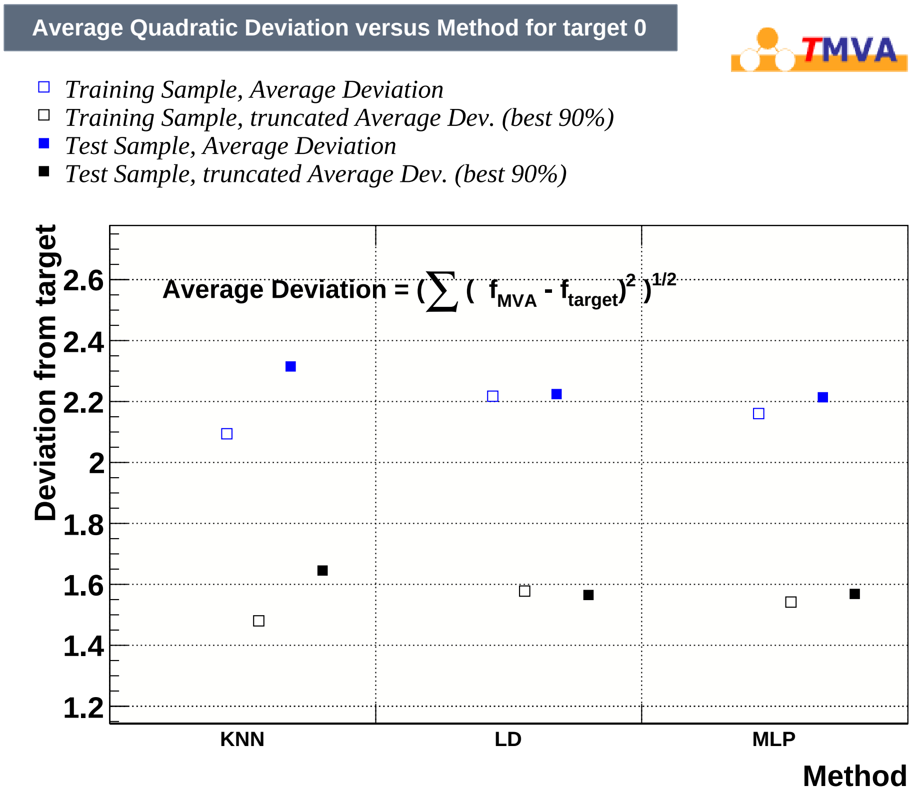

Figure 6.10: Average quadratic deviations for different machine learning methods.

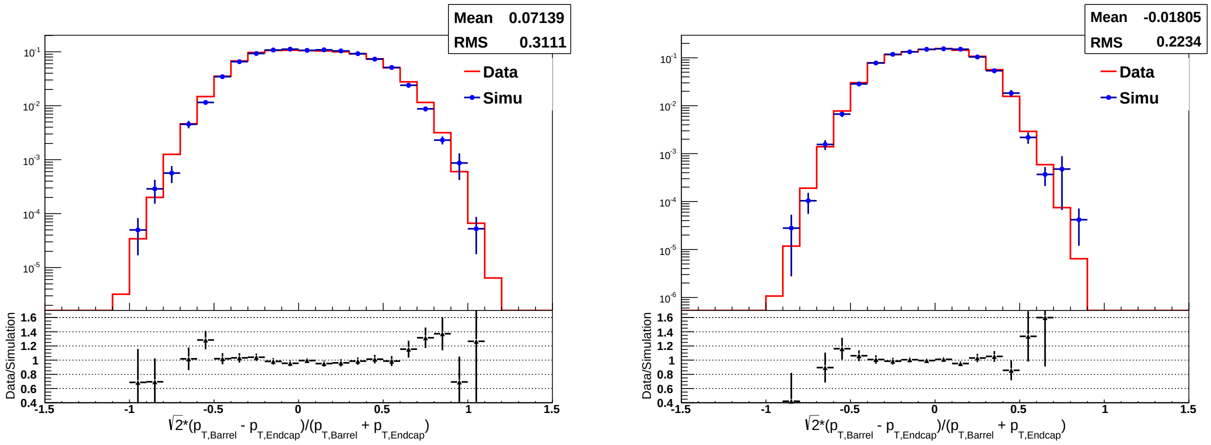

Figure 6.11: Uncorrected relative difference in p_T for back-to-back Barrel-Endcap di-jets.

Figure 6.12: Corrected relative difference in p_T for back-to-back Barrel-Endcap di-jets.

6.5 Jet Mass Correction

Even though the jet invariant mass is small compared to the jet transverse momentum, and may not contribute much in a dijet invariant mass calculation, it is still an important jet property and is not negligible in calculating the dijet invariant mass. The detector-level jet invariant mass tends to be lower than its real value, as will be shown below. Hence, similar corrections are also made here to correct the jet invariant mass back to its true value (particle level).

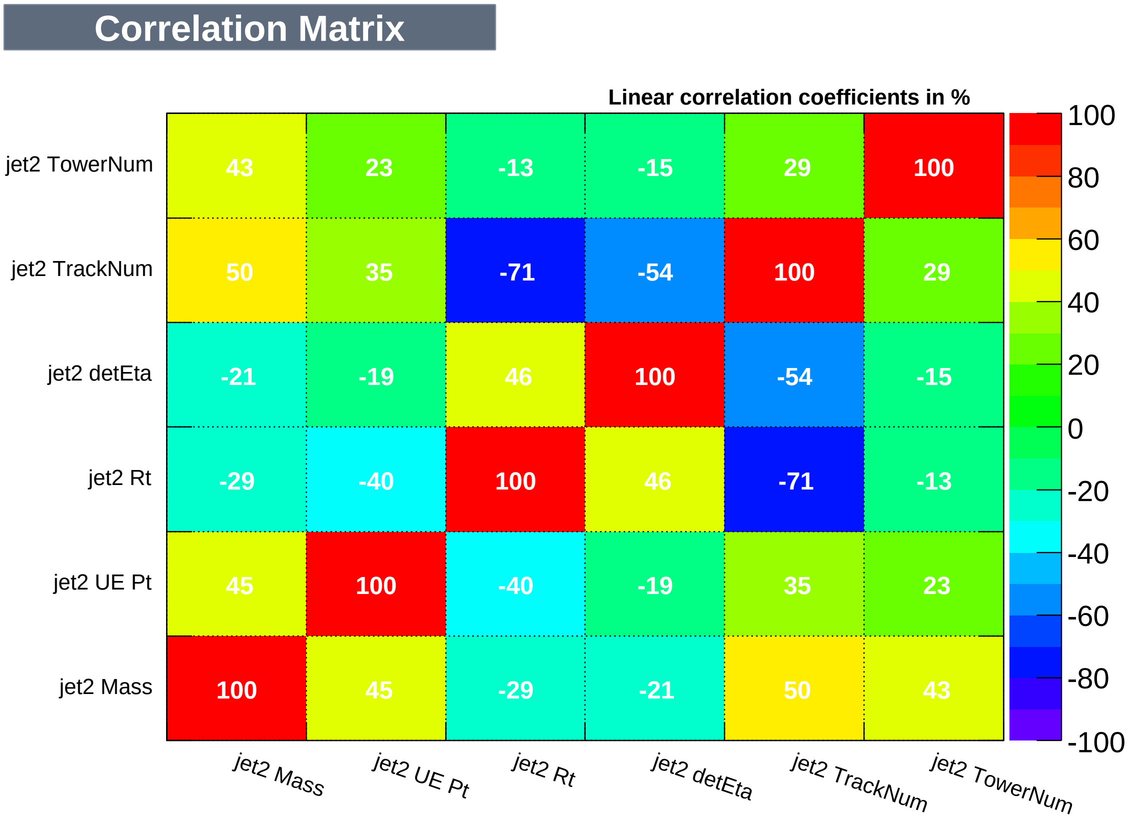
Correlation Matrix

Linear correlation coefficients in %

	jet2 Mass	jet2 UE Pt	jet2 Rt	jet2 detEta	jet2 TrackNum	jet2 TowerNum
jet2 TowerNum	43	23	-13	-15	29	100
jet2 TrackNum	50	35	-71	-54	100	29
jet2 detEta	-21	-19	46	100	-54	-15
jet2 Rt	-29	-40	100	46	-71	-13
jet2 UE Pt	45	100	-40	-19	35	23
jet2 Mass	100	45	-29	-21	50	43

Figure 6.13: Correlation between different variables for Endcap jet mass corrections.

The invariant mass of the jet and detector pseudorapidity $\eta_{detector}$ are the two key inputs in this correction. The jet p_T, neutral fraction R_t, track multiplicity n_{track} and tower multiplicity n_{tower} relate to the jet's content, and serve as important extra inputs that should benefit the learning process. Fig. 6.13 shows the correlations among different variables. The variables are generally correlated in ways that are expected. Jet tower and track multiplicities are positively correlated with the jet transverse momentum and its invariant mass. Jet invariant mass is also negatively correlated with the detector pseudorapidity, which means the falling tracking efficiency at higher pseudorapidity also affects the jet invariant mass measurement. Hence the choice of variables used here is reasonable.

After making the Underlying Event subtraction, a lot of jets have a mass close to zero, as shown in Fig. 5.4, which means these jets are almost massless. The large number of zero-mass samples would effect the training process, and may lead to biased results. To solve this problem, the correction was only applied if the jet mass was larger than 0.2 GeV. For the jet invariant mass (for both Barrel and Endcap jets), the method and variables are chosen as below:

- Method: Multilayer Perceptron (MLP).
- Variables: detector level jet mass m_{jet}, detector level p_T, detector pseudorapidity $\eta_{detector}$, neutral fraction R_t, track multiplicity n_{track}, tower multiplicity n_{tower}.
- Target: particle level jet invariant mass.

The JP2, JP1 and UnJP samples are trained separately, same as before. In Figs. 6.14 and 6.16, we show the Barrel and Endcap jet particle level invariant mass over its uncorrected values before the mass correction. The overall spread and differences are large. In Figs. 6.15 and 6.17 are shown the same plots after mass correction, demonstrating large improvements due to this correction.

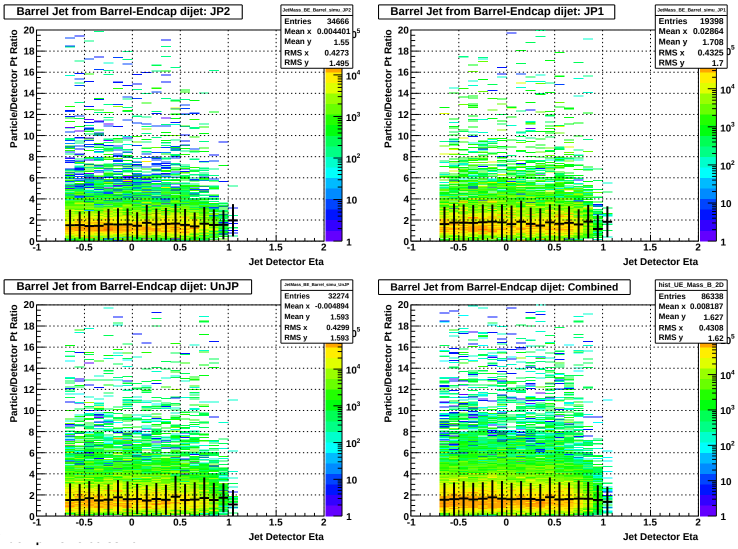

Figure 6.14: Mass shift: Barrel jet particle/detector mass ratio vs. detector η for different triggers.

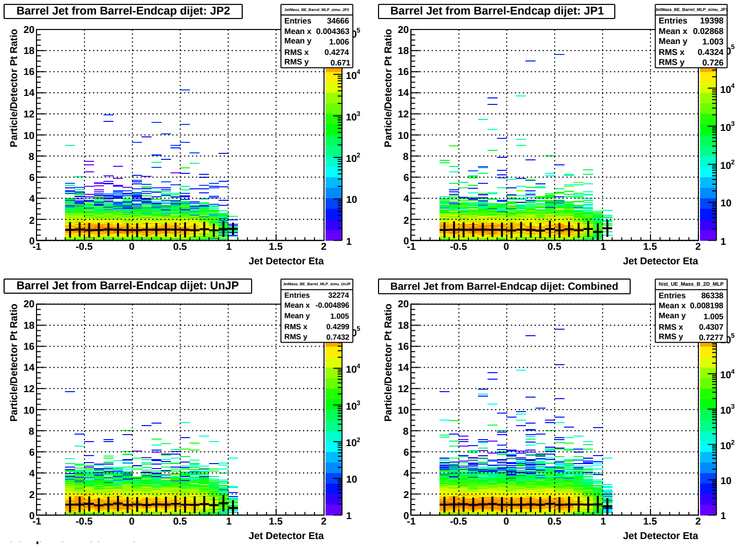

Figure 6.15: Mass shift: Barrel jet particle/output from the machine learning mass ratio vs. detector η for different triggers.

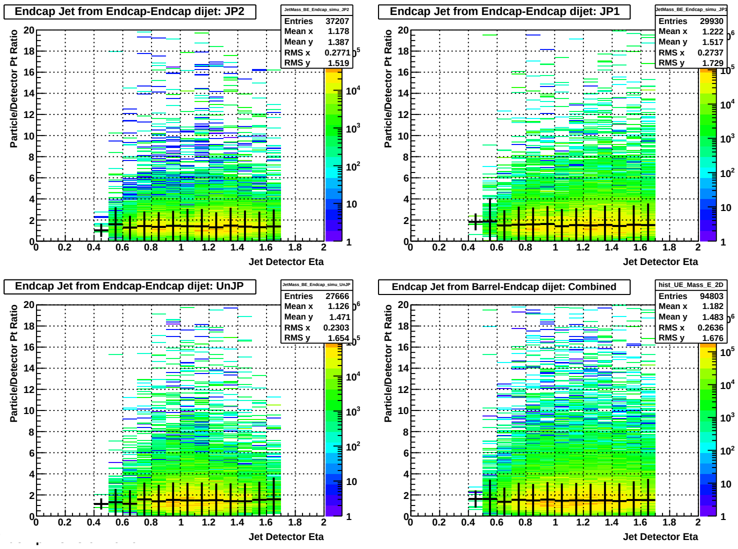

Figure 6.16: Mass shift: Endcap jet particle/detector mass ratio vs. detector η for different triggers.

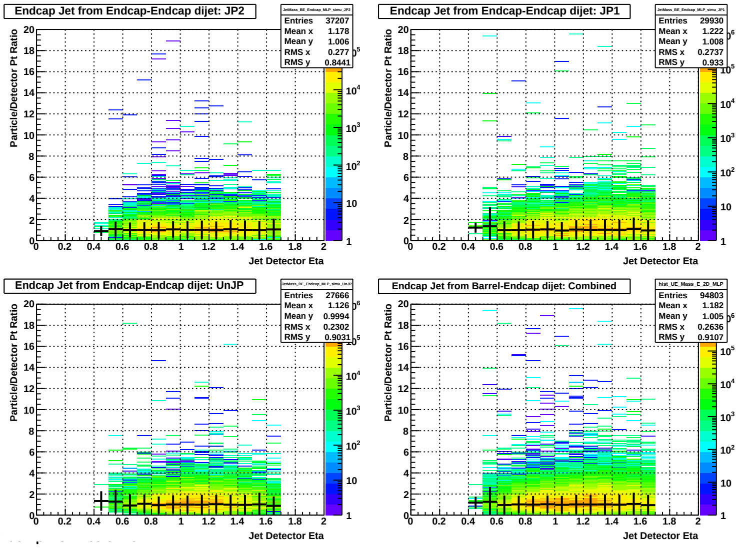

Figure 6.17: Mass shift: Endcap jet particle/output from the machine learning mass ratio vs. detector η for different triggers.

6.6 Other Jet Corrections

As discussed previously, Barrel and Endcap jets are separately corrected in p_T and mass. The corrected jet's 4-vector momentum then has the same direction, but improved values for p_T and mass after the corrections, as we describe below.

The jet pseudorapidity (η) and azimuthal angle (ϕ) are measured with very good precision. Figs. 6.18 and 6.19 show the jet η difference between particle level and detector level ($\eta_{true} - \eta_{measured}$) as a function of the jet detector pseudorapidity for Barrel and Endcap jets, respectively. The differences are small and no obvious bias is found in the spectra. Figs. 6.20 and 6.21 show the jet ϕ difference between particle level and detector level ($\phi_{true} - \phi_{measured}$) as a function of the jet detector pseudorapidity for Barrel and Endcap jets, respectively, which also look good. Hence we decided not to correct the jet direction (η, ϕ) in this analysis.

Event-by-event di-jet invariant mass comparisons are shown in Fig. 6.22. The left two plots are before we made the p_T and mass corrections and the right two plots are after we made the corrections. The upper two plots are distributions of the ratio of particle level di-jet mass over the detector level di-jet mass; the lower two plots are the difference of the two di-jet masses over their sum. The average ratio changes from 1.13 to 1.01, and the spread is narrower with about 15% improvement in the resolution. The difference ratio is also reduced from 0.048 to -0.008, and the distribution is also narrower. In general, the discrepancies between particle level and the detector level di-jet invariant mass are reduced, which is what we expected after making the corrections.

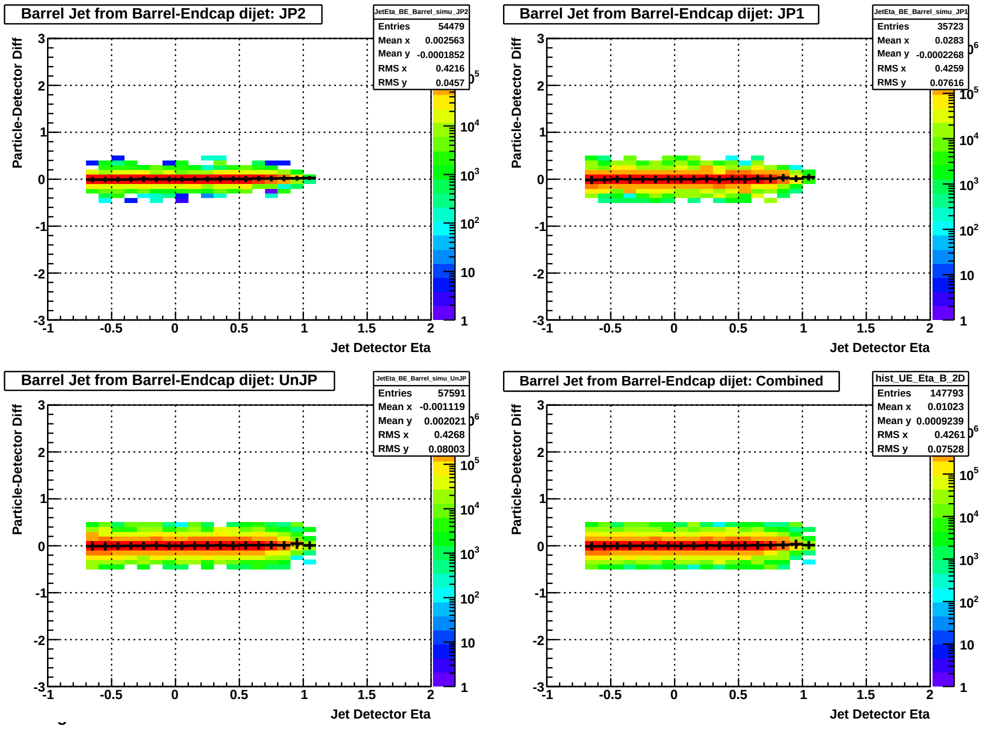

Figure 6.18: Barrel jet particle - detector η difference vs. detector η for different triggers.

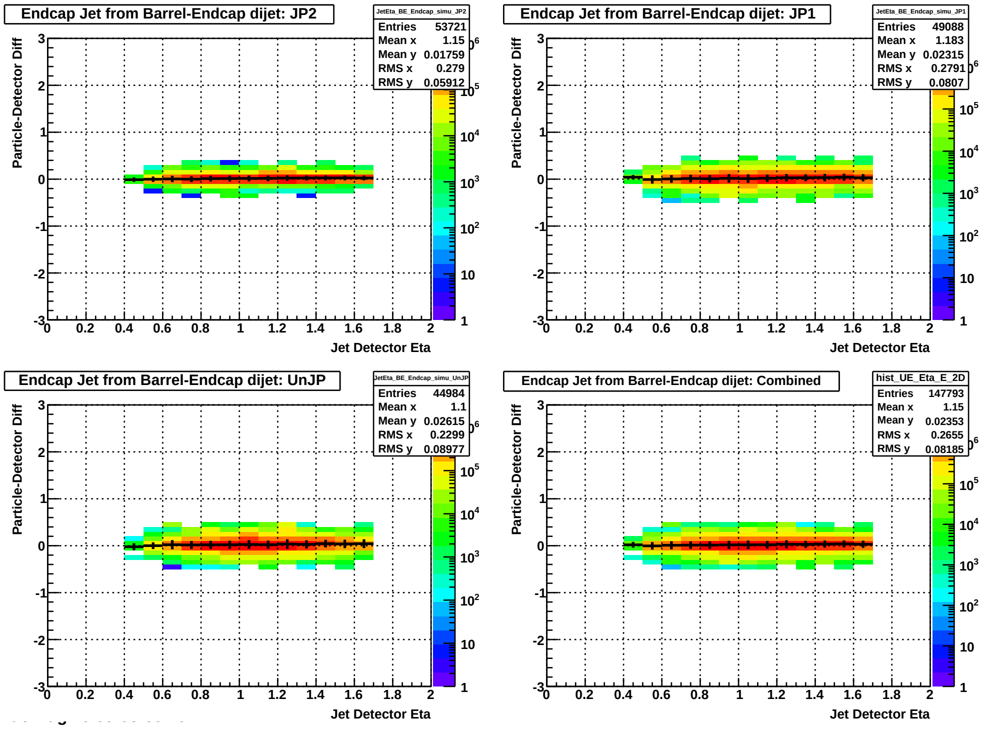

Figure 6.19: Endcap jet particle - detector η difference vs. detector η for different triggers.

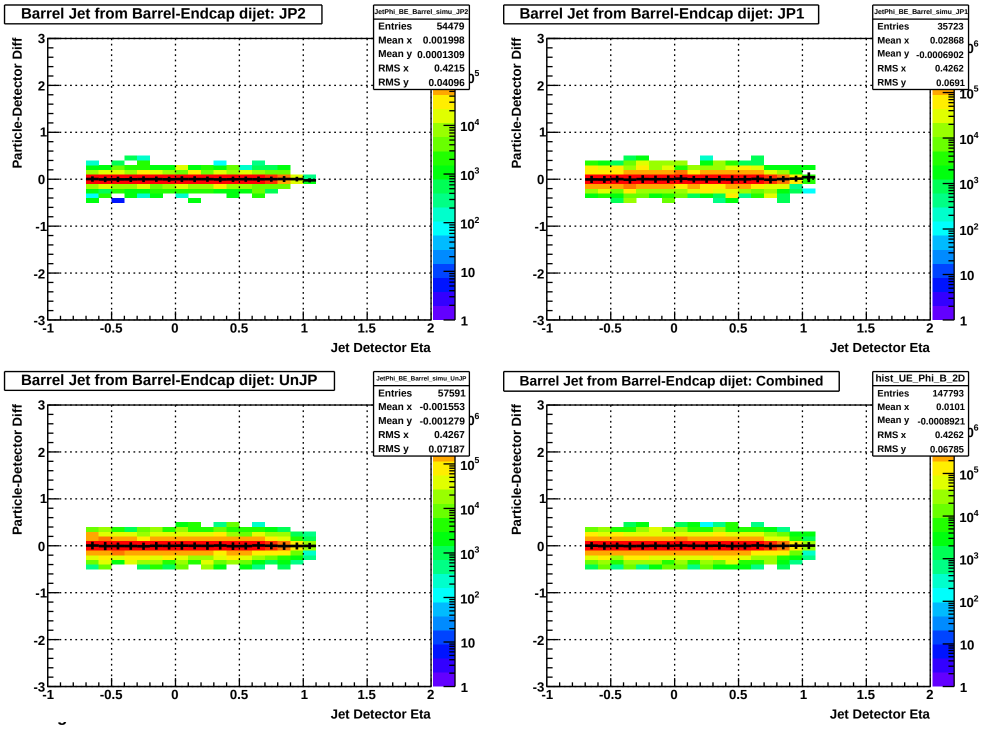

Figure 6.20: Barrel jet particle - detector ϕ difference vs. detector η for different triggers.

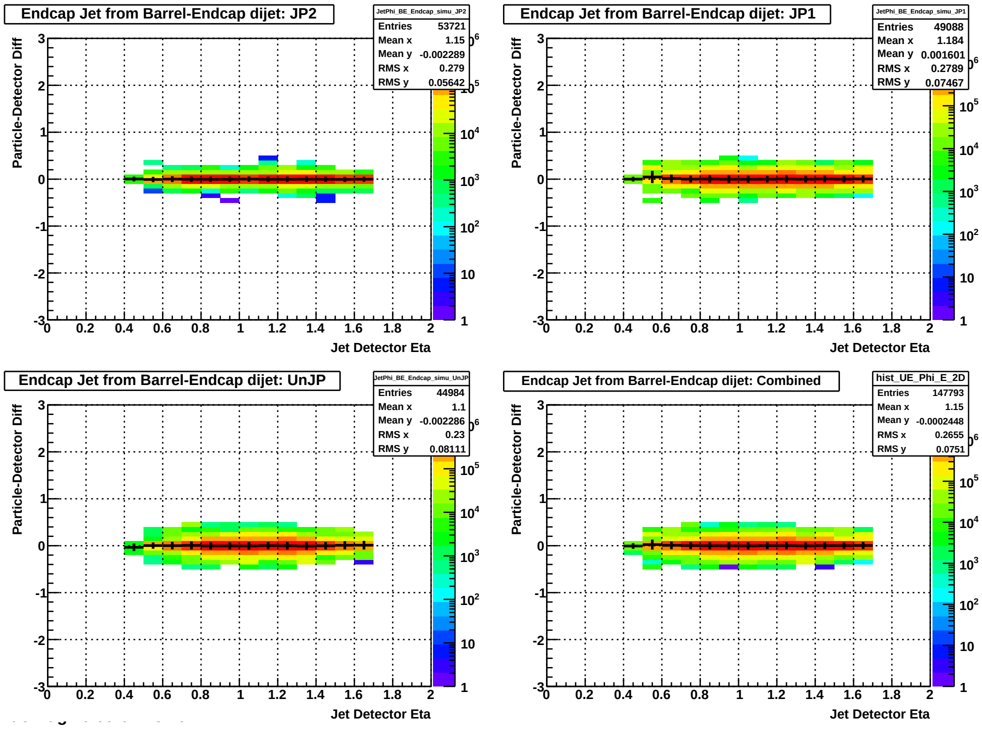

Figure 6.21: Endcap jet particle - detector ϕ difference vs. detector η for different triggers.

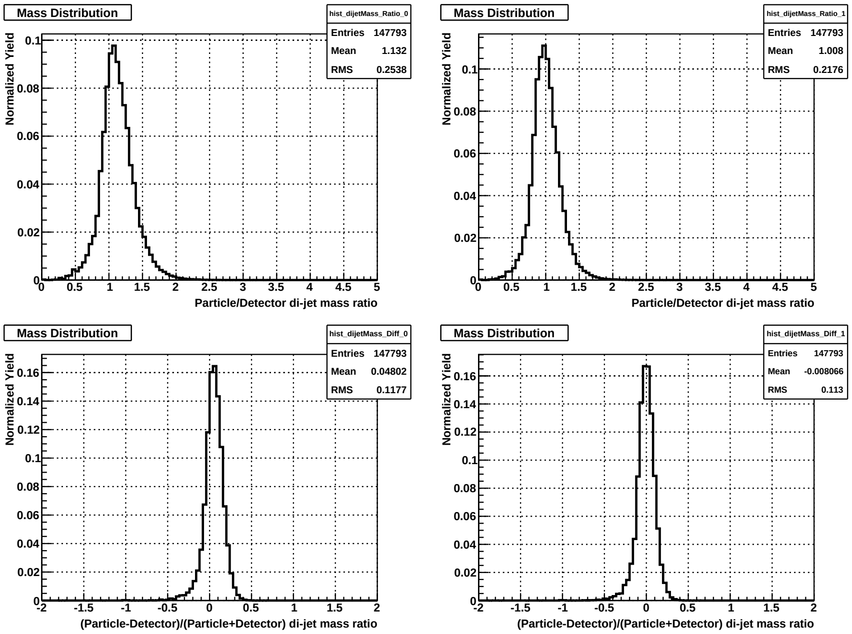

Figure 6.22: Di-jet mass comparision between the particle level and detector level: particle level over detector level ratio before the corrections are made (upper left); particle level over detector level after the corrections (upper right); difference ratio before corrections (lower left); difference ratio after corrections (lower right).

CHAPTER 7

Double-spin Asymmetries

As has been discussed in the first chapter, the main observable used to study the gluon polarization ΔG at RHIC is the longitudinal double-spin asymmetry, A_{LL}. STAR has presented A_{LL} measurements for inclusive jets [68], [39], dijet production at middle rapidity [46], and intermediate π^0 production [78]. These results have placed strong constraints on the gluon helicity distribution in the proton.

The longitudinal double-spin asymmetry, A_{LL}, is defined as:

$$A_{LL} \equiv \frac{\sigma_{++} - \sigma_{+-}}{\sigma_{++} + \sigma_{+-}}, \tag{7.1}$$

where σ_{++} and σ_{+-} are the differential production cross sections when the beam protons have equal and opposite helicities, respectively. Experimentally, sorting the yields by beam spin state enables a determination of the longitudinal double-spin asymmetry A_{LL} at STAR to be evaluated as:

$$A_{LL} = \frac{\sum(P_Y P_B)[(N^{++} + N^{--}) - R_3(N^{+-} + N^{-+})]}{\sum(P_Y P_B)^2[(N^{++} + N^{--}) + R_3(N^{+-} + N^{-+})]}, \tag{7.2}$$

where $P_{Y,B}$ are the polarizations of the yellow and blue beams, and N^{++}, N^{--}, N^{+-} and N^{-+} are the dijet yields from beam bunches with the same (first two) and opposite (latter two) helicity configurations, respectively. The first index denotes the helicity of the yellow beam, while the second index shows the helicity of the blue beam bunches. R_3 is the ratio of the integrated luminosities for these configurations. The sum is over individual data runs, which generally ranged from 10 to 60 minutes in length, which is short compared to the nominal time required for changes in beam conditions. These will be discussed in the following sections.

The statistical error on A_{LL} is calculated using the usual error propagation techniques:

$$\delta A_{LL} = \frac{\sqrt{\sum(P_Y^2 P_B^2)[(N^{++} + N^{--}) + R_3^2(N^{+-} + N^{-+})]}}{\sum(P_Y P_B)^2[(N^{++} + N^{--}) + R_3(N^{+-} + N^{-+})]}. \tag{7.3}$$

A detailed derivation is presented in appendix B.

7.1 Beam Polarization

As has been discussed in chapter 2, the beam polarizations are measured by the proton-Carbon (pC) polarimeters and a polarized hydrogen gas jet (H-Jet). The first is used to measure relative polarizations, and the gas jet is for absolute measurements. The beams are not 100% polarized, so the measured A_{LL} needs to be scaled by the polarizations. For the 2009 *pp* 200 GeV data, the average polarization was about 56% for the blue beam and 57% for the yellow beam.

In order to account for polarization loss over time, an initial polarization P_0, a slope $\frac{dp}{dt}$ (polarization change over time), and an initial time t_0 were also provided for each fill. During the data analysis, the value of the polarization was determined from the Unix timestamp t of each event using the equation:

$$P(t) = P_0 \times e^{\frac{dp}{dt}(t-t_0)}. \tag{7.4}$$

The average polarization value reported by the polarimetry group for each fill was weighted by the luminosity over the course of that fill. This means that as long as the number of events sampled scales proportionally with the luminosity, the average polarization would be the correct value to use. This proportionality roughly holds for the JP2 events, as that trigger was take-all throughout the run, so its event rate should scale with the instantaneous luminosity. The JP1 trigger, however, was prescaled, and the prescale value was chosen in proportion to the instantaneous luminosity at the beginning of each run. This means that JP1 events are taken at a higher rate at the end of fills, when the luminosity is lower. Thus, using the average polarization value for the JP1 sample would tend to overestimate the beam polarizations appropriate for this sample. Calculating A_{LL} using the beam polarizations found as a function of event time alleviates this problem.

7.2 Spin Patterns

The collider assigns a spin pattern for each bunch crossing, which encodes the helicity of each beam in the collision. There are four spin patterns used for typical fills, and the polarization direction of each bunch in the two beams will match one of the patterns shown in Table 7.1. These four spin patterns were cycled through fill-by-fill over the course of Run 9. Only events with a valid spin pattern were retained.

Pattern	Yellow Beam	Blue Beam
P_1	+ + - - + + - -	+ - + - - + - +
P_2	+ + - - + + - -	- + - + + - + -
P_3	- - + + - - + +	+ - + - - + - +
P_4	- - + + - - + +	- + - + + - + -

Table 7.1: The four spin patterns used in 2009. The '+' indicates positive helicity and the '-' indicates negative helicity.

The colliding bunch helicity combination is encoded as a 'Spin-4' value at STAR, as indicated in Table 7.2. The information on the spin pattern for a specific event is stored in an offline database, so the Spin-4 value for any bunch crossing can be found easily. For a given spin pattern, each bunch crossing has a set Spin-4 value.

Spin-4	Yellow Beam	Blue Beam
5	+	+
6	-	+
9	+	-
10	-	-

Table 7.2: Spin pattern and polarization states.

Each bunch crossing is assigned a unique number (0-119). Those in the yellow abort gap (31-39) and the blue abort gap (111-119) were discarded, as these events arise from beam background only. The relative luminosity analysis found that bunch crossings 20, 60, 78, 79, and 80 were problematic in 2009, so all events from those bunch crossings were also dropped from the analysis.

7.3 Relative Luminosities

As shown in equation 7.2, the relative luminosities are needed between different spin patterns. The physics asymmetry defined in equation 7.1 measures the underlying physics process under the assumption that all spin state combinations are equally sampled. However, because there are only a limited number of bunch crossings available in the collider, and not all bunches have the same intensity, some spin state combinations may sample more luminosity than others. Therefore, each count must be normalized by the associated luminosity. The relative luminosity factors are ratios of helicity-combination luminosities, constructed in such a way to cancel out false asymmetries which would arise from the different combinations of the sampled luminosities. Getting the relative luminosities correct is an essential ingredient in the extraction of A_{LL} and other spin asymmetries.

For the 2009 pp200 data set, the relative luminosities were measured at STAR by the spin-sorted BBC coincidence yields, which have high rates and are independent of the detectors that are used to measure the dijet yields. Relative luminosities were also calculated using the ZDC system, and the difference between these two values (BBC and ZDC) was used in estimating systematic errors. More details can be found in [79].

There are six different relative luminosities for different spin pattern combinations:

$$R_1 = \frac{\mathcal{L}^{++} + \mathcal{L}^{-+}}{\mathcal{L}^{+-} + \mathcal{L}^{--}} \tag{7.5a}$$

$$R_2 = \frac{\mathcal{L}^{++} + \mathcal{L}^{+-}}{\mathcal{L}^{-+} + \mathcal{L}^{--}} \tag{7.5b}$$

$$R_3 = \frac{\mathcal{L}^{++} + \mathcal{L}^{--}}{\mathcal{L}^{+-} + \mathcal{L}^{-+}} \tag{7.5c}$$

$$R_4 = \frac{\mathcal{L}^{++}}{\mathcal{L}^{--}} \tag{7.5d}$$

$$R_5 = \frac{\mathcal{L}^{-+}}{\mathcal{L}^{--}} \tag{7.5e}$$

$$R_6 = \frac{\mathcal{L}^{+-}}{\mathcal{L}^{--}} \quad , \tag{7.5f}$$

where R_3 is the quantity needed to properly normalize the helicity-sorted yields in calculations of A_{LL}. The other luminosity ratios are useful in the calculation of the various false asymmetries.

7.4 False Asymmetries

In addition to the longitudinal double-spin asymmetry (equation 7.2), four other useful asymmetries can be calculated, as defined in equation 7.6. These four quantities provide checks on the analysis scheme, because they are expected to be zero in this data set:

$$A_L^{Y,B} = \frac{\sigma_+ - \sigma_-}{\sigma_+ + \sigma_-} \tag{7.6a}$$

$$A_{LL}^{ls} = \frac{\sigma_{--} - \sigma_{++}}{\sigma_{--} + \sigma_{++}} \tag{7.6b}$$

$$A_{LL}^{us} = \frac{\sigma_{-+} - \sigma_{+-}}{\sigma_{-+} + \sigma_{+-}} \quad . \tag{7.6c}$$

These false asymmetries can be expressed in terms of the measured spin yields, as shown in equation 7.7. A_L^Y and A_L^B measure the longitudinal single-spin asymmetries for the yellow and blue beams. They arise from parity-violating effects due to the weak interactions, and are therefore expected to be negligible, relative to the statistical uncertainties. A_{LL}^{ls} and A_{LL}^{us} are the like and unlike sign double-spin asymmetries, and should be zero for the case of like helicities and opposite helicities in both beams. A_{LL}^{ls} is also sensitive only to parity-violating effects, while A_{LL}^{us} is expected to be null by rotational invariance, as collisions in which the yellow beam has positive helicity and the blue beam has negative helicity should be the same as the reverse case.

$$A_L^Y = \frac{\sum P_Y[(N^{--} + N^{-+}) - R_1(N^{++} + N^{+-})]}{\sum P_Y^2[(N^{--} + N^{-+}) + R_1(N^{++} + N^{+-})]} \tag{7.7a}$$

$$A_L^B = \frac{\sum P_B[(N^{--} + N^{-+}) - R_2(N^{++} + N^{+-})]}{\sum P_B^2[(N^{--} + N^{-+}) + R_2(N^{++} + N^{+-})]} \tag{7.7b}$$

$$A_{LL}^{ls} = \frac{\sum P_Y P_B(N^{--} - R_4 N^{++})}{\sum P_Y^2 P_B^2(N^{--} - R_4 N^{++})} \tag{7.7c}$$

$$A_{LL}^{us} = \frac{\sum P_Y P_B(R_6 N^{-+} - R_5 N^{+-})}{\sum P_Y^2 P_B^2(R_6 N^{-+} - R_5 N^{+-})} \quad . \tag{7.7d}$$

These four asymmetries provide important cross checks on the A_{LL} measurements, because the values for these asymmetries should be very small. Significant deviations from zero in any of these four asymmetries would indicate a problem with the calculation of relative luminosities or the asymmetry itself. Figs. 7.1, 7.2, 7.3 and 7.4 show these four additional asymmetries for the Barrel-Endcap dijet full sample ($-0.8 < \eta_1 < 0.8$ and $0.8 < \eta_2 < 1.8$), East Barrel-Endcap ($-0.8 < \eta_1 < 0.$ and $0.8 < \eta_2 < 1.8$), West Barrel-Endcap ($0. < \eta_1 < 0.8$ and $0.8 < \eta_2 < 1.8$) and Endcap-Endcap ($0.8 < \eta_{1,2} < 1.8$) dijet topologies, respectively. The 'false' asymmetries are found to have reasonable χ^2 values, and all the fits are consistent with zero.

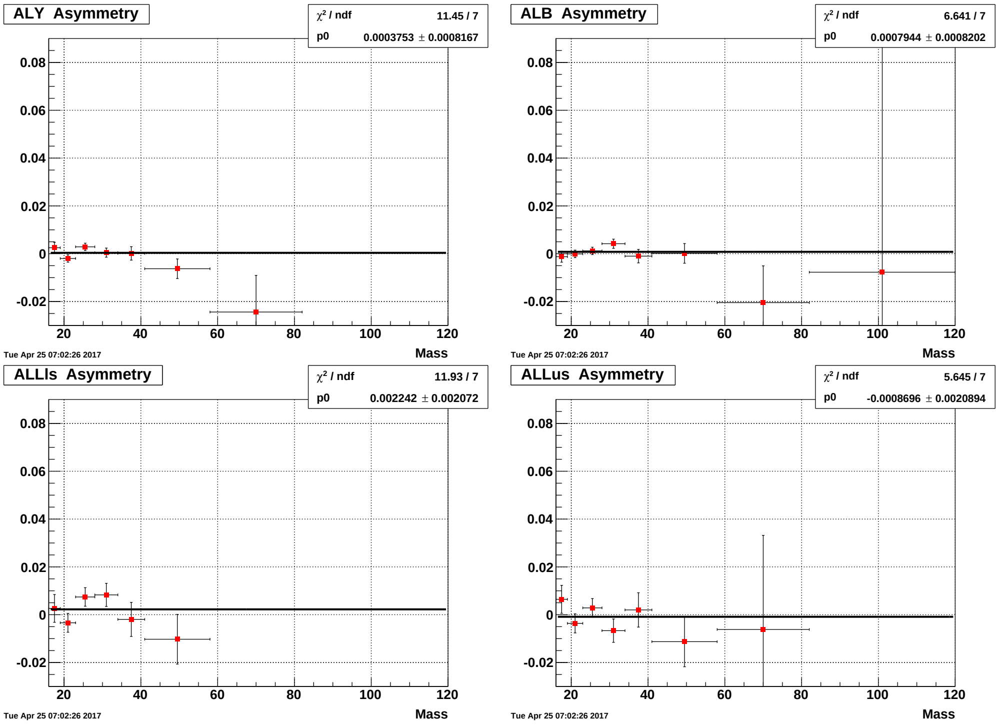

Figure 7.1: Dijet false asymmetries: Barrel-Endcap full topology.

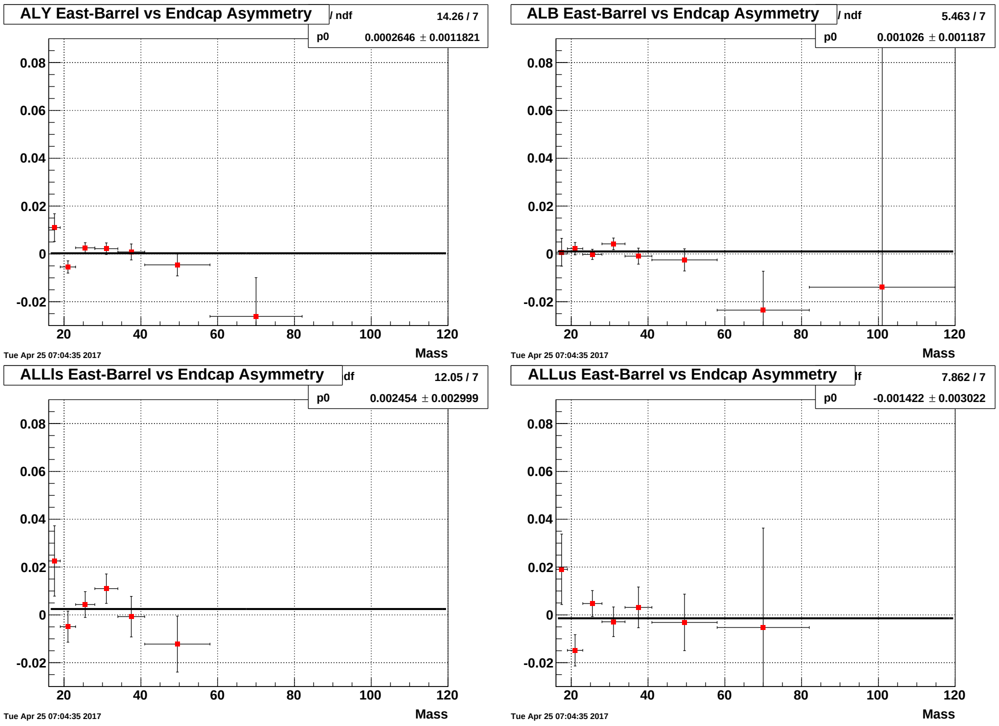

Figure 7.2: Dijet false asymmetries: EastBarrel-Endcap.

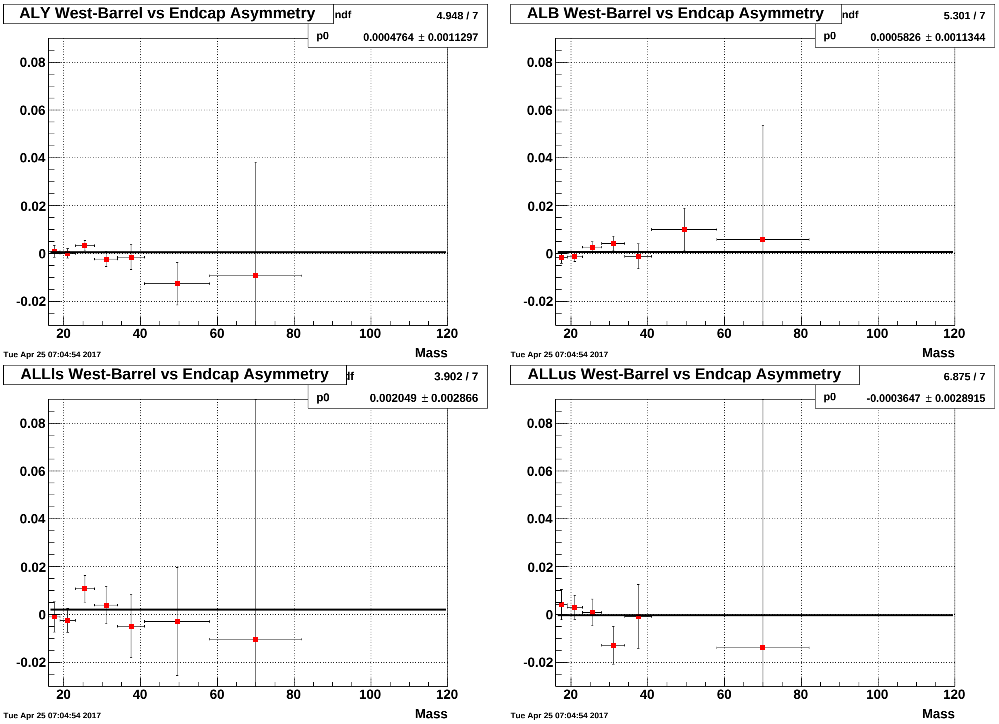

Figure 7.3: Dijet false asymmetries: WestBarrel-Endcap.

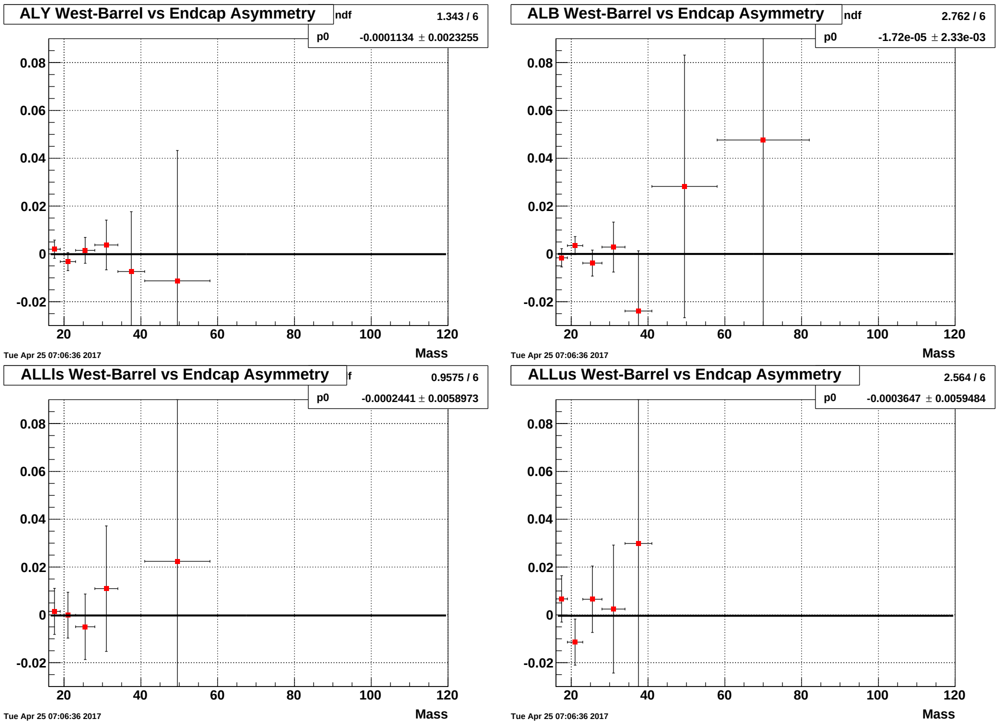

Figure 7.4: Dijet false asymmetries: Endcap-Endcap.

7.5 Data Corrections

Various corrections were applied for both the dijet invariant mass and the double-spin asymmetry. These corrections are summarized in tables 7.3 and 7.4, and discussed in more detail below.

7.5.1 Dijet Invariant Mass Shift

In order to compare our results with theoretical predictions, which are calculated at the parton level, a determination of the parton level dijet invariant mass of each data point was made by applying a simple mass shift to each point. This mass correction accounts for the difference in parton and particle level dijet invariant mass scales.

In previous jet-by-jet corrections, the jet energy had already been corrected back to particle level, so the mass shift is found by comparing the particle level dijet masses to the matching parton level dijet masses in simulation. For a given mass bin, the mass difference was calculated by finding the difference between the parton level dijet mass and the particle level dijet mass ($\Delta M = M_{parton} - M_{particle}$) event-by-event for all the dijets that fell into the given mass bin. The mass shift is the mean value of this calculation at each bin. The final data points are plotted at their average particle level mass + mass shift, which should be close to the average mass at the parton level. Fig. 7.5 shows the average mass shift for the four different dijet topologies.

7.5.2 Trigger and Reconstruction Bias

In parton-parton interactions, there are three different subprocesses that dominate: quark-quark (qq), quark-gluon (qg), and gluon-gluon (gg) elastic scattering. Values of A_{LL} extracted from the data represent an admixture of the asymmetries produced from these three dominant partonic scattering sub-processes. The mixture, however, can be altered in the measurement process. For example, the STAR jet-patch trigger may be more efficient for certain subprocesses. This would alter the sub-process fractions in the data set, compared to the underlying physical fractions, and thereby shift the measured A_{LL}. Further distortions can arise due to systematic shifts caused by the

Barrel-Endcap Full Topology

Bin	Ave Mass(GeV)	Mass Shift(GeV)	A_{LL}	Trigger and Reco Shift	Errors
1	17.744	0.755	-0.00501	0.00062	0.00044
2	21.037	0.867	0.01085	0.00079	0.00025
3	25.315	0.995	0.00436	0.00090	0.00025
4	30.598	1.086	0.00415	0.00102	0.00044
5	36.893	1.346	0.00157	0.00150	0.00071
6	46.086	1.597	0.01188	0.00234	0.00084
7	63.704	1.755	0.02019	0.00549	0.00511

Endcap-Endcap

Bin	Ave Mass(GeV)	Mass Shift(GeV)	A_{LL}	Trigger and Reco Shift	Errors
1	17.535	0.965	0.00189	-0.00017	0.00062
2	20.786	0.915	-0.00778	-0.00080	0.00076
3	24.980	1.334	0.02147	0.00071	0.00111
4	30.167	1.569	0.04204	0.00055	0.00299
5	36.131	2.746	0.08638	0.00907	0.00507

Table 7.3: Dijet parton level corrections for Barrel-Endcap and Endcap-Endcap topologies.

East Barrel-Endcap

Bin	Ave Mass(GeV)	Mass Shift(GeV)	A_{LL}	Trigger and Reco Shift	Errors
1	18.070	0.370	-0.01647	0.00052	0.00057
2	21.215	0.895	0.00643	0.00059	0.00036
3	25.408	1.167	0.00609	0.00119	0.00033
4	30.677	1.538	0.00266	0.00098	0.00057
5	36.951	1.400	-0.00631	0.00160	0.00086
6	46.239	1.772	0.01149	0.00192	0.00087
7	63.835	1.892	0.01976	0.00685	0.00557

West Barrel-Endcap

Bin	Ave Mass(GeV)	Mass Shift(GeV)	A_{LL}	Trigger and Reco Shift	Errors
1	17.683	0.828	-0.00289	0.00052	0.00051
2	20.933	0.850	0.01345	0.00060	0.00034
3	25.217	0.805	0.00251	-0.00010	0.00038
4	30.469	0.323	0.00659	0.00007	0.00068
5	36.752	1.203	0.02076	-0.00035	0.00125
6	45.513	0.914	0.01334	0.00227	0.00232
7	62.568	0.256	0.02395	-0.00776	0.00526

Table 7.4: Dijet parton level corrections for the two Barrel-Endcap topologies.

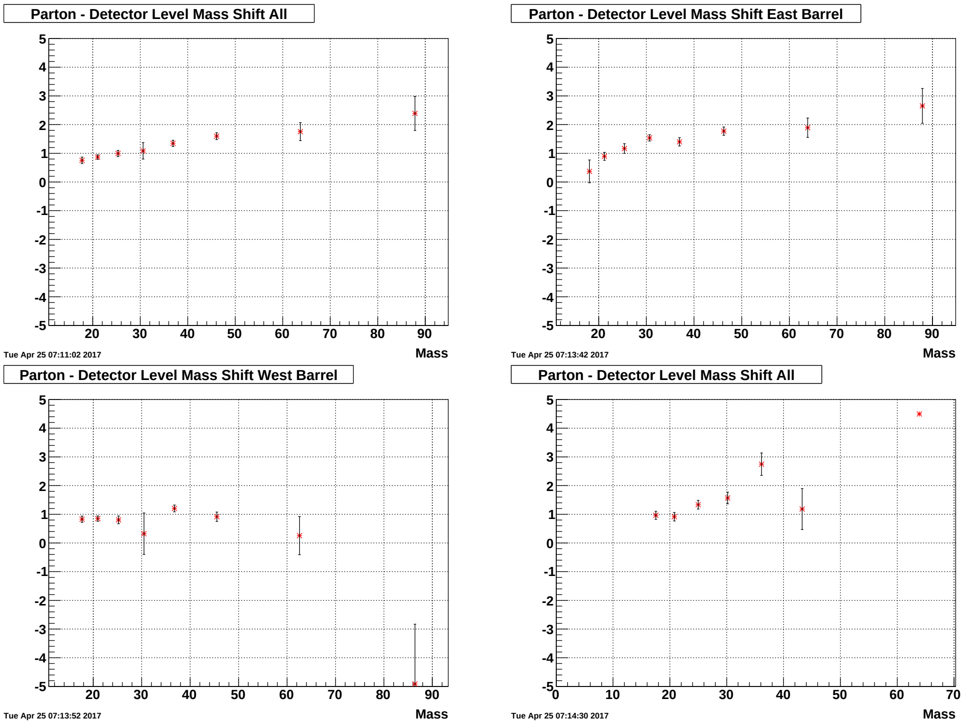

Figure 7.5: Dijet invariant mass shifts for Barrel-Endcap dijet full topology (upper left), East Barrel-Endcap (upper right), West Barrel-Endcap (lower left) and Endcap-Endcap topology.

finite resolution of the detector coupled with a rapidly falling invariant mass distribution, which would thus change the subprocess fraction associated with a given mass. Jets with more neutral energy (high R_t) are preferentially selected in the Endcap due to the falling tracking efficiency, and R_t is also correlated with the sub-processes. To address these concerns, trigger and reconstruction bias corrections were applied to the raw A_{LL} values to compensate for these effects.

Determination of the biases introduced by the trigger and jet reconstruction depends on the details of the polarized parton distribution functions. These must necessarily be taken from theory, and so must account for the uncertainty in polarized gluon contributions. Parameterizations of the polarized parton distribution functions are combined with PYTHIA parton kinematic variables to generate predictions of A_{LL} vs. the dijet invariant mass for a particular model, at both the parton and detector levels. The NNPDFPol1.1 set [17] has 100 replicas and is therefore very applicable for this calculation.

The determination of the trigger and reconstruction bias correction follows the same procedure as has been used in the 2012 pp 200 GeV inclusive jet measurement analysis [41] using the 100 replica NNPDF sets:

1. For each event, find the parton level dijet from the full, unbiased PYTHIA sample. Apply only the $\Delta\phi$, jet η, and asymmetric p_T cuts. Plot A_{LL} from the polarized PDFs versus the parton level dijet mass. This is shown in the upper left plots of Figs. 7.6, 7.7, 7.8, and 7.9.

2. Fit the parton level theory curve with a 3rd order polynomial functions, extract the A_{LL} from the fitting functions (lower left plot in Figs. 7.6, 7.7, 7.8, and 7.9).

3. For each event, find the detector level dijet from the simulation sample which passed the trigger filter. Apply all detector level cuts, but do not require detector level to particle level matching. Plot A_{LL} of the polarized PDFs versus the detector level dijet mass (upper right plot in Figs. 7.6, 7.7, 7.8, and 7.9). Final A_{LL} is the trigger fraction weighted sum of the A_{LL} from the L2JetHigh and JP1 triggers. Place points at mass-weighted mean of the bin.

4. Calculate ΔA_{LL} for each mass bin at the shifted mass point. ΔA_{LL} is the difference between the parton and detector level A_{LL} evaluated at the shifted detector level mass. Values are shown in the lower right plots of Figs. 7.6, 7.7, 7.8, and 7.9.

The trigger and reconstruction bias correction in each mass bin was calculated by evaluating $\Delta A_{LL} = A_{LL}^{detector}(M_{detector}) - A_{LL}^{parton}(M_{detector} + \Delta M_{Shift})$ for the 100 replica NNPDF sets. The final correction is the average of the 100 ΔA_{LL}, which means the final data point is $A_{LL}^{final} = A_{LL}^{raw} - \Delta A_{LL}$.

The uncertainty for the theoretical A_{LL} is determined by adding in quadrature the errors from the two trigger samples, weighted by the trigger fractions. For each trigger sample, the error was evaluated as $\delta A_{LL} = \sqrt{\frac{\sum_i^N (A_{LL}^i - A_{LL}^{ave})}{N}}$ at each mass bin; the A_{LL}^i is the theoretical value at a given x_1, x_2 and Q^2 for event ID i; A_{LL}^{ave} is the average values in given mass bins.

The uncertainties of the detector level and unbiased parton level from the NNPDF best values were added in quadrature and were assigned as the systematic errors on the dijet A_{LL}. In Fig. 7.6 are the plots used for the correction estimation for the Barrel-Endcap full topology, Fig. 7.7 is the same for East Barrel-Endcap, Fig. 7.8 is for West Barrel-Endcap, and Fig. 7.9 is for Endcap-Endcap.

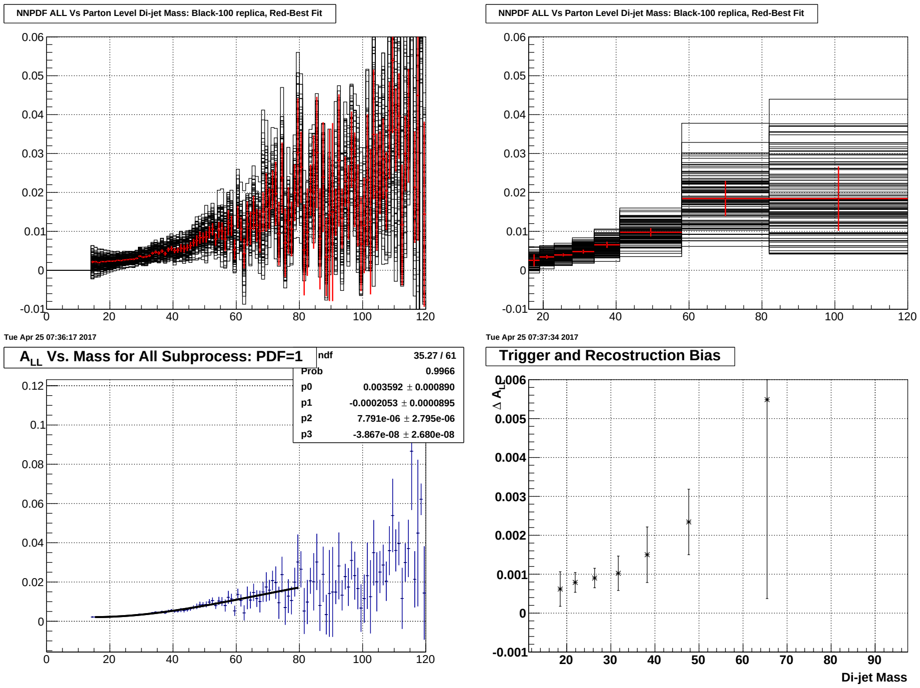

Figure 7.6: Dijet NNPDF 100 replica A_{LL} of the Barrel-Endcap full topology: parton level (upper left), detector level (upper right), parton level fit extractions (lower left) and final corrections (lower right).

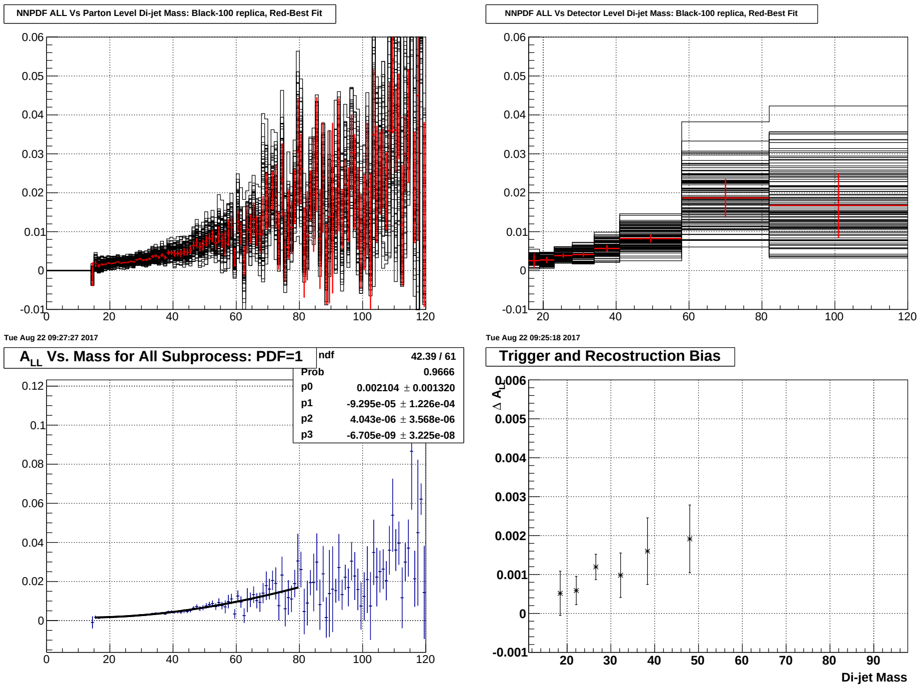

Figure 7.7: Dijet NNPDF 100 replica A_{LL} of the East Barrel-Endcap: parton level (upper left), detector level (upper right), parton level fit extractions (lower left) and final corrections (lower right).

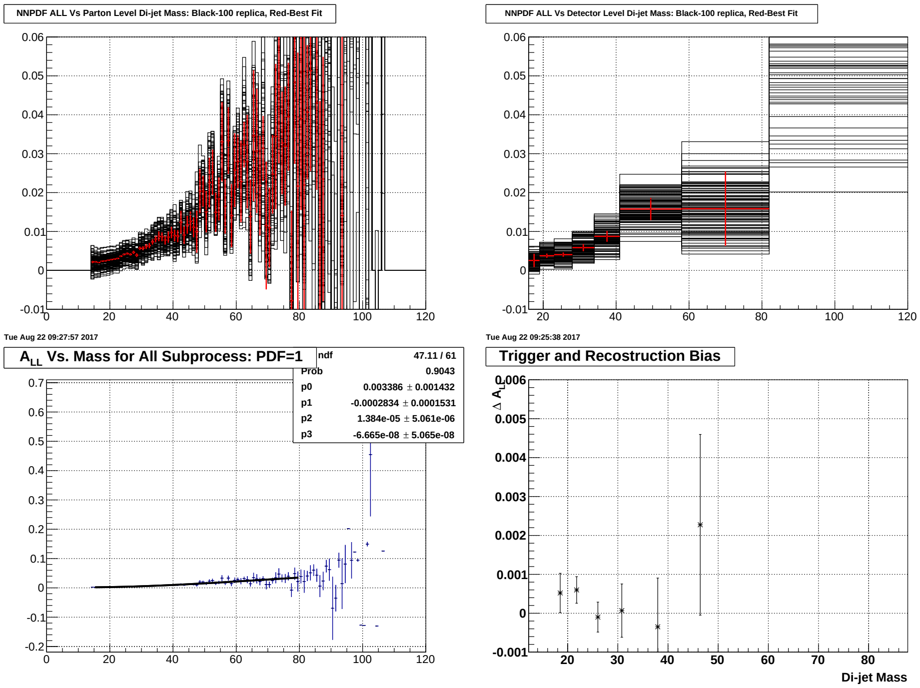

Figure 7.8: Dijet NNPDF 100 replica A_{LL} of the West Barrel-Endcap: parton level (upper left), detector level (upper right), parton level fit extractions (lower left) and final corrections (lower right).

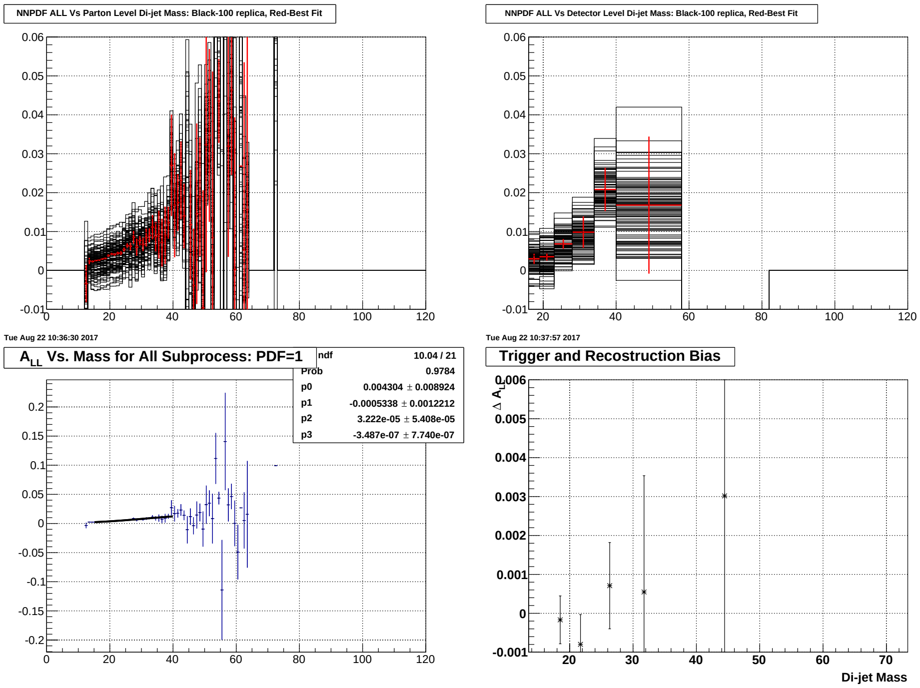

Figure 7.9: Dijet NNPDF 100 replica A_{LL} of the Endcap-Endcap: parton level (upper left), detector level (upper right), parton level fit extractions (lower left) and final corrections (lower right).

7.6 Systematic Errors

Most systematic errors were determined in the same way as used for the 2009 Barrel-Barrel dijet measurements [46]. The systematic uncertainties of the 2009 pp 200 GeV dijet A_{LL} were broken down into two categories: systematic errors on the dijet mass (x-axis uncertainties) and those on the A_{LL} values (y-axis uncertainties). The systematic errors on A_{LL} include the polarization uncertainty, the relative luminosity uncertainty, underlying event systematic uncertainty, trigger bias and reconstruction uncertainty, and the residual transverse double spin asymmetry uncertainty. The systematic errors on the dijet mass are due to the jet energy scale uncertainties, tracking efficiency uncertainties, jet p_T and mass shift uncertainties, dijet invariant mass shift uncertainties and PYTHIA tune uncertainties. Tables 7.10 and 7.11 summarize the errors on the dijet invariant mass, while Tables 7.12 and 7.13 are the errors on dijet A_{LL}.

The polarization uncertainty was determined by the RHIC polarimetry group and was found to be 6.5% [39]. The relative luminosity systematic is the same as from the inclusive jet analysis, which evaluated BBC/ZDC differences and the false asymmetry magnitudes to arrive at a value of ±0.0005.

7.6.1 Residual Transverse Component

Due to imperfect tuning of the spin rotators in the collider, the polarization may acquire a residual transverse component. In conjunction with the C-AD group, the ratio of the transverse polarization over the total polarization $t = P_T/P$, and the azimuthal angles ϕ of the transverse polarization, were measured for both yellow and blue beams in the BBCs and ZDCs. Results are shown in Tables 7.5 and 7.6. Data taken before fill 10969 (run 10173048) has a large residual transverse polarization in the blue beam; then the spin rotators were adjusted to minimize that effect.

We assume that this systematic error would not change significantly in different detector regions, so we use exactly the same method as was used in the 2009 Barrel-Barrel dijet measurement, which

	ZDC	BBC
Yellow	t = 0.16 ± 0.02, ϕ = -0.8 ± 0.1	t = 0.15 ± 0.02, ϕ = -0.5 ± 0.1
Blue	t = 0.27 ± 0.01, ϕ = -0.9 ± 0.1	t = 0.25 ± 0.02, ϕ = -1.5 ± 0.1

Table 7.5: Transverse polarization factors before rotator adjustment.

	ZDC	BBC
Yellow	t = 0.12 ± 0.10, ϕ = -1.4 ± 0.8	t = 0.13 ± 0.02, ϕ = -0.5 ± 0.1
Blue	t = 0.04 ± 0.07, ϕ = -2.2 ± 1.9	t = 0.10 ± 0.03, ϕ = -1.4 ± 0.1

Table 7.6: Transverse polarization factors after rotator adjustment.

was adopted from the 2009 inclusive jet paper [39]. The systematic is evaluated as:

$$\delta A_{LL} = |\tan\theta_Y \tan\theta_B \cos(\phi_Y - \phi_B) A_\Sigma|, \tag{7.8}$$

where θ and ϕ are the polar and azimuthal angles of the polarization vectors, and the $\tan\theta$ (equal to t = P_T/P) terms were calculated for the periods before and after the rotator tuning and then weighted by the fraction of the events collected during the respective periods. To simplify the calculation, the $\cos(\phi_Y - \phi_B)$ term was set to 1. Because there was no transverse running during Run 9, the A_Σ values used were taken from Run 6. These values were all consistent with zero, so to be conservative, the statistical error on the A_Σ measurement was taken and used in the calculation of the systematic. The A_Σ were measured as a function of jet p_T. For a given dijet mass point, a linear extrapolation as used to get the δA_Σ at the p_T which is half of that mass, as shown in Fig. 7.10. δA_Σ was then scaled down by the product of the yellow and blue transverse components of the polarization, $\tan\theta_Y \tan\theta_B$, which were calculated separately from the BBC measurements. The $\tan\theta_Y$ and $\tan\theta_B$ were also weighted by the relative fraction of events before (91%) and after (9%) the rotator adjustments. The residual transverse double spin asymmetry uncertainty is of the same order of magnitude as the relative luminosity uncertainty. Final values are shown in Tables 7.12 and 7.13.

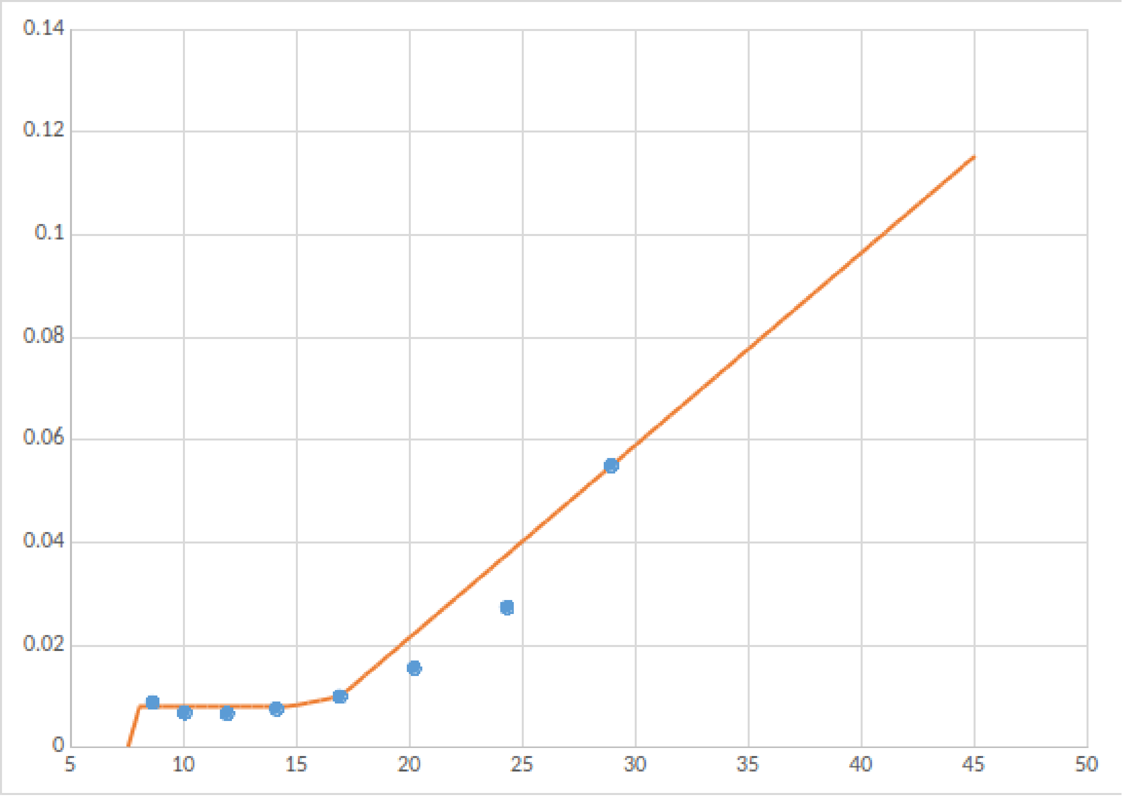

Figure 7.10: 2006 inclusive jet δA_Σ as function of the jet transverse momentum p_T.

7.6.2 Underlying Events Asymmetry

The underlying event contribution to A_{LL} was determined by measuring the average underlying event correction ΔM and the $A_{LL}^{\Delta M}$ in the data:

$$A_{LL}^{\Delta M} = \frac{1}{P_Y P_B} \frac{(\langle \Delta M \rangle^{++} + \langle \Delta M \rangle^{--}) - (\langle \Delta M \rangle^{+-} + \langle \Delta M \rangle^{-+})}{(\langle \Delta M \rangle^{++} + \langle \Delta M \rangle^{--}) + (\langle \Delta M \rangle^{+-} + \langle \Delta M \rangle^{-+})} \quad , \tag{7.9}$$

where $\Delta M = M_{dijet} - M_{dijet,UE}$. $M_{dijet,UE}$ is the dijet invariant mass after the underlying event correction. Since the beams are not 100% polarized, beam polarizations are included in this calculation. The final $A_{LL}^{\Delta M}$ is the weighted average of values from each fill.

Fig. 7.11 shows the final measured $A_{LL}^{\Delta M}$ values for all the dijet bins, and the results from a zero-th order polynomial fit. The measured $A_{LL}^{\Delta M}$ comes directly from the data, and has not been corrected for effects due to finite detector efficiencies, etc. The fitted results show the value is consistent with zero across all bins.

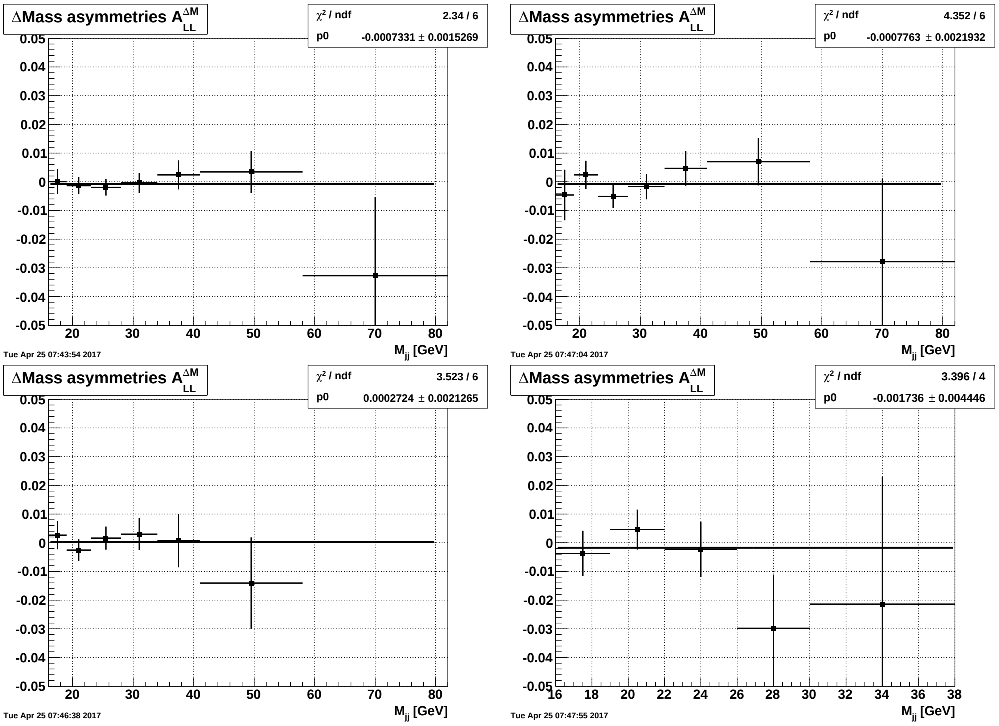

Figure 7.11: Dijet underlying events systematic: δA_{LL}, Barrel-Endcap full topology (upper left), East Barrel-Endcap (upper right), West Barrel-Endcap (lower left) and Endcap-Endcap(lower right).

To estimate the underlying event contribution, it is assumed that the underlying event adds extra energy to the jet, which effectively shifts the dijet spectrum in the positive direction. Adopting the equation from the 2012 pp 500 GeV inclusive jet analysis [41]:

$$\delta A_{LL}^{\Delta M} = \frac{\int_{M_{min}-\langle\Delta M\rangle\times A_{LL}^{\Delta M}}^{M_{max}-\langle\Delta M\rangle\times A_{LL}^{\Delta M}} \frac{d\sigma}{dm}dm - \int_{M_{min}+\langle\Delta M\rangle\times A_{LL}^{\Delta M}}^{M_{max}+\langle\Delta M\rangle\times A_{LL}^{\Delta M}} \frac{d\sigma}{dm}dm}{\int_{M_{min}-\langle\Delta M\rangle\times A_{LL}^{\Delta M}}^{M_{max}-\langle\Delta M\rangle\times A_{LL}^{\Delta M}} \frac{d\sigma}{dm}dm + \int_{M_{min}+\langle\Delta M\rangle\times A_{LL}^{\Delta M}}^{M_{max}+\langle\Delta M\rangle\times A_{LL}^{\Delta M}} \frac{d\sigma}{dm}dm} \quad , \tag{7.10}$$

where $\frac{d\sigma}{dm}$ is the unpolarized dijet cross section, and $\langle\Delta M\rangle$ is the mean spin-independent underlying event correction. Here the dijet cross section is taken from Ct10nlo [12].

7.6.3 Jet Energy Scale

The systematic error on the reconstructed dijet mass comes predominantly from the jet energy scale uncertainty. Contributions from the $\eta - \phi$ position uncertainties for individual jets are not considered. The energy deposited in the BEMC/EEMC has its uncertainty, which will contribute to the jet energy measured in this analysis. Both charged tracks and neutral particles deposit energy in the towers; thus the systematic uncertainty on the jet energy comes from both the neutral energy uncertainty and the track uncertainty. The jet energy scale uncertainties had contributions from two parts: one from the scale and status uncertainties of the EMC towers, and the other from the TPC track transverse momentum uncertainty and the tower track response uncertainty.

The tower scale uncertainties are scaled by the average neutral fraction of all jets in the dijet mass bin. The relative uncertainties for the EMC towers are below:

- For BEMC, tower status: 1.0%; scale uncertainty 4.6%; (from the 2009 pp 200 GeV BEMC calibration [46]).
- For EEMC, tower status: 1.0%; scale uncertainty 4.5%(from the 2009 pp 200 GeV π_0 anslysis [80]).

The hadron response uncertainty for the calorimeters is 0.025, from the 2009 pp 200 GeV Barrel-Barrel dijet measurement. The average EMC response to hadrons was taken to be 30%, and the track response uncertainty was taken to be 9% (both taken from Ref. [81]). The tracking efficiency was estimated to be 81% [82] and the fraction of the EMC response in the projected tower was estimated as 50%. Finally, a scale factor from charged to total hadrons of 1/0.86 (from Ref. [81]) was used. The EMC tower hadron response uncertainty was then calculated as $(1/0.86 - 0.5 \times 0.81)/0.81 \times 0.03 \times 0.09 = 0.025$. So the calorimeter hadron response uncertainty is taken to be 2.5%. This value was scaled by the average charged energy fraction of the jets in each dijet mass bin. Due to the tracking efficiency limit, most tracks can not be measured in the forward EEMC region. But tracks still deposit energy in the EMC towers, so this value is not a bad approximation for the uncertainty estimate in the EEMC region.

The total jet energy scale systematic is then taken as the quadrature sum of the BEMC scale uncertainty (which has been scaled by the neutral fraction), the track p_T uncertainty, and the hadron response uncertainty, both of which have been scaled by the average charged fraction.

To be more specific: the energy deposited in the BEMC/EEMC has an uncertainty which will contribute to the jet energy measured in this analysis. Both charged tracks and neutral particles deposit energy in the towers, so the systematic uncertainty on the jet energy is coming from the neutral energy uncertainty and the track uncertainty. The fractional neutral energy uncertainty is due to the calibration gain and its efficiency, that is:

$$\Delta f_{jet,neutral} = R_t \times \sqrt{(\Delta gain)^2 + (\Delta eff)^2}, \tag{7.11}$$

where R_t is the average neutral energy fraction. In this calculation, the neutral efficiency is the tower status uncertainty, and the gain uncertainty is the tower scale uncertainty. In Tables 7.7 and 7.8 are the final values used in this analysis.

The fractional track uncertainty has contributions from the TPC track momentum uncertainty and from the tower track response uncertainty, which combined to be $\Delta f_{track} = 0.025$, and so we have:

$$\Delta f_{jet,charged} = (1 - R_t) \times \Delta f_{track}. \tag{7.12}$$

Then $\Delta f_{jet,scale} = \sqrt{\Delta f^2_{jet,neutral} + \Delta f^2_{jet,charged}}$. The final systematic errors on dijet mass is:

$$\Delta M = M \times \Delta f_{dijet,scale}, \tag{7.13}$$

where M is the shifted dijet invariant mass point, and:

$$\Delta f_{dijet,scale} = \frac{1}{2}\sqrt{(\Delta f_{jet_{Barrel},scale})^2 + (\Delta f_{jet_{Endcap},scale})^2}. \tag{7.14}$$

7.6.4 Tracking Efficiency Uncertainty

The uncertainty on the dijet mass due to tracking efficiencies in the TPC is also considered in this analysis. It is estimated by taking the difference of the average dijet invariant mass shift from detector level to parton level between (1) using the full set of reconstructed tracks from the TPC, and (2) by using a partial set of reconstructed tracks from the TPC. The partial set of reconstructed

Barrel-Endcap Full Topology

Bin	Jet_{Barrel} R_t	Jet_{Endcap} R_t
1	0.467	0.521
2	0.468	0.540
3	0.460	0.559
4	0.440	0.570
5	0.416	0.574
6	0.397	0.572
7	0.388	0.557

Endcap-Endcap Full Topology

Bin	Jet_1 R_t	Jet_2 R_t
1	0.551	0.509
2	0.536	0.535
3	0.479	0.547
4	0.435	0.513
5	0.413	0.480

Table 7.7: Average R_t for each jet in dijet mass bins.

East Barrel-Endcap

Bin	Jet_{Barrel} R_t	Jet_{Endcap} R_t
1	0.471	0.487
2	0.473	0.519
3	0.466	0.557
4	0.448	0.577
5	0.421	0.585
6	0.398	0.584
7	0.383	0.565

West Barrel-Endcap

Bin	Jet_{Barrel} R_t	Jet_{Endcap} R_t
1	0.466	0.527
2	0.465	0.553
3	0.454	0.562
4	0.426	0.559
5	0.404	0.547
6	0.396	0.529
7	0.432	0.488

Table 7.8: Average R_t for each jet in dijet mass bins.

tracks from the TPC is usually chosen by randomly rejecting a certain percent of tracks from the full set before jet reconstruction. In this analysis, the rejection fraction was chosen to be 7%, which means rejecting seven tracks in every 100 tracks. The final results are shown in Fig. 7.12.

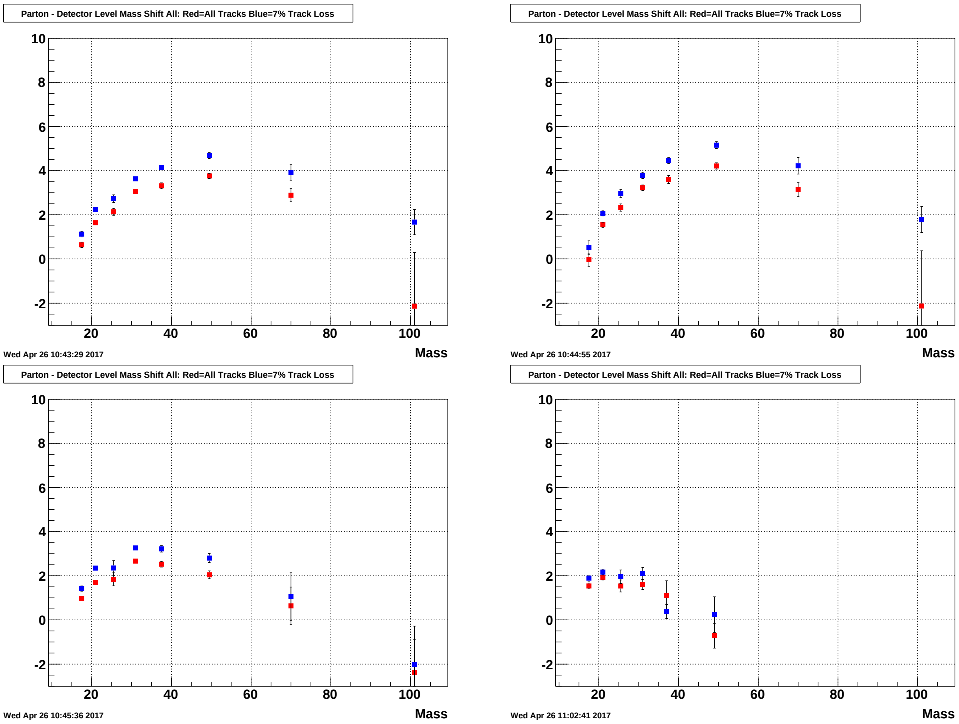

Figure 7.12: Dijet mass shift due to tracking inefficiency: 7% track loss (blue) and no track loss (red); Barrel Endcap Full topology (upper left); EastBarrel Endcap (upper right); WestBarrel Endcap (lower left); Lower right-Endcap Endcap (lower right).

7.6.5 Dijet Mass Shift Systematic

The dijet invariant mass shift from particle to parton level has been presented in a previous section. The systematic error on the dijet mass shift was determined by adding in quadrature the errors from the two trigger samples, weighted by the trigger fractions. This error was dominated by the limited statistics of the simulation sample.

7.6.6 Underlying Events Systematic Errors on Dijet Mass

The underlying event systematic uncertainty on jet energy was taken as the difference of the underlying event contribution to the dijet invariant mass between the data and simulation. Results are shown in Fig. 7.13.

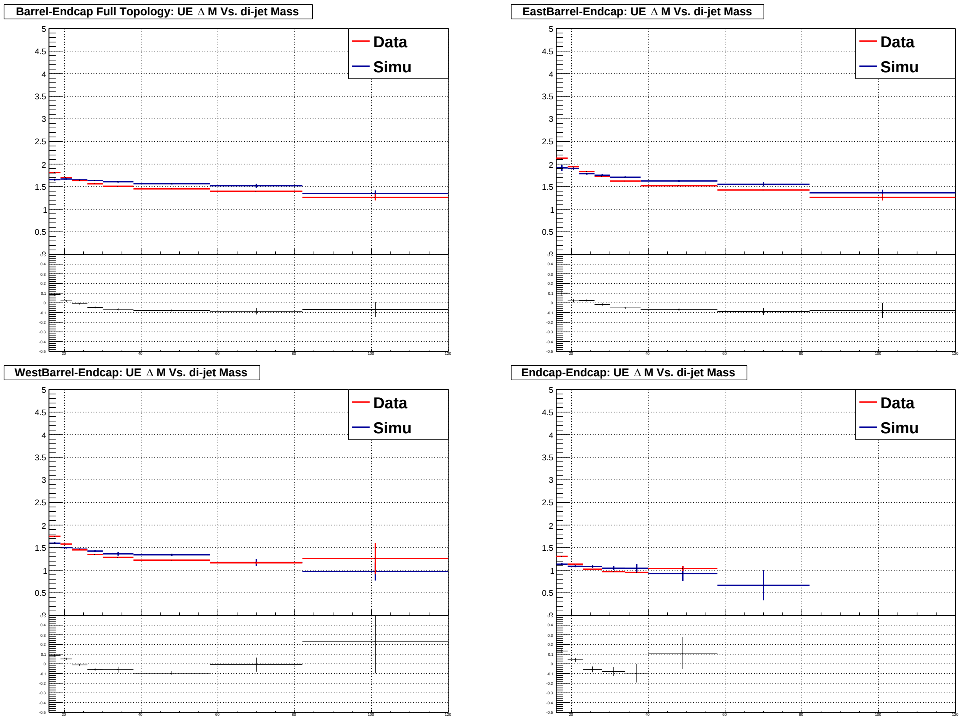

Figure 7.13: Dijet underlying event delta mass comparison for different topologies.

7.6.7 PYTHIA Tune Uncertainties

Technically, PYTHIA parameters can be varied independently to fit various data sets. There are several tune sets available in PYTHIA. The dijet invariant mass shift uncertainties due to choice of the PYTHIA tune are estimated in the analysis by utilizing the possible variants provided for Perugia0 in the PYTHIA version of 6.4.26 and Perugia2012 in PYTHIA6.4.28. Table 7.9 lists some descriptions for specific PYTHIA tunes (see the PYTHIA tune manual [73] for more details).

Tune ID	Description
PYTHIA6.4.26 Perugia0	
320	Default
321	HARD - higher amount activity from perturbative physics
322	SOFT - lower amount activity from perturbative physics
323	Different balance between MPI and ISR and a different energy scaling
324	NOCR - An update of NOCR-Pro
325	Uses the MRST LO* PDF set
326	Uses the CTEQ6L1 PDF set
327	FSR outside resonance decays increased to agree with the level inside
328	‘K’ factor on the QCD scattering cross sections used in the MPI
PYTHIA6.4.28 Perugia2012	
370	Default

Table 7.9: PYTHIA tune and its variants.

The mass shifts due to choice of PYTHIA tune were calculated using:

$$\Delta M = M_{parton} - M_{particle,UE} \tag{7.15a}$$

$$\delta M_{tune_i} = \Delta M_{tune_i} - \Delta M_{tune_{320}} \tag{7.15b}$$

$$\delta M_{tune} = (\Delta M_{tune_{321}} - \Delta M_{tune_{322}})/2 \tag{7.15c}$$

$$Systematic\ Errors = \sqrt{\Sigma_i \delta M^2_{tune_i}}, \tag{7.15d}$$

where $M_{particle,UE}$ is the dijet invariant mass after underlying event subtraction. We compare the mass shifts between the PYTHIA6.4.26 Perugia0 (Official 2009 pp 200 GeV embedding usage), Tune 321 to Tune 328 (Perugia0 related sets), and PYTHIA6.4.28(Official 2012 pp 500 GeV embedding usage). The differences among these shifts are the PYTHIA tune systematics, see Fig. 7.14. Tune 328 is related to underlying events, but the underlying event systematic on the dijet invariant mass was estimated by the disagreement in underlying event ΔM between the data and embedding sample, so tune 328 was not used. In addition, tunes 321 and 322 focus on the same particular uncertainty test, so half of the absolute difference between the pair was used. The final values we used are the quadratic sum of the difference between those shifts from different tune sets.

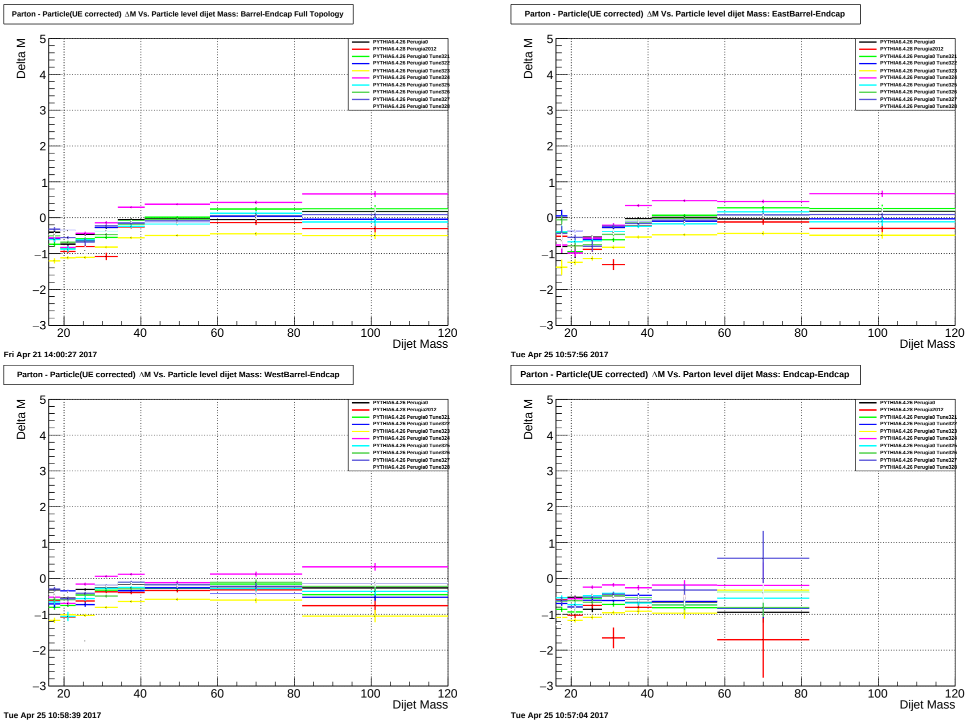

Figure 7.14: Dijet PYTHIA tune systematic: Barrel-Endcap full topology (upper left), East Barrel-Endcap (upper right), West Barrel-Endcap (lower left) and Endcap-Endcap (lower right).

7.6.8 Jet p_T and Mass Correction Systematic Uncertainties

The jet transverse momentum p_T and invariant mass M corrections were made using the machine learning method, as has been discussed in chapter 6. The Multilayer Perceptron is the main algorithm used in the correction. As noted before, for the MLP, a slight change of the parameters, such as the number of layers and nodes, may impact the learning process. Different algorithms may emphasize slightly different behaviors, which would also have some influence. So the systematic errors due to choice of machine learning algorithm were calculated in three different situations.

1. Different sample size used for training:
    - Systematic test 1: change the size of the data set used for training.
2. Different parameters for MLP:
    - Systematic test 2: change the number of layers.

Barrel-Endcap Full Topology

Bin	Energy	Tracking	Mass Shift	M.L.	UE Syst.	Tune Syst.	Total
1	0.344	0.242	0.112	0.122	0.156	0.875	0.997
2	0.412	0.298	0.079	0.089	0.035	0.557	0.764
3	0.499	0.298	0.109	0.073	0.015	0.803	1.000
4	0.599	0.291	0.286	0.078	0.073	1.018	1.254
5	0.718	0.411	0.109	0.159	0.099	0.696	1.103
6	0.888	0.462	0.119	0.317	0.114	0.659	1.251
7	1.203	0.515	0.312	0.623	0.122	0.679	1.635

Endcap-Endcap Full Topology

Bin	Energy	Tracking	Mass Shift	M.L.	UE Syst.	Tune Syst.	Total
1	0.355	0.178	0.141	0.161	0.173	0.500	0.695
2	0.419	0.117	0.149	0.128	0.048	0.897	1.017
3	0.496	0.210	0.151	0.107	0.058	0.860	1.033
4	0.574	0.248	0.204	0.084	0.077	1.307	1.468
5	0.684	0.358	0.390	0.091	0.091	0.519	1.017

Table 7.10: Dijet invariant mass systematics.

- Systematic test 3: change the number of neuron nodes.

3. Different machine learning methods:

   - Systematic test 4: use the linear discriminant (LD) method.
   - Systematic test 5: use the k-Nearest Neighbour (k-NN) method.

For each event, we can perform the jet p_T and mass corrections using the different settings and methods listed above. We then calculate the dijet invariant mass differences between these samples relative to the default standard setting (MLP). The results from different machine learning methods (LD and k-NN) and the different MLP settings (test 1, test 2, test 3) were added in quadrature. The square root of the quadrature sum is the final systematic error.

East Barrel-Endcap

Bin	Energy	Tracking	Mass Shift	M.L.	UE Syst.	Tune Syst.	Total
1	0.337	0.275	0.397	0.159	0.216	1.150	1.320
2	0.412	0.258	0.139	0.140	0.040	0.683	0.862
3	0.504	0.318	0.168	0.098	0.046	0.785	1.006
4	0.615	0.282	0.110	0.081	0.029	1.203	1.387
5	0.727	0.431	0.144	0.144	0.085	0.720	1.132
6	0.902	0.471	0.145	0.262	0.106	0.723	1.288
7	1.212	0.541	0.337	0.509	0.126	0.694	1.622

West Barrel-Endcap

Bin	Energy	Tracking	Mass Shift	M.L.	UE Syst.	Tune Syst.	Total
1	0.345	0.225	0.109	0.116	0.154	1.025	1.127
2	0.412	0.330	0.093	0.078	0.080	0.908	1.060
3	0.493	0.258	0.135	0.083	0.016	0.874	1.048
4	0.575	0.299	0.722	0.097	0.077	0.684	1.193
5	0.697	0.347	0.118	0.207	0.077	0.642	1.040
6	0.840	0.379	0.162	0.553	0.118	0.407	1.166
7	1.126	0.207	0.665	2.520	0.009	0.556	2.901

Table 7.11: Dijet invariant mass systematic.

Barrel-Endcap Full Topology

Bin	Trans Residual	UE	Trigger and Reco.	Total
1	0.00028	0.00025	0.00044	0.00058
2	0.00028	0.00054	0.00025	0.00066
3	0.00028	0.00089	0.00025	0.00097
4	0.00032	0.00034	0.00044	0.00064
5	0.00064	0.00059	0.00071	0.00112
6	0.00126	0.00127	0.00084	0.00198
7	0.00243	0.00153	0.00511	0.00586

Endcap-Endcap Full Topology

Bin	Trans Residual	UE	Trigger and Reco.	Total
1	0.00028	0.00186	0.00062	0.00198
2	0.00028	0.00221	0.00076	0.00235
3	0.00028	0.00061	0.00111	0.00130
4	0.00028	0.00444	0.00299	0.00536
5	0.00042	0.00444	0.00507	0.00675

Table 7.12: Dijet A_{LL} systematics.

East Barrel-Endcap

Bin	Trans Residual	UE	Trigger and Reco.	Total
1	0.00028	0.00068	0.00057	0.00093
2	0.00028	0.00141	0.00036	0.00148
3	0.00028	0.00157	0.00033	0.00163
4	0.00033	0.00103	0.00057	0.00122
5	0.00065	0.00131	0.00086	0.00170
6	0.00128	0.00219	0.00087	0.00268
7	0.00244	0.00219	0.00557	0.00646

West Barrel-Endcap

Bin	Trans Residual	UE	Trigger and Reco.	Total
1	0.00028	0.00101	0.00051	0.00117
2	0.00028	0.00138	0.00034	0.00145
3	0.00028	0.00049	0.00038	0.00068
4	0.00031	0.00113	0.00068	0.00135
5	0.00062	0.00094	0.00125	0.00168
6	0.00118	0.00213	0.00232	0.00336
7	0.00225	0.00213	0.00526	0.00610

Table 7.13: Dijet A_{LL} systematics.

7.7 Final Results

The advantage of a correlation observable at forward pseudorapidity range is its ability to constrain and probe lower initial state kinematics. A_{LL} is presented for several different topologies: Barrel-Endcap dijets, which have one of the jets in the BEMC and the other in the EEMC; East Barrel-Endcap dijets, with the Barrel jet at negative pseudorapidity while the West Barrel-Endcap dijets involve a Barrel jet at positive pseudorapidity; and Endcap-Endcap dijets, in which both jets are emitted at forward rapidity. Events from the specific topologies arise from asymmetric partonic collisions, and are preferentially between a high momentum (high x and therefore highly polarized) quark and a low momentum gluon. The control over initial kinematics achievable with dijets can be seen in Fig. 7.15, which presents the partonic momentum fraction distributions (weighted by partonic $\hat{a}_{LL}$) of the gluons as obtained from PYTHIA for a sample of detector level dijets with $16.0 < M < 19.0$ GeV/c^2. The asymmetric nature of the collisions can be seen in the separation of the high- and low-x distributions, and the increased reach to lower x shows the advantage of this measurement.

Barrel-Endcap Full Topology

	Dijet Mass(GeV)		A_{LL}		
Bin	Mass	Sys. Error	A_{LL}	Stat. Error	Sys. Error
1	18.499	0.997	-0.00563	0.00411	0.00058
2	21.904	0.764	0.01006	0.00280	0.00066
3	26.310	1.000	0.00346	0.00275	0.00097
4	31.683	1.254	0.00313	0.00343	0.00064
5	38.239	1.103	0.00007	0.00506	0.00112
6	47.683	1.251	0.00954	0.00738	0.00198
7	65.459	1.635	0.01470	0.02763	0.00586

Endcap-Endcap

	Dijet Mass(GeV)		A_{LL}		
Bin	Mass	Sys. Error	A_{LL}	Stat. Error	Sys. Error
1	18.500	0.695	0.00206	0.00683	0.00198
2	21.700	1.017	-0.00698	0.00679	0.00235
3	26.314	1.033	0.02076	0.00975	0.00130
4	31.736	1.468	0.04149	0.01873	0.00536
5	38.878	1.017	0.07731	0.04511	0.00675

Table 7.14: Dijet A_{LL}: full topology.

EastBarrel-Endcap

	Dijet Mass(GeV)		A_{LL}		
Bin	Mass	Sys. Error	A_{LL}	Stat. Error	Sys. Error
1	18.440	1.320	-0.01699	0.01041	0.00093
2	22.110	0.862	0.00584	0.00461	0.00148
3	26.575	1.006	0.00490	0.00382	0.00163
4	32.214	1.387	0.00168	0.00436	0.00122
5	38.351	1.132	-0.00791	0.00600	0.00170
6	48.012	1.288	0.00957	0.00831	0.00268
7	65.727	1.622	0.01291	0.02919	0.00646

WestBarrel-Endcap

	Dijet Mass(GeV)		A_{LL}		
Bin	Mass	Sys. Error	A_{LL}	Stat. Error	Sys. Error
1	18.511	1.127	-0.00341	0.00448	0.00117
2	21.782	1.060	0.01285	0.00354	0.00145
3	26.022	1.048	0.00261	0.00395	0.00068
4	30.793	1.193	0.00652	0.00557	0.00135
5	37.955	1.040	0.02111	0.00937	0.00168
6	46.427	1.166	0.01107	0.01608	0.00336
7	62.824	2.901	0.03171	0.08576	0.00610

Table 7.15: Dijet A_{LL}: Barrel-Endcap different topologies.

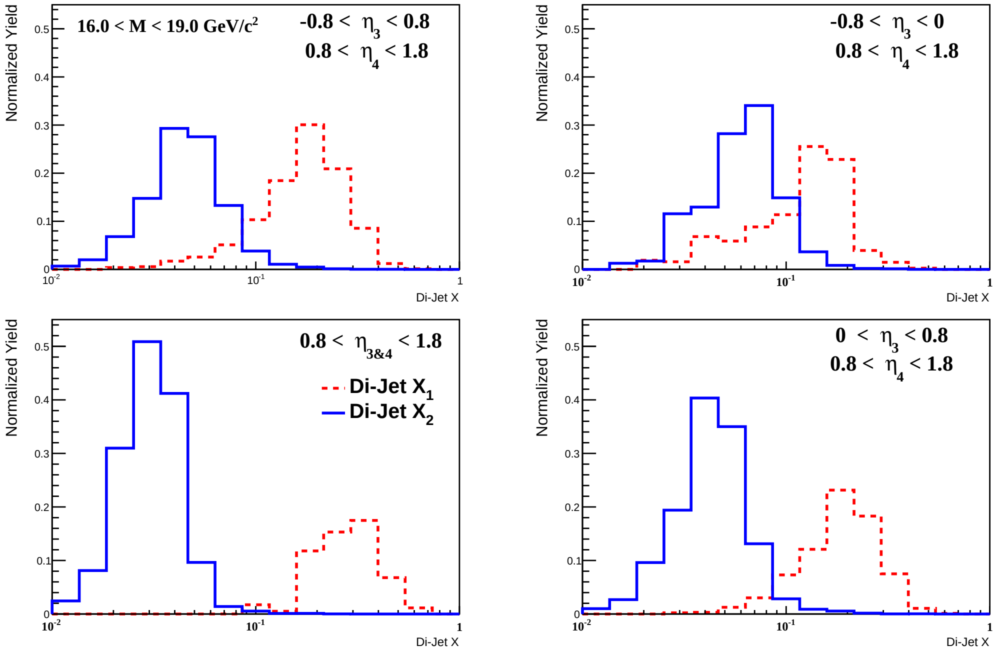

Figure 7.15: *pp* 200 GeV Dijet kinematics for Barrel-Endcap full topology (upper left), East Barrel-Endcap (upper right), West Barrel-Endcap (lower right) and Endcap-Endcap (lower left) for the lowest dijet invariant mass bin 16.0 – 19.0 GeV/c^2. x_1 is always associated with the parton moving initially toward the Endcap.

Values of A_{LL} extracted from the data represent an admixture of the asymmetries produced from the three dominant partonic scattering sub-processes: qq, qg, and gg. The STAR trigger is more efficient for certain sub-processes, altering the sub-process fractions in the data set and thereby shifting the measured A_{LL}. Further distortions can arise due to systematic shifts caused by the finite resolution of the detector coupled with a rapidly falling invariant mass distribution. Corrections were applied to the raw A_{LL} values to compensate for these effects, as discussed in detail in the previous chapter.

Tables 7.14 and 7.15 show the final values measured for A_{LL} in this work for Barrel-Endcap, East Barrel-Endcap, West Barrel-Endcap, and Endcap-Endcap dijet topologies. Total error estimates for both M and A_{LL} are also listed. Figs. 7.16, 7.17 and 7.18 show the forward dijet A_{LL} values as a function of dijet invariant mass, which has been corrected back to the parton level. The heights of the uncertainty boxes represent the total systematic error due to trigger and reconstruction bias, combined with the error due to residual transverse polarization components in the beams as well as the systematic errors from underlying events. The relative luminosity uncertainty results in a scaling uncertainty that is common to all points, and is represented by the gray band on the horizontal axis. The widths of the uncertainty boxes represent the systematic error associated with the corrected dijet mass values and, in addition to contributions from the uncertainty on the correction to the parton level, include the uncertainties on calorimeter tower gains and efficiencies, as well as TPC momentum resolution and tracking efficiencies. Further uncertainties were added in quadrature to account for the PYTHIA tune variations and underlying events contributions.

The dijet x_1 and x_2 kinematic distributions shown in Fig. 7.15 are matched with the four dijet double-spin asymmetry A_{LL} distributions in Fig. 7.16, 7.17 and 7.18. Compared to the kinematic distributions for the dijet measurement at Barrel-Barrel mid-rapidity shown in Fig. 1.13, it is clear that extending the measurement into the Endcap region probes lower x values, and results in a much cleaner separation between x_1 and x_2, especially for the Endcap-Endcap topology.

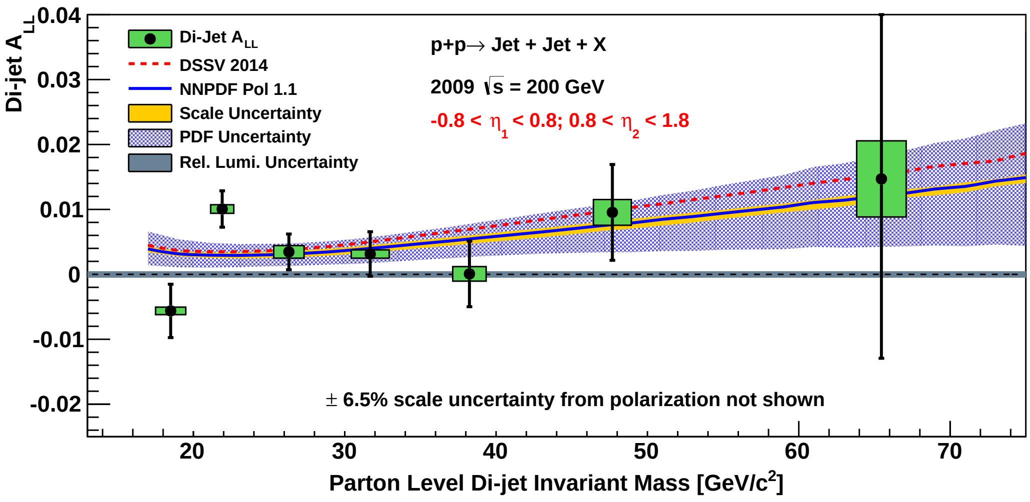

Figure 7.16: Dijet A_{LL} vs. parton-level invariant mass for Barrel-Endcap full topology.

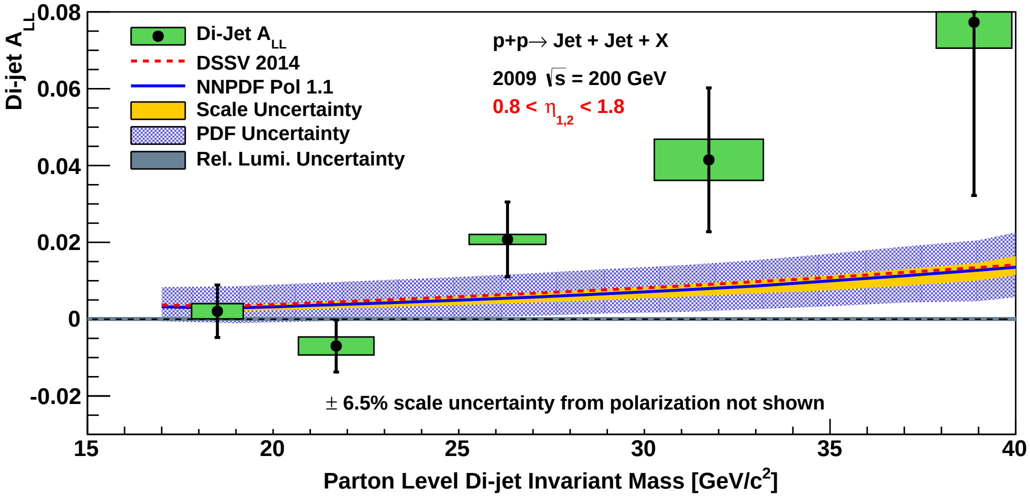

Figure 7.17: Dijet A_{LL} vs. parton-level invariant mass for Endcap-Endcap topology.

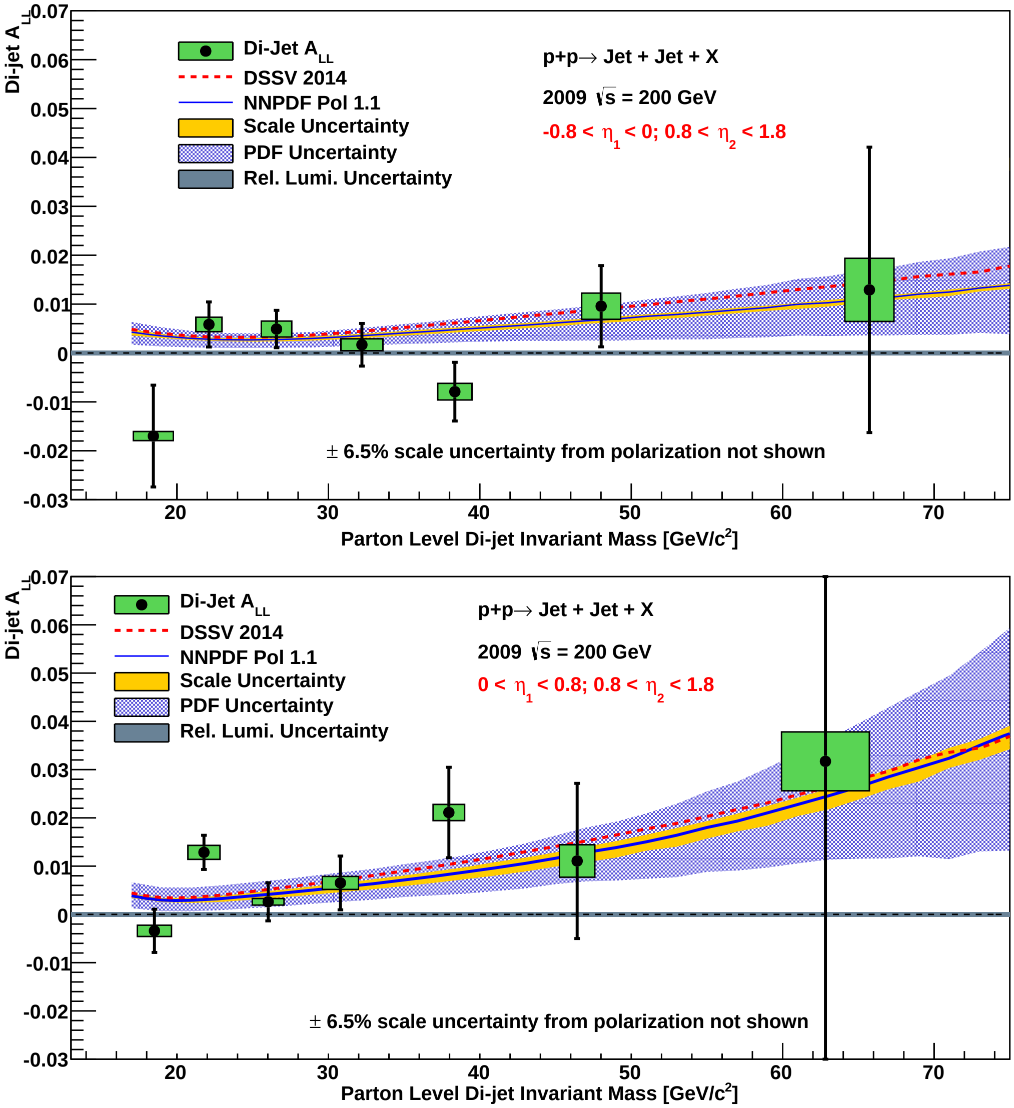

Figure 7.18: Dijet A_{LL} vs. parton-level invariant mass for East Barrel-Endcap (upper plot) and West Barrel-Endcap (lower plot).

7.8 Comparison to Theory

The asymmetry results extracted from data in this work are compared to two different theoretical predictions, both derived from global fits to previous polarized DIS and RHIC data. Theoretical A_{LL} values were obtained from the dijet production code of deFlorian *et al.* [83], using the DSSV2014 [35] and NNPDFpol1.1 [17] polarized PDF sets as input. The unpolarized PDF sets used in the denominator of the asymmetry were MRST2008 [84] and NNPDF2.3 [85], respectively. Uncertainty bands representing the sensitivity to factorization and renormalization scale (solid, yellow) and polarized PDF uncertainty (hatched, blue) were generated for the NNPDF results.

In order to get a quantitative comparison to the theoretical prediction, a χ^2 test between the data and theory was calculated based on the discussion in [86]. The expression for the χ^2 is:

$$\chi^2 = \sum_{i=1}^{N}(\frac{m_i - t_i - \beta_{1i}r_1 - \beta_{2i}r_2}{\sigma_i})^2 + r_1^2 + r_2^2, \tag{7.16}$$

where $\{m_i\}$ is a set of measurements from data (measured A_{LL}), t_i is the true value (theoretical A_{LL} value of the ith measured quantity) and σ_i is the uncorrelated error of the measurement (quadrature sum of the statistical and uncorrelated systematic errors on A_{LL}).

In this calculation, there are two correlated systematic errors. One is associated with the relative luminosity ($\beta_1 = 0.0005$ in this measurement) and the other is associated with the jet energy scale. The error associated with the jet energy scale is $\beta_2 = \frac{\partial A_{LL}}{\partial M} \times \delta M$; the differential factor is from a 3rd order polynomial fit of the theory curve (similar to what has been done when calculating the trigger and reconstruction bias), and δM is the systematic error on the dijet invariant mass. r_1 and r_2 are the corresponding free parameters associated with these two correlated errors. Optimizing the χ^2 relative to r_1 and r_2, the expression for the χ^2 is (a detailed derivation can be found in appendix B):

$$\chi^2 = \sum_{i=1}^{N}(\frac{m_i - t_i}{\sigma_i})^2 - (A^{-1})_{11}B_1^2 - (A^{-1})_{22}B_2^2 - 2(A^{-1})_{12}B_1B_2, \tag{7.17}$$

where B_j is a 2×1 matrix:

$$B = \begin{bmatrix} \sum_{i=1}^{N} \frac{\beta_{1i}(m_i - t_i)}{\sigma_i^2} \\ \sum_{i=1}^{N} \frac{\beta_{2i}(m_i - t_i)}{\sigma_i^2} \end{bmatrix}, \tag{7.18}$$

and $A_{jj'}$ is a 2×2 symmetric matrix:

$$A = \begin{bmatrix} 1 + \sum_{i=1}^{N} (\frac{\beta_{1i}}{\sigma_i})^2 & \sum_{i=1}^{N} (\frac{\beta_{1i} * \beta_{2i}}{\sigma_i^2}) \\ \sum_{i=1}^{N} (\frac{\beta_{1i} * \beta_{2i}}{\sigma_i^2}) & 1 + \sum_{i=1}^{N} (\frac{\beta_{2i}}{\sigma_i})^2 \end{bmatrix}. \tag{7.19}$$

Combining all the values described in previous sections, the values for χ^2, r_1 and r_2 at different dijet topologies and for these theory models can be calculated separately. The final results are shown in tables 7.16 and 7.17:

	DSSV			
	Barrel-Endcap	Endcap-Endcap	East Barrel-Endcap	West Barrel-Endcap
χ^2/NDF	2.09	1.58	1.65	1.64
χ^2	12.52	9.45	9.92	9.82
r_1	-0.10	0.01	-0.23	0.08
r_2	-0.08	0.06	-0.10	0.06

Table 7.16: χ^2 and r_1, r_2 for data/theory comparison for the DSSV model.

	NNPDF			
	Barrel-Endcap	Endcap-Endcap	East Barrel-Endcap	West Barrel-Endcap
χ^2/NDF	2.00	1.61	1.49	1.74
χ^2	11.97	9.64	8.95	10.42
r_1	0.11	0.02	-0.15	0.18
r_2	0.00	0.07	-0.04	0.10

Table 7.17: χ^2 and r_1, r_2 for data/theory comparison for the NNPDF model.

Overall, the data are seen to be in good agreement with current theoretical expectations. In all topologies, $\chi^2/NDF < 2.1$. This suggests that incorporating these results into global analyses may not change the value of $\Delta g(x)$ significantly, but should lead to reduced uncertainties on this quantity, especially at lower Bjorken-x.

CHAPTER 8

Conclusions and Outlook

The spin of the proton can be decompsed into contributions from the intrinsic quark spin, the orbital angular momentum, and the intrinsic gluon spin. From polarized deep inelastic scattering studies, we know that the quarks only contribute $\sim 30\%$ to the total spin of the proton. Measuring the polarization of the gluons inside the proton is a key observable to solve the 'spin crisis' problem, not only to understand proton structure in its own right, but also to serve as a tool for uncovering properties of the strong interaction in the non-perburbative regime. RHIC is the world's first and only accelerator capable of colliding polarized protons, and its kinematic regime is particularly sensitive to the gluon's interactions. Therefore polarized pp collisions at RHIC provide a unique opportunity to unravel the internal structure and the QCD dynamics of nucleons with unprecedented preciesion.

Previous data from RHIC have been added to the DSSV and NNPDF global analyses. Including the STAR 2009 inclusive jet A_{LL} results showed, for the first time, a nonzero gluon polarization in the region of sensitivity. However, at lower Bjorken x, the behavior and shape of the gluon helicity distribution is still poorly constrained. Compared to inclusive jet measurements, correlation measurements such as dijets capture more information from the hard scattering initial states, and may place better constrains on the functional form of the gluon helicity. Forward dijet measurements, which arise from asymmetric partonic collisions, extend the current dijet program at mid-rapidity and probe lower momentum gluons.

To carry out these forward jet measurements, however, presented several experimental challenges. Machine learning methods have been a hot topic in recent yerars, and there are many important problems in high energy physics that can only be solved using machine learning methods. These vary from online data filtering and reconstruction to offline data analysis. Applying machine learning methods to solve the problems of limited tracking efficiency in the Endcap Electromagetic Calorimeter (EEMC) resulted in a significant improvement in the measurements. The results looks reasonable and promising.

In summary, the first forward region dijet longitudinal double-spin asymmetries from STAR pp collisions at $\sqrt{s}$ = 200 GeV are reported. The measured dijet A_{LL} values in the forward region are presented for several different topologies based on the jet pesudorapidities. The A_{LL} results support the most recent DSSV and NNPDF predictions, which included the 2009 RHIC inclusive jet and pion data, and should help to reduce the uncertainties at the lower x regions in further global fits.

In 2015, STAR recorded 52 pb^{-1} of longitudinally polarized data at 200 GeV, which is about twice the statistics of 2009. Furthermore, in 2012 STAR recorded 82 pb^{-1} of longitudinally polarized data at $\sqrt{s}$ = 500 GeV and in 2013, 300 pb^{-1} were collected under similar beam conditions. As shown in Fig. 8.1, at the higher collision energy of 500 GeV, the interacting partons will have much lower momentum fractions. This, combined with the increased statistics, should lead to higher precision dijet A_{LL} measurements from STAR that will help to better constrain the value and shape of $\Delta g(x)$ at low Bjorken-x.

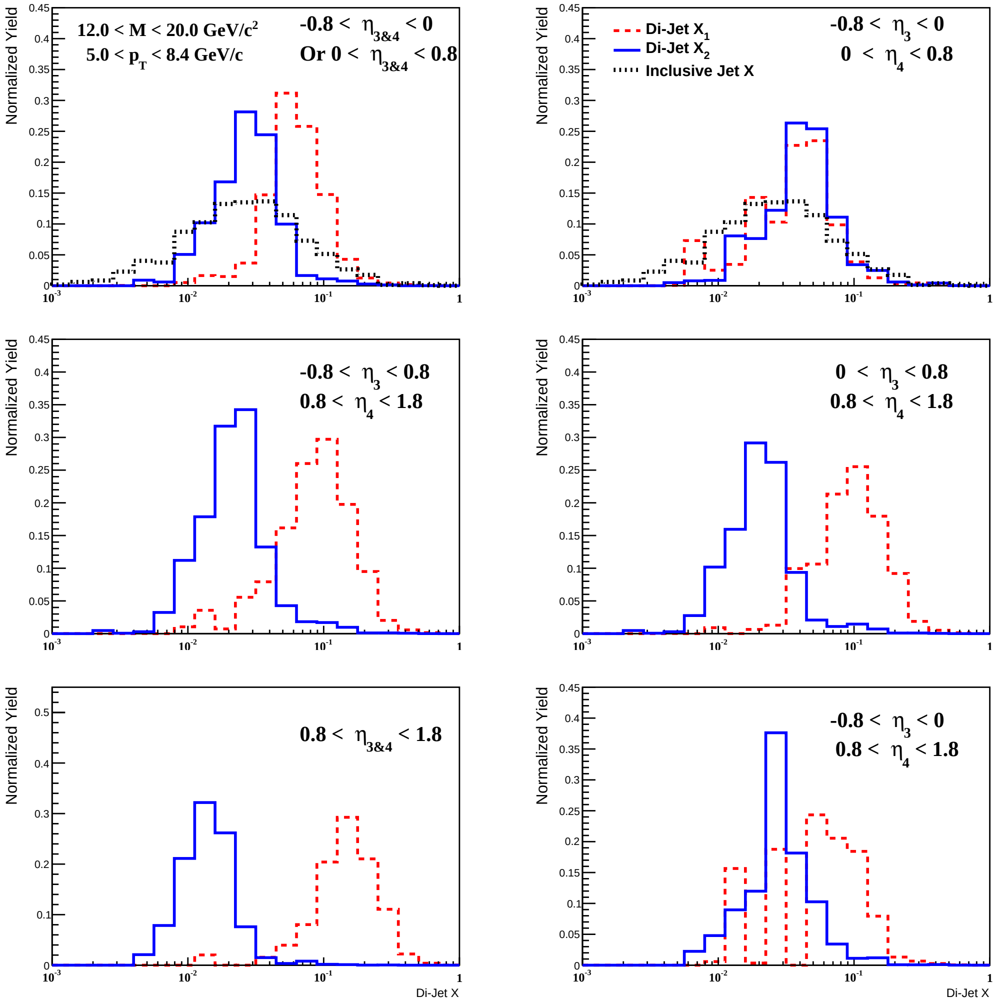

Figure 8.1: *pp* 500 GeV dijet kinematics for Barrel-Barrel same sign (upper left), Barrel-Barrel opposite sign (upper right) and inclusive jet (black line); Barrel-Endcap full topology (middle left), East Barrel-Endcap(middle right), West Barrel-Endcap (lower right) and Endcap-Endcap (lower left).

APPENDIX A

List of Runs and Fills Used in this Analysis

10120063 10120065 10120078 10120079 10120082 10120085 10120086 10120093 10120097 10120100 10121001 10121017 10121020 10121022 10121029 10121039 10121040 10121043 10121044 10122006 10122007 10122010 10122013 10122014 10122015 10122016 10122017 10122019 10122022 10122023 10122024 10122047 10122048 10122049 10122050 10122054 10122055 10122060 10122061 10122065 10122067 10122071 10122086 10122087 10122095 10122099 10123004 10123007 10123010 10123086 10123087 10123090 10124013 10124014 10124037 10124038 10124044 10124045 10124046 10124049 10124050 10124053 10124062 10124066 10124071 10124072 10124075 10124076 10124110 10124111 10124113 10125001 10125008 10125009 10125010 10125014 10125015 10125016 10125017 10125022 10125023 10125075 10125076 10125080 10125083 10125091 10126003 10126004 10126005 10126012 10126017 10126018 10126019 10126024 10126025 10126026 10126083 10126084 10126087 10126088 10126089 10126090 10127008 10127009 10127011 10128041 10128043 10128046 10128047 10128048 10128049 10128050 10128052 10128053 10128054 10128055 10128056 10128059 10128060 10128061 10128063 10128065 10128066 10128070 10128072 10128094 10128098 10128099 10128100 10128101 10128102 10129003 10129005 10129006 10129007 10129008 10129011 10129048 10129050 10130011 10130012 10130014 10130015 10131009 10131012 10131029 10131039 10131040 10131041 10131042 10131043 10131045 10131047 10131052 10131075 10131076 10134021 10134024 10134025 10134026 10134027 10134028 10134030 10134035 10134036 10134037 10134044 10134085 10134086 10134101 10134102 10134103 10135001 10135002 10135005 10135006 10135007 10135008 10135009 10135011

10135016 10135017 10135018 10135030 10135058 10135059 10135063 10135064 10135065
10135066 10135070 10135072 10135076 10135077 10135081 10135082 10135083 10136001
10136011 10136012 10136017 10136019 10136020 10136021 10136024 10136025 10136026
10136027 10136028 10136030 10136031 10136035 10136036 10136037 10136061 10136063
10136069 10136070 10136071 10136073 10136074 10136077 10136078 10136079 10136092
10136096 10136097 10136099 10136100 10137003 10137004 10137006 10137008 10137045
10137046 10137048 10137049 10137051 10137052 10137055 10137059 10137060 10137061
10137063 10137064 10137065 10137066 10137067 10138008 10138011 10138012 10138013
10138014 10138016 10138021 10138022 10138023 10138024 10138025 10138026 10138027
10138030 10138032 10138047 10138049 10138052 10138053 10138054 10138055 10138098
10138099 10138100 10139002 10139003 10139007 10139008 10139009 10139010 10139014
10139015 10139017 10139018 10139038 10139040 10139044 10139067 10139068 10139069
10139070 10139073 10139074 10139076 10139077 10139102 10139107 10140002 10140005
10140006 10140007 10140010 10140011 10141010 10141013 10141018 10141019 10141020
10141023 10141025 10141026 10141027 10141030 10141031 10141032 10142029 10142031
10142034 10142035 10142036 10142041 10142042 10142043 10142044 10142047 10142050
10142056 10142057 10142058 10142086 10142093 10142098 10143007 10143008 10143009
10143014 10143015 10143018 10143023 10143025 10143026 10143027 10143029 10143043
10143044 10143045 10143047 10143051 10143052 10143053 10143054 10143058 10143062
10143063 10143064 10143065 10143076 10143077 10143078 10143082 10143083 10143085
10143086 10143090 10143092 10143095 10143098 10143099 10143102 10143103 10143104
10143106 10144001 10144002 10144003 10144022 10144026 10144027 10144028 10144029
10144030 10144034 10144035 10144036 10144037 10144044 10144045 10144046 10144072
10144074 10144075 10144076 10144083 10144085 10144087 10144090 10144091 10144092
10144093 10144098 10145011 10145012 10145013 10145016 10145018 10145027 10145030
10145032 10145034 10145036 10145038 10145042 10145046 10145047 10145070 10145072
10145073 10145076 10145078 10145079 10145081 10145082 10146040 10146047 10146048

10146049 10146050 10146051 10146052 10146054 10146055 10146073 10146084 10146086
10146087 10146091 10148002 10148005 10148006 10148021 10148025 10148026 10148027
10148028 10148033 10148034 10148035 10149008 10149012 10149023 10149024 10149025
10149026 10149028 10149031 10149032 10149033 10149034 10149035 10149087 10150001
10150005 10150008 10150009 10150010 10150011 10150012 10150013 10150018 10150021
10150022 10150024 10150025 10150052 10150053 10150056 10150057 10151001 10151002
10151003 10151004 10151005 10151006 10151034 10151035 10151039 10151040 10151041
10151042 10151043 10151044 10151045 10151046 10151047 10152001 10152004 10152005
10152006 10152007 10152008 10152009 10152010 10154060 10154061 10154064 10154065
10154066 10154067 10154068 10154083 10155001 10155010 10155014 10155015 10155016
10155019 10155020 10155022 10155095 10155097 10156004 10156007 10156008 10156009
10156011 10156013 10156031 10156034 10156037 10156038 10156039 10156040 10156058
10156086 10156087 10156090 10156092 10156093 10156095 10156096 10157001 10157004
10157005 10157015 10157016 10157019 10157020 10157021 10157022 10157023 10157027
10157051 10157052 10157056 10157057 10157058 10158001 10158004 10158010 10158013
10158014 10158015 10158016 10158017 10158018 10158021 10158042 10158043 10158047
10158048 10158049 10158050 10158051 10158054 10158055 10158074 10158075 10158076
10158079 10158080 10158082 10158083 10158086 10158087 10158089 10158090 10159006
10159039 10159040 10159044 10159045 10159046 10159048 10159049 10160005 10160006
10160009 10160010 10160011 10160012 10160013 10160014 10160016 10160017 10160071
10160072 10160075 10160077 10160078 10160079 10160081 10160084 10161005 10161006
10161010 10161011 10161014 10161015 10161016 10161019 10161020 10161021 10161025
10161026 10161027 10161030 10162006 10162007 10162010 10162024 10162025 10162029
10162030 10162031 10162032 10162033 10162034 10162035 10162036 10162037 10162038
10162040 10163048 10163051 10163052 10163053 10163054 10163055 10163056 10163059
10164002 10164009 10164010 10164011 10164013 10164016 10164017 10164018 10164025
10164026 10164029 10164030 10164031 10164034 10164057 10164060 10164061 10164062

10164067 10164078 10164079 10164082 10165007 10165008 10165015 10165016 10165017
10165018 10165019 10165022 10165023 10165024 10165027 10166061 10166067 10167007
10167008 10167009 10167012 10167013 10167014 10167015 10167016 10167017 10167020
10167048 10167049 10167050 10167053 10167054 10167056 10167057 10167058 10167059
10169005 10169006 10169009 10169010 10169012 10169013 10169014 10169021 10169030
10169031 10169032 10169033 10169041 10169042 10169043 10169044 10169047 10169048
10169049 10169065 10169070 10169074 10169075 10169076 10169077 10169078 10169080
10170003 10170011 10170012 10170013 10170016 10170017 10170018 10170019 10170023
10170024 10170025 10170026 10170029 10170045 10170046 10170047 10170050 10170052
10170053 10170054 10170060 10170061 10170064 10170065 10170075 10170078 10170081
10170089 10171011 10171014 10171015 10171016 10171019 10171021 10171022 10171025
10171034 10171036 10171037 10171041 10171042 10171043 10171044 10171045 10171048
10171060 10171061 10171069 10171070 10171071 10171078 10172001 10172002 10172003
10172007 10172060 10172061 10172064 10172077 10172079 10172082 10172083 10172085
10172089 10172090 10172094 10173007 10173008 10173009 10173012 10173013 10173015
10173016 10173017 10173031 10173032 10173033 10173039 10173048 10173051 10173053
10173055 10174012 10174013 10174016 10174023 10174025 10174026 10174027 10174028
10174031 10174044 10174045 10174048 10174049 10174050 10174051 10174052 10174094
10175005 10175008 10175009 10175010 10175011 10175012 10175013 10175014 10175019
10175038 10176001 10176008 10176016 10176017 10176018 10176020 10176022 10176025
10176028 10177055 10177056 10177057 10177060 10177061 10178022 10178023 10178026
10178029 10178036 10179005 10179006 10179007 10179008 10179009 10179010 10179018
10179019 10179022 10179031 10179032 10179033 10179042 10179043 10179044 10179045
10179085 10179086 10179088 10179096 10179097 10179098 10180003 10180004 10180007
10180021 10180022 10180027 10180028 10180029 10180030

List of Fills:

10682 10704 10756 10786 10855 10889 10953 10971 10683 10706 10758 10789 10866 10890

10954 10973 10684 10708 10761 10790 10869 10904 10955 10986 10685 10712 10763 10791 10870 10919 10959 10987 10688 10713 10773 10800 10875 10920 10960 11001 10689 10729 10777 10806 10876 10921 10961 11002 10690 10746 10781 10814 10877 10932 10963 11003 10695 10748 10782 10820 10878 10935 10964 11005 10696 10753 10783 10825 10880 10937 10967 11006 10700 10754 10784 10826 10881 10951 10968 10703 10755 10785 10854 10884 10952 10970 10717 10730 10764 10813 10924 10957 10720 10749 10765 10864 10925 10998 10727 10759 10778 10902 10956

APPENDIX B

Some Derivations

B.1 Di-jet Kinematics Derivation

B.1.1 Di-jet Invariant Mass

We start with the 4-momentum vector:

$$P = \begin{bmatrix} E \\ p_x \\ p_y \\ p_z \end{bmatrix}, \tag{B.1}$$

If we define $y = \frac{1}{2}\ln\left(\frac{E+p_z}{E-p_z}\right)$ (pseudorapidity), and $p_T = \sqrt{p_x^2 + p_y^2}$ with ϕ as the relative angle, then $p_x = p_T \cos\phi$ and $p_y = p_T \sin\phi$. We see that:

$$y = \frac{1}{2}\ln\left(\frac{E+p_z}{E-p_z}\right) = \ln\left(\sqrt{\frac{E+p_z}{E-p_z}}\right) = \ln\left(\frac{E+p_z}{\sqrt{E^2-p_z^2}}\right) = \ln\left(\frac{E+p_z}{m_T^2}\right) \tag{B.2a}$$

$$-y = -\frac{1}{2}\ln\left(\frac{E+p_z}{E-p_z}\right) = \ln\left(\sqrt{\frac{E-p_z}{E+p_z}}\right) = \ln\left(\frac{E-p_z}{\sqrt{E^2-p_z^2}}\right) = \ln\left(\frac{E-p_z}{m_T^2}\right), \tag{B.2b}$$

where $m_T = \sqrt{m^2 + p_x^2 + p_y^2}$ is the transverse mass. Then the energy and z component of momentum can be written as: $E = m_T \cosh y$ and $p_z = m_T \sinh y$.

The di-jet invariant mass is $M = \sqrt{(P_3 + P_4)^2}$, where P_3 and P_4 are the 4-momenta of two outgoing partons. We can express the individual 4-momenta as:

$$P_3 = \begin{bmatrix} m_T \cosh y_3 \\ p_T \cos \phi_3 \\ p_{T,3} \sin \phi_3 \\ m_{T,3} \sinh y_3 \end{bmatrix}, P_4 = \begin{bmatrix} m_T \cosh y_4 \\ p_T \cos \phi_4 \\ p_{T,4} \sin \phi_4 \\ m_{T,4} \sinh y_4 \end{bmatrix} \tag{B.3}$$

$$M = \sqrt{(P_3^2 + P_4^2 + 2P_3 * P_4)^2}, \tag{B.4}$$

where $P^2 = m^2$, and the cross term is:

$$\begin{aligned} P_3 * P_4 &= m_{T,3} m_{T,4} (\cosh y_3 \cosh y_4 - \sinh y_3 \sinh y_4) - p_{T,3} p_{T,4} (\cos \phi_3 \cos \phi_4 + \sin \phi_3 \sin \phi_4) \\ &= \sqrt{m_3^2 + p_{T3}^2} \sqrt{m_4^2 + p_{T4}^2} cosh(y_3 - y_4) - 2 p_{T3} p_{T4} cos(\phi_3 - \phi_4). \end{aligned} \tag{B.5}$$

Then the di-jet invariant mass is:

$$M = \sqrt{m_3^2 + m_4^2 + 2\sqrt{m_3^2 + p_{T3}^2} \sqrt{m_4^2 + p_{T4}^2} cosh(y_3 - y_4) - 2 p_{T3} p_{T4} cos(\phi_3 - \phi_4)}. \tag{B.6}$$

B.1.2 Scattering Kinematic Approximations

For simplicity, we assume that partons are massless and only move in the z-direction. Then the initial 4-momenta can be written as:

$$P_1 = \frac{\sqrt{s}}{2} \begin{bmatrix} x_1 \\ 0 \\ 0 \\ x_1 \end{bmatrix}, \qquad P_2 = \frac{\sqrt{s}}{2} \begin{bmatrix} x_2 \\ 0 \\ 0 \\ x_2 \end{bmatrix}. \tag{B.7}$$

Define the initial state 4-momentum as $q = P_1 + P_2$, the invariant M would be:

$$M = \sqrt{q^2} = \sqrt{s x_1 x_2}. \tag{B.8}$$

The pesudorapidity can be defined using the momentum fractions:

$$\cosh y = \frac{E}{\sqrt{E^2 - p_z^2}} = \frac{1}{2}\frac{x_1 + x_2}{\sqrt{x_1 x_2}} \tag{B.9a}$$

$$\sinh y = \frac{p_z}{\sqrt{E^2 - p_z^2}} = \frac{1}{2}\frac{x_1 - x_2}{\sqrt{x_1 x_2}}. \tag{B.9b}$$

Then the pesudorapidity of the momentum q is:

$$y = \frac{1}{2}\ln\left(\frac{E - p_z}{E + p_z}\right) = \frac{1}{2}\ln\left(\frac{x_1}{x_2}\right). \tag{B.10}$$

The Lorentz transformation is given by:

$$\Lambda(y) = \begin{bmatrix} \cosh y & 0 & 0 \sinh y & \\ 0 & 1 & 0 & 0 \\ 0 & 0 & 1 & 0 \\ \sinh y & 0 & 0 \cosh y & \end{bmatrix} = \frac{1}{2\sqrt{x_1 x_2}} \begin{bmatrix} x_1 + x_2 & 0 & 0 & x_1 - x_2 \\ 0 & 1 & 0 & 0 \\ 0 & 0 & 1 & 0 \\ x_1 - x_2 & 0 & 0 & x_1 + x_2 \end{bmatrix}. \tag{B.11}$$

In the center of mass frame, the outgoing partons can be written as:

$$P_3^* = p_T \begin{bmatrix} \cosh y^* \\ \cos\phi \\ \sin\phi \\ \sinh y^* \end{bmatrix}, \quad P_4^* = p_T \begin{bmatrix} \cosh y^* \\ -\cos\phi \\ -\sin\phi \\ -\sinh y^* \end{bmatrix}. \tag{B.12}$$

In the lab frame, using the Lorentz Transformation, we get:

$$
\begin{aligned}
P_3 = \Lambda(y)P_3^* = p_T \begin{bmatrix} \cosh y & 0 & 0 & \sinh y \\ 0 & 1 & 0 & 0 \\ 0 & 0 & 1 & 0 \\ \sinh y & 0 & 0 & \cosh y \end{bmatrix} \begin{bmatrix} \cosh y^* \\ \cos\phi \\ \sin\phi \\ \sinh y^* \end{bmatrix} &= p_T \begin{bmatrix} \cosh(y+y^*) \\ \cos\phi \\ \sin\phi \\ \sinh(y+y^*) \end{bmatrix} \\
P_4 = \Lambda(y)P_4^* = p_T \begin{bmatrix} \cosh y & 0 & 0 & \sinh y \\ 0 & 1 & 0 & 0 \\ 0 & 0 & 1 & 0 \\ \sinh y & 0 & 0 & \cosh y \end{bmatrix} \begin{bmatrix} \cosh y^* \\ -\cos\phi \\ -\sin\phi \\ -\sinh y^* \end{bmatrix} &= p_T \begin{bmatrix} \cosh(y-y^*) \\ -\cos\phi \\ -\sin\phi \\ \sinh(y-y^*) \end{bmatrix}
\end{aligned}. \tag{B.13}
$$

In the lab frame, we can define the outgoing partons as:

$$
P_3 = p_T \begin{bmatrix} \cosh y_3 \\ \cos\phi_3 \\ \sin\phi_3 \\ \sinh y_3 \end{bmatrix}, \quad P_4 = p_T \begin{bmatrix} \cosh y_4 \\ \cos\phi_4 \\ \sin\phi_4 \\ \sinh y_4 \end{bmatrix}. \tag{B.14}
$$

Then $y_3 = y + y^*$ and $y_4 = y - y^*$, where $y = \frac{y_3+y_4}{2}$ and $y^* = \frac{y_3-y_4}{2}$. The invariant mass is $M = 2p_T \cosh y^*$ using the center-of-mass frame $P_3^* + P_4^*$. Using equation B.10, we can rewrite the expression:

$$
\begin{aligned}
x_1 &= \sqrt{x_1 x_2} e^y = \frac{M}{\sqrt{s}} e^y = \frac{p_T}{\sqrt{s}} 2\cosh y^* e^y = \frac{p_T}{\sqrt{s}} (e^{y_3} + e^{y_4}) \\
x_2 &= \sqrt{x_1 x_2} e^{-y} = \frac{p_T}{\sqrt{s}} (e^{-y_3} + e^{-y_4}).
\end{aligned} \tag{B.15}
$$

The center-of-mass frame scattering angle can be expressed in terms of the pseudorapidity:

$$
\cos\theta^* = \frac{\sinh y^*}{\sqrt{\cos^2\phi + \sin^2\phi + \sinh^2 y^*}} = \tanh y^* = \tanh\left(\frac{y_3 - y_4}{2}\right). \tag{B.16}
$$

B.2 A_{LL} Derivation

In this section, details of the derivation of expressions for A_{LL} and δA_{LL} will be shown. This calculation is based on Brian Page's thesis.

B.2.1 Double Spin Asymmetry, A_{LL}

The final A_{LL} values are the combination of different measurements from each run. For a single fill, A_{LL} can be expressed as:

$$A_{LL} = \frac{1}{P_B P_Y} \frac{(N^{++} + N^{--}) - R(N^{+-} + N^{-+})}{(N^{++} + N^{--}) + R(N^{+-} + N^{-+})}, \tag{B.17}$$

where P_B and P_Y are the polarizations of the beams, and R is the relative luminosity, while the N^{++} and N^{+-} are the spin-sorted yields. To simply the calculation, we can use the single-spin asymmetry with fewer terms:

$$A_i = \frac{1}{P_i} \frac{N_i^+ - R_i N_i^-}{N_i^+ + R_i N^-}. \tag{B.18}$$

The associated uncertainty for A_i can then be expressed as:

$$\begin{aligned}\sigma_i^2 &= (\frac{\partial A_i}{\partial N_i^+}\sigma_{N_i^+})^2 + (\frac{\partial A_i}{\partial N_i^-}\sigma_{N_i^-})^2 + (\frac{\partial A_i}{\partial P_i}\sigma_{P_i})^2 + (\frac{\partial A_i}{\partial R_i}\sigma_{R_i})^2 \\ &= \frac{1}{P_i^2(N_i^+ + R_i N^-)^2}[(1 - P_i A_i)^2\sigma_{N_i^+}^2 + (1 + P_i A_i)^2 R_i^2 \sigma_{N_i^-}^2 + (1 + P_i A_i)^2 (N^-)^2 \sigma_{R_i}^2] + \frac{A_i^2}{P_i^2}\sigma_{P_i}^2.\end{aligned} \tag{B.19}$$

To get the best value of the asymmetry ($\bar{A}$), the maximum likelihood method is used to minimize the function:

$$\chi^2 = \sum_{i=1}^{N} (\frac{A_i - \bar{A}}{\sigma_i})^2. \tag{B.20}$$

Then we can get:

$$\begin{aligned} 2\chi\frac{\partial\chi}{\partial x_i} &= \sum_{i=1}^{N}2(\frac{A_i-\bar{A}}{\sigma_i})(\frac{1}{\sigma_i}) = 0 \\ \sum_{i=1}^{N}\frac{A_i}{\sigma_i^2} &= \sum_{i=1}^{N}\frac{\bar{A}}{\sigma_i^2} \\ \bar{A} &= \frac{\sum_i^N(A_i/\sigma_i^2)}{\sum_i^N(1/\sigma_i^2)}. \end{aligned} \tag{B.21}$$

To get the final expression, we need to calculate and simplify the σ_i. The scale uncertainty from polarization is about 6.5%, $A_i \sim 10^{-2}$, $P_i \sim 50\%$, $(\sigma_{N_i})^2 = N$, $R_i \sim 1$ and $\sigma_{R_i} \sim 0$. With these assumptions, we can ignore the last two terms, and the uncertainty can be approximated as:

$$\sigma_i^2 \approx \frac{1}{P_i^2(N_i^+ + R_iN^-)}. \tag{B.22}$$

Then the $\bar{A}$ is:

$$\bar{A} = \frac{\sum_{i=1}^N P_i(N_i^+ - R_iN^-)}{\sum_{i=1}^N P_i^2(N_i^+ + R_iN^-)}. \tag{B.23}$$

Replacing the polarization and spin state yields, the final double spin asymmetry A_{LL} can be expressed as:

$$A_{LL} = \frac{\sum_{i=1}^N P_{B,i}P_{Y,i}[(N_i^{++} + N_i^{--}) - R_{3,i}(N_i^{+-} + N_i^{-+})]}{\sum_{i=1}^N P_{B,i}^2P_{Y,i}^2[(N_i^{++} + N_i^{--}) + R_{3,i}(N_i^{+-} + N_i^{-+})]}. \tag{B.24}$$

B.2.2 A_{LL} Uncertainty

Similar to what has been calculated before, the uncertainty in $\bar{A}$ can be expressed as:

$$\sigma_{\bar{A}}^2 = \sum_{i=1}^{N}[(\frac{\partial\bar{A}}{\partial N_i^+}\sigma_{N_i^+})^2 + (\frac{\partial\bar{A}}{\partial N_i^-}\sigma_{N_i^-})^2 + (\frac{\partial\bar{A}}{\partial P_i}\sigma_{P_i})^2 + (\frac{\partial\bar{A}}{\partial R_i}\sigma_{R_i})^2]. \tag{B.25}$$

We still ignore the last two terms here, and the differential can be written as:

$$\frac{\partial\bar{A}}{\partial N_j^+} = \frac{P_j}{\sum_{i=1}^N P_i^2(N_i^+ + R_iN^-)}(1 - P_j\bar{A}) \tag{B.26}$$

$$\frac{\partial \bar{A}}{\partial N_j^-} = \frac{-P_j R_j}{\sum_{i=1}^N P_i^2 (N_i^- + R_i N^-)} (1 + P_j \bar{A}). \tag{B.27}$$

Then the uncertainty is:

$$\sigma_{\bar{A}}^2 = \frac{\sum_{i=1}^N P_i^2 [(1 - P_i \bar{A})^2 N_i^+ + (1 + P_i \bar{A})^2 R_i^2 N_i^-]}{(\sum_{i=1}^N P_i^2 (N_i^+ + R_i N^-))^2} \tag{B.28}$$

. $\bar{A} \sim 10^{-2}$ is small and can be neglected in the expression. Then the final expression is:

$$\sigma_{\bar{A}}^2 = \frac{\sum_{i=1}^N P_i^2 (N_i^+ + R_i^2 N_i^-)}{[\sum_{i=1}^N P_i^2 (N_i^+ + R_i N^-)]^2}. \tag{B.29}$$

Placing the proper beam polarization, relative luminosity, and yield factors into the equation, then the statistical uncertainty of A_{LL} is:

$$\delta A_{LL} = \frac{\sqrt{\sum_{i=1}^N P_{B,i}^2 P_{Y,i}^2 [(N_i^{++} + N_i^{--}) + R_{3,i}^2 (N_i^{+-} + N_i^{-+})]}}{\sum_{i=1}^N P_{B,i}^2 P_{Y,i}^2 [(N_i^{++} + N_i^{--}) + R_{3,i} (N_i^{+-} + N_i^{-+})]}. \tag{B.30}$$

The statistical error is approximately equal to $\delta A_{LL} \approx \frac{1}{P_B P_Y} \frac{1}{\sqrt{N}}$, where $P_{Y,B}$ are the average beam polarizations for blue and yellow beams, and N is the total yield, summed over all spin states.

B.3 χ^2 Derivation

In this section I will show the derivation of the χ^2 analysis. The calculation is based on [86] appendix B. The purpose of this calculation is to derive the appropriate expression of the χ^2 for data with correlated systematic errors. The defining condition is that χ^2 should obey a chi-squared distribution, and it is:

$$\chi^2 = \sum_{i=1}^{N} (\frac{m_i - t_i - \sum_j \beta_{ji} r_j}{\sigma_i})^2 + \sum_{j=1}^{K} r_j^2, \tag{B.31}$$

where $\{m_i\}$ is a set of measurements, and $i = 1, 2, 3, ..., N$. t_i is the true value (theoretical value of the ith measured quantity). σ_i is the uncorrelated error of measurement. And there are K correlated errors denoted as $\beta_{1i}, \beta_{2i}, ..., \beta_{Ki}$.

χ^2 is a function of $r_1, ..., r_K$, and these variables could be used as fitting parameters to account for the systematic errors: minimizing χ^2 with respect to r_j can provide the best model to correct for the systematic error.

We can rewrite the expression to be:

$$\chi^2 = \sum_{i=1}^{N}(\frac{m_i - t_i}{\sigma_i})^2 - \sum_{j=1}^{K} 2B_j r_j + \sum_{j,j'=1}^{K} A_{jj'} r_j r_{j'}, \tag{B.32}$$

where B_j is a vector with K components or ($K \times 1$ matrix),

$$B \rightarrow B_j = \sum_{i=1}^{N} \beta_{ji}(m_i - t_i)/\sigma_i^2, \tag{B.33}$$

and $A_{jj'}$ is a $K \times K$ symmetric matrix, is:

$$A \rightarrow A_{jj'} = \delta_{jj'} + \sum_{i=1}^{N} \beta_{ji}\beta_{j'i}/\sigma_i^2. \tag{B.34}$$

If we define the free parameters r_j as a $K \times 1$ matrix, then to minimize the χ^2 we get:

$$\begin{aligned} 2\chi\frac{\partial\chi}{\partial r_{j'}} &= -2B_{j'} + 2\sum_{j=1}^{K} A_{jj'} r_j = 0 \\ \sum_{j=1}^{K} A_{jj'} r_j &= B_{j'} \\ Ar &= B \\ r &= A^{-1}B. \end{aligned} \tag{B.35}$$

Then the final expression of the χ^2 is:

$$
\begin{aligned}
\chi^2 &= \sum_{i=1}^{N}(\frac{m_i - t_i}{\sigma_i})^2 - 2B^T r + r^T A r \\
&= \sum_{i=1}^{N}(\frac{m_i - t_i}{\sigma_i})^2 - 2B^T A^{-1} B + (A^{-1}B)^T A A^{-1} B \\
&= \sum_{i=1}^{N}(\frac{m_i - t_i}{\sigma_i})^2 - B^T A^{-1} B \\
&= \sum_{i=1}^{N}(\frac{m_i - t_i}{\sigma_i})^2 - \sum_{j}^{K}\sum_{j'}^{K} B_j (A^{-1})_{jj'} B_{j'} .
\end{aligned}
\tag{B.36}
$$

APPENDIX C

Code Structure and Parameters

C.1 EEMC Gains Into the Simulation

For the 2009 pp 200 GeV data, the EEMC calibration was done much later than the embedding production, which means the EEMC trigger information may not be very precise in the simulation. A significant amount of computing time is needed to fully simulate the STAR detector response to a Pythia event, so an afterburner method was needed for the measurements in the EEMC region.

In order to implement the method, we need to figure out the program flow of the simulation. Simulation starts from the Pythia events (physics), which then go into Geant. The simulated energies are multiplied by the EMC tower gain factors from the database to get the corresponding ADC values, and then converted to the same format as the data. The ADC values are used in the trigger simulator for the trigger category determination.

The idea is to recalculate the skim trees, which store all the trigger informations from the jet finder. The method is simple: change the tower adc to a new value by $Adc_{new} = Adc_{old} \times \frac{Gain_{new}}{Gain_{old}} + pedestal$ before the event goes into the trigger simulator. The key simulators for EEMC are the L2Emulator and EemcTriggerSimu. As shown in chapter 2, the data and simulation agreement is better after we implemented the new EEMC gains.

C.2 TMVA Parameters

The parameter settings for Multilayer Perceptron are:

- BookMethod(TMVA::Types::kMLP, “MLP", “!H:!V:VarTransform=Norm:NeuronType=tanh:

NCycles=10000:HiddenLayers=N+100:EstimatorType=MSE:TestRate=10: LearningRate=0.02: NeuronInputType=sum:DecayRate=0.6:TrainingMethod=BFGS: Sampling=0.1:SamplingEpoch=0.8: ConvergenceImprove=1e-6: ConvergenceTests=15:!UseRegulator");

The parameter settings for Linear Discriminant (LD) are:

- BookMethod(TMVA::Types::kLD, “LD",“!H:!V:VarTransform=None");

The parameter settings for K-Nearest Neighbour (KNN) are:

- BookMethod(TMVA::Types::kKNN, “KNN",“nkNN=20:ScaleFrac=0.8:SigmaFact=1.0: Kernel=Gaus:UseKernel=F:UseWeight=T:!Trim");

Bibliography

[1] M. Gell-Mann. A schematic model of baryons and mesons. *Physics Letters*, 8(3):214 – 215, 1964.

[2] G Zweig. An SU_3 model for strong interaction symmetry and its breaking; Version 1. Technical Report CERN-TH-401, CERN, Geneva, Jan 1964.

[3] G Zweig. An SU_3 model for strong interaction symmetry and its breaking; Version 2. (CERN-TH-412):80 p, Feb 1964.

[4] M. Breidenbach, J. I. Friedman, H. W. Kendall, E. D. Bloom, D. H. Coward, H. DeStaebler, J. Drees, L. W. Mo, and R. E. Taylor. Observed behavior of highly inelastic electron-proton scattering. *Phys. Rev. Lett.*, 23:935–939, Oct 1969.

[5] E. D. Bloom, D. H. Coward, H. DeStaebler, J. Drees, G. Miller, L. W. Mo, R. E. Taylor, M. Breidenbach, J. I. Friedman, G. C. Hartmann, and H. W. Kendall. High-energy inelastic $e - p$ scattering at $6° and 10°$. *Phys. Rev. Lett.*, 23:930–934, Oct 1969.

[6] David J. Gross and Frank Wilczek. Ultraviolet behavior of non-abelian gauge theories. *Phys. Rev. Lett.*, 30:1343–1346, Jun 1973.

[7] H. David Politzer. Reliable perturbative results for strong interactions? *Phys. Rev. Lett.*, 30:1346–1349, Jun 1973.

[8] Matthew D. Schwartz. *QUANTUM FIELD THEORY and the STANDARD MODEL*. Cambridge University Press, 2014.

[9] Jerome I. Friedman. Deep inelastic scattering: Comparisons with the quark model. *Rev. Mod. Phys.*, 63:615–627, Jul 1991.

[10] Henry W. Kendall. Deep inelastic scattering: Experiments on the proton and the observation of scaling. *Rev. Mod. Phys.*, 63:597–614, Jul 1991.

[11] Richard E. Taylor. Deep inelastic scattering: The early years. *Rev. Mod. Phys.*, 63:573–595, Jul 1991.

[12] C. Patrignani et al. Review of Particle Physics. *Chin. Phys.*, C40(10):100001, 2016.

[13] Yuri L. Dokshitzer. Calculation of the Structure Functions for Deep Inelastic Scattering and e+ e- Annihilation by Perturbation Theory in Quantum Chromodynamics. *Sov. Phys. JETP*, 46:641–653, 1977. [Zh. Eksp. Teor. Fiz.73,1216(1977)].

[14] V. N. Gribov and L. N. Lipatov. Deep inelastic e p scattering in perturbation theory. *Sov. J. Nucl. Phys.*, 15:438–450, 1972. [Yad. Fiz.15,781(1972)].

[15] Guido Altarelli and G. Parisi. Asymptotic Freedom in Parton Language. *Nucl. Phys.*, B126:298–318, 1977.

[16] Richard D. Ball et al. Parton distributions for the LHC Run II. *JHEP*, 04:040, 2015.

[17] Emanuele R. Nocera, Richard D. Ball, Stefano Forte, Giovanni Ridolfi, and Juan Rojo. A first unbiased global determination of polarized pdfs and their uncertainties. *Nuclear Physics B*, 887:276 – 308, 2014.

[18] M. Anselmino, A. Efremov, and E. Leader. The Theory and phenomenology of polarized deep inelastic scattering. *Phys. Rept.*, 261:1–124, 1995. [Erratum: Phys. Rept.281,399(1997)].

[19] Christine A. Aidala, Steven D. Bass, Delia Hasch, and Gerhard K. Mallot. The Spin Structure of the Nucleon. *Rev. Mod. Phys.*, 85:655–691, 2013.

[20] Steven D. Bass. The Spin structure of the proton. *Rev. Mod. Phys.*, 77:1257–1302, 2005.

[21] Steven D. Bass. The Proton spin puzzle: Where are we today? *Mod. Phys. Lett.*, A24:1087–1101, 2009.

[22] S. E. Kuhn, J. P. Chen, and E. Leader. Spin Structure of the Nucleon - Status and Recent Results. *Prog. Part. Nucl. Phys.*, 63:1–50, 2009.

[23] R. Windmolders. An Introduction to the evaluation of spin structure functions from experimental data. In *10th Rhodanien Seminar: The Spin in Physics Turin, Italy, March 3-8, 2002*, 2002.

[24] J. Ashman et al. An Investigation of the Spin Structure of the Proton in Deep Inelastic Scattering of Polarized Muons on Polarized Protons. *Nucl. Phys.*, B328:1, 1989.

[25] J. D. Bjorken. Inelastic scattering of polarized leptons from polarized nucleons. *Phys. Rev. D*, 1:1376–1379, Mar 1970.

[26] John Ellis and Robert Jaffe. Sum rule for deep-inelastic electroproduction from polarized protons. *Phys. Rev. D*, 9:1444–1446, Mar 1974.

[27] V. Yu. Alexakhin et al. The Deuteron Spin-dependent Structure Function g1(d) and its First Moment. *Phys. Lett.*, B647:8–17, 2007.

[28] R.L. Jaffe and Aneesh Manohar. The g1 problem: Deep inelastic electron scattering and the spin of the proton. *Nuclear Physics B*, 337(3):509 – 546, 1990.

[29] Xiangdong Ji, Xiaonu Xiong, and Feng Yuan. Probing parton orbital angular momentum in longitudinally polarized nucleon. *Phys. Rev. D*, 88:014041, Jul 2013.

[30] M. Wakamatsu. Gauge-invariant decomposition of nucleon spin. *Phys. Rev. D*, 81:114010, Jun 2010.

[31] Xiang-Song Chen, Xiao-Fu Lü, Wei-Min Sun, Fan Wang, and T. Goldman. Spin and orbital angular momentum in gauge theories: Nucleon spin structure and multipole radiation revisited. *Phys. Rev. Lett.*, 100:232002, Jun 2008.

[32] B. L. G. Bakker, E. Leader, and T. L. Trueman. Critique of the angular momentum sum rules and a new angular momentum sum rule. *Phys. Rev. D*, 70:114001, Dec 2004.

[33] Xiangdong Ji. Gauge-invariant decomposition of nucleon spin. *Phys. Rev. Lett.*, 78:610–613, Jan 1997.

[34] Elliot Leader, Aleksander V. Sidorov, and Dimiter B. Stamenov. Determination of polarized parton densities from a qcd analysis of inclusive and semi-inclusive deep inelastic scattering data. *Phys. Rev. D*, 82:114018, Dec 2010.

[35] Daniel de Florian, Rodolfo Sassot, Marco Stratmann, and Werner Vogelsang. Evidence for polarization of gluons in the proton. *Phys. Rev. Lett.*, 113:012001, Jul 2014.

[36] Elke-Caroline Aschenauer et al. The RHIC Cold QCD Plan for 2017 to 2023: A Portal to the EIC. 2016.

[37] Gerry Bunce, Naohito Saito, Jacques Soffer, and Werner Vogelsang. Prospects for spin physics at RHIC. *Ann. Rev. Nucl. Part. Sci.*, 50:525–575, 2000.

[38] Elke-Caroline Aschenauer et al. The RHIC SPIN Program: Achievements and Future Opportunities. 2015.

[39] L. Adamczyk et al. Precision measurement of the longitudinal double-spin asymmetry for inclusive jet production in polarized proton collisions at $\sqrt{s} = 200$ GeV. *Phys. Rev. Lett.*, 115:092002, Aug 2015.

[40] A. Adare et al. Inclusive double-helicity asymmetries in neutral-pion and eta-meson production in $\vec{p} + \vec{p}$ collisions at $\sqrt{s} = 200$ GeV. *Phys. Rev.*, D90(1):012007, 2014.

[41] Zilong Chang. Gluon Polarization in Longitudinally Polarized *pp* Collisions at STAR. *Int. J. Mod. Phys. Conf. Ser.*, 40:1660021, 2016.

[42] Daniel de Florian, Rodolfo Sassot, Marco Stratmann, and Werner Vogelsang. Global analysis of helicity parton densities and their uncertainties. *Phys. Rev. Lett.*, 101:072001, Aug 2008.

[43] Daniel de Florian, Rodolfo Sassot, Marco Stratmann, and Werner Vogelsang. Extraction of spin-dependent parton densities and their uncertainties. *Phys. Rev. D*, 80:034030, Aug 2009.

[44] Unbiased determination of polarized parton distributions and their uncertainties. *Nuclear Physics B*, 874(1):36 – 84, 2013.

[45] Johannes BlçIJĽmlein and Helmut BæđŽttcher. Qcd analysis of polarized deep inelastic scattering data. *Nuclear Physics B*, 841(1):205 – 230, 2010.

[46] L. Adamczyk et al. Measurement of the cross section and longitudinal double-spin asymmetry for dijet production in polarized pp collisions at $\sqrt{s} = 200$ GeV. *Phys. Rev. D*, 95:071103, Apr 2017.

[47] S. Mrenna T. Sjostrand and P. Z. Skands. Pythia 6.4 physics and manual. *Journal of High Energy Physics*, 2006(05):026, 2006.

[48] E. C. Aschenauer et al. The RHIC Spin Program: Achievements and Future Opportunities. 2013.

[49] M. Harrison, T. Ludlam, and S. Ozaki. Rhic project overview. *Nuclear Instruments and Methods in Physics Research Section A: Accelerators, Spectrometers, Detectors and Associated Equipment*, 499(2):235 – 244, 2003. The Relativistic Heavy Ion Collider Project: RHIC and its Detectors.

[50] H. Hahn et al. The RHIC design overview. *Nucl. Instrum. Meth.*, A499:245–263, 2003.

[51] M. Harrison, Stephen G. Peggs, and T. Roser. The RHIC accelerator. *Ann. Rev. Nucl. Part. Sci.*, 52:425–469, 2002.

[52] M. Kinsho, K. Ikegami, A. Takagi, and Y. Mori. Production of polarized negative deuterium ion beam with dual optical pumping. *Review of Scientific Instruments*, 67(3):1362–1364, 1996.

[53] A. Zelensky et al. Optically pumped polarized H- ion source for RHIC spin physics. *Rev. Sci. Instrum.*, 73:888–891, 2002. [,194(2002)].

[54] I Alekseev, C Allgower, M Bai, Y Batygin, L Bozano, K Brown, G Bunce, P Cameron, E Courant, S Erin, J Escallier, W Fischer, R Gupta, K Hatanaka, H Huang, K Imai, M Ishihara, A Jain, A Lehrach, V Kanavets, T Katayama, T Kawaguchi, E Kelly, K Kurita, S.Y Lee, A Luccio, W.W MacKay, G Mahler, Y Makdisi, F Mariam, W McGahern, G Morgan, J Muratore, M Okamura, S Peggs, F Pilat, V Ptitsin, L Ratner, T Roser, N Saito, H Satoh, Y Shatunov, H Spinka, M Syphers, S Tepikian, T Tominaka, N Tsoupas, D Underwood, A Vasiliev, P Wanderer, E Willen, H Wu, A Yokosawa, and A.N Zelenski. Polarized proton collider at rhic. *Nuclear Instruments and Methods in Physics Research Section A: Accelerators, Spectrometers, Detectors and Associated Equipment*, 499(2):392 – 414, 2003. The Relativistic Heavy Ion Collider Project: RHIC and its Detectors.

[55] H. Okada et al. Absolute polarimetry at RHIC. *AIP Conf. Proc.*, 980:370–379, 2008.

[56] H. Okada, I.G. Alekseev, A. Bravar, G. Bunce, S. Dhawan, R. Gill, W. Haeberli, O. Jinnouchi, A. Khodinov, Y. Makdisi, A. Nass, N. Saito, E.J. Stephenson, D.N. Svirida, T. Wise, and A. Zelenski. Measurement of the analyzing power an in pp elastic scattering in the cni region with a polarized atomic hydrogen gas jet target. *Physics Letters B*, 638(5):450 – 454, 2006.

[57] A. Zelenski, A. Bravar, D. Graham, W. Haeberli, S. Kokhanovski, Y. Makdisi, G. Mahler, A. Nass, J. Ritter, T. Wise, and V. Zubets. Absolute polarized h-jet polarimeter development, for rhic. *Nuclear Instruments and Methods in Physics Research Section A: Accelerators, Spectrometers, Detectors and Associated Equipment*, 536(3):248 – 254, 2005. Polarized Sources and Targets for the 21st Century. Proceedings o f the 10th International Workshop on Polarized Sources and Targets.

[58] Clemens Adler, Alexei Denisov, Edmundo Garcia, Michael J. Murray, Herbert Strobele, and Sebastian N. White. The RHIC zero degree calorimeter. *Nucl. Instrum. Meth.*, A470:488–499,

2001.

[59] J. Kiryluk. Local polarimetry for proton beams with the STAR beam beam counters. In *Spin physics. Polarized electron sources and polarimeters. Proceedings, 16th International Symposium, SPIN 2004, Trieste, Italy, October 10-16, 2004, and Workshop, PESP 2004, Mainz, Germany, October 7-9, 2004*, pages 718–721, 2005.

[60] M. Anderson et al. The Star time projection chamber: A Unique tool for studying high multiplicity events at RHIC. *Nucl. Instrum. Meth.*, A499:659–678, 2003.

[61] M. Beddo et al. The STAR barrel electromagnetic calorimeter. *Nucl. Instrum. Meth.*, A499:725–739, 2003.

[62] Star 2009 eemc mip calibration.

[63] K. H. Ackermann et al. STAR detector overview. *Nucl. Instrum. Meth.*, A499:624–632, 2003.

[64] F. S. Bieser et al. The STAR trigger. *Nucl. Instrum. Meth.*, A499:766–777, 2003.

[65] Ahmed Ali and Gustav Kramer. Jets and QCD: A Historical Review of the Discovery of the Quark and Gluon Jets and its Impact on QCD. *Eur. Phys. J.*, H36:245–326, 2011.

[66] Gavin P. Salam. Towards Jetography. *Eur. Phys. J.*, C67:637–686, 2010.

[67] Matteo Cacciari, Gavin P. Salam, and Gregory Soyez. FastJet User Manual. *Eur. Phys. J.*, C72:1896, 2012.

[68] Abelev et al. Longitudinal double-spin asymmetry for inclusive jet production in $\vec{p} + \vec{p}$ collisions at $\sqrt{s} = 200$ GeV. *Phys. Rev. Lett.*, 100:232003, Jun 2008.

[69] L. Adamczyk et al. Longitudinal and transverse spin asymmetries for inclusive jet production at mid-rapidity in polarized $p + p$ collisions at $\sqrt{s} = 200$ GeV. *Phys. Rev.*, D86:032006, 2012.

[70] Gerald C. Blazey et al. Run II jet physics. In *QCD and weak boson physics in Run II. Proceedings, Batavia, USA, March 4-6, June 3-4, November 4-6, 1999*, pages 47–77, 2000.

[71] Matteo Cacciari, Gavin P. Salam, and Gregory Soyez. The Anti-k(t) jet clustering algorithm. *JHEP*, 04:063, 2008.

[72] Matteo Cacciari, Gavin P. Salam, and Gregory Soyez. The anti- k t jet clustering algorithm. *Journal of High Energy Physics*, 2008(04):063, 2008.

[73] Peter Z. Skands. The Perugia Tunes. In *Proceedings, 1st International Workshop on Multiple Partonic Interactions at the LHC (MPI08): Perugia, Italy, October 27-31, 2008*, pages 284–297, 2009.

[74] S. Agostinelli et al. GEANT4: A Simulation toolkit. *Nucl. Instrum. Meth.*, A506:250–303, 2003.

[75] Charged jet cross sections and properties in proton-proton collisions at $\sqrt{s} = 7$ TeV. *Phys. Rev. D*, 91:112012, Jun 2015.

[76] Matteo Cacciari and Gavin P. Salam. Pileup subtraction using jet areas. *Phys. Lett.*, B659:119–126, 2008.

[77] Andreas Hocker et al. TMVA - Toolkit for Multivariate Data Analysis. *PoS*, ACAT:040, 2007.

[78] L. Adamczyk et al. Neutral pion cross section and spin asymmetries at intermediate pseudorapidity in polarized proton collisions at $\sqrt{s} = 200$ GeV. *Phys. Rev. D*, 89:012001, Jan 2014.

[79] Hal Spinka Bernd Surrow James Hayes-Wehle, Joe Seele. Relative luminosity analysis for run9 pp 200 gev running. Nov. 2012.

[80] Ting Lin. Longitudinal Double-Spin Asymmetries for Forward Di-jet Production in Polarized *pp* Collisions at $\sqrt{s} = 200$ GeV. In *22nd International Symposium on Spin Physics (SPIN 2016) Urbana, IL, USA, September 25-30, 2016*, 2017.

[81] S. Frixione, Z. Kunszt, and A. Signer. Three-jet cross sections to next-to-leading order. *Nuclear Physics B*, 467(3):399 – 442, 1996.

[82] Liaoyuan Huo. In-Jet Tracking Efficiency Analysis for the STAR Time Projection Chamber in Polarized Proton-Proton Collisions at sqrt(s) = 200GeV. Master's thesis, Texas A&M University, (2012).

[83] Daniel de Florian, Stefano Frixione, Adrian Signer, and Werner Vogelsang. Next-to-leading order jet cross sections in polarized hadronic collisions. *Nuclear Physics B*, 539(3):455 – 476, 1999.

[84] A. D. Martin, W. J. Stirling, R. S. Thorne, and G. Watt. Parton distributions for the LHC. *Eur. Phys. J.*, C63:189–285, 2009.

[85] Richard D. Ball, Valerio Bertone, Stefano Carrazza, Luigi Del Debbio, Stefano Forte, Alberto Guffanti, Nathan P. Hartland, and Juan Rojo. Parton distributions with QED corrections. *Nucl. Phys.*, B877:290–320, 2013.

[86] D. Stump, J. Pumplin, R. Brock, D. Casey, J. Huston, J. Kalk, H. L. Lai, and W. K. Tung. Uncertainties of predictions from parton distribution functions. i. the lagrange multiplier method. *Phys. Rev. D*, 65:014012, Dec 2001.

Ting Lin

Curriculum Vitae

Education

2014 Dec. – 2017 Dec. **Ph.D Degree**, *Indiana University*, Bloomington, IN, USA.

2013 Aug. – 2014 Dec. **Master of Science**, *Indiana University*, Bloomington, IN, USA.

2009 Aug. – 2013 Jun. **Bachelor of Science - Physics**, *University of Science and Technology of China (USTC)*, Hefei, Anhui, China.

Research Experience

2014 May – Now **Research Assistant**, *Nuclear Physics Group*, CEEM, Indiana University.
Advisor: Scott W. Wissink

2012 $pp500$ Endcap Di-jet Longitudinal Double-Spin Asymmetries

2009 $pp200$ Endcap Di-jet Longitudinal Double-Spin Asymmetries

2009 $pp200$ Endcap Inclusive π^0 fast simulation

2015 July – Now **Endcap Electromagnetic Calorimeter (EEMC) Software Coordinator**, *Software and Computing Group at STAR*.

2017 $pp500$ EEMC Calibration: Pedestal and Status table Production

2017 $pp500$ EEMC/BEMC Timing Scan Analysis

2016 $AuAu$ EEMC Calibration: Pedestal and Status table Production

2015 $pp200$ EEMC Calibration: Pedestal and Status table Production

2009 $pp200$ EEMC Calibration: Gain Calibration

On-call expert for the EEMC

2012 Jun. – 2013 May **Undergraduate Research Experience**, *Modern Physics Department*, University of Science and Technology of China, Advisor: Liang Han, Minghui Liu.

THESIS: Electro-Weak Correction in the Measurement of the Weak Mixing Angle at D$\emptyset$

Standard Model Higgs boson in Zγ decay mode – fast simulation

Anomalous Triple Gauge Coupling (TGC) in W/Zγ production – fast simulation

Research Related Experience

2016 Aug. **Student**, *11th Hadron Collider Physics Summer School 2016 (HCPSS)*, Fermilab, Fermi National Accelerator Laboratory, Batavia, IL, USA.

Conference Presentation

2017 Oct. 2016 Fall Meeting of the APS Division of Nuclear Physics, Vancouver, BC Canada
"Longitudinal Double-Spin Asymmetries for Forward Di-jet Production in Polarized pp Collisions at $\sqrt{s}$ = 200 GeV"

Conference Poster

2017 Sept. 22nd International Spin Symposium, UIUC, Champaign, IL, USA
"Longitudinal Double-Spin Asymmetries for Forward Di-jet Production in Polarized pp Collisions at $\sqrt{s}$ = 200 GeV"

Conference Proceedings

Longitudinal Double-Spin Asymmetries for Forward Di-jet Production in Polarized pp Collisions at $\sqrt{s}$ = 200 GeV, 22nd International Spin Symposium, arXiv:1705.02655

Teaching Experience

2016 Jun. – 2016 Aug. **Associate Instructor**, *Physics Department*, Indiana University.
Instructor: Daniel Beeker

- Instructor of the Lab section of course PHYS-P 201. Answering the questions at Physics Forum

2013 Aug. – 2014 May **Associate Instructor**, *Physics Department*, Indiana University.
Instructor: Daniel Beeker

- Grader of the course PHYS-P 221, PHYS-P 332. Answering the questions at Physics Forum

Awards

2016 Best Poster Presentation Award, 22nd International Spin Symposium
2012 Scholarship for Outstanding Student - Bronze Award, USTC
2011 Research-Oriented Physics Experiment Contest–Third Prize, USTC
2011 Scholarship for Outstanding Student - Bronze Award, USTC
2009 Outstanding Freshman Scholarship - Bronze Award, USTC

Volunteer Experience

2013-2014	**Volunteer for Physics, Astronomy, Mathematics and Geology Open House, Indiana University**. Prepare some Hands-On science, guide people through the activity and explain some physics principles
2014-2015	**Volunteer for Office of International Student, Indiana University**. Help the office to translate documents from Chinese to English.
2009-2013	**Member of the Volunteer Team of the Physics College, USTC**. Member of the Volunteer Service Team, helping the children (6 to 13 ages) to better accomplish their education.

Computer skills

Basic	C/C++, FORTRAN, PYTHON, LINUX/UNIX AND WINDOWS OS
Intermediate	HTML, LaTeX, Office, Mathematica, Origin Lab